

# The Magnetic Field from Cylindrical Arc Coils and Magnets: A Compendium with New Analytic Solutions for Radial Magnetisation and Azimuthal Current

Matthew Forbes<sup>\*1</sup> William S. P. Robertson<sup>1</sup> Anthony C. Zander<sup>1</sup> Johannes J. H. Paulides<sup>2</sup>

<sup>1</sup>The University of Adelaide

<sup>2</sup>Advanced Electromagnetics Group

<sup>\*</sup>matthew.forbes@adelaide.edu.au

This article provides analytic solutions for the magnetic field of coils and magnets that have a non-axisymmetric cylindrical geometry with a rectangular cross-section. New analytic solutions are provided for radially magnetised permanent magnet arcs, thin coil disc sectors, and thick coil sectors. If components of the 3-D field are not representable in closed-form or as canonical Legendre elliptic integrals, the exact solution is given in terms of a series of regularised beta functions. The limit and hence spatial convergence is found to these series, giving a well-defined and fast solving algorithm for computation. The equations can be readily applied to find the magnetostatic field in linear or non-linear systems that contain a large set of elements. Example applications are provided to demonstrate how the field can be used to calculate forces and benchmark computational efficiency of the equations. A thorough review of the preceding literature and background theory is provided before a detailed methodology obtaining the analytic solutions contained in this compendium, and further related geometries in cylindrical or spherical coordinates. This is the first article to comprehensively solve the field equations for this collection of electromagnetic geometries.

## 1 Introduction

A vast number of engineering-relevant analytic formulations exist in literature for calculating the magnetic field from particular shaped coils and permanent magnets with various current densities or magnetisation directions, respectively. Collections of these elemental solutions, with superposition and without loss of generality, are useful towards the modelling and subsequent optimisation in a range of systems or applications, such as: wireless power transfer [1, 2], energy recovery [3], magnetic imaging [4], magnetic levitation [5], or electric machines [6].

Description and computation of the analytic magnetic field solutions, due to a constant and uniform Cartesian magnetisation, is well-understood for cuboid [7, 8, 9] and polyhedron geometries [10, 11, 12]. Although there are numerous articles on circular cylindrical shapes with well-defined analytic formulations (Section 2), analytic solutions are not known for all principal (Cartesian and cylindrical) magnetisation directions: diametric, radial, azimuthal, axial. This article presents analytic solutions for the 3-D magnetic field from cylindrical arc-shaped magnets with a rectangular cross-section and principal magnetisation, with one of these cases illustrated in Figure 1. Solutions of the magnetic field from a coil with a constant and uniform azimuthal current distribution, including degenerate 2-D and 1-D cases, are included as they are closely-linked to the analysis on magnets.

Toward the scientific description of physical systems, literature has tabulated a comprehensive wealth of mathematical identities, transforms, integrals, and special functions, that are commonly seen in the wide class of formulations (e.g. NIST/DLMF [13], the Bateman manuscripts [14], Gradshteyn and Ryzhik [15]). These are useful for even the most fundamental of electromagnetism problems, where for example, the magnetic field from a 1-D current loop is known to have an analytic solution that is expressed with special functions. More complex electromagnetism problems, particularly non-

axisymmetric 2-D or 3-D geometries, may currently require in-part or entirely, a numeric integral or infinite series expansion. The discretisation of the solution space from a numeric integral, especially when a system has a number of these elements, leads to a large computational requirement for a parametric study. Alternatively, series expansions may require a large number of terms to converge in the near-field, where accurate solutions are required for the characterisation of systems with a small air-gap – leading to similar issues as the numeric integral.

The challenge exists that there is no programmatic way to discover all analytic solution forms for a particular problem, especially when it comes to those not expressible in closed-form, but in terms of special functions and/or a series expansion. The benefit of finding an explicit (non-integral) solution is not limited to computational efficiency; it is also inherently non-dimensional and provides insight into the mathematical and physical structure of the problem. A numerical study

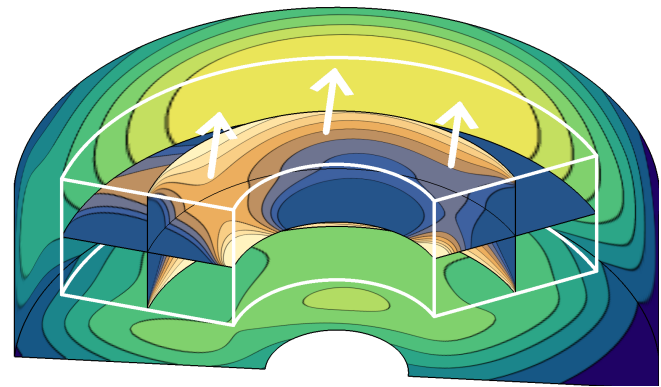


Figure 1: This article presents magnetic field solutions for cylindrical arc geometries with various magnetisations or current densities. Shown is the field magnitude from a permanent magnet with diametric magnetisation.

provides no direct link between input and output parameters, thus cannot provide such an understanding on the geometrical picture [16, pg.99]. The benefit to converting an integral representation to an explicit solution in terms of a canonical special function is on the proviso that it is well-understood in literature with known structure and optimised methods of computation. That being said, not all special functions are equivalently amicable to computation, and may have an arguable improvement over standard numerical integration (e.g., certain hypergeometric functions are computationally expensive).

The choice of Green's function  $1/r$  effects the solution form. In cylindrical coordinates  $1/r$  can be represented as an elementary function, or as any number of integral-series forms (e.g. the Fourier-Bessel series containing the Lipschitz-Hankel integral, shown in Appendix E). For cylindrical geometries, it is known in-general in the literature (shown in Section 2) that the elementary  $1/r$  used to solve Poisson's equation leads to solutions containing elliptic integrals, and the integral-series leads to solutions containing hypergeometric functions. The former is the most prevalent due to it being numerically simple to solve [17, §3]; however, explicit solutions are not commonly found in literature for all magnetic field components, requiring a numeric integral at least partially. Contrary, the latter integral-series are analytically simple as they contain elementary terms, but are numerically complex as they involve a series expansion [18, §7]. In this article, analytic solutions are given by hierarchy — where a solution can not be expressed in elementary functions or as an elliptic integral, we express as a series containing the regularised beta function. The series are shown to be absolutely convergent and avoid spatial issues with calculation on varying parameters [19].

Analytic solutions herein do not strictly pertain to linear and anisotropic matter, void of demagnetisation. Real-world systems contain permanent magnets with a non-unity relative permeability and/or isotropic matter such as iron. The magnetic field from both can be approximated by an equivalent set of linear permanent magnets with an iterative process [20]. This is an important motivation as such outcomes are only practicable using exact fast-solving equations. The appropriate inclusion of iron can achieve a region of magnetisation  $\approx 50\%$  higher than a permanent magnet at room temperature [21], and can be magnetised in any direction. Using analytic solutions one can quickly sample a multivariate solution space for an optimal region, yet this still requires a starting topology found via rule of thumb, previous research, or an optimal segmentation algorithm [22, 23]. The analytic solutions presented in this article can provide feedback into these algorithms on the shape and position of iron elements.

The primary scope of this article is derivation of the magnetic fields, although examples using these solutions for the efficient calculation of forces are provided (that also extend to torques). As well as being exact, analytic solutions tend to imply computational benefit; however, benchmarking is complex due to practical uses requiring the calculation of the field at a number of spatial points and sources, thus efficiency is impacted from the choice of coding language, use of control structures and flow, and CPU usage. The magnetic field is used in calculating figures of merit, with the derivative used for small magnetic particles, and integral used for a distri-

bution of sources. For example, in an electromechanical system one can: optimise global force or torque, minimise or maximise the field through a region, calculate the magnetic inductance/back-EMF, or use static cases with perturbation theory to estimate profiles with time/displacement-variant coil current and/or relative movements of magnetic sources. For semi-analytic methods, spatially accurate (or consistent) solutions are important when discretising the field contour over a closed surface to not introduce further error with a non-zero numeric divergence.

## 1.1 Key contributions & motivation

The authors required an analytic solution for a radially magnetised permanent magnet (or iron segment) and thick coil for a 3-D model of a non-axisymmetric tubular linear synchronous motor. These solutions did not exist in literature, and the methods required for a solution led to an improved methodology and analytic simplification for related integrals. Those have a common topology and boundary conditions: a permanent magnet with alternate magnetisation vectors or thin coils.

**(a) Compendium of previous disparate work** The first comprehensive set of new analytic magnetic field derivations and solutions, summarised in Table 1. The rationale of an ‘improved solution’ terminology is defined in the opening to Section 2. This compendium exists as there is scope within the solution set for an improved methodology and further simplification and/or investigation to some already known analytic solutions. In addition, this article provides a comprehensive derivation for all cases, including a comparison with FEA (when appropriate), handling of all singularities, and reduced formulae for special cases (hollow, solid, axisymmetric). The inherent benefit of a compendium is the common methodology and consistent mathematical notation.

**(b) Mixed boundary conditions** A review and application of background theory, demonstrating that each model (current, charge, filament) need not be applied to a problem in isolation. The formulation of a problem in multiple mathematically equivalent models gives integral transforms that are otherwise difficult to intuit and can lead to analytic solutions.

**(c) Transformed Legendre elliptic integral** A methodology for solving the collection of equations in this article using an integral transform for the circular cylindrical arc (1-D, 2-D, or 3-D) geometry that:

- Avoids cumbersome trigonometric identities and allows partial fraction expansion;
- Ensures the integral reduces into components containing an elementary function, Legendre elliptic integral, and/or non-elliptic integral;
- Removes the requirement of having to find a particular elliptic integral form from a table [24];
- Produces a transformed Legendre elliptic integral form that has a correctly bound amplitude  $0 < \phi < \pi/2$ , reducing numeric processes and simplifying computation.

**(d) Canonical Beta series solutions** When a part of the solution cannot be expressed as an elementary or elliptic function, we can express this in terms of a series of regularised beta functions. This is an improvement to the standard hypergeometric series in literature, providing:

- A significant improvement in computation by reducing to a special case of the hypergeometric function;
- The use of recurrence relations to find the series limits and ensure absolute convergence;
- An absolute remainder or a related tolerance parameter for the partial sum that ensures a uniform spatial convergence. This mathematically defines the near-field and far-field for a region, showing the regions that require more terms for an accurate partial sum;
- Suggested algorithms for the computation that without, the authors argue, render such series of limited use for large scale parametric studies in the near-field of permanent magnets or coils (e.g. small air-gaps and use of the Maxwell stress tensor);
- A new closed-form expression to a hypergeometric/beta series.

## 1.2 Article structure

Section 2 identifies the new analytic solutions presented in this article. Some solutions from the literature are re-introduced, in order to: form the compendium, demonstrate methodology, and provide further simplifications to the solution and include special cases.

Section 3 contains the significant novelty of this article. Significant challenges in the derivation of the analytic solutions are overcome. This section defines the coordinate transforms and geometric parameterisations required, and solves a series of examples that integrate  $1/r$ . The examples link an integral form to a solution form, and results are used as components directly in later sections. In the case of a series solution, we find the limit to each series in order to have an algorithm to efficiently compute a partial sum.

Section 4 solves the 3-D magnetic field from azimuthal current densities in the geometries: 1-D filament, 2-D disc, 2-D shell, and 3-D volume.

Section 5 solves the 3-D magnetic field from a 3-D volume with principal magnetisations: diametric, radial, azimuthal, and axial.

Section 6 presents examples using the magnetic field solutions for efficient calculation of forces.

For readers that wish to view a specific magnetic field solution, the sections are listed in Table 1.

## 2 Preceding literature

We consider literature relevant to the cylindrical arc geometries, shown in Table 1. If a solution existed in the literature, note that we have not simply reproduced it here. We provide a unique and comprehensive methodology for solving each problem, compare results with FEA, and provide a simplified

solution and/or singularity treatment for each geometry. The comprehensive methodology and presented solutions thus extends the prior disparate works — unifying them with a common methodology and consistent mathematical notation.

A closed-form solution here is defined as an elementary solution, containing only algebraic expressions and/or a finite sum of elementary functions [13, §4]. It can be argued that closed-form extends to additionally include a finite sum of special functions; however, we define these in the broader set of (fully) analytic solutions. The focus is the identification of relevant integrals that have an exact analytic solution and do not require a numeric approximation.

## 2.1 Brief history

The advent of permanent magnets in the 1960s [21] led to the discovery of modern Nd-Fe-B alloys in the 1980s [25, 26]. The powder metallurgy process gives a magnetic material that can be assumed approximately homogeneous with uniform magnetisation and unity relative permeability. Therefore, this region of matter can be accurately modelled by Laplace's equation and the integral form. Due to this, since the 1980s, analytic formulations for the magnetic field of permanent magnets have received great interest for use in the modelling and optimisation of permanent magnet devices. A predominant amount of literature focuses on descriptions of periodic multipole arrays [27, 28] (e.g. the Halbach array) as opposed to the solution for individual elements.

Well before modern permanent magnets, coils could be manufactured and adequately modelled as a set of filaments of wire (current loops) with DC current and minimal losses (e.g., the Helmholtz coil). Analytic simplification and elliptic integral tabulation was of interest for practical use of the filament in engineering applications up to the 1950s [29, 30]. In the 1960s early digital computer implementations used the filament approach with fundamental Legendre elliptic integral expressions to describe the field from complex systems [31, 32]. Interest in this area of computational physics continues, with recent papers on using the magnetic field from a filament [33].

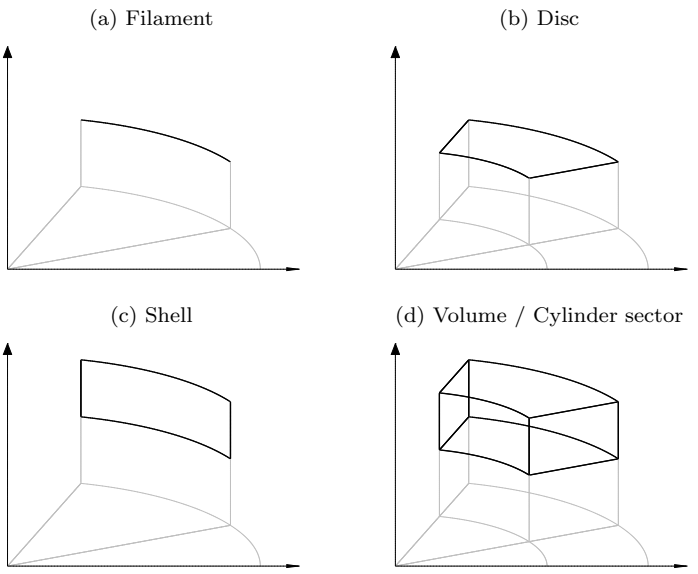
Most coil and permanent magnet analytic solutions contain in-part an elliptic integral that can arguably be considered computationally analogous to the closed-form expressions with algorithms from (to name a few): Bulirsch [34, 35]; contributions from Carlson for NIST [13, 36]; a large series of articles by Fukushima [37]; online repositories with additional contributions [38, 39].

## 2.2 Magnets

The original axisymmetric (cylinder) analytic integral formulations were given by Furlani for axial [40], radial [41], and diametric (bipolar/transverse/Cartesian) [42] magnetisations. These formulations describe the volume of magnetisation with a summation of surface integrals with a charge or current density. A method for completing the first integration is shown by Furlani for all vector components, with a variation of elementary functions, approximations, and/or numerical integration methods used for the remaining integral. There are a number of articles for all principal magnetisation directions that

Table 1: Summary of the new general (non-axisymmetric) analytic magnetic field solutions developed in this article for cylindrical arc geometries compared to those existing in literature. Legend: no previous solution **X**; previous or new solution **✓**; improved solution **✓✓**; bold highlights a previously unavailable analytic solution.

Source	Type	Previous work	This work	Section
Current	Filament	✓	✓✓	4.1
	<b>Disc</b>	<b>X</b>	✓	<b>4.2</b>
	Shell	✓	✓✓	4.3
Magnetisation	<b>Volume</b>	<b>X</b>	✓	<b>4.4</b>
	Diametric	✓	✓✓	5.1
	<b>Radial</b>	<b>X</b>	✓	<b>5.2</b>
	Azimuthal	✓	✓✓	5.3
	Axial	✓	✓✓	5.4



provide iterative simplifications by in-part or fully analytic solutions (including alternate Green's functions) for either the axisymmetric or non-axisymmetric (cylinder arc/sector) geometry. These are summarised as follows.

'Arbitrary' magnetisation is a term commonly used in the literature that implies Cartesian magnetisation, the sum of diametric and axial magnetisation basis vectors. Recently, the complete and singularity-free solution for arbitrary magnetization was given by [43] for an axisymmetric geometry, also including the field gradient, by using Bulirsh's integrals and the Heuman lambda function. Arbitrary magnetisation, however, does not describe the cylindrical magnetisations in the radial and azimuthal directions, which are also included in the solutions presented in this article.

### 2.2.1 Diametric

An axisymmetric analytic solution was given by [44], that firstly solved the scalar potential with an infinite series of hypergeometric functions. A finite number of terms in this scalar potential were symbolically differentiated to give an accurate and simple solution for the magnetic field in the far field.

Another axisymmetric analytic solution was given by [45] using complete elliptic integrals. Similar to [44], the scalar potential was first given and the elliptic integrals directly differentiated. A simplified form is given here Eq.(283), that by inspection contains similar terms to [45], that is derived without differentiation or a fixed magnetisation direction requirement. An alternate solution to [45] was later given by [46] with direct integration. Using the MATLAB code of [46], the authors can verify equivalent (to 8 s.f.) numeric solutions at the tabulated field points as detailed in Table K.2 for the (real) azimuthal and axial components, but do not find agreement with the results for the radial component.

No known analytic solution was originally found for the

non-axisymmetric case; however, during the preparation of this manuscript, [47] was published that solves the diametric (& axial with superposition) field equations. The analytic solutions of [47] can handle singular cases, and have excellent agreement in comparison to an FEA model. The solutions presented herein were derived independently, and are in a significantly simplified analytic form (251). Using the Python code of [47], the authors can verify equivalent (to 8 s.f.) numeric solutions at the tabulated field points as shown in Table K.2. Care should be taken by the reader in comparing these derivations as we present results for the **B**-field that require the addition of **M** inside the magnet, whereas [47] gives an equation for the **H**-field.

Notable contributions are given by [48, 49, 50, 51] with foundational numeric solutions.

### 2.2.2 Radial

Partial analytic solutions for the magnetic field components are given [52, 53] for the axisymmetric case. These papers did not consider the volumetric charge component (A31), that was shown previously by [54] and verified using FEA<sup>1</sup>. Using a similar approach to [44], the axisymmetric analytic solution is given by [56] as a compact series of hypergeometric functions.

A series of three papers ensued by the author(s) of [52] for the non-axisymmetric case: [57] continued to not include the volumetric charge component; [58] provides a closed-form azimuthal component, equivalent to Eqs.(302), (301); [59] gives an analytic solution for the radial component containing an imaginary component and a numeric solution for the axial component.

<sup>1</sup>[53] did ameliorate the solution of [52], removing imaginary components. The circular case of the Legendre integral  $\Pi(\theta, a^2, k)$  (E21) can be transformed to the Heuman lambda function  $\Lambda(\theta, b^2, k)$  [55, §5]. This was used in [53] to avoid singularities with  $\Pi$  in the plane of the source distribution; however, in this article we directly deal with these singularities (e.g. (200))

No fully analytic solution for the non-axisymmetric case was found in the literature.

### 2.2.3 Azimuthal

The only analytic solution found in literature for the azimuthal (tangential) magnetisation is [60], perhaps due to the axisymmetric case being ‘insulating’, having no external magnetic field. The solution of [60] is in closed form, given in (324). This solution was extrapolated by [60] as analogous to a cylindrical arc with radial current  $\mathbf{J} = (J_\rho/\rho')\mathbf{e}'_\rho$  (Section 3) [61]. Although not directly comparable, this is an important observation as it links a closed-form expression to multiple integral forms, illustrated by Figure 2 (from Table J.1, Table J.2). The uniform circumferential current loops on the shell and disc surfaces require a non-uniform axial volumetric current distribution to maintain continuity; the sum gives a magnetic field equivalent to that of two polarised sections of charge.

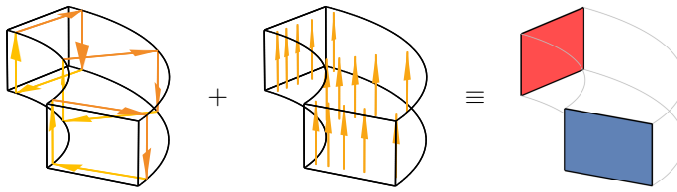


Figure 2: Surfaces of current and a volume of current that are equivalent to surfaces of charge.

In actuality, this current density [61] is a degenerate case of the uniform current density  $\mathbf{J} = J_\rho \mathbf{e}'_\rho$  as the integral with respect to  $\rho'$  reduces in order. Both solutions are captured within those of the disc (159) and volume (214) with an azimuthal current density, and analytic solutions can be found by inspection of the results in this article (using elliptic integrals and incomplete beta functions).

### 2.2.4 Axial

In parallel to the work from Section 2.2.2, the articles [52, 53] also present the first iteration of analytic solutions for the axisymmetric case with axial magnetisation. The radial component of the field was reproduced from [62] in [52], and [53] gave an improved real-valued solution for the axial component.

Eloquent analytic solutions using elliptic integrals are given by [63] (axisymmetric) and [64] (non-axisymmetric), for which we obtain identical solutions (Eqs. (363), (349)). The derivation is omitted from [64], citing the method of [65] with a simplification of the analytic solution. Further notable solutions are given in [66] (axisymmetric) and [67] (non-axisymmetric).

The previously discussed articles by Selvaggi for diametric [44] and radial magnetisation [56] use an integral-series Green’s function for the axisymmetric geometry. For axial magnetisation, Selvaggi [68] demonstrates a similar analytic solution for both the axisymmetric and non-axisymmetric cases using a series containing hypergeometric functions — importantly, claiming a ‘quick’ convergence. The ‘standard’ Legendre elliptic integrals well-describe the field from these regular cylindrical shapes because the series expansion converges on

the exact solution rapidly and with a low number of terms [69, 70, 37]. These articles [44, 56, 68] are important as they demonstrate a general series that may similarly well-describe the geometry (source/field) and converge on the exact solution with a reasonably low number of terms. What the articles do not provide is a detailed error analysis or method for choosing an appropriate number of terms. Additionally, the non-axisymmetric case contains a doubly-infinite series with no investigation into the reduction of such a series, or specification on how to complete the partial sum. These considerations lead to computational inefficiency in the magnetic near field. This is the primary topic addressed in Section 3.

## 2.3 Coils

A number of authors provide analytic solutions to multiple cylindrical structures with an azimuthal current density. Examples of this foundational work are given by Snow [71], Conway [72], and Urankar [73] in a series of five articles. In the following review, each geometry is considered individually for simplicity: filament (current loop), disc (annulus, pancake coil), shell (sheet, thin coil, thin solenoid), and volume (cylinder sector, thick coil, thick solenoid).

### 2.3.1 Filament

The axisymmetric filament (or current loop) is a fundamental derivation from classic texts on basic electromagnetism [74, pg.142], [75, pg.290], with an analytic solution in terms of Legendre elliptic integrals (150). A filament approach is appropriate when the cross-sectional area of a wire (conductor) is negligible compared to the field (observation) point. For a coil with a complex cross-sectional shape, superposition can be used to produce a simple analytic approximation [31, 76].

The non-axisymmetric arc filament is useful for modelling end-windings or rounded rectangular/polygonal coils. The first analytic solution was given in [73] in terms of Legendre elliptic integrals and Jacobi elliptic functions. This was later given in a simplified form [77] with Cartesian coordinates, using only Legendre elliptic integrals (with Cylindrical coordinates in Eq.(132)). 40 years later from [73], authors continue to use these filamentary analytic solutions: toward higher-order problems [33], a re-derivation [78], or to find further computational improvement via analytic approximation [79, 80, 81].

### 2.3.2 Disc

The article of Snow [71] is intriguing as, dependent on geometry (shell, disc, or layered volume of either), solutions are given in terms of Legendre elliptic integrals or spherical harmonic series (of Legendre polynomials). The commentary identifies that no solution was found as a finite sum, or is possible, for the axial magnetic field component of the disc. Literature is limited on this particular geometry, with seemingly more interest on Bitter discs with radial currents. Work towards an analytic solution using only Legendre elliptic integrals shows that there is a component left that requires numeric integration [82].

Conway noted the disc and related geometries from Snow (even related physical problems [83]) can be formulated using

the Fourier-Bessel integral series (also named a toroidal harmonic, cylindrical harmonic, or Bessel-Laplace series), and those can always be evaluated in terms of elliptic integrals using recurrence relations [72]. An analytic solution for the axisymmetric disc was given for any radial distribution of azimuthal current as a series of Legendre (and Heuman) elliptic integrals. Following the discussion of Section 2.2.4 with the analytic solutions of Selvaggi, there is sparse discussion on the convergence of these series solutions.

No fully analytic solution for the non-axisymmetric case was found in the literature.

### 2.3.3 Shell

The analytic solution for the axisymmetric shell was given in terms of Legendre elliptic integrals [71, eq.39] (205) (and later in [84] using the Heuman lambda function, as in [53]). With solutions over 50 years later for the axial permanent magnet [52], researchers again noted the mathematical equivalence between different physical models [66]; comparison of (205) and (364) shows that the 3-D field from two shells of current is equivalent to that of two discs of charge (Figure 3, where the section surfaces of current disappear when axisymmetric). Notable further discussions are given by [38, 85].

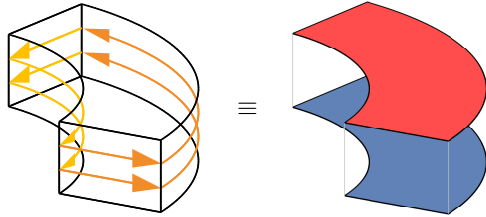


Figure 3: Surfaces of current that are equivalent to orthogonal surfaces of charge.

An analytic solution for the non-axisymmetric case was given by [86] as part of a more general solution of a conic shell (when the inclination is  $\pi/2$ ), in terms of Legendre elliptic integrals (190).

### 2.3.4 Volume

Following the disc discussion of Section 2.3.2, Snow [71] found an analytic solution from the scalar potential using differentiation and Legendre polynomial recurrence relations. This gave a series solution including associated Legendre polynomials for both the radial and axial field components. Conway [72] performed an axial integration on the disc vector potential to give a solution again in terms of a series of elliptic integrals, but only gave a magnetic field solution for the first term of the series. Each term in the series requires the use of reduction formulas to get to the canonical elliptic integrals.

Conway later gave a simplified numerical solution or implementation using trigonometric/periodic integrands [87], that whilst do not form an analytic solution, may form a computationally simpler procedure due to the analytic solution complexity. This argument was similarly made in [88], claiming special functions (for this problem) may provide no special advantage for numeric computation, and proposes a simple

numerical routine. Continuing, [89] provided a similar solution that included analytic solutions for the singular regions of the integrals. A number of authors made contribution to simplifying the solutions for the axisymmetric [90, 91, 92] and non-axisymmetric [93, 94, 95] cases that reduce the solution into various combinations (part analytic, part numeric) containing: elementary functions, elliptic integrals, and a single integration along the azimuth.

A different approach was shown in [96] to [71] or [72], using a non-standard polynomial series for the field result of a shell, with an analysis on convergence. An analytic solution from a radial integration of the shell was not found, and instead an analytic approximation was given as with other previous work [81, 97]. It has also been possible to approximate the field of the coil using an equivalent permanent magnet, using a boundary element method to find a region of magnetisation that produces an equivalent magnetic field to the azimuthal current density [98, 99].

No fully analytic solution for the non-axisymmetric case was found in the literature.

## 2.4 Summary

To the best knowledge of the authors there are no analytic solutions in the literature for the non-axisymmetric cases of a permanent magnet with radial magnetisation, a disc with azimuthal current, or a cylindrical volume element with azimuthal current. A parallel analytic solution was only recently presented for a permanent magnetic with diametric magnetisation.

## 3 Methods: Integral transforms and discussion

The discussion in the following subsections provides the rationale behind the analytic solution forms to be presented in this article. This is done via a series of examples that demonstrate the methodology, and the examples each directly form a part of a solution for the magnetic field from a cylindrical arc coil or permanent magnet.

A detailed review of the background theory is given in Appendix A and a summary of notation with nomenclature is given in Appendix B.

### 3.1 Geometry

The topology investigated in this article is shown in Figure 4. Cylindrical orthonormal bases are defined for the: location of the field point

$$\mathbf{r} = \rho \mathbf{e}_\rho + z \mathbf{e}_z; \quad (1)$$

location of the source point

$$\mathbf{r}' = \rho' \mathbf{e}'_\rho + z' \mathbf{e}'_z, \quad (2)$$

where  $\rho' \in [\rho'_1, \rho'_2]$ ,  $\varphi' \in [\varphi'_1, \varphi'_2]$ ,  $z' \in [z'_1, z'_2]$ ; and magnetisation directionality

$$\mathbf{M}(\mathbf{r}) = M_\rho \mathbf{e}_\rho + M_\varphi \mathbf{e}_\varphi + M_z \mathbf{e}_z, \quad (3)$$

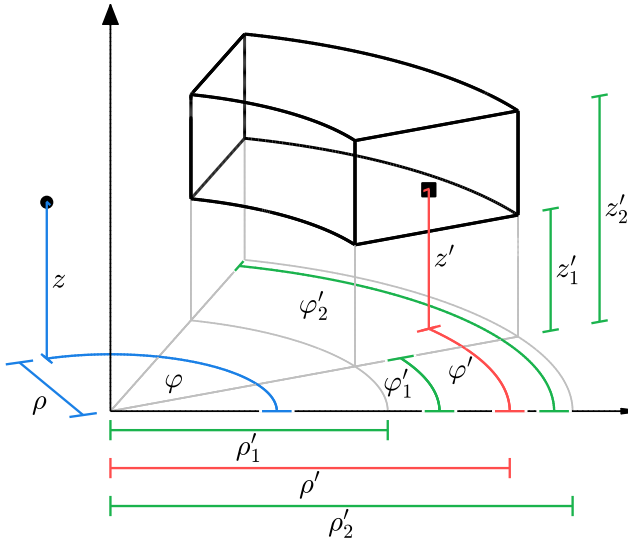


Figure 4: Parameterisation of geometry for a rectangular cylindrical sector. Primed cylindrical parameters define the integration region of source points (square) with respect to a field point (circle).

where we have superposition of uniform spatial components of the magnetisation  $M$  in each basis vector. For Cartesian (or transverse/diametric) magnetisation

$$\begin{aligned} \mathbf{M}_\perp(\mathbf{r}) &= M_\perp(\cos\varphi^*\mathbf{e}_x + \sin\varphi^*\mathbf{e}_y), \\ &= M_\perp[\cos(\varphi^* - \varphi)\mathbf{e}_\rho + \sin(\varphi^* - \varphi)\mathbf{e}_\varphi] \end{aligned} \quad (4)$$

with the cylindrical parameter  $\varphi^*$  for the magnetisation direction. For integration, the cylindrical source (primed) basis is projected onto the field point (unprimed) basis, with cylindrical parameters relative to a fixed Cartesian frame of reference, giving:

$$\begin{aligned} \mathbf{r}' &= \rho'\cos(\varphi - \varphi')\mathbf{e}_\rho - \rho'\sin(\varphi - \varphi')\mathbf{e}_\varphi + z'\mathbf{e}_z, \\ \mathbf{M}(\mathbf{r}, \mathbf{r}') &= [M_\rho \cos(\varphi - \varphi') + M_\varphi \sin(\varphi - \varphi')]\mathbf{e}_\rho \\ &\quad + [M_\varphi \cos(\varphi - \varphi') - M_\rho \sin(\varphi - \varphi')]\mathbf{e}_\varphi + M_z\mathbf{e}_z, \\ \mathbf{M}_\perp(\mathbf{r}, \mathbf{r}') &= M_\perp[\cos(\varphi^* - \varphi)\mathbf{e}_\rho + \sin(\varphi^* - \varphi)\mathbf{e}_\varphi]. \end{aligned} \quad (5)$$

In this article we do not consider directional variance in the current density, and only a uniform spatial component in the azimuthal direction of

$$\mathbf{J} = J_\varphi \mathbf{e}'_\varphi, \quad (6)$$

where

$$\mathbf{e}'_\varphi = \sin(\varphi - \varphi')\mathbf{e}_\rho + \cos(\varphi - \varphi')\mathbf{e}_\varphi. \quad (7)$$

Dimensionally, we have

$$\frac{d\mathbf{I}}{d\rho' dz'} = \mathbf{J} \quad (8)$$

$$\frac{d\mathbf{I}}{d\rho'} \text{ or } \frac{d\mathbf{I}}{dz'} = \mathbf{K} \quad (9)$$

with the filament current

$$\mathbf{I} = I_\varphi \mathbf{e}'_\varphi \quad (10)$$

and surface current

$$\mathbf{K} = K_\varphi \mathbf{e}'_\varphi. \quad (11)$$

The outward facing normals  $\mathbf{n}(\mathbf{r}, \mathbf{r}')$  for each surface of the rectangular cylindrical sector are:

$$\text{shell, } \mathbf{n}_\rho(\mathbf{r}, \mathbf{r}') = \pm[\cos(\varphi - \varphi')\mathbf{e}_\rho - \sin(\varphi - \varphi')\mathbf{e}_\varphi]; \quad (12)$$

$$\text{section, } \mathbf{n}_\varphi(\mathbf{r}, \mathbf{r}') = \pm[\sin(\varphi - \varphi')\mathbf{e}_\rho + \cos(\varphi - \varphi')\mathbf{e}_\varphi]; \quad (13)$$

$$\text{disc, } \mathbf{n}_z(\mathbf{r}, \mathbf{r}') = \pm\mathbf{e}_z. \quad (14)$$

### 3.2 Elliptic integral

To demonstrate the solution process involving an elliptic integral, we consider an example of the line integral along the azimuth

$$\int_{\varphi'_1}^{\varphi'_2} \hat{G}(\rho', \varphi - \varphi', z') d\varphi' \quad (15)$$

with inverse distance function

$$\hat{G} = \frac{1}{|\mathbf{r} - \mathbf{r}'|} = \frac{1}{\sqrt{T^2 - 2\rho\rho' \cos\Phi}} \quad (16)$$

being the Green's function (A17) with constants removed, where

$$\Phi = \varphi - \varphi', \quad (17)$$

$$Z = z - z', \quad (18)$$

$$L^2 = \rho^2 + Z^2, \quad (19)$$

$$T^2 = L^2 + \rho'^2. \quad (20)$$

The successive substitutions for simplifying the trigonometric argument of (15) are  $2\hat{\phi} - \pi = \varphi - \varphi'$  and

$$\hat{\phi} = \begin{cases} \sin^{-1} t, & \text{for } -\frac{\pi}{2} \leq \hat{\phi} \leq \frac{\pi}{2}, \\ \pi - \sin^{-1} t, & \text{for } \frac{\pi}{2} < \hat{\phi} \leq \pi, \\ -\pi - \sin^{-1} t, & \text{for } -\pi < \hat{\phi} < -\frac{\pi}{2}, \end{cases} \quad (21)$$

where the  $t$ -substitution is useful for partial-fraction expansion and significantly simplifies the solution steps, avoiding tedious factorisation and reliance upon finding trigonometric identities as employed in preceding literature. The  $\hat{\phi}$ -substitution formats the radicand into a standard form, for reasons to become apparent. Following is the new form of (15),

$$\hat{G}(\rho', 2\cos^{-1} t, z') = \frac{1}{\sqrt{\varrho^2 + Z^2 - 4\rho\rho't}} \quad (22)$$

with the integral transformation

$$\int_{\varphi'_1}^{\varphi'_2} \hat{G} d\varphi' = \frac{2}{R} \sum_{q=1}^2 (-1)^q \operatorname{sgn}(\Phi_q) \int_1^{\cos(\frac{1}{2}\Phi_q)} \frac{dt}{w(t)}, \quad (23)$$

where  $\operatorname{sgn}$  is the sign function, and we define the summation notation  $\varphi'_q \in \{\varphi'_1, \varphi'_2\}$  (Appendix B) to simplify the definite

integral and the variables

$$\varrho = \rho + \rho', \quad (24)$$

$$R^2 = \varrho^2 + Z^2, \quad (25)$$

$$k^2 = 4\rho\rho'/R^2, \quad (26)$$

$$w^2 = (1 - t^2)(1 - k^2t^2). \quad (27)$$

The modulus  $k < 1$  if both  $\rho \neq \rho'$  and  $Z \neq 0$ , and  $k > 0$  if  $\rho \neq 0$ . With the amplitude  $\phi$  in the upper integral limit, there is an invariant integrand due to the change of variable  $(\partial\phi/\partial t)$  and a sign change from the integration range (21) to use  $\sin^{-1} t$  continuously. This introduces an issue with the integration limit domain not having a one-to-one mapping; therefore, the integral is split about the line of symmetry at  $\varphi - \varphi'_q = 0$  and negated when  $\varphi'_q > \varphi$ . The sign function represents this branch point of the  $t$ -substitution.

From the integrand of (23), we can expect answers in the form of  $P(t, w(t))$ , where  $P$  is a rational function of  $t$  and  $w$  (G14). When  $w^2$  is a polynomial of the first or second degree then  $\int P dt$  reduces to an elementary function, else when of a third or fourth degree, then we have an elliptic integral. Elliptic integrals can always be reduced to any of three canonical Legendre forms [100, pg.589]. Modern literature has considered the use of symmetric elliptic integrals that can be reduced to two canonical Carlson forms [101], that are free from modulus and argument transforms ([24, pg.38]) that may be required in the Legendre form. For comparison the Carlson algorithms were implemented as part of this work; however, no significant computational or mathematical reductions were found and solutions using these forms have been omitted for brevity.

The integration limits of (23), when split about 0, naturally give rise to expressions in terms of both the complete and incomplete elliptic integrals. In this case, Legendre's integrals of the first kind (E19), (E23) gives the elegant solution

$$\int_{\varphi'_1}^{\varphi'_2} \hat{G} d\varphi' = -\frac{2}{R} \sum_{q=1}^2 (-1)^q F(\phi_q; k^2), \quad 0 < \phi < \frac{\pi}{2} \quad (28)$$

where

$$\phi = \frac{1}{2}(\Phi + \pi). \quad (29)$$

The sign function is absorbed by elliptic integrals as they are odd functions and the complete elliptic portion of the integral cancels over the summation. It appears standard in literature to consider (28) a complete solution; however, for evaluation time and robustness, the elliptic integrals should be correctly bound with the amplitude  $0 \leq \phi \leq 2\pi$ , thus removing the odd components and reducing numerical procedures. This is especially important when using Legendre's integrals of the third kind as they are a function of three variables. Applying the elliptic integral transforms (E27) and (E28) gives

$$\begin{aligned} \int_{\varphi'_1}^{\varphi'_2} \hat{G} d\varphi' &= \frac{2}{R} \sum_{q=1}^2 (-1)^q [(1 - \text{sgn } \Phi_q) K(k^2) \\ &\quad - \text{sgn } (\Phi_q \Psi_q) F(\frac{1}{2}|\Psi_q|; k^2)], \quad -\frac{\pi}{2} \leq \phi < \frac{3\pi}{2} \end{aligned} \quad (30)$$

where  $\Psi = |\Phi| - \pi$  and  $\Phi \equiv 2\phi - \pi$ . The intricacy of the transform from (28) to (30) is shown in TABLE 2.

Table 2: Transformation of the function  $F(\phi; k^2)$  with elliptic amplitude  $-\pi/2 \leq \phi < 3\pi/2$  or cylindrical angle  $\varphi - \varphi'$ , assuming  $0 \leq \varphi < 2\pi$  and  $0 \leq \varphi' \leq 2\pi$ .

Transformation	Amplitude $\phi$	Angle $\varphi - \varphi'$
$-K(k^2)$	$\phi = -\frac{\pi}{2}$	$\varphi - \varphi' = -2\pi$
$-F(\frac{1}{2} \Psi ; k^2)$	$-\frac{\pi}{2} < \phi < 0$	$ \varphi - \varphi'  > \pi, \quad \varphi < \varphi'$
0	$\phi = 0$	$\varphi - \varphi' = -\pi$
$F(\frac{1}{2} \Psi ; k^2)$	$0 < \phi < \frac{\pi}{2}$	$ \varphi - \varphi'  < \pi, \quad \varphi < \varphi'$
$K(k^2)$	$\phi = \frac{\pi}{2}$	$\varphi = \varphi'$
$2K(k^2) - F(\frac{1}{2} \Psi ; k^2)$	$\frac{\pi}{2} < \phi < \pi$	$ \varphi - \varphi'  < \pi, \quad \varphi > \varphi'$
$2K(k^2)$	$\phi = \pi$	$\varphi - \varphi' = \pi$
$2K(k^2) + F(\frac{1}{2} \Psi ; k^2)$	$\pi < \phi < \frac{3\pi}{2}$	$ \varphi - \varphi'  > \pi, \quad \varphi > \varphi'$

Whenceforth, we define the transformed Legendre form

$$F(\phi; k^2) = (\text{sgn } \Phi - 1)K(k^2) + \text{sgn } (\Phi\Psi)F(\frac{1}{2}|\Psi|; k^2) \quad (31)$$

that is interchangeable within the definite integral

$$F(\phi_q; k^2) = F(\phi_q; k^2), \quad (32)$$

and outside, it is shifted

$$F(\phi; k^2) = F(\phi + \pi; k^2). \quad (33)$$

To extend the input range  $\forall \phi$ , we define the staircase  $n$ , square wave  $q$ , and triangle wave  $t$  functions:

$$\tilde{\Phi} = \Phi/(2\pi), \quad (34)$$

$$n = \lfloor \tilde{\Phi} \rfloor, \quad (35)$$

$$q = (-1)^{\lfloor 2\tilde{\Phi} + 1 \rfloor}, \quad (36)$$

$$t = 1 - 2|\lfloor \tilde{\Phi} \rfloor - \tilde{\Phi}|, \quad (37)$$

where  $\lfloor x \rfloor$  is the floor function (E36), and we define the shorthand nint( $x$ )  $\equiv \lfloor x \rfloor$  that rounds  $\frac{1}{2}$  to the nearest even integer. These give the generalised form

$$F(\phi; k^2) = 2nK(k^2) + qF(\frac{\pi}{2}t; k^2), \quad (38)$$

with conditions  $F(0; k^2) = 0$  and  $F(\pi/2; k^2) = K(k^2)$ . This definition returns (30) to a compact expression of form (28)

$$\int_{\varphi'_1}^{\varphi'_2} \hat{G} d\varphi' = -\frac{2}{R} \sum_{q=1}^2 (-1)^q F(\phi_q; k^2), \quad \forall \phi. \quad (39)$$

The replacement of  $F(\phi; k^2)$  is readily extended to  $E(\phi; k^2)$  and  $\Pi(\phi; a^2, k^2)$ ,

$$E(\phi; k^2) = 2nE(k^2) + qE(\frac{\pi}{2}t; k^2), \quad (40)$$

$$\Pi(\phi; a^2, k^2) = 2n\Pi(a^2; k^2) + q\Pi(\frac{\pi}{2}t; a^2, k^2), \quad (41)$$

with conditions  $E(0; k^2) = 0$ ,  $E(\pi/2; k^2) = E(k^2)$ ,  $\Pi(0; a^2, k^2) = 0$ , and  $\Pi(\pi/2; a^2, k^2) = \Pi(a^2; k^2)$ .

The transformed Legendre forms are valid in all four quadrants of a unit circle and have the simplest input range on the normal Legendre form for reducing numerical procedures.

### 3.3 Fourier-Bessel integral-series

We additionally define the transformed incomplete elliptic integral of Legendre's type

$$D(\phi; k^2) = \frac{1}{k^2} \left( F(\phi; k^2) - E(\phi; k^2) \right), \quad (42)$$

(E22) that is used for both analytic and numeric simplification [102, pg.43],[34, 103] (e.g. the Bulirsch integrals: cel( $\sqrt{(1-k^2)}, 1, 0, 1$ ), el2( $\tan \phi, \sqrt{(1-k^2)}, 0, 1$ )).

## 3.3 Fourier-Bessel integral-series

It is shown in Section 3.2 that using an elementary solution to the Poisson equation may result in elementary and/or elliptic integrals along an azimuth source. The free space Green's function (A17) becomes difficult to work with as the azimuthal and radial components of  $\mathbf{r}'$  are not separable. The introduction of integrands from successive integrations (from a formulation such as a surface or volume) that are of higher degree, or contain an inverse trigonometric function, often do not reduce to a known canonical form.

Separability is introduced from an integral solution to the Poisson equation, used to find a sequence of eigenfunctions to match the boundary conditions in given coordinates. This integral-series solution for the Green's function in cylindrical coordinates is given by [18, pg.1263]

$$\hat{G}(\rho', \varphi - \varphi', z') = \sum_{\nu=0}^{\infty} \epsilon_{\nu} \cos [\nu(\varphi - \varphi')] I(\nu, \nu, 0), \quad (43)$$

that contains a special case of the Lipschitz-Hankel integral  $I(\mu, \eta, \lambda)$  (E1)

$$I(\nu, \nu, 0) = \int_0^{\infty} e^{-|z-z'|s} J_{\nu}(\rho s) J_{\nu}(\rho' s) ds, \quad (44)$$

where  $\epsilon_{\nu}$  is the Neumann factor with  $\epsilon_0 = 1$  and  $\epsilon_n = 2 \forall n > 0$  [18, pg.744]. An equivalent form commonly seen, in-lieu of (44) in (43), is (E2). There are also a number of additional alternate eigenfunctions expressions, such as those in terms of: Legendre polynomials [104]; Legendre functions (E3); elliptic functions (E4); hypergeometric functions (E5); or an infinite sum of gamma functions (E10). The introduction of an additional infinite series in (E10) is to the benefit of finding a canonical form for an integral, as will now be shown.

### 3.3.1 Radial integral

We consider a second example in contrast to (15), the integral of (43) along a radius. Using (E10) in lieu of (44) along with the substitution  $\rho' = \rho'_m \sqrt{t}$  gives

$$\begin{aligned} \int_{\rho'_1}^{\rho'_2} \hat{G} d\rho' &= \frac{1}{2\sqrt{\pi}L} \sum_{m=1}^2 (-1)^m \rho'_m \sum_{\nu,p=0}^{\infty} \epsilon_{\nu} \cos [\nu(\varphi - \varphi')] \\ &\times \left( \frac{\rho'_m}{L^2} \right)^{\nu+2p} \frac{\Gamma(\nu + 2p + \frac{1}{2})}{\Gamma(\nu + p + 1)p!} f_m(\rho, \nu) \end{aligned} \quad (45)$$

where  $\rho'_m \in \{\rho'_1, \rho'_2\}$  is the definite integral summation notation and

$$f_m(\rho, \nu) = \int_0^t \frac{t^{-\frac{1}{2}+\frac{\nu}{2}+p}}{[1 + (\rho'^2/L^2)t]^{\frac{1}{2}+\nu+2p}} dt. \quad (46)$$

By inspection of (E7), the inner integral  $f(\rho, \nu)$  in (45) is a hypergeometric series, that combined with the recurrence relation (E32), becomes

$$f_m(\rho, \nu) = \frac{2}{\nu + 2p + 1} F \left( \begin{array}{c} \frac{1}{2} + \nu + 2p, \frac{1}{2} + \frac{1}{2}\nu + p \\ \frac{3}{2} + \frac{1}{2}\nu + p \end{array}; -\frac{\rho'^2}{L^2} \right), \quad (47)$$

where  $F \left( \begin{array}{c} a,b \\ c \end{array}; \lambda \right)$  is the Gauss hypergeometric function  ${}_2F_1$  (E6). The authors experienced issues with the numeric stability of calculating such series of hypergeometric functions with a non-symbolic fixed precision method; completing a partial sum with enough terms for satisfactory near-field accuracy. Such issues are explored in-depth by [19]. Symbolic calculations of this series were found cumbersome relative to directly solving the integral of (45) with standard numeric methods.

The hypergeometric series of (47) has ensured convergence for  $\rho'^2/L^2 < 1$  [105], where  $L^2$  is the radius of convergence. Suggested treatment for these series are well-documented in [106]. For a series of form (E12) the Pfaff linear transform (E13) can be applied. The advantage of this transform, in the context of this problem formulation, is that the hypergeometric series becomes universally convergent. Applied to (47),

$$f_m(\rho, \nu) = \frac{2}{\nu + 2p + 1} \left( \frac{L^2}{T_m^2} \right)^{\frac{1}{2}+\nu+2p} F \left( \begin{array}{c} \frac{1}{2} + \nu + 2p, 1 \\ \frac{3}{2} + \frac{1}{2}\nu + p \end{array}; z_m^2 \right), \quad (48)$$

where

$$z^2 = \rho'^2/T^2. \quad (49)$$

From here, it is known that hypergeometric series typically reduce with special cases to sums of elementary functions [106, pg.89], that provide the practical benefit of faster solution times, while avoiding issues with numeric instability. After significant efforts by the authors to identify the relationship, such a transform can be seen by inspection with (E14), where the incomplete beta function  $B(\lambda; a, b)$  (E15) is a special case of the hypergeometric function. From (45), we now have the radial integration in a new form

$$\begin{aligned} \int_{\rho'_1}^{\rho'_2} \hat{G} d\rho' &= \frac{1}{2\sqrt{\pi}} \sum_{m=1}^2 (-1)^m \sum_{\nu,p=0}^{\infty} \epsilon_{\nu} \cos [\nu(\varphi - \varphi')] \\ &\times \left( \frac{\rho}{L} \right)^{\nu+2p} \frac{\Gamma(\nu + 2p + \frac{1}{2})}{\Gamma(\nu + p + 1)p!} \\ &\times B(z_m^2; \frac{1}{2} + \frac{1}{2}\nu + p, \frac{1}{2}\nu + p), \end{aligned} \quad (50)$$

where each term in the series is fast-solving and numerically stable. Of mathematical note, the limits of integration to the Green's function only remain in the expression within the incomplete beta function. As the elliptic integral well-describes an azimuth, the beta function well-describes the radius.

It is prudent to consider a simplification of (50), to remove rational numbers in favour of integers where possible, towards further use of recurrence relations. To do this, we introduce the regularised beta function (E16); however, this introduces a singularity at  $\nu = p = 0$ , similar to that seen in (E11). Therefore, the series requires splitting: firstly to expand the

cases  $\nu = 0$  and  $\nu \geq 1$ , then when  $\nu = 0$ , splitting  $p = 0$  and  $p \geq 1$ . This gives three terms: an elementary first order approximation; a single series; and a double series:

$$\int_{\rho'_1}^{\rho'_2} \hat{G} \, d\rho' = \sum_{m=1}^2 (-1)^m (\alpha_m^{(1)} + \beta_m^{(1)} + \gamma_m^{(1)}), \quad (51)$$

where

$$\alpha_m^{(1)} = \tanh^{-1} z_m \quad (52)$$

$$\beta_m^{(1)} = \sum_{p=0}^{\infty} \Xi_m(-1, p+1), \quad (53)$$

$$\gamma_m^{(1)} = 2 \sum_{\nu, p=0}^{\infty} \cos[(\nu+1)(\varphi-\varphi')] \Xi_m(\nu, p). \quad (54)$$

A partial fraction expansion is used to give the basic integral  $B(\frac{1}{2}, 0, \lambda)$  (E18), Legendre's duplication formula (E9) is applied to allow transformation of the Gamma function to factorial form (hence, the binomial coefficients (E30) from the recurrence relations (E34), (E32)), and a canonical function containing the regularised beta function  $I(\lambda; a, b)$

$$\Xi_m(\nu, p) = \frac{1}{\nu+2p+1} \binom{\nu+2p+1}{p} \left(\frac{\rho}{2L}\right)^{\nu+2p+1} \times I(z_m^2; \frac{1}{2}\nu+p+1, \frac{1}{2}\nu+p+\frac{1}{2}). \quad (55)$$

The method shown in this section is applied to find all series solutions in this article. This can also be applied to closely related geometries outside the scope of this article.

### 3.3.2 Axial integral

The same process as (45) with the substitution  $z - z' = (z - z'_n)\sqrt{t}$  gives

$$\begin{aligned} \int_{z'_1}^{z'_2} \hat{G} \, dz' &= -\frac{1}{2\sqrt{\pi(\rho^2 + \rho'^2)}} \sum_{n=1}^2 (-1)^n Z_n \sum_{\nu, p=0}^{\infty} \epsilon_{\nu} \\ &\times \cos[\nu(\varphi - \varphi')] \left(\frac{\rho\rho'}{\rho^2 + \rho'^2}\right)^{\nu+2p} \frac{\Gamma(\nu+2p+\frac{1}{2})}{\Gamma(\nu+p+1)p!} \\ &\times \int_0^t t^{-1/2} \left(1 + \frac{Z_n}{\rho^2 + \rho'^2} t\right)^{-\nu-2p-\frac{1}{2}} dt, \end{aligned} \quad (56)$$

and using the same process as in (45) to (51) yields

$$\int_{z'_1}^{z'_2} \hat{G} \, dz' = -\sum_{n=1}^2 (-1)^n \text{sgn}(Z_n) \left(\alpha_n^{(2)} + \frac{1}{2}\beta_n^{(2)} + \gamma_n^{(2)}\right), \quad (57)$$

where  $z'_n \in \{z'_1, z'_2\}$  is the definite integral summation notation and

$$\alpha_n^{(2)} = \tanh^{-1} y_n, \quad (58)$$

$$\beta_n^{(2)} = \sum_{p=0}^{\infty} \xi_n(-1, p+1), \quad (59)$$

$$\gamma_n^{(2)} = \sum_{\nu, p=0}^{\infty} \cos[(\nu+1)(\varphi-\varphi')] \xi_n(\nu, p), \quad (60)$$

and

$$\begin{aligned} \xi_n(\nu, p) &= \frac{1}{\nu+2p+1} \binom{\nu+2p+1}{p} \left(\frac{\rho\rho'}{\rho^2 + \rho'^2}\right)^{\nu+2p+1} \\ &\times I(y_n^2; \frac{1}{2}, \nu+2p+1) \end{aligned} \quad (61)$$

with

$$y^2 = Z^2/T^2. \quad (62)$$

## 3.4 Reduction of the double infinite series

A solution in terms of an elliptic integral (Section 3.2) may be considered a preferred analytic solution compared to numerous forms of the Fourier-Bessel integral-series, discussed in Section 3.3.1. However, the use of these series gives separability of the radial and azimuth functional that is less obdurate when looking for an explicit integral solution. This produces a decoupled integral that can be calculated precisely with elementary and/or beta type functions. As an example to demonstrate this reasoning we consider an extension to (51); completing both the disc and shell surface integrals before the complete volumetric triple integral.

### 3.4.1 Radial integral

Integrating (51) gives the surface integral

$$\begin{aligned} \int_{\varphi'_1}^{\varphi'_2} \int_{\rho'_1}^{\rho'_2} \hat{G} \, d\rho' d\varphi' &= \\ \sum_{m=1}^2 (-1)^m \int_{\varphi'_1}^{\varphi'_2} &\left(\alpha_m^{(1)} + \beta_m^{(1)} + \gamma_m^{(1)}\right) d\varphi'. \end{aligned} \quad (63)$$

All three integrals are completed by inspection, in particular

$$\int_{\varphi'_1}^{\varphi'_2} \gamma_m^{(1)} d\varphi' = -\sum_{m=1}^2 (-1)^m \delta_{m,q}^{(1)} \quad (64)$$

with

$$\delta_{m,q}^{(1)} = 2 \sum_{\nu, p=0}^{\infty} \frac{\sin[(\nu+1)\Phi_q]}{\nu+1} \Xi_m(\nu, p). \quad (65)$$

The double infinite series  $\delta_{m,q}$  of (50), (51) and (64) is an artefact introduced to solve the radial integral of (45). The first question that arises from this term is, what is the optimal way to sum the series given a finite number of terms? Does the series approach the limit at a higher rate with increasing the  $p$  index proportionally higher than the  $\nu$  index? An approach may be to fix the order of summation using a summation identity (E35) to sum an index at an increased rate; however, the ideal result is to find a closed-form expression for one of the summations, and this will now be shown. From (64) using (E35), a finite series for  $p$  is

$$\delta_{m,q}^{(1)} = 2 \sum_{\nu=0}^{\infty} \sum_{p=0}^{\lfloor \nu/2 \rfloor} \frac{\sin[(\nu-2p+1)\Phi_q]}{\nu-2p+1} \Xi_m(\nu-2p, p). \quad (66)$$

The regularised beta function of  $\Xi_m(\nu-2p, p)$  is now also independent of the  $p$  summation. The two integral representations of the finite trigonometric series, adapted from [106],

## 3.4 Reduction of the double infinite series

pg.225], are

$$\sum_{p=0}^n \binom{2n+1}{p} \frac{\sin[(2n-2p+1)x]}{2n-2p+1} = 2^{2n} \int_0^x \cos^{2n+1} x \, dx \quad (67)$$

when  $\nu$  is even,  $\nu = 2n$ , and

$$\sum_{p=0}^{n-1} \binom{2n}{p} \frac{\sin[(2n-2p)x]}{2n-2p} = 2^{2n-1} \int \cos^{2n} x \, dx - \frac{x}{2} \binom{2n}{n} \quad (68)$$

when  $\nu$  is odd,  $\nu = 2n-1$ . Using the substitution  $t = \sin^2 x$ , the integral of (67) can be expressed as

$$\begin{aligned} \int_0^x \cos^{2n+1} x \, dx &= \frac{1}{2} \operatorname{sgn}(\sin x) \int_0^{\sin^2 x} \frac{(1-t)^n}{\sqrt{t}} \, dt \\ &= \frac{1}{2} \operatorname{sgn}(\sin x) B(\sin^2 x; \frac{1}{2}, n+1), \end{aligned} \quad (69)$$

that is of the form of an incomplete Beta function. The sgn function corrects the sign change from the substitution. The same substitution is used for the integral of (68); however, some added treatment is required as  $\int \cos^{2n} x \, dx$  is a non-negative function. As such, the substitution is only valid in the range  $-\pi/2 < x < \pi/2$  and requires extension for all real numbers. Treatment for the substitution is similar to that when a continuous function is integrated to return a seemingly discontinuous function. Adapted from [107], an algorithm for the continuous expression  $g(x)$ , with  $\hat{g}(x)$  in the range  $a \leq x < b$  is

$$g(x) = \int f(\sin x, \cos x) \, dx = \hat{g}(x) + \left( \lim_{x \rightarrow b} \hat{g}(x) \right) \left[ \frac{x-b}{b-a} \right], \quad (70)$$

where

$$\hat{g}(x) = \int f[\phi(x)] \phi'(x) \, dx, \quad (71)$$

$b$  is the singularity,  $b-a$  is the period, and  $\phi(x)$  is the choice of substitution. Thus for the integral of (68):

$$\begin{aligned} \int_0^x \cos^{2n} x \, dx &= \frac{1}{2} \operatorname{sgn}(x) \int_0^{\sin^2 x} \frac{(1-t)^{n-\frac{1}{2}}}{\sqrt{t}} \, dt, \\ &\text{for } -\pi/2 < x < \pi/2 \\ &= \frac{1}{2} \operatorname{sgn}(x) B(\sin^2 x; \frac{1}{2}, n + \frac{1}{2}), \\ &\text{for } -\pi/2 < x < \pi/2 \\ &= \frac{1}{2} s(x) B(\sin^2 x; \frac{1}{2}, n + \frac{1}{2}) \\ &\quad + B(\frac{1}{2}, n + \frac{1}{2}) \left( 1 + \left[ \frac{x}{\pi} - 1 \right] \right), \end{aligned} \quad (72)$$

where the limit returns the complete beta function (E17). The nearest integer function is used in-lieu of the floor function, shifted to handle the singularities at  $\pm\pi/2$ . The square wave  $\operatorname{sgn}[\sin(2x)]$  captures the sign of the incomplete beta function, except for at the discontinuity, where a second shifted square wave (using the Liouville function) is used to correct the sign

$$s(x) = \begin{cases} 1, & \text{for } \operatorname{sgn}[\sin(2x)] > 0, \\ (-1)^{\lfloor x/\pi+1/2 \rfloor}, & \text{for } \operatorname{sgn}[\sin(2x)] = 0, \\ -1, & \text{for } \operatorname{sgn}[\sin(2x)] < 0. \end{cases} \quad (73)$$

The final surface integral that is free of the double infinite series is

$$\begin{aligned} &\int_{\varphi'_1}^{\varphi'_2} \int_{\rho'_1}^{\rho'_2} \hat{G} \, d\rho' d\varphi' \\ &= \sum_{m,q=1}^2 (-1)^{m+q} \left( \varphi'_q \alpha_m^{(1)} + \varphi'_q \beta_m^{(1)} - \delta_{m,q}^{(1)} \right), \end{aligned} \quad (74)$$

where

$$\delta_{m,q}^{(1)} = \sum_{\nu=0}^{\infty} \Xi_m(\nu, 0) \chi_q(\nu). \quad (75)$$

The closed-form solution is divided into even and odd terms

$$\chi(\nu) = v(\nu+1) \chi^{(\zeta)}(\nu) + v(\nu) [\chi^{(\eta)}(\nu) + \chi^{(\iota)}(\nu)], \quad (76)$$

where

$$\chi^{(\zeta)}(\nu) = 2^\nu \operatorname{sgn}(\sin \Phi) B(\sin^2 \Phi; \frac{1}{2}, \frac{1}{2}\nu + 1) \quad (77)$$

$$\chi^{(\eta)}(\nu) = 2^\nu s(\Phi) B(\sin^2 \Phi; \frac{1}{2}, \frac{1}{2}\nu + 1) \quad (78)$$

$$\chi^{(\iota)}(\nu) = 2^{\nu+1} \omega B(\frac{1}{2}, \frac{1}{2}\nu + 1) - \left( \frac{\nu+1}{\frac{\nu}{2} + \frac{1}{2}} \right) \Phi \quad (79)$$

and

$$\omega = 1 + \lfloor \Phi/\pi - 1 \rfloor, \quad (80)$$

$$v(\nu) = \nu - 2 \lfloor \nu/2 \rfloor. \quad (81)$$

To form a compact expression  $v(\nu)$  is defined in-lieu of a conditional statement for the cases (67) and (68). Of interesting note, the summation of  $\beta^{(1)}$  is independent of azimuthal source terms, and the summation of  $\delta^{(1)}$  only contains radial source terms within the argument of the regularised beta function. An alternate form of (75) is given in (103).

### 3.4.2 Axial integral

By inspection of (74), the axial integral of (57) is

$$\begin{aligned} \int_{z'_1}^{z'_2} \int_{\varphi'_1}^{\varphi'_2} \hat{G} \, d\varphi' dz' &= -\frac{1}{2} \sum_{n,q=1}^2 (-1)^{n+q} \operatorname{sgn}(Z_n) \\ &\quad \times \left( 2\varphi'_q \alpha_n^{(2)} + \varphi'_q \beta_n^{(2)} - \delta_{n,q}^{(2)} \right), \end{aligned} \quad (82)$$

where  $\alpha_n^{(2)}$ ,  $\beta_n^{(2)}$  are defined in (58), (59), and

$$\delta_{n,q}^{(2)} = \sum_{\nu=0}^{\infty} \xi_n(\nu, 0) \chi_q(\nu). \quad (83)$$

### 3.4.3 Volume integral

The volume integral of  $\hat{G}$  can be approached via (74) or (82). From (74), reverting the incomplete beta function to a series via the transforms (E6, E14), and using the substitution from

(56) we have

$$\begin{aligned} & \int_{z'_1}^{z'_2} \int_{\varphi'_1}^{\varphi'_2} \int_{\rho'_1}^{\rho'_2} \hat{G} d\rho' d\varphi' dz' = \sum_{m,q=1}^2 (-1)^{m+q} \\ & \times \left\{ \varphi'_q \int_{z'_1}^{z'_2} \alpha_m^{(1)} dz' + \frac{\rho \rho_m'^2}{4(\rho^2 + \rho_m'^2)^{3/2}} \sum_{n=1}^2 (-1)^n Z_n \right. \\ & \times \sum_{\nu,p=0}^{\infty} \left[ \frac{\rho^p \rho_m'^{2\nu+p}}{(\rho^2 + \rho_m'^2)^{\nu+p}} \left( \frac{\chi_q(\nu)}{2^{p+1}} \frac{\Gamma(\nu+p+\frac{3}{2})}{\Gamma(\frac{p}{2}+\frac{3}{2})\Gamma(\nu+\frac{p}{2}+2)} \right. \right. \\ & \times \int_0^1 t^{-\frac{1}{2}} \left( 1 + \frac{Z_n^2}{\rho^2 + \rho_m'^2} t \right)^{-\nu-p-3/2} dt \\ & - \frac{\varphi'_q}{\sqrt{\pi}} \left( \frac{\rho \rho_m'}{\rho^2 + \rho_m'^2} \right)^{p+1} \frac{\Gamma(p+\frac{3}{2})\Gamma(\nu+2p+\frac{5}{2})}{\Gamma(p+2)^2\Gamma(\nu+p+\frac{5}{2})} \\ & \left. \left. \times \int_0^1 t^{-\frac{1}{2}} \left( 1 + \frac{Z_n^2}{\rho^2 + \rho_m'^2} t \right)^{-\nu-2p-5/2} dt \right) \right] \}. \end{aligned} \quad (84)$$

The elementary  $z'$ -integral is solved using the product rule and a partial fraction expansion. The  $t$ -integrals are solved using the same process from (45) to (51), that are by inspection hypergeometric functions. The result directly follows as

$$\begin{aligned} & \int_{z'_1}^{z'_2} \int_{\varphi'_1}^{\varphi'_2} \int_{\rho'_1}^{\rho'_2} \hat{G} d\rho' d\varphi' dz' = \sum_{m,n,q=1}^2 (-1)^{m+n+q} \\ & \times [\varphi'_q \alpha_{m,n}^{(3)} - \frac{1}{2} \text{sgn}(Z_n) \rho'_m (\frac{1}{8} \sqrt{\pi} \varphi'_q \beta_{m,n}^{(3)} - \gamma_{m,n,q}^{(3)})] \end{aligned} \quad (85)$$

where

$$\begin{aligned} \alpha_{m,n}^{(3)} &= \rho \tan^{-1} \left( \frac{\rho'_m Z_n}{\rho T_{m,n}} \right) - Z_n \tanh^{-1} \left( \frac{\rho'_m}{T_{m,n}} \right) \\ & - \rho'_m \ln(Z_n + T_{m,n}) \end{aligned} \quad (86)$$

$$\beta_{m,n}^{(3)} = \sum_{p,\nu=0}^{\infty} \binom{2+2p}{1+p} \frac{1}{4^p (1+p)!} \tau_{m,n}(\nu, p), \quad (87)$$

$$\gamma_{m,n,q}^{(3)} = \sum_{\nu,p=0}^{\infty} \frac{\chi_q(p)}{(2+\frac{p}{2})_{1+p/2}} \tau_{m,n}(\nu, \frac{p}{2} - \frac{1}{2}). \quad (88)$$

$(n)_k$  is the Pochhammer symbol (E31). A final canonical beta series term is defined

$$\tau(\nu, p) = (\frac{5}{2} + \nu + p)_{p+1/2} \left( \frac{\rho'}{\rho} \right)^\nu \xi(1 + \nu + 2p, 0) \quad (89)$$

in addition to  $\Xi$  and  $\xi$ , that arose from integration of the Fourier-Bessel integral-series radially and axially, respectively. The  $\tau$  term arose from the axial integration of  $\Xi$ , and contains  $\xi$ .

The double infinite series from the surface integrals (63) and (82) were shown to reduce to a single infinite series (75), (83). A double infinite series returns with the volume integral (85). A similar reduction can be found for the volume integral by shifting of the  $\tau$ -series summand  $\tau(\nu - 2p, p)$  (E35) to give an answer in the form of  $f(\nu, p) {}_2F_1 - g(\nu, p) {}_3F_2$ , where the finite sum is found by subtraction of the generalised hypergeometric function (for example, see [106, pg.207]). Nonetheless, empirically, this direction was not found by the authors to be of computational benefit – for reducing the rate of convergence or avoiding numerical issues – compared to the presented form (87), (88).

### 3.5 Series convergence and spatial remainder

To highlight and quantify the robustness of the solutions presented in this article, in this section we consider the asymptotic expansion of the integrals:  $\beta^{(1)}, \delta^{(1)}$  (74);  $\beta^{(2)}, \delta^{(2)}$  (82);  $\beta^{(3)}, \gamma^{(3)}$  (85). For classical electromagnetic formulations, previous work has not quantified the convergence of hypergeometric (now shown to be of the beta type) series solutions in the near-field, or the error with summing a finite number of terms. To do so, we want to find the limit

$$L = \lim_{p \rightarrow \infty} \left| \frac{f(p+1)}{f(p)} \right|, \quad (90)$$

to check whether the series is convergent. If so, the maximum remainder after  $p$  terms is [108]

$$R \leq \frac{f(p+1)}{1-L} \quad \text{or} \quad R \leq \frac{f(p)f(p+1)}{f(p)-f(p+1)}, \quad (91)$$

if the ratio  $f(p+1)/f(p)$  is a increasing or decreasing sequence, respectively. The combination of both remainders gives an error interval.

#### 3.5.1 Axisymmetric series

For the  $\beta^{(1)}$ -summation we have the ratio

$$\begin{aligned} \frac{\Xi(-1, p+2)}{\Xi(-1, p+1)} &= \frac{(p+1)(3+2p)}{2(p+2)^2} \frac{\rho^2}{L^2} \\ &\times \left[ 1 - \frac{(3+2p)\rho'^2 + 2(p+1)L^2}{2(p+1)T^2} F \left( \frac{2p+\frac{5}{2}, 1}{p+\frac{5}{2}}; z^2 \right)^{-1} \right] \end{aligned} \quad (92)$$

which is an increasing sequence, determined from the derived recurrence relation (G4) and transform (G5). We can consider the limit of the products of (92), assuming each limit exists. The limit of the  $p$ -polynomials are solved by inspection, and the limit of the hypergeometric function is found from (G11), giving

$$\lim_{p \rightarrow \infty} \left| \frac{\Xi(-1, p+2)}{\Xi(-1, p+1)} \right| = \begin{cases} \frac{4\rho^2 \rho'^2}{T^2}, & \text{if } z^2 < \frac{1}{2}, \\ \frac{\rho^2}{L^2}, & \text{if } z^2 > \frac{1}{2}, \end{cases} \quad (93)$$

that is singular when  $\rho' = L$  ( $z^2 = \frac{1}{2}$ ) and is absolutely convergent as  $L < 1$  in both cases. We introduce the nondimensional parameters

$$\tilde{\rho} = \rho/\rho', \quad (94)$$

$$\tilde{Z} = Z/\rho', \quad (95)$$

so that the result is scalable, giving

$$\begin{aligned}\tilde{\beta}^{(1)} &= \sum_{p=0}^{\infty} \frac{1}{2p+2} \binom{2p+2}{p+1} \left( \frac{\tilde{\rho}^2}{4(\tilde{\rho}^2 + \tilde{Z}^2)} \right)^{p+1} \\ &\quad \times I\left( \frac{1}{1+\tilde{\rho}^2+\tilde{Z}^2}; p+\frac{3}{2}, p+1 \right)\end{aligned}\quad (96)$$

$$\tilde{L}^{(1)} = \begin{cases} \left( \frac{2\tilde{\rho}}{1+\tilde{\rho}^2+\tilde{Z}^2} \right)^2, & \text{if } (1+\tilde{\rho}^2+\tilde{Z}^2) > 2, \\ \frac{\tilde{\rho}^2}{\tilde{\rho}^2+\tilde{Z}^2}, & \text{if } (1+\tilde{\rho}^2+\tilde{Z}^2) < 2. \end{cases}\quad (97)$$

Independent to the change of parameters,  $\Xi(\nu, p)$  is nondimensional, thus the remainder is nondimensional. A spatial plot of  $\tilde{\beta}^{(1)}$  does not have any direct physical meaning, as it is a term of the definite integral, whence the integration constants have been removed; however, with  $z' = 0$  we have a disc on the  $\tilde{\rho}$ -axis with a normalised radius of 1.

For the  $\beta^{(2)}$ -summation we have the ratio

$$\begin{aligned}\frac{\xi(-1, p+2)}{\xi(-1, p+1)} &= \frac{2(p+1)(3+2p)}{(p+2)^2} \left( \frac{\rho\rho'}{\rho^2+\rho'^2} \right)^2 \left[ 1 + \left( 1 \right. \right. \\ &\quad \left. \left. + \frac{(5+4p)(\rho^2+\rho'^2)}{2(3+2p)T^2} \right) \frac{1}{4(1+p)} F\left( \frac{2p+\frac{5}{2}, 1}{\frac{3}{2}}; y^2 \right)^{-1} \right]\end{aligned}\quad (98)$$

that is an increasing sequence (G3) and determined from the transform (G6). As with (92), the limit of the  $p$ -polynomials are solved by inspection. The limit of the hypergeometric function is found via the transform (G10), that in-part, moves the location of the single large parameter toward finding a known limit (G13). This gives

$$\begin{aligned}F\left( \frac{2p+\frac{5}{2}, 1}{\frac{3}{2}}; y^2 \right) &= \frac{\sqrt{\pi}}{2|Z|} \frac{T^{4+4p+1}}{(\rho^2+\rho'^2)^{2+2p}} \frac{\Gamma(2+2p)}{\Gamma(\frac{5}{2}+2p)} \\ &\quad - \frac{T^2}{4(p+1)|Z|^2} F\left( \frac{\frac{1}{2}, 1}{3+2p}; 1-y^{-2} \right)\end{aligned}\quad (99)$$

(with  $a = 1$  in (G10) the imaginary component of the transform vanishes) that highlights the reciprocal hypergeometric function of (98)  $\rightarrow 0$  and the hypergeometric function of (99)  $\rightarrow 1$  as  $p \rightarrow \infty$ . Therefore, the limit is

$$\lim_{p \rightarrow \infty} \left| \frac{\xi(-1, p+2)}{\xi(-1, p+1)} \right| = \left( \frac{2\rho\rho'}{\rho^2+\rho'^2} \right)^2,\quad (100)$$

and the series with nondimensional parameters is

$$\begin{aligned}\tilde{\beta}^{(2)} &= \sum_{p=0}^{\infty} \frac{1}{2p+2} \binom{2p+2}{p+1} \left( \frac{\tilde{\rho}}{1+\tilde{\rho}^2} \right)^{2p+2} \\ &\quad \times I\left( \frac{\tilde{Z}^2}{1+\tilde{\rho}^2+\tilde{Z}^2}; \frac{1}{2}, 2+2p \right)\end{aligned}\quad (101)$$

$$\tilde{L}^{(2)} = \left( \frac{2\tilde{\rho}}{1+\tilde{\rho}^2} \right)^2.\quad (102)$$

With the caveats of  $\tilde{\beta}^{(1)}$ , the spatial plot of  $\tilde{\beta}^{(2)}$  with  $z' = 0$  is a shell parallel to the  $\tilde{Z}$ -axis with a normalised radius of 1, that terminates at the  $\tilde{\rho}$ -axis.

Using (96) and (97), the remainder after summing a finite number of terms in the  $\tilde{\beta}^{(1)}$  series is shown in Figure 5a. Using (101) and (102), the remainder after summing a finite number of terms in the  $\tilde{\beta}^{(2)}$  series is shown in Figure 5b. A figure for the minimum number of terms required to meet a chosen remainder is not shown; however, the contours are spatially equivalent: the higher the remainder, the more terms are required. The equations and plot quantify the region that is well-defined by a first order approximation, and the region where machine precision may come into effect, due to the decreasing value of each term. Depending on the order of accuracy required for a problem, and field location relative to the source, the expected number of terms to calculate is visualised. When these series are applied in the solution to a physical problem, the remainder is scaled by physical constants or other coefficients. In using these series in the solution, these results fundamentally quantify a termination criterion for summing the finite series that is spatially variant.

### 3.5.2 Non-axisymmetric series

To remove  $\nu$ -terms of half integer order, towards use of recurrence relations, (75) is rewritten without the conditional expression

$$\delta_{m,q}^{(1)} = \sum_{\nu=0}^{\infty} \left[ \zeta_{m,q}^{(1)}(\nu) + \eta_{m,q}^{(1)}(\nu) + \iota_{m,q}^{(1)}(\nu) \right],\quad (103)$$

with each term

$$\zeta_{m,q}^{(1)}(\nu) = \Xi_m(2\nu, 0) \chi_q^{(\zeta)}(2\nu),\quad (104)$$

$$\eta_{m,q}^{(1)}(\nu) = \Xi_m(2\nu+1, 0) \chi_q^{(\eta)}(2\nu+1),\quad (105)$$

$$\iota_{m,q}^{(1)}(\nu) = \Xi_m(2\nu+1, 0) \chi_q^{(\iota)}(2\nu+1).\quad (106)$$

For a finite number of combined series terms  $P \in \mathbb{Z}_{\geq 0}$  (or  $P \notin \mathbb{Z} \setminus \mathbb{N}$ ), (103) can be written

$$\delta_{m,q}^{(1)}(P) = \sum_{\nu=0}^{\lfloor P/2 \rfloor} \zeta_{m,q}^{(1)}(\nu) + \sum_{\nu=0}^{\lfloor (P-1)/2 \rfloor} \left[ \eta_{m,q}^{(1)}(\nu) + \iota_{m,q}^{(1)}(\nu) \right],\quad (107)$$

that is summed with the same terms and order as (75). For an odd  $P$ , the number of terms in each series is equal, and thus there are  $P/2$  terms in each series. A similar process from (92) to (93) is undertaken; the algebra is tedious but the asymptotic expansion becomes equivalent for each. We have the product

$$I(z^2; \nu + \alpha, \nu + \beta) I(\sin^2 \Phi; \frac{1}{2}, \nu + \alpha)\quad (108)$$

in (104) and (105) that has the recurrence relation (G7) and transform (G8). The hypergeometric function with one larger parameter is transformed into a hypergeometric function with two large parameters (G9), thus giving an expansion of the familiar form (G11). The hypergeometric functions  $F(a, b, c, \sin^2 \Phi_q)$  all  $\rightarrow 0$  as  $\nu \rightarrow \infty$ . For the  $\delta^{(1)}$  series we have the limits

$$\begin{aligned}\lim_{\nu \rightarrow \infty} \left| \frac{\zeta^{(1)}(\nu+1)}{\zeta^{(1)}(\nu)} \right| &= \lim_{\nu \rightarrow \infty} \left| \frac{\eta^{(1)}(\nu+1)}{\eta^{(1)}(\nu)} \right| \\ &= \lim_{\nu \rightarrow \infty} \left| \frac{\iota^{(1)}(\nu+1)}{\iota^{(1)}(\nu)} \right| = \begin{cases} \frac{4\rho^2 \varrho'^2}{T^2}, & \text{if } z^2 < \frac{1}{2}, \\ \frac{\rho^2}{L^2}, & \text{if } z^2 > \frac{1}{2}, \end{cases}\end{aligned}\quad (109)$$

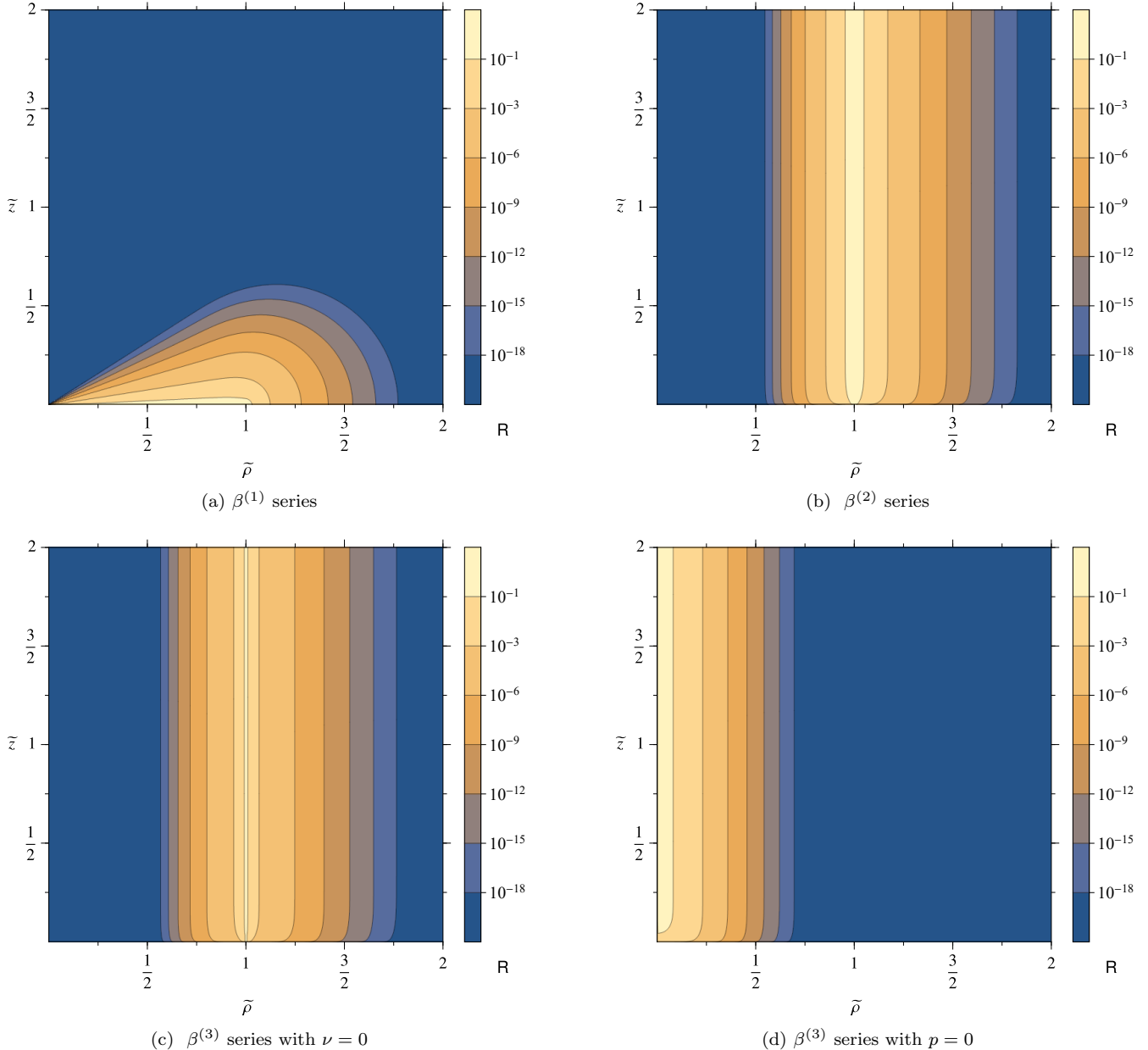


Figure 5: The maximum remainder  $R$  after summing the first 100 terms ( $P = 99$ ) in the canonical series of incomplete beta functions. Distributions are symmetric about the  $\tilde{\rho}$  axis.

that are equivalent to the  $\beta^{(1)}$  series (93), remainder is now a sum of three remainders.

As with (103), (83) is rewritten

$$\delta_{n,q}^{(2)} = \sum_{\nu=0}^{\infty} \left[ \zeta_{n,q}^{(2)}(\nu) + \eta_{n,q}^{(2)}(\nu) + \iota_{n,q}^{(2)}(\nu) \right], \quad (110)$$

with each term

$$\zeta_{n,q}^{(2)}(\nu) = \xi_n(2\nu, 0) \chi_q^{(\zeta)}(2\nu), \quad (111)$$

$$\eta_{n,a}^{(2)}(\nu) = \xi_n(2\nu+1,0) \chi_a^{(\eta)}(2\nu+1), \quad (112)$$

$$\iota_{n,a}^{(2)}(\nu) = \xi_n(2\nu+1,0) \chi_a^{(\iota)}(2\nu+1). \quad (113)$$

Using the same process from (98) to (100), with an equivalent

discussion from (109), we have the limits for the  $\delta^{(2)}$  series

$$\begin{aligned} \lim_{\nu \rightarrow \infty} \left| \frac{\zeta^{(2)}(\nu + 1)}{\zeta^{(2)}(\nu)} \right| &= \lim_{\nu \rightarrow \infty} \left| \frac{\eta^{(2)}(\nu + 1)}{\eta^{(2)}(\nu)} \right| \\ &= \lim_{\nu \rightarrow \infty} \left| \frac{\iota^{(2)}(\nu + 1)}{\iota^{(2)}(\nu)} \right| = \left( \frac{2\rho\rho'}{\rho^2 + \rho'^2} \right)^2 \end{aligned} \quad (114)$$

that is equivalent to the  $\beta^{(2)}$  series (100).

### 3.5.3 Double series

There is an additional complexity with how to sum the double series. There may exist multiple sets of terms in the series that sum together to achieve a particular remainder. Also, there may not be a sequence that is strictly increasing or decreasing due to the order in which the terms are summed. Optimal theory on how to sum a double series is out of the

scope of this article; however, a logical method is required for the practical implementation of the series. With the spatial significance shown in Figure 5a and Figure 5b for a single series, one point may require orders of magnitude more terms to converge than another. With a double series, not only does that remain true, but with reference to (85), each particular point may require significantly differing  $\nu$  and  $p$  indexes to reach a maximal remainder. Blindly summing many terms for all points spatially will result in a computational burden. Analysing the rate of change of the cumulative sum will not give a reliable result across the entire spatial region.

Let the summand of  $\beta^{(3)}$  be  $\check{\beta}^{(3)}(\nu, p)$ , then repeating the process from (98) to (100) gives the ‘column and row’ limits to the double sum

$$\lim_{p \rightarrow \infty} \left| \frac{\check{\beta}^{(3)}(\nu, p+1)}{\check{\beta}^{(3)}(\nu, p)} \right| = \left( \frac{2\rho\rho'}{\rho^2 + \rho'^2} \right)^2, \quad (115)$$

$$\lim_{\nu \rightarrow \infty} \left| \frac{\check{\beta}^{(3)}(\nu+1, p)}{\check{\beta}^{(3)}(\nu, p)} \right| = \frac{\rho'^2}{\rho^2 + \rho'^2}. \quad (116)$$

The results of (115) and (116) demonstrate absolute convergence of the overall series. The series with nondimensional parameters is

$$\begin{aligned} \tilde{\beta}^{(3)} = \sum_{\nu, p=0}^{\infty} & \frac{(\frac{5}{2} + n + p)_{1/2+p}}{4^p (2 + n + 2p)(1 + p)!} \binom{2 + 2p}{1 + p} \\ & \times \frac{1}{\tilde{\rho}^\nu} \left( \frac{\tilde{\rho}}{1 + \tilde{\rho}^2} \right)^{2+n+2p} I \left( \frac{\tilde{Z}^2}{1 + \tilde{\rho}^2 + \tilde{Z}^2}; \frac{1}{2}, 2 + n + 2p \right) \end{aligned} \quad (117)$$

$$\tilde{\Gamma}^{(3)} = \begin{cases} \left( \frac{2\tilde{\rho}}{1 + \tilde{\rho}^2} \right)^2, & p \rightarrow \infty, \\ \frac{1}{1 + \tilde{\rho}^2}, & \nu \rightarrow \infty, \end{cases} \quad (118)$$

with the remainder after summing a finite number of terms in the  $\tilde{\beta}^{(3)}$  series shown in Figure 5c for  $p \rightarrow \infty$  and Figure 5d for  $\nu \rightarrow \infty$ . The significance of this result is that spatially, there is not a region that will require both a high  $\nu$  and  $p$  index, rather regions where both are low or only one is high. In computation, whilst this appears as a double integral, it will practically calculate as a single summation. The remainder for the double series can thus be effectively estimated.

As with (103), (88) is rewritten

$$\gamma_{m,n,q}^{(3)} = \sum_{\nu, p=0}^{\infty} \left[ \zeta_{m,n,q}^{(3)}(\nu, p) + \eta_{m,n,q}^{(3)}(\nu, p) + \iota_{m,n,q}^{(3)}(\nu, p) \right], \quad (119)$$

with each term

$$\zeta_{m,n,q}^{(3)}(\nu, p) = \frac{\chi_q^{(\zeta)}(2p)}{(2 + p)_{1+p}} \tau_{m,n}(\nu, p - \frac{1}{2}), \quad (120)$$

$$\eta_{m,n,q}^{(3)}(\nu, p) = \frac{\chi_q^{(\eta)}(2p + 1)}{(\frac{5}{2} + p)_{3/2+p}} \tau_{m,n}(\nu, p), \quad (121)$$

$$\iota_{m,n,q}^{(3)}(\nu, p) = \frac{\chi_q^{(\iota)}(2p + 1)}{(\frac{5}{2} + p)_{3/2+p}} \tau_{m,n}(\nu, p). \quad (122)$$

Repeating the process preceding (114) gives the limits

$$\begin{aligned} \lim_{p \rightarrow \infty} \left| \frac{\zeta^{(3)}(\nu, p+1)}{\zeta^{(3)}(\nu, p)} \right| &= \lim_{p \rightarrow \infty} \left| \frac{\eta^{(3)}(\nu, p+1)}{\eta^{(3)}(\nu, p)} \right| \\ &= \lim_{p \rightarrow \infty} \left| \frac{\iota^{(3)}(\nu, p+1)}{\iota^{(3)}(\nu, p)} \right| = \left( \frac{2\rho\rho'}{\rho^2 + \rho'^2} \right)^2, \end{aligned} \quad (123)$$

$$\begin{aligned} \lim_{\nu \rightarrow \infty} \left| \frac{\zeta^{(3)}(\nu+1, p)}{\zeta^{(3)}(\nu, p)} \right| &= \lim_{\nu \rightarrow \infty} \left| \frac{\eta^{(3)}(\nu+1, p)}{\eta^{(3)}(\nu, p)} \right| \\ &= \lim_{\nu \rightarrow \infty} \left| \frac{\iota^{(3)}(\nu+1, p)}{\iota^{(3)}(\nu, p)} \right| = \frac{\rho'^2}{\rho^2 + \rho'^2}, \end{aligned} \quad (124)$$

that are equivalent to the  $\beta^{(3)}$  series (115) and (116), respectively.

### 3.6 Results & verification

This section gives rationale to the analytic solution forms presented in the remainder of the article, and how these were calculated and verified through numerical methods.

#### 3.6.1 Singular regions

From the singularity in the Green’s free space function ( $\mathbf{r} - \mathbf{r}' = 0$ ), the analytic solutions contain surfaces of discontinuity from the abrupt jump in the magnetic field (A18)-(A21) from an infinite change in charge or current. Outside this closed or open surface, the magnetic field is continuous, and any singularities are removable. In general, it can be assumed that the magnetic field across the bounding surface of a magnet or coil is undefined, where  $(\rho = \rho') \wedge (\varphi = \varphi') \wedge (z = z')$ . In each analytic solution, points of interest are investigated that are partial permutations, located on the:

shell plane,  $\rho = \rho'_m$ ;

section plane,  $\varphi = \varphi'_q$ ;

disc plane,  $z = z'_n$ ;

axial line,  $(\rho = \rho'_m) \wedge (\varphi = \varphi'_q)$ ;

azimuthal line,  $(\rho = \rho'_m) \wedge (z = z'_n)$ ;

radial line,  $(\varphi = \varphi'_q) \wedge (z = z'_n)$ .

Removable singularities on these coincident planes and/or lines to the bounding surface may arise as artefacts from definite integral limits and/or are limiting cases of special functions. The special cases of the analytic solution at these removable singularities are significantly simpler and are beneficial to improving computational efficiency, notwithstanding the numeric issue of an undefined or unbounded result. Due to this observation, these special cases are always of interest towards analytic solutions for the force between two magnets or coils which can be readily found when surfaces of discontinuity are collinear or coplanar (Section 6.3). For numeric force calculations using the Maxwell stress tensor (385), computation may significantly simplify with an appropriately chosen surface.

Limiting cases of the general non-axisymmetric solution investigated are: on the axis,  $\rho = 0$ ; axisymmetric,  $\varphi'_q = \{0, 2\pi\}$ ; solid,  $\rho'_1 = 0$ ; and axisymmetric & solid,  $(\rho'_1 = 0) \wedge (\varphi'_q = \{0, 2\pi\})$ . These limiting cases have common removable singularities to the general non-axisymmetric solution.

Alternatively, to avoid numeric singularities the field point can be shifted  $\mathbf{r} \rightarrow \mathbf{r} + \epsilon$ , where  $|\epsilon|$  adds (at least) the smallest digit of precision used in numerical operations; forming an approximate solution that may be identical to finite precision. This method reduces the solution complexity and avoids coding conditional statements. This method is not used for results presented in this article, where instead solutions are given for the removable singularities. The rationale for this approach is in the use of the magnetic field solutions in subsequent equations. There is complexity in choosing  $\epsilon$  when superimposing solutions from a large collection of coils and magnets. This also avoids carrying through error with an approximate solution using  $\epsilon$ ; all summands of a definite integral (Appendix B), for a particular field point, are not singular simultaneously.

### 3.6.2 Numeric integral comparison

All analytic results were compared with the original integral formulation using the default algorithm of `NIntegrate` in Mathematica V12 (Wolfram Research, Inc., Champaign, IL, USA) to 8 decimal places (provided in the supplementary material Appendix I). The elliptic integrals were calculated using the inbuilt algorithms for `EllipticK`, `EllipticE`, `EllipticF`, `EllipticPi`, and `CarlsonRC`. The numeric integrals were calculated using IEEE double-precision floating-point for `AccuracyGoal`  $a = 53 \log_{10} 2$  and single-precision floating-point for `PrecisionGoal`  $p = 24 \log_{10} 2$  with a maximum error  $< 10^{-a} + |x|10^{-p}$  for representing  $x$ . The number of correct decimal digits in the numeric integral is thus  $\approx 8 - 11$  for magnetic fields from  $1 - 0.001\text{T}$ . The `WorkingPrecision` was set to the machine precision of  $53 \log_{10} 2$ , that is, numbers rounded to the nearest  $2 \times 2^{-53}$  for internal computations.

### 3.6.3 Analytic series tolerance & algorithms

A partial sum is computed for any infinite summation that forms part of an analytic result. A finite number of series terms  $P$  (107) can be chosen dependent upon the precision required, similar to previous numeric integral discussion. Theoretically  $P = \infty$  gives an exact solution; however in practice, accuracy to some fixed numerical precision may be observed with a low number for  $P$  due to the series rate of convergence. This is shown in Section 3.5, but it is highly contingent upon the spatial location of the field point relative to the singularity in the asymptotic expansion. For this reason, computing the series based upon a prior choice of  $P$  is inefficient as it is dependent on field point location, and becomes complicated when multiple infinite sums form part of an analytic result. A single tolerance parameter  $T$  is used for all summations that: removes the choice of  $P$  for each partial sum; is independent of field point location and reduces computational requirements across a set of field points; and homogenises convergence across the solution space (a high  $P \forall \mathbf{r}$  will give a precise answer in the far-field relative to the near-field, but far-field computations will likely contain the summation of terms  $\ll \epsilon$ ).

From (91), if the tolerance is equal to the remainder of form  $1 \times 10^{-n}$ , then meeting the criterion  $T = R \geq |f(n+1)| / (1 - L)$  gives an error of no greater than  $n$  decimal places

Table 3: The magnetic field basis vectors that require a series in part of the solution, with an algorithm to compute the partial sum to a tolerance.

Geometry	Source	Solution	Series	Algorithm
Disc	$K_\varphi$	$B_z$ (172)	$\beta^{(1)}, \delta^{(1)}$	1
		$\dot{B}_z$ (179)	$\beta^{(1)}$	
Volume	$J_\varphi$	$B_\rho$ (221)	$\beta^{(1)}, \delta^{(3)}$	4
		$\dot{B}_\rho$ (233)	$\beta^{(1)}, \vartheta$	
		$B_z$ (227)	$\beta^{(2)}, \delta^{(2)}, \beta^{(3)}, \gamma^{(3)}$	
Volume	$M_\rho$	$\dot{B}_z$ (236)	$\beta^{(2)}, \beta^{(3)}$	2, 3
		$B_z$ (303)	$\beta^{(1)}, \delta^{(1)}$	
		$\dot{B}_z$ (312)	$\beta^{(1)}$	

to the exact solution. In actuality, the series may have constant coefficient, be a component of a solution, and/or be a summand in a finite series (e.g.  $\sum_{m,n,q=0}^1 f_{m,n,q}$ ). Thus,  $R$  can only ever be proportional to the actual result remainder. The use of  $T$  only implies a relation to  $R$ . The exact relation varies between problems, but the point is that  $T$  acts as a homogeneous tuning parameter; increasing or decreasing the number of terms in a logical manner.

A summary of the series in this article is given in Table 3, with four algorithms that all use  $T$  given in Appendix D. Algorithm 3 for the double series reduces  $T$  by an order of magnitude to account for the sum of remainders from the ‘row or columns’ of the summation. The  $\delta^{(1,2)}$ , and  $\gamma^{(3)}$  series are each computed using the sum of the  $\zeta^{(1,2,3)}$ ,  $\eta^{(1,2,3)}$ ,  $\iota^{(1,2,3)}$  series, respectively. The requirement for a global tolerance parameter and summing algorithms becomes clear with  $B_z$  (227), that has 8 summations requiring the use of an algorithm, that are nested within the 8 summations of the definite integral, totalling 64 calls of an algorithm for a single field point. For the particular field point, each summation has a different spatial convergence as that field point is spatially variant with respect to each summation. Optimisation of these calculations is out of the scope of this article; however, without the provided method that uses the series limits for computation of partial-sum solutions, their practical use would be questionable. Although a detailed analysis of the relative convergence and computational performance of the various algorithms has not been undertaken (Algorithm 1 is shown in Section 6.1), it is important to note that the analytic solutions provided do converge and are computationally robust in close proximity to surfaces, which is not the case for approaches using hypergeometric functions in the literature.

### 3.6.4 FEA comparison

The coil and magnet FEA models are solved using Maxwell 3D, within the ANSYS Electronics Desktop 2022 R1 (ANSYS, Inc., Canonsburg, PA, USA). The material properties have a relative permeability of 1 with: a magnetic coercivity of  $-955 \text{kA/m}$  ( $|\mathbf{M}| = 955 \text{kA/m} \approx 1.2 \text{T}$ ) and bulk conductivity of 0 for the magnet; and a magnetic coercivity of 0 and bulk conductivity of  $58 \text{MS/m}$  for the coil. The coil can

be modelled as either a current density with  $1 \text{ MA/m}^2$  or as a stranded current with  $20 \text{ A}$  (based upon the model dimensions). A model with a 2D surface of revolution can be used in some cases; however, as this does not include the internal field, only results from 3D models are given here.

The target was  $\approx 500k$  tetrahedrons with curvilinear meshing for each magnet (13 passes, 30% refinement per pass), and ‘adaptive meshing’ that subdivides the elements with the highest energy error with each mesh refinement. The total energy error is the ratio of the error  $= \nabla \cdot \mathbf{B}$  to the total energy in the model. This is one measure of convergence of the solution, with the other being the delta energy, the difference between the total energy in each successive mesh refinement. These convergence values are given in tables for each magnetisation of the rectangular cylindrical arc sectors. The convergence values for the special cases (solid, axisymmetric) are omitted, yet similar, to the general hollow non-axisymmetric case. For a specific tabulated field point comparing a result between the FEA model and analytic equation, a local spherical mesh refinement was done around the point, with a diameter of  $1\text{mm}$  and maximum element length of  $0.3\text{mm}$ . The comparisons were quantified using

$$|\Delta \mathbf{B}| = \left| \frac{|\mathbf{B}_{\text{Analytic}}| - |\mathbf{B}_{\text{FEA}}|}{\frac{1}{2}(|\mathbf{B}_{\text{Analytic}}| + |\mathbf{B}_{\text{FEA}}|)} \right|. \quad (125)$$

The rationale for a FEA comparison is to check the analytic formulation, not quantify computational improvement; however, a benchmarking of computational performance relative to using analytic solutions is given in Sections 6.3 and 6.4. There are several confounding factors which influence the performance results, both relating to the problem domain and the implementation of the solutions. The important observation is if there are spatial trends or significant differences between results from the analytical solutions and the FEA model. This is not expected with the given convergence criteria, as in regions with a high field gradient and/or close to a singularity, there is an increased mesh density. Significant differences (large error %) are expected due to numerical noise when the analytic result is zero, or close to zero.

## 4 Azimuthal current densities: formulation and solution

In this section, integral solutions are derived from a filament model formulation (A39) of azimuthal current densities with 0D, 1D, and 2D cross-sections: forming a filament, disc or shell, and volume, respectively.

We present improved solutions for the non-axisymmetric filament and shell geometries, and new solutions for the non-axisymmetric disc and volume geometries. An analytic solution for the filament is considered foundational as it demonstrates the simplicity of an explicit solution using the method of Section 3.2. Analytic solutions for the disc and shell directly form part of the solution for permanent magnets in the following Section 5.

### 4.1 Filament – azimuthal current density

A 0D azimuthal current is defined  $\mathbf{I} = I_\varphi \mathbf{e}'_\varphi$  and illustrated in Figure 6. Using the filament model formulation, the vector

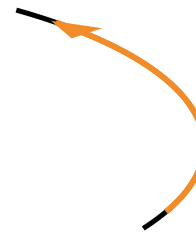


Figure 6:  $\mathbf{I}$  along the path  $\mathbf{e}'_\varphi$ .

potential is

$$\mathbf{A}(\mathbf{r}) = \frac{I_\varphi \mu_0}{4\pi} \rho' \int_{\varphi'_1}^{\varphi'_2} \frac{\mathbf{e}'_\varphi}{|\mathbf{r} - \mathbf{r}'|} d\varphi', \quad (126)$$

with magnetic field

$$\mathbf{B}(\mathbf{r}) = \frac{I_\varphi \mu_0}{4\pi} \rho' \int_{\varphi'_1}^{\varphi'_2} \mathbf{e}'_\varphi \times \frac{\mathbf{r} - \mathbf{r}'}{|\mathbf{r} - \mathbf{r}'|^3} d\varphi'. \quad (127)$$

The three components of the magnetic field are:

$$\mathbf{B}(\mathbf{r}) = \frac{I_\varphi \mu_0}{4\pi} [B_\rho(\mathbf{r}) \mathbf{e}_\rho + B_\varphi(\mathbf{r}) \mathbf{e}_\varphi + B_z(\mathbf{r}) \mathbf{e}_z]. \quad (128)$$

$$B_\rho(\mathbf{r}) = \rho' Z \int_{\varphi'_1}^{\varphi'_2} \cos(\varphi - \varphi') \hat{G}^3 d\varphi', \quad (129)$$

$$B_\varphi(\mathbf{r}) = -\rho' Z \int_{\varphi'_1}^{\varphi'_2} \sin(\varphi - \varphi') \hat{G}^3 d\varphi', \quad (130)$$

$$B_z(\mathbf{r}) = \rho' \int_{\varphi'_1}^{\varphi'_2} [\rho' - \rho \cos(\varphi - \varphi')] \hat{G}^3 d\varphi'. \quad (131)$$

From (129)-(131), a solution is found of form

$$\mathbf{B}(\rho > 0) = \frac{I_\varphi \mu_0}{4\pi} \sum_{q=1}^2 (-1)^q (\check{B}_\rho \mathbf{e}_\rho + \check{B}_\varphi \mathbf{e}_\varphi + \check{B}_z \mathbf{e}_z), \quad (132)$$

where  $\check{B}_b$  denotes the summand from the definite integral of  $B_b$ . This notation is of use for handling removable singularities or special cases in the infinite solution space.

#### 4.1.1 Radial component – filament current

Applying the  $\phi$  and  $t$  substitutions (21) to (129) gives

$$B_\rho = \frac{2\rho' Z}{R^3} \sum_{q=1}^2 (-1)^q \operatorname{sgn}(\Phi_q) \int_{\cos(\frac{1}{2}\Phi_q)}^1 \frac{1 - 2t^2}{(1 - k^2 t^2) w(t)} dt, \quad (133)$$

using a full partial-fraction expansion of form (G15),

$$\frac{1 - 2t^2}{1 - k^2 t^2} = \frac{2}{k^2} \left( 1 - \frac{1 - \frac{1}{2}k^2}{1 - k^2 t^2} \right). \quad (134)$$

Thus, by inspection this gives the transformed Legendre form

$$B_\rho = \frac{Z}{\rho R} \sum_{q=1}^2 (-1)^q [\mathsf{F}(\phi_q; k^2) - (1 - \frac{1}{2}k^2) \Pi(\phi_q; k^2, k^2)]. \quad (135)$$

Further, applying the well-known special case of  $\Pi(\theta, k^2, k^2)$  (E29) we find

$$\check{B}_\rho = \frac{Z}{\rho R} [\mathsf{F}(\phi_q; k^2) - (1 + \frac{1}{2}\bar{k}^2) \mathsf{E}(\phi_q; k^2)] - \frac{k^2 T^2 Z \sin \Phi_q}{2\rho \bar{R}^2 \hat{G}_q^{-1}}, \quad (136)$$

where

$$\bar{\varrho} = \rho - \rho', \quad (137)$$

$$\bar{k}^2 = 4\rho\rho'/\bar{R}^2, \quad (138)$$

$$\bar{R}^2 = \bar{\varrho}^2 + Z^2. \quad (139)$$

#### 4.1.2 Azimuthal component – filament current

Applying the  $\phi$  and  $t$  substitutions to (130) gives

$$B_\varphi = \frac{4\rho' Z}{R^3} \sum_{q=1}^2 (-1)^q \int_{\cos(\frac{1}{2}\Phi_q)}^1 \frac{t}{(1 - k^2 t^2)^{3/2}} dt, \quad (140)$$

that by inspection gives the closed-form solution

$$\check{B}_\varphi = -\frac{Z}{\rho} \hat{G}_q. \quad (141)$$

#### 4.1.3 Axial component – filament current

Applying the  $\phi$  and  $t$  substitutions to (131) gives

$$B_z = \frac{2\rho'}{R^3} \sum_{q=1}^2 (-1)^q \operatorname{sgn}(\Phi_q) \int_1^{\cos(\frac{1}{2}\Phi_q)} \frac{\rho' + \rho(1 - 2t^2)}{(1 - k^2 t^2) w(t)} dt, \quad (142)$$

that is of the same form as (133) with

$$\frac{\rho' + \rho(1 - 2t^2)}{1 - k^2 t^2} = \frac{2\rho}{k^2} \left( 1 + \frac{k^2(\rho + \rho') - 2\rho}{2\rho(1 - k^2 t^2)} \right). \quad (143)$$

The transformed Legendre form follows by inspection

$$B_z = -\frac{1}{R} \sum_{q=1}^2 (-1)^q \left[ \mathsf{F}(\phi_q; k^2) - \frac{\bar{T}^2}{R^2} \Pi(\phi_q; k^2, k^2) \right], \quad (144)$$

that as with (135), is

$$\check{B}_z = -\frac{1}{R} \left( \mathsf{F}(\phi_q; k^2) - \frac{\bar{T}^2}{R^2} \mathsf{E}(\phi_q; k^2) \right) + \frac{k^2 \bar{T}^2 \sin \Phi_q}{2\bar{R}^2 \hat{G}_q^{-1}}, \quad (145)$$

where

$$\bar{T}^2 = L^2 - \rho'^2. \quad (146)$$

#### 4.1.4 Singularities – filament current

The summands of (132) can be evaluated at all field points given a substitution on the azimuthal line. From (142)

$$\begin{aligned} \check{B}_\rho &\rightarrow 0, \\ \check{B}_\varphi &\rightarrow 0, \\ \check{B}_z &\rightarrow -\frac{\operatorname{sgn}(\Phi_q)}{2\rho'} \tanh^{-1}(\sin \phi_q), \end{aligned} \quad (147)$$

for  $(\rho = \rho') \wedge (z = z')$ , with the substitutions done before integration.

#### 4.1.5 Special cases – filament current

For a general solution, this section has conditional substitutions for (132).

**(a) Along the axis** Where the cylindrical basis is not defined, we convert (127) to a Cartesian basis, set  $\rho = 0$ , and complete the trivial integral

$$\begin{aligned} \mathbf{B}(\mathbf{r}) &\rightarrow \frac{I_\varphi \mu_0}{4\pi} \frac{\rho'}{(\rho'^2 + Z^2)^{3/2}} \sum_{q=1}^2 (-1)^q \\ &\quad \times (Z \sin \varphi'_q \mathbf{e}_x - Z \cos \varphi'_q \mathbf{e}_y + \rho' \varphi'_q \mathbf{e}_z). \end{aligned} \quad (148)$$

**(b) Axisymmetric** For a loop we have  $\varphi'_q = \{0, 2\pi\}$  and thus symmetry about  $\varphi$ . Complete elliptic integrals are expected in a solution for an axisymmetric geometry; the transformed Legendre forms are not required. There is free choice of the azimuthal integration limits to take advantage of the elliptic integral symmetries (Table 2). With choice of  $\varphi'_q = \{-\pi, \pi\}$ , the  $q$ -summation can be removed from the transformed Legendre terms in the axisymmetric case if the summand becomes twice the negative. For example with  $\phi_q = \{\pi, 0\}$

$$\begin{aligned} \sum_{q=1}^2 (-1)^q \mathsf{F}(\phi_q; k) &= \mathsf{F}(0; k^2) - \mathsf{F}(\pi; k^2) \\ &= -2K(k^2), \end{aligned} \quad (149)$$

where the same pattern holds for  $\mathsf{E}$  and  $\Pi$ .  $B_\varphi$  must vanish due to orthogonality, and with free choice of  $\varphi$ , the auxiliary trigonometric terms go to zero. By inspection of (136) and (145)

$$\mathbf{B}(\mathbf{r}) \rightarrow \frac{I_\varphi \mu_0}{4\pi} (\check{B}_\rho \mathbf{e}_\rho + \check{B}_z \mathbf{e}_z), \quad (150)$$

for  $(\varphi'_1 = 0) \wedge (\varphi'_2 = 2\pi) \wedge (\rho > 0)$ , where

$$\begin{aligned} \check{B}_\rho &= \frac{2Z}{\rho R} \left( \frac{\bar{T}^2}{\bar{R}} \mathsf{E}(k^2) - K(k^2) \right), \\ \check{B}_z &= \frac{2}{R} \left( K(k^2) - \frac{\bar{T}^2}{\bar{R}^2} \mathsf{E}(k^2) \right). \end{aligned} \quad (151)$$

From (148) and (150),

$$\mathbf{B}(\mathbf{r}) \rightarrow \frac{I_\varphi \mu_0}{2} \frac{\rho'^2}{(\rho'^2 + Z^2)^{3/2}} \mathbf{e}_z, \quad (152)$$

for  $(\varphi'_1 = 0) \wedge (\varphi'_2 = 2\pi) \wedge (\rho = 0)$ .

Equations (150) and (152) are equivalent to a standard textbook result [109, pg. 291].

## 4.2 Disc – azimuthal current density

A 1D azimuthal current is defined  $\mathbf{K} = K_\varphi \mathbf{e}'_\varphi \in [\rho'_1, \rho'_2]$  and illustrated in Figure 7. Using the filament model formulation,

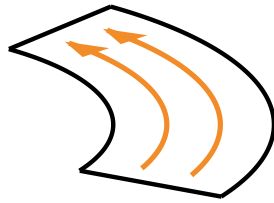


Figure 7:  $\mathbf{K}$  along the path  $\mathbf{e}'_\varphi$ .

the vector potential is

$$\mathbf{A}(\mathbf{r}) = \frac{K_\varphi \mu_0}{4\pi} \int_{\varphi'_1}^{\varphi'_2} \int_{\rho'_1}^{\rho'_2} \frac{\rho' \mathbf{e}'_\varphi}{|\mathbf{r} - \mathbf{r}'|} d\rho' d\varphi', \quad (153)$$

with magnetic field

$$\mathbf{B}(\mathbf{r}) = \frac{K_\varphi \mu_0}{4\pi} \int_{\varphi'_1}^{\varphi'_2} \int_{\rho'_1}^{\rho'_2} \rho' \mathbf{e}'_\varphi \times \frac{\mathbf{r} - \mathbf{r}'}{|\mathbf{r} - \mathbf{r}'|^3} d\rho' d\varphi'. \quad (154)$$

The three components of the magnetic field are:

$$\mathbf{B}(\mathbf{r}) = \frac{K_\varphi \mu_0}{4\pi} [B_\rho(\mathbf{r}) \mathbf{e}_\rho + B_\varphi(\mathbf{r}) \mathbf{e}_\varphi + B_z(\mathbf{r}) \mathbf{e}_z] \quad (155)$$

where

$$B_\rho(\mathbf{r}) = Z \int_{\varphi'_1}^{\varphi'_2} \int_{\rho'_1}^{\rho'_2} \rho' \cos(\varphi - \varphi') \hat{G}^3 d\rho' d\varphi', \quad (156)$$

$$B_\varphi(\mathbf{r}) = -Z \int_{\varphi'_1}^{\varphi'_2} \int_{\rho'_1}^{\rho'_2} \rho' \sin(\varphi - \varphi') \hat{G}^3 d\rho' d\varphi', \quad (157)$$

$$B_z(\mathbf{r}) = \int_{\varphi'_1}^{\varphi'_2} \int_{\rho'_1}^{\rho'_2} \rho' [\rho' - \rho \cos(\varphi - \varphi')] \hat{G}^3 d\rho' d\varphi'. \quad (158)$$

From (156)-(158), a solution is found of form

$$\mathbf{B}(\rho > 0) = \frac{K_\varphi \mu_0}{4\pi} \sum_{m,q=1}^2 (-1)^{m+q} (\check{B}_\rho \mathbf{e}_\rho + \check{B}_\varphi \mathbf{e}_\varphi + \check{B}_z \mathbf{e}_z), \quad (159)$$

with equivalent notation and use as (132).

### 4.2.1 Radial component – disc current

From (133) we now have an additional integral with separation

$$B_\rho = 2Z \sum_{q=1}^2 (-1)^q \operatorname{sgn}(\Phi_q) \int_{\cos(\frac{1}{2}\Phi_q)}^1 \frac{1 - 2t^2}{\sqrt{1 - t^2}} \times \int_{\rho'_1}^{\rho'_2} \frac{\rho'}{[L^2 + 2(1 - 2t^2)\rho\rho' + \rho'^2]^{3/2}} d\rho' dt. \quad (160)$$

The radial integrand of (160) is a proper rational function, and therefore has an elementary solution using partial fractions

(F16) of

$$B_\rho = \frac{2}{Z} \sum_{m,q=1}^2 (-1)^{m+q} \frac{\operatorname{sgn}(\Phi_q)}{R_m} \times \int_1^{\cos(\frac{1}{2}\Phi_q)} \frac{(1 - 2t^2)(L^2 + \rho\rho'_m(1 - 2t^2))}{(1 - a^2t^2)(1 - \bar{a}^2t^2)w_m(t)} dt, \quad (161)$$

with  $w_m^2(t) = (1 - t^2)(1 - k_m^2 t^2)$  (subsequent notation per (27), Appendix B), and definitions

$$a^2 = 2\rho/(\rho + L), \quad (162)$$

$$\bar{a}^2 = 2\rho/(\rho - L). \quad (163)$$

The denominator of (161) was factorised using the polynomial roots. The partial fraction expansion

$$\frac{(1 - 2t^2)[L^2 + \rho\rho'_m(1 - 2t^2)]}{(1 - a^2t^2)(1 - \bar{a}^2t^2)} = -\frac{\rho'_m}{\rho} \left[ 1 - \frac{\rho L}{Z^2 \rho'_m} \left( \frac{L - \rho'_m}{\bar{a}^2(1 - a^2t^2)} + \frac{L + \rho'_m}{a^2(1 - \bar{a}^2t^2)} \right) \right] \quad (164)$$

gives by inspection the transformed Legendre form

$$\check{B}_\rho = \frac{2Z}{\rho} \frac{\rho'_m}{R_m} \left[ F(\phi_q; k_m^2) - \frac{\rho L}{Z^2 \rho'_m} \times \left( \frac{\bar{S}_m^2}{\bar{a}^2} \Pi(\phi_q; a^2, k_m^2) + \frac{S_m^2}{a^2} \Pi(\phi_q; \bar{a}^2, k_m^2) \right) \right], \quad (165)$$

where

$$S^2 = L + \rho' \quad (166)$$

$$\bar{S}^2 = L - \rho'. \quad (167)$$

### 4.2.2 Azimuthal component – disc current

From (141) we now have the integral

$$B_\varphi = -\frac{Z}{\rho} \sum_{q=1}^2 (-1)^q \int_{\rho'_1}^{\rho'_2} \frac{d\rho'}{\sqrt{L^2 - 2\rho \cos(\Phi_q)\rho' + \rho'^2}}, \quad (168)$$

that gives the basic integral (F19)

$$\check{B}_\varphi = -\frac{Z}{\rho} \ln \left( \rho'_m - \rho \cos(\Phi_q) + \hat{G}_{m,q}^{-1} \right). \quad (169)$$

### 4.2.3 Axial component – disc current

From (142) we now have an additional integral with separation

$$B_z = 2 \sum_{q=1}^2 (-1)^q \operatorname{sgn}(\Phi_q) \int_{\cos(\frac{1}{2}\Phi_q)}^1 \frac{1}{\sqrt{1 - t^2}} \times \int_{\rho'_1}^{\rho'_2} \left( \frac{L^2 + \rho(1 - 2t^2)\rho'}{[L^2 + 2(1 - 2t^2)\rho\rho' + \rho'^2]^{3/2}} - [L^2 + 2(1 - 2t^2)\rho\rho' + \rho'^2]^{-1/2} \right) d\rho' dt, \quad (170)$$

where the improper rational function of the integrand with respect to  $\rho'$  has been expanded using partial fractions. The

first integrand of (170) is solved with (F16) and we transform the second with (23):

$$B_z = 2 \sum_{m,q=1}^2 (-1)^{m+q} \frac{\rho'_m \operatorname{sgn}\Phi_q}{R_m} \int_{\cos(\frac{1}{2}\Phi_q)}^1 \frac{dt}{w_m^2(t)} + \int_{\varphi'_1}^{\varphi'_2} \int_{\rho'_1}^{\rho'_2} \hat{G} d\rho' d\varphi'. \quad (171)$$

The  $t$ -integral gives by inspection the transformed Legendre form and the  $\hat{G}$ -integral is expressed as the series from (74):

$$\check{B}_z = \frac{2\rho'_m}{R_m} F(\phi_q; k_m^2) + \varphi'_q \alpha_m^{(1)} + \varphi'_q \beta_m^{(1)} - \delta_{m,q}^{(1)}. \quad (172)$$

#### 4.2.4 Check

The results of this section can be validated by examining the limit as  $\rho'_1 \rightarrow \rho'_2$ , where the disc approaches a filament. To complete this, first substitute  $K_\varphi = I_\varphi / (\rho'_2 - \rho'_1)$ , thus from the limit, the current density returns a constant current. Second, the substitutions  $\rho'_1 = \tilde{\rho} - \epsilon$  and  $\rho'_2 = \tilde{\rho} + \epsilon$  are made, introducing a parameter for the limit to be taken about. A power series expansion about  $\epsilon = 0$  of  $f(\epsilon)$  can thus be made where  $f_1, f_2, \dots \rightarrow 0$  and hence  $f_0 = \lim_{\epsilon \rightarrow 0} f(\epsilon)$  returns the magnetic flux components of the filament. Similar checks are possible for the subsequent subsections, although are omitted from this article.

#### 4.2.5 Singularities – disc current

The summands of (159) can be evaluated at all field points given the conditional substitutions given in this section.

**(a) On the disc plane** The radial and azimuthal components vanish, giving

$$\begin{aligned} \check{B}_\rho &\rightarrow 0, \\ \check{B}_\varphi &\rightarrow 0, \end{aligned} \quad (173)$$

for  $z = z'$ .

**(b) On the azimuthal line** When  $k^2 = 1$  in (172), the transformed Legendre form  $F(\phi; 1)$  will lead to  $K(1)$ , an unbound result. To resolve this, we need to employ the special case

$$F(\phi; 1) \rightarrow \sin \phi R_C(1, \cos^2 \phi) \quad (174)$$

for  $(\rho = \rho'_m) \wedge (z = z')$ , in addition to the cases of (173). The inverse Gudermannian function  $\operatorname{gd}^{-1}(a)$  is only defined  $-\pi/2 < a < \pi/2$ , avoided by the use of the symmetric (Carlson) elliptic integral  $R_C(x, y)$ , that is elementary in the range  $[0, 2\pi]$ .

**(c) On the radial line** Covered by (173) for  $(\varphi = \varphi'_q) \wedge (z = z')$ .

#### 4.2.6 Special cases – disc current

For a general solution, this section has conditional substitutions for (159).

**(a) Along the axis** Integrating (148) with respect to  $\rho'$  gives

$$\mathbf{B}(\mathbf{r}) \rightarrow \frac{K_\varphi \mu_0}{4\pi} \sum_{m,q=1}^2 (-1)^{m+q} (\check{B}_x \mathbf{e}_x + \check{B}_y \mathbf{e}_y + \check{B}_z \mathbf{e}_z), \quad (175)$$

for  $\rho = 0$ , where

$$\begin{aligned} \check{B}_x &= -\sin \varphi'_q \frac{Z}{\sqrt{\rho_m'^2 + Z^2}}, \\ \check{B}_y &= \cos \varphi'_q \frac{Z}{\sqrt{\rho_m'^2 + Z^2}}, \\ \check{B}_z &= -\varphi'_q \left( \frac{\rho'_m}{\sqrt{\rho_m'^2 + Z^2}} - \tanh^{-1} \frac{\rho'_m}{\sqrt{\rho_m'^2 + Z^2}} \right), \end{aligned} \quad (176)$$

for  $z \neq z'$ . For the singularity in (176),

$$\begin{aligned} \check{B}_x &\rightarrow 0, \\ \check{B}_y &\rightarrow 0, \\ \check{B}_z &\rightarrow \varphi'_q \ln \rho'_m, \end{aligned} \quad (177)$$

for  $z = z'$ .

**(b) Axisymmetric** For a loop we have  $\varphi'_q = \{0, 2\pi\}$  that transforms the elliptic integrals as discussed with (149). From (165) and (172)

$$\mathbf{B}(\mathbf{r}) \rightarrow \frac{K_\varphi \mu_0}{4\pi} \sum_{m=1}^2 (-1)^m (\check{B}_\rho \mathbf{e}_\rho + \check{B}_z \mathbf{e}_z), \quad (178)$$

for  $(\varphi'_1 = 0) \wedge (\varphi'_2 = 2\pi) \wedge (\rho > 0)$ , where

$$\begin{aligned} \check{B}_\rho &= -\frac{4\rho'_m Z}{\rho R_m} \left[ K(k_m^2) - \frac{\rho L}{Z^2 \rho'_m} \right. \\ &\quad \times \left. \left( \frac{\bar{S}_m^2}{\bar{a}^2} \Pi(a^2; k_m^2) + \frac{S_m^2}{a^2} \Pi(\bar{a}^2; k_m^2) \right) \right], \end{aligned} \quad (179)$$

$$\check{B}_z = 2\pi [\alpha_m^{(1)} + \beta_m^{(1)}] - \frac{4\rho'_m}{R_m} K(k_m^2).$$

In (179) the unbound result  $\Pi(1; k_m^2)$  (when  $a^2 = 1$  or  $\bar{a}^2 = 1$ ) occurs when  $z = z'$ , that from (173), gives  $\check{B}_\rho = 0$ . By inspection of (65) it is clear that the  $\delta$ -series is the ‘non-axisymmetric’ term and will disappear. This leaves the ‘axisymmetric’ radial  $\beta$ -series from  $\check{B}_z$ .

From (175) and (178) with  $\varphi'_q \rightarrow 2\pi$ ,

$$\mathbf{B}(\mathbf{r}) \rightarrow \frac{K_\varphi \mu_0}{4\pi} \sum_{m=1}^2 (-1)^m \check{B}_z \mathbf{e}_z, \quad (180)$$

for  $(\varphi'_1 = 0) \wedge (\varphi'_2 = 2\pi) \wedge (\rho = 0)$ , requiring  $\check{B}_z \rightarrow 2\pi \ln \rho'_m$  when  $z = z'$ .

**(c) Solid** There is no reduction of the summation; however, a singularity is found in (165) that requires the conditional substitutions

$$\check{B}_\rho \rightarrow \frac{L}{\rho} \tanh^{-1} \frac{\rho \sin \Phi_q}{Z}, \quad (181)$$

for  $\rho'_1 = 0$ , and

$$\check{B}_\rho \rightarrow 0, \quad (182)$$

for  $(\rho'_1 = 0) \wedge (z = z')$ .

**(d) Axisymmetric & Solid** The solution is given by (178) except from (181) we have

$$\dot{B}_\rho \rightarrow 0, \quad (183)$$

for  $\rho'_1 = 0$ .

### 4.3 Shell – azimuthal current density

A 1D azimuthal current is defined  $\mathbf{K} = K_\varphi \mathbf{e}'_\varphi \in [z'_1, z'_2]$  and illustrated in Figure 8. Using the filament model formulation,



Figure 8:  $\mathbf{K}$  along the path  $\mathbf{e}'_\varphi$ .

the vector potential is

$$\mathbf{A}(\mathbf{r}) = \frac{K_\varphi \mu_0}{4\pi} \rho' \int_{z'_1}^{z'_2} \int_{\varphi'_1}^{\varphi'_2} \frac{\mathbf{e}'_\varphi}{|\mathbf{r} - \mathbf{r}'|} d\varphi' dz' \quad (184)$$

with magnetic field

$$\mathbf{B}(\mathbf{r}) = \frac{K_\varphi \mu_0}{4\pi} \rho' \int_{z'_1}^{z'_2} \int_{\varphi'_1}^{\varphi'_2} \mathbf{e}'_\varphi \times \frac{\mathbf{r} - \mathbf{r}'}{|\mathbf{r} - \mathbf{r}'|^3} d\varphi' dz'. \quad (185)$$

The three components of the magnetic field are:

$$\mathbf{B}(\mathbf{r}) = \frac{K_\varphi \mu_0}{4\pi} [B_\rho(\mathbf{r}) \mathbf{e}_\rho + B_\varphi(\mathbf{r}) \mathbf{e}_\varphi + B_z(\mathbf{r}) \mathbf{e}_z] \quad (186)$$

where

$$B_\rho(\mathbf{r}) = \rho' \int_{z'_1}^{z'_2} \int_{\varphi'_1}^{\varphi'_2} \frac{(z - z') \cos(\varphi - \varphi')}{\hat{G}^{-3}} d\varphi' dz', \quad (187)$$

$$B_\varphi(\mathbf{r}) = \rho' \int_{z'_1}^{z'_2} \int_{\varphi'_1}^{\varphi'_2} \frac{(z' - z) \sin(\varphi - \varphi')}{\hat{G}^{-3}} d\varphi' dz', \quad (188)$$

$$B_z(\mathbf{r}) = \rho' \int_{z'_1}^{z'_2} \int_{\varphi'_1}^{\varphi'_2} \frac{\rho' - \rho \cos(\varphi - \varphi')}{\hat{G}^{-3}} d\varphi' dz'. \quad (189)$$

From (187)-(189), a solution is found of form

$$\mathbf{B}(\rho > 0) = \frac{K_\varphi \mu_0}{4\pi} \sum_{n,q=1}^2 (-1)^{n+q} (\check{B}_\rho \mathbf{e}_\rho + \check{B}_\varphi \mathbf{e}_\varphi + \check{B}_z \mathbf{e}_z), \quad (190)$$

with equivalent notation and use as (132).

#### 4.3.1 Radial component – shell current

From (133) we now have an additional integral with separation

$$\begin{aligned} B_\rho &= 2\rho' \sum_{q=1}^2 (-1)^q \operatorname{sgn}(\Phi_q) \int_{\cos(\frac{1}{2}\Phi_q)}^1 \frac{1 - 2t^2}{\sqrt{1 - t^2}} \\ &\times \int_{z'_1}^{z'_2} \frac{z - z'}{[\rho^2 + 2(1 - 2t^2)\rho\rho' + \rho'^2 + (z - z')^2]^{3/2}} dz' dt \end{aligned} \quad (191)$$

that is solved using (F16) to give

$$B_\rho = 2\rho' \sum_{n,q=1}^2 (-1)^{n+q} \frac{\operatorname{sgn}\Phi_q}{R_n} \int_{\cos(\frac{1}{2}\Phi_q)}^1 \frac{1 - 2t^2}{w_m(t)} dt. \quad (192)$$

By inspection, we have the difference of two elliptic integrals

$$\check{B}_\rho = \frac{2\rho'}{R_n} [\mathcal{F}(\phi_q; k_n^2) - 2\mathcal{D}(\phi_q; k_n^2)]. \quad (193)$$

#### 4.3.2 Azimuthal component – shell current

From (141) we now have the integral

$$\begin{aligned} B_\varphi &= -\frac{1}{\rho} \sum_{q=1}^2 (-1)^q \\ &\times \int_{z'_1}^{z'_2} \frac{z - z'}{\sqrt{\rho^2 - 2\rho\rho' \cos\Phi_q + \rho'^2 + (z - z')^2}} dz', \end{aligned} \quad (194)$$

that is solved using (F17) to give

$$\check{B}_\varphi = \frac{1}{\rho} \hat{G}_{n,q}^{-1}. \quad (195)$$

#### 4.3.3 Axial component – shell current

From (142) we now have an additional integral

$$\begin{aligned} B_z &= 2\rho' \sum_{q=1}^2 (-1)^q \operatorname{sgn}(\Phi_q) \int_{\cos(\frac{1}{2}\Phi_q)}^1 \frac{\rho' + \rho(1 - 2t^2)}{\sqrt{1 - t^2}} \\ &\times \int_{z'_1}^{z'_2} \frac{dz' dt}{[\rho^2 + 2(1 - 2t^2)\rho\rho' + \rho'^2 + (z - z')^2]^{3/2}}, \end{aligned} \quad (196)$$

that is solved directly from (F16)

$$\begin{aligned} B_z &= \frac{2\rho'}{(\rho + \rho')^2} \sum_{n,q=1}^2 (-1)^{n+q} \frac{Z_n}{R_n} \operatorname{sgn}\Phi_q \\ &\times \int_{\cos(\frac{1}{2}\Phi_q)}^1 \frac{\rho' + \rho(1 - 2t^2)}{(1 - k_n^2 t^2) w_n(t)} dt. \end{aligned} \quad (197)$$

The integrand of (197) is of equivalent form to (142) with a different elliptic characteristic, thus the solution is known to be

$$\check{B}_z = \frac{Z_n}{R_n} \left( \mathcal{F}(\phi_q; k_n^2) + \frac{\rho'^2 - \rho^2}{\rho^2} \Pi(\phi_q; \kappa^2, k_n^2) \right), \quad (198)$$

where

$$\kappa^2 = 4\rho\rho'/\rho^2. \quad (199)$$

#### 4.3.4 Singularities – shell current

The summands of (190) can be evaluated at all field points given the conditional substitutions given in this section.

**(a) On the shell plane** For the singularity with  $\Pi(\phi; \kappa^2, k^2)$  in (198), from (197)

$$\check{B}_z \rightarrow \frac{Z_n}{\sqrt{Z_n^2 + 4\rho'^2}} \mathcal{F} \left( \phi_q; \frac{4\rho'^2}{Z_n^2 + 4\rho'^2} \right) \quad (200)$$

for  $\rho = \rho'$ , with the substitution done before integration.

(b) **On the axial line** Covered by (200) for  $(\rho = \rho') \wedge (\varphi = \varphi'_q)$ .

(c) **On the azimuthal line** Covered by (200) and (174) for  $(\rho = \rho') \wedge (z = z'_n)$ .

### 4.3.5 Special cases – shell current

For a general solution, this section has conditional substitutions for (190), at specific field points or when considering simplified geometry.

(a) **Along the axis** Integrating (148) with respect to  $z'$  gives

$$\mathbf{B}(\mathbf{r}) \rightarrow \frac{K_\varphi \mu_0}{4\pi} \sum_{n,q=1}^2 (-1)^{n+q} (\check{B}_x \mathbf{e}_x + \check{B}_y \mathbf{e}_y + \check{B}_z \mathbf{e}_z), \quad (201)$$

for  $\rho = 0$ , where

$$\begin{aligned} \check{B}_x &= \frac{\rho' \sin \varphi'_q}{\sqrt{\rho'^2 + Z_n^2}}, \\ \check{B}_y &= -\frac{\rho' \cos \varphi'_q}{\sqrt{\rho'^2 + Z_n^2}}, \\ \check{B}_z &= -\frac{\varphi'_q Z_n}{\sqrt{\rho'^2 + Z_n^2}}, \end{aligned} \quad (202)$$

for  $z \neq z'_n$ . For the singularity in (202),

$$\begin{aligned} \check{B}_x &\rightarrow \sin \varphi'_q, \\ \check{B}_y &\rightarrow -\cos \varphi'_q, \\ \check{B}_z &\rightarrow 0, \end{aligned} \quad (203)$$

for  $z = z'_n$ .

(b) **Axisymmetric** For a loop we have  $\varphi'_q = \{0, 2\pi\}$  that transforms the elliptic integrals as discussed with (149). From (193) and (198)

$$\mathbf{B}(\mathbf{r}) \rightarrow \frac{K_\varphi \mu_0}{4\pi} \sum_{n=1}^2 (-1)^n (\check{B}_\rho \mathbf{e}_\rho + \check{B}_z \mathbf{e}_z), \quad (204)$$

for  $(\varphi'_1 = 0) \wedge (\varphi'_2 = 2\pi) \wedge (\rho > 0)$ , where

$$\begin{aligned} \check{B}_\rho &= \frac{4\rho'}{R_n} [2D(k_n^2) - K(k_n^2)], \\ \check{B}_z &= -\frac{2Z_n}{R_n} \left( K(k_n^2) + \frac{\rho'^2 - \rho^2}{\rho'^2} \Pi(\kappa^2; k_n^2) \right). \end{aligned} \quad (205)$$

In (205) the unbound result  $\Pi(1; k_n^2)$  (when  $\kappa^2 = 1$ ) occurs when  $\rho = \rho'$ , that from (200), gives

$$\check{B}_z \rightarrow -2 \frac{Z_n}{\sqrt{Z_n^2 + 4\rho'^2}} K \left( \frac{4\rho'^2}{Z_n^2 + 4\rho'^2} \right). \quad (206)$$

From (202) and (204) with  $\varphi'_q \rightarrow 2\pi$ ,

$$\mathbf{B}(\mathbf{r}) \rightarrow \frac{K_\varphi \mu_0}{4\pi} \sum_{n=1}^2 (-1)^n \check{B}_z \mathbf{e}_z \quad (207)$$

for  $(\varphi'_1 = 0) \wedge (\varphi'_2 = 2\pi) \wedge (\rho = 0)$ .

## 4.4 Volume – azimuthal current density

A 2D azimuthal current is defined  $\mathbf{J} = J_\varphi \mathbf{e}'_\varphi \in ([\rho'_1, \rho'_2] \cup [z'_1, z'_2])$  and illustrated in Figure 9. Using the filament model

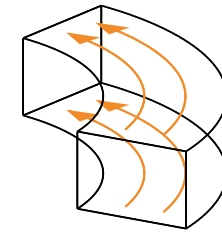


Figure 9:  $\mathbf{J}$  along the path  $\mathbf{e}'_\varphi$ .

formulation, the vector potential is

$$\mathbf{A}(\mathbf{r}) = \frac{J_\varphi \mu_0}{4\pi} \int_{z'_1}^{z'_2} \int_{\varphi'_1}^{\varphi'_2} \int_{\rho'_1}^{\rho'_2} \frac{\rho' \mathbf{e}'_\varphi}{|\mathbf{r} - \mathbf{r}'|} d\rho' d\varphi' dz'. \quad (208)$$

with magnetic field

$$\mathbf{B}(\mathbf{r}) = \frac{J_\varphi \mu_0}{4\pi} \int_{z'_1}^{z'_2} \int_{\varphi'_1}^{\varphi'_2} \int_{\rho'_1}^{\rho'_2} \rho' \mathbf{e}'_\varphi \times \frac{\mathbf{r} - \mathbf{r}'}{|\mathbf{r} - \mathbf{r}'|^3} d\rho' d\varphi' dz'. \quad (209)$$

The three components of the magnetic field are:

$$\mathbf{B}(\mathbf{r}) = \frac{J_\varphi \mu_0}{4\pi} [B_\rho(\mathbf{r}) \mathbf{e}_\rho + B_\varphi(\mathbf{r}) \mathbf{e}_\varphi + B_z(\mathbf{r}) \mathbf{e}_z] \quad (210)$$

where

$$B_\rho(\mathbf{r}) = \int_{z'_1}^{z'_2} \int_{\varphi'_1}^{\varphi'_2} \int_{\rho'_1}^{\rho'_2} \frac{\rho'(z - z') \cos(\varphi - \varphi')}{\hat{G}^{-3}} d\rho' d\varphi' dz', \quad (211)$$

$$B_\varphi(\mathbf{r}) = \int_{z'_1}^{z'_2} \int_{\varphi'_1}^{\varphi'_2} \int_{\rho'_1}^{\rho'_2} \frac{\rho'(z' - z) \sin(\varphi - \varphi')}{\hat{G}^{-3}} d\rho' d\varphi' dz', \quad (212)$$

$$B_z(\mathbf{r}) = \int_{z'_1}^{z'_2} \int_{\varphi'_1}^{\varphi'_2} \int_{\rho'_1}^{\rho'_2} \frac{\rho'[\rho' - \rho \cos(\varphi - \varphi')]}{\hat{G}^{-3}} d\rho' d\varphi' dz'. \quad (213)$$

From (211)-(213), a solution is found of form

$$\mathbf{B}(\rho > 0) = \frac{J_\varphi \mu_0}{4\pi} \sum_{m,n,q=1}^2 (-1)^{m+n+q} (\check{B}_\rho \mathbf{e}_\rho + \check{B}_\varphi \mathbf{e}_\varphi + \check{B}_z \mathbf{e}_z), \quad (214)$$

with an equivalent notation and use as (132).

### 4.4.1 Radial component – volume current

From (160) we now have an additional integral with separation

$$\begin{aligned} B_\rho &= 2 \sum_{q=1}^2 (-1)^q \operatorname{sgn}(\Phi_q) \int_{\cos(\frac{1}{2}\Phi_q)}^1 \frac{1 - 2t^2}{\sqrt{1 - t^2}} \int_{\rho'_1}^{\rho'_2} \rho' \\ &\quad \times \int_{z'_1}^{z'_2} \frac{(z - z') dz' d\rho' dt}{[\rho^2 + 2\rho\rho'(1 - 2t^2) + \rho'^2 + (z - z')^2]^{3/2}}, \end{aligned} \quad (215)$$

where the integral with respect to  $z'$  is solved using (F16) to give

$$B_\rho = 2 \sum_{n,q=1}^2 (-1)^{n+q} \operatorname{sgn}(\Phi_q) \int_{\cos(\frac{1}{2}\Phi_q)}^1 \frac{1-2t^2}{\sqrt{1-t^2}} \times \int_{\rho'_1}^{\rho'_2} \frac{\rho'}{\sqrt{L_n^2 + 2(1-2t^2)\rho\rho' + \rho'^2}} d\rho' dt, \quad (216)$$

and the integral with respect to  $\rho'$  is solved using (F15) and (F18)

$$B_\rho = 2 \sum_{m,n,q=1}^2 (-1)^{m+n+q} \operatorname{sgn}(\Phi_q) R_{n,m} \times \int_{\cos(\frac{1}{2}\Phi_q)}^1 \frac{(1-2t^2)(1-k_{n,m}^2 t^2)}{w_{m,n}(t)} dt + \rho \sum_{n=1}^2 (-1)^n \int_{\varphi'_1}^{\varphi'_2} \int_{\rho'_1}^{\rho'_2} \cos^2(\varphi - \varphi') \hat{G}_n d\rho' d\varphi'. \quad (217)$$

The first integral of (217) can be solved by inspection when expanding the numerator and using the recurrence relation (G16)

$$\int \frac{t^4 dt}{w(t)} = \frac{1}{3k^2} \left( tw(t) + 2(1+k^2) \int \frac{t^2 dt}{w(t)} - \int \frac{dt}{w(t)} \right), \quad (218)$$

and the second integral has been differentiated (F19) and transformed (23). The  $\rho'$  integral of (217) is known from (51), which leaves the elementary  $\varphi'$  integral

$$\int \frac{\cos[(\nu+1)(\varphi-\varphi')] dt}{\cos^{-2}(\varphi-\varphi')} = \frac{1}{4} \left( \frac{\sin[(\nu-1)(\varphi-\varphi')]}{\nu-1} + \frac{2\sin[(\nu+1)(\varphi-\varphi')]}{\nu+1} + \frac{\sin[(\nu+3)(\varphi-\varphi')]}{\nu+3} \right) \quad (219)$$

where the second term on the right-hand side is an element of the  $\delta^{(1)}$ -series (65) and the other two are shifted  $\nu \rightarrow \nu \pm 2$ . To simplify this result and handle the singularity at  $\nu = 1$  we define the function

$$\lambda(\nu) = \begin{cases} \sum_{n=0}^2 \binom{2}{n} \frac{\sin[(\nu+2n-1)\Phi]}{\nu+2n-1}, & \text{for } \nu \neq 1, \\ \Phi + \sum_{n=1}^2 \binom{2}{n} \frac{\sin[(\nu+2n-1)\Phi]}{\nu+2n-1}, & \text{for } \nu = 1. \end{cases} \quad (220)$$

The result of (217) is now given

$$\check{B}_\rho = \frac{1}{2} \left( -\frac{4}{3} \sin \Phi_q \hat{G}_{m,n,q}^{-1} - \rho \delta_{m,n,q}^{(3)} + \frac{4}{3} R_{m,n} [\mathcal{F}(\phi_q; k_{n,m}^2) + (k_{n,m}^2 - 2) \mathcal{D}(\phi_q; k_{n,m}^2)] - \rho [\Phi_q + \frac{1}{2} \sin(2\Phi_q)] (\alpha_{m,n}^{(1)} + \beta_{m,n}^{(1)}) \right), \quad (221)$$

where

$$\delta_{m,n,q}^{(3)} = \sum_{\nu=0}^{\infty} \Xi_{m,n}(\nu, 0) \sum_{p=0}^{\lfloor \nu/2 \rfloor} \binom{\nu+1}{p} \lambda_q(\nu - 2p). \quad (222)$$

The authors did not find any practicable simplification or reduction to this double series, even with a closed-form component of  $\lambda(\nu - 2p)$ , shown by (66) to (75). The expression solves fast and converges quickly when summed with an equal number of indexed  $\nu$ - and  $p$ -terms. The change of form to a nested finite series removes the beta function from the second summation to simplify calculation and fix the summation order to a single index. We do not explicitly show the row and column limits to this series; however, the series is of a similar form to (96). Our conjecture is that spatial convergence of this series is similar to Figure 5a and the tolerance for the finite sum can be found by  $\beta_{m,n}^{(1)}$ . This calculation is shown with Algorithm 4 in Appendix D.

#### 4.4.2 Azimuthal component – volume current

From (168) we have the additional integral

$$B_\varphi = -\frac{1}{\rho} \sum_{q=1}^2 (-1)^q \int_{\rho'_1}^{\rho'_2} \cdot \int_{z'_1}^{z'_2} \frac{(z-z') dz' d\rho'}{\sqrt{\rho^2 - 2\rho \cos(\Phi_q) \rho' + \rho'^2 + (z-z')^2}}, \quad (223)$$

that is solved by inspection of (F17) to give

$$B_\varphi = \frac{1}{\rho} \sum_{n,q=1}^2 (-1)^{n+q} \int_{\rho'_1}^{\rho'_2} \sqrt{L_n^2 - 2\rho \cos(\Phi_q) \rho' + \rho'^2} d\rho', \quad (224)$$

then using (F18) to give

$$\check{B}_\varphi = \frac{1}{2\rho} \left[ (\rho'_m - \rho \cos \Phi_q) \hat{G}_{n,m,q}^{-1} + (Z_n^2 + \rho^2 \sin^2 \Phi_q) \times \ln(\rho'_m - \rho \cos \Phi_q + \hat{G}_{n,m,q}^{-1}) \right]. \quad (225)$$

#### 4.4.3 Axial component – volume current

From (171) we have an additional integral; however this time we identify the first integrand to be a double integral of  $\hat{G}$ :

$$B_z = \int_{z'_2}^{z'_1} \int_{\varphi'_1}^{\varphi'_2} \int_{\rho'_1}^{\rho'_2} \hat{G} d\rho' d\varphi' dz' - \sum_{m=1}^2 (-1)^m \rho'_m \int_{z'_2}^{z'_1} \int_{\varphi'_2}^{\varphi'_1} \hat{G}_m d\varphi' dz'. \quad (226)$$

The volume and surface integrals are known from (85) and (82) respectively. Combining the solution to each integral gives

$$\check{B}_z = \varphi'_q \alpha_{m,n}^{(3)} + \frac{1}{2} \rho'_m \operatorname{sgn}(Z_n) (2\varphi'_q \alpha_{m,n}^{(2)} + \varphi'_q \beta_{m,n}^{(2)}) - \delta_{m,n,q}^{(2)} - \frac{1}{8} \sqrt{\pi} \varphi'_q \beta_{m,n}^{(3)} + \gamma_{m,n,q}^{(3)}. \quad (227)$$

#### 4.4.4 Singularities – volume current

The summands of (214) can be evaluated at all field points given the conditional substitutions given in this section.

**(a) On the azimuthal line** This is covered by (174) for  $(\rho = \rho') \wedge (z = z'_n)$ .

**(b) On the radial line** To avoid  $\log(0)$ ,

$$\check{B}_\varphi \rightarrow -\frac{\rho'_m(\rho'_m - 2\rho)|\bar{\varrho}_m|}{2\rho\bar{\varrho}_m}, \quad (228)$$

for  $(\varphi = \varphi'_q) \wedge (z = z'_n)$ , that is substituted before integration in (224).

#### 4.4.5 Special cases – volume current

For a general solution, this section has conditional substitutions for (214), at specific field points or when considering simplified geometry.

**(a) Along the axis** Integrating (201) with respect to  $\rho'$  gives

$$\mathbf{B}(\mathbf{r}) \rightarrow \frac{J_\varphi \mu_0}{4\pi} \sum_{m,n,q=1}^2 (-1)^{m+n+q} (\check{B}_x \mathbf{e}_x + \check{B}_y \mathbf{e}_y + \check{B}_z \mathbf{e}_z) \quad (229)$$

for  $\rho = 0$ , where

$$\begin{aligned} \check{B}_x &= \sqrt{\rho'^2_m + Z_n^2} \sin \varphi'_q, \\ \check{B}_y &= -\sqrt{\rho'^2_m + Z_n^2} \cos \varphi'_q, \\ \check{B}_z &= -\varphi'_q Z_n \tanh^{-1} \frac{\rho'_m}{\sqrt{\rho'^2_m + Z_n^2}}, \end{aligned} \quad (230)$$

for  $z \neq z'_n$ . For the singularity in  $\check{B}_z$ ,

$$\check{B}_z \rightarrow 0, \quad (231)$$

for  $z = z'_n$ .

**(b) Axisymmetric** For a loop we have  $\varphi'_q = \{0, 2\pi\}$  that transforms the elliptic integrals as discussed with (149). From (221) and (227)

$$\mathbf{B}(\mathbf{r}) \rightarrow \frac{J_\varphi \mu_0}{4\pi} \sum_{m,n=1}^2 (-1)^{m+n} (\check{B}_\rho \mathbf{e}_\rho + \check{B}_z \mathbf{e}_z) \quad (232)$$

for  $(\varphi'_1 = 0) \wedge (\varphi'_2 = 2\pi) \wedge (\rho > 0)$ . By inspection of (221) we have

$$\begin{aligned} \check{B}_\rho &= -\frac{4}{3} R_{m,n} [K(k_{n,m}^2) + (k_{n,m}^2 - 2)D(k_{n,m}^2)] \\ &\quad + \pi\rho \left( \alpha_{m,n}^{(1)} + \beta_{m,n}^{(1)} + \vartheta_{m,n} \right), \end{aligned} \quad (233)$$

where

$$\vartheta = \begin{cases} \sum_{\nu=0}^{\infty} \Xi(\nu, 0) \sum_{p=0}^{\lfloor \nu/2 \rfloor} \binom{\nu+1}{p} & \text{for } \nu - 2p = 1, \\ 0 & \text{for } \nu - 2p \neq 1. \end{cases} \quad (234)$$

In (179) we saw the ‘non-axisymmetric’  $\delta$ -series disappear, and we have something similar here with the ‘ $\lambda$ -series’; however, the singularity from the  $\varphi'$  integral at  $\nu = 1$  does not disappear. In (222) this singularity is shifted by the series

identity (E35) and is at  $\nu - 2p = 1$ . From (234) we can observe that only the odd terms of the series are non-zero

$$\begin{aligned} \vartheta &= \sum_{\nu=0}^{\infty} v(\nu) \Xi(\nu, 0) \sum_{p=0}^{\frac{1}{2}(\nu-1)} \binom{\nu+1}{p} \\ &= \sum_{\nu=0}^{\infty} v(\nu) \Xi(\nu, 0) \binom{\nu+1}{\frac{\nu}{2} - \frac{1}{2}}, \\ &\equiv \sum_{\nu=0}^{\lfloor (P-1)/2 \rfloor} \Xi(2\nu+1, 0) \binom{2\nu+2}{\nu}, \end{aligned} \quad (235)$$

and thus there is a closed-form expression for the nested summation and a simplified finite sum (107) for large  $P$ . Equation (211) now reduces to a form containing a single summation in (233).

By inspection of (227) we have

$$\begin{aligned} \check{B}_z &= 2\pi [\alpha_{m,n}^{(3)} + \frac{1}{2}\rho'_m \operatorname{sgn}(Z_n) \\ &\quad \times (2\alpha_{m,n}^{(2)} + \beta_{m,n}^{(2)} - \frac{1}{8}\sqrt{\pi}\beta_{m,n}^{(3)})]. \end{aligned} \quad (236)$$

where the  $\delta^{(2)}$  and  $\gamma^{(3)}$  series have disappeared. From (229) and (232) with  $\varphi'_q \rightarrow 2\pi$ , we have

$$\mathbf{B}(\mathbf{r}) \rightarrow \frac{J_\varphi \mu_0}{4\pi} \sum_{m,n=1}^2 (-1)^{m+n} \check{B}_z \mathbf{e}_z \quad (237)$$

for  $(\varphi'_1 = 0) \wedge (\varphi'_2 = 2\pi) \wedge (\rho = 0)$ .

## 4.5 Verification & Summary

An indirect comparison of the analytic results with FEA for the disc ((159) Section 4.2) and shell ((190) Section 4.3) are given respectively for radially (298) and axially (349) magnetised magnets in the following Section 5.

A direct comparison with FEA is given for the axisymmetric coil results (232) of Section 4.4. The FEA model requires continuity in the current path which can be achieved with the complete circuit existing within the solution region, or with the path entering and exiting the solution region via the boundary. This second method works well with a symmetric boundary condition, but if used with the non-axisymmetric coil sector, it will distort the magnetic field near the source/boundary to maintain a net zero divergence. Workarounds involve modelling a rounded rectangle that contains the coil sector, or adding fictitious wires to move the coil sector away from the boundary. Both methods introduce uncertainty and complexity into the comparison with the analytic result and are omitted.

Magnetic field surfaces from the rectangular coil sector calculated using the analytical formulation (214) developed here are given in Figure 10 for a fixed tolerance  $T = 10^{-7}$ . The outer surfaces Figure 10d and Figure 10e converge faster compared to the inner surfaces Figure 10b and Figure 10c. This effect is shown in the axisymmetric, or revolved sector, in Figure 11. The algorithms spatially converge uniformly as the tolerance increases — except around the singular planes in the series (shown in Figure 5). About these singular planes, the required number of terms for a set tolerance rapidly approaches infinity. In a less-abstract dimensionalised figure,

this is shown in Figure 11c. Good agreement with FEA is shown spatially, except for within the coil and near the axis, that require a proportionally larger number of terms. The difference can be visualised with Figure 11b across the surfaces with a jump discontinuity, that is captured with FEA, whereas the analytical series have a smooth contour transition.

A qualitative view of the field directionality is given in Figure 11d, and Table 4 provides reference output values for the equations in Section 4.4. Further reference results for the non-axisymmetric filament, disc, shell, and volume are provided in the supplementary material of Appendix I. This contains a numeric evaluation (details in Section 3.6.2) of all analytic integrals of this section compared with all analytic solutions, inclusive of singular and special cases. Comparison to both the numeric and FEA results confirm the accuracy and robustness of the developed analytical solutions.

## 5 Principal magnetisations: formulation and solution

In this section, integral solutions are derived from current (A26) and/or charge (A31) model formulations with principal magnetisation directions: diametric, radial, azimuthal, and axial. For each, we choose a model that minimises the number of integrals to be solved by firstly avoiding the volume integral. If the magnetisation is curl-free, the volume integral vanishes in the current model. If the magnetisation is divergence-free, the volume integral vanishes in the charge model. In the case that both are true, the surface integrals tend to reduce advantageously with the charge model due to orthogonality, having a dot product over cross product (currents must form closed loops). Regardless, a solution for the complete set of integrals from both models can be shown.

A complete set of integrals are shown in Table J.1 for principal magnetisations in cylindrical coordinates, excepting constants, with related illustrations in Figure J.2. All equations are solved either directly within this section, were solved in Section 3.3, or are solved indirectly due to mathematical equivalence. From Table J.1, an example of mathematical equivalences is chosen for illustrative purposes. Of particular interest are geometries containing a zero component of axial flux. The axial components are shown to typically not be well-described by elliptic functions, rather a type of incomplete beta function (Section 3).

The current carrying surfaces that describe a permanent magnet with uniform radial magnetisation are the disc (J4-J6) and section (J22-J24). The axial component of flux only comes from the two disc surfaces. An alternate formulation that describes this permanent magnet is a shell of uniform charge (J16-J18), and a gradient of volumetric charge (J31-J33) that varies in magnitude by  $1/\rho$ . Thus, we can write the

interesting equivalence

$$\begin{aligned} & \int_{\rho'_1}^{\rho'_2} \int_{\varphi'_1}^{\varphi'_2} \hat{G}^3 [\rho'^2 - \rho \rho' \cos(\varphi - \varphi')] d\varphi' d\rho' \Big|_{z'_1}^{z'_2} \\ &= \int_{\rho'_1}^{\rho'_2} \int_{\varphi'_1}^{\varphi'_2} \int_{z'_1}^{z'_2} \hat{G}^3 (z - z') dz' d\varphi' d\rho' \\ &\quad - \rho' \int_{\varphi'_1}^{\varphi'_2} \int_{z'_1}^{z'_2} \hat{G}^3 (z - z') dz' d\varphi' \Big|_{\rho'_1}^{\rho'_2}. \end{aligned} \quad (238)$$

The benefit to observing (238) is we have changed the integration region and reduced the order of  $\rho'$  — a form shown to not be obviously malleable to a closed-form or analytic solution (158). This represents an interesting use-case with the apparent use of both the charge and current models to solve a field component from a volumetric current distribution formulated from the filament model (226).

A more straight-forward transform is given by a permanent magnet with uniform azimuthal magnetisation (J3, J27, J30). This orthogonalisation between the charge and current models gives

$$\begin{aligned} & \rho \int_{\rho'_1}^{\rho'_2} \int_{\varphi'_1}^{\varphi'_2} \hat{G}^3 \rho' \sin(\varphi - \varphi') d\varphi' d\rho' \Big|_{z'_1}^{z'_2} \\ &= \int_{\rho'_1}^{\rho'_2} \int_{z'_1}^{z'_2} \hat{G}^3 (z - z') dz' d\rho' \Big|_{\varphi'_1}^{\varphi'_2}. \end{aligned} \quad (239)$$

Further transforms can be deduced as required within this problem space, with an extreme example given in Section 6.4.

### 5.1 Diametric magnetisation

Diametric magnetisation is defined by the angle  $\varphi^*$  with  $\mathbf{M}_\perp(\mathbf{r}, \mathbf{r}') = M_\perp [\cos(\varphi^* - \varphi) \mathbf{e}_\rho + \sin(\varphi^* - \varphi) \mathbf{e}_\varphi]$ . Using the charge model formulation, the scalar potential is

$$\phi(\mathbf{r}) = \frac{1}{4\pi} \oint_S \frac{\mathbf{M}_\perp(\mathbf{r}, \mathbf{r}') \cdot \mathbf{n}(\mathbf{r}, \mathbf{r}')}{|\mathbf{r} - \mathbf{r}'|} da' \quad (240)$$

with magnetic field

$$\mathbf{B}(\mathbf{r}) = \frac{\mu_0}{4\pi} \oint_S \frac{(\mathbf{r} - \mathbf{r}') [\mathbf{M}_\perp(\mathbf{r}, \mathbf{r}') \cdot \mathbf{n}(\mathbf{r}, \mathbf{r}')]}{|\mathbf{r} - \mathbf{r}'|^3} da'. \quad (241)$$

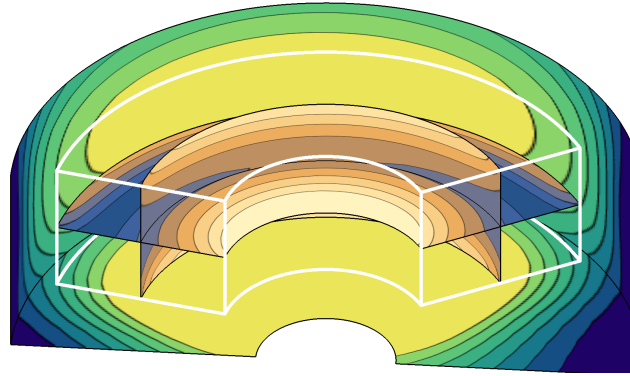
After expanding, the three components of the magnetic field are due to shell<sup>(1)</sup> and section<sup>(2)</sup> surfaces of charge:

$$B_\rho(\mathbf{r}) = \frac{M_\perp \mu_0}{4\pi} [B_\rho^{(1)}(\mathbf{r}) + B_\rho^{(2)}(\mathbf{r})], \quad (242)$$

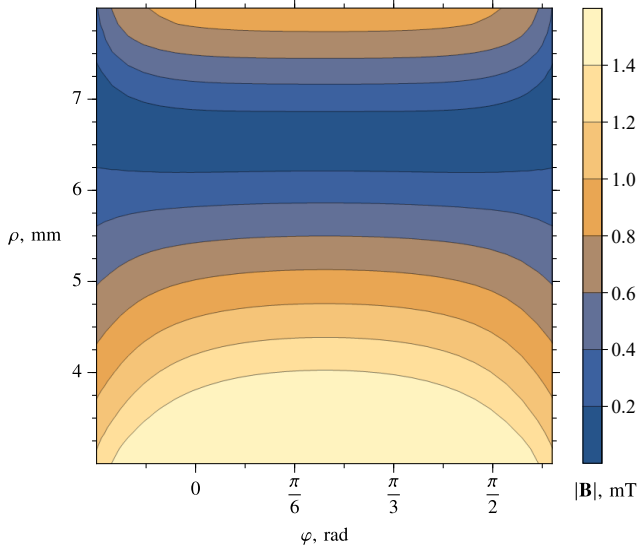
$$B_\varphi(\mathbf{r}) = \frac{M_\perp \mu_0}{4\pi} [B_\varphi^{(1)}(\mathbf{r}) + B_\varphi^{(2)}(\mathbf{r})], \quad (243)$$

$$B_z(\mathbf{r}) = \frac{M_\perp \mu_0}{4\pi} \underbrace{[B_z^{(1)}(\mathbf{r})]}_{\text{shell}} + \underbrace{[B_z^{(2)}(\mathbf{r})]}_{\text{section}}, \quad (244)$$

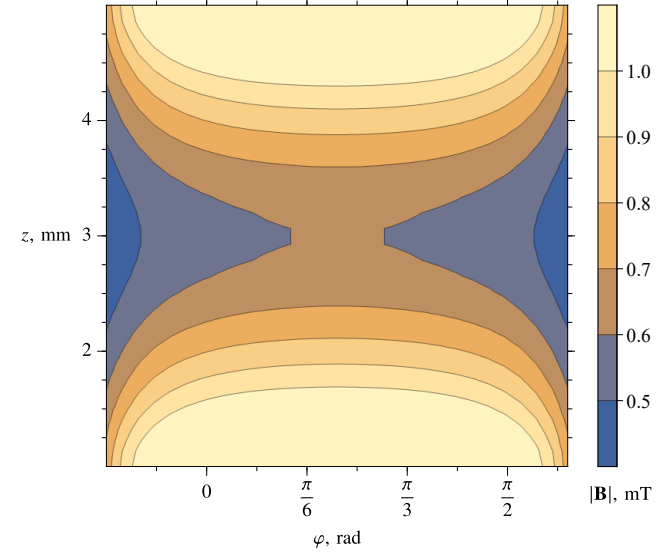
as illustrated in Figure 12. From (245)-(250), shown next to



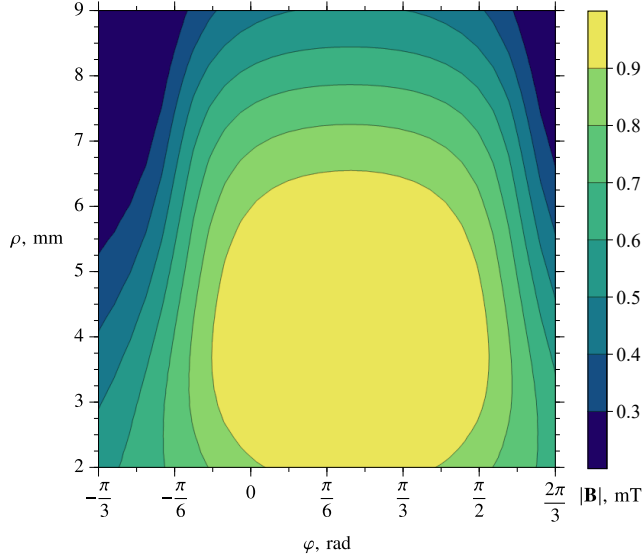
(a) Visualisation of the cylindrical surfaces in Cartesian coordinates for azimuthal current density. Magnitudes are normalised for continuous contours.



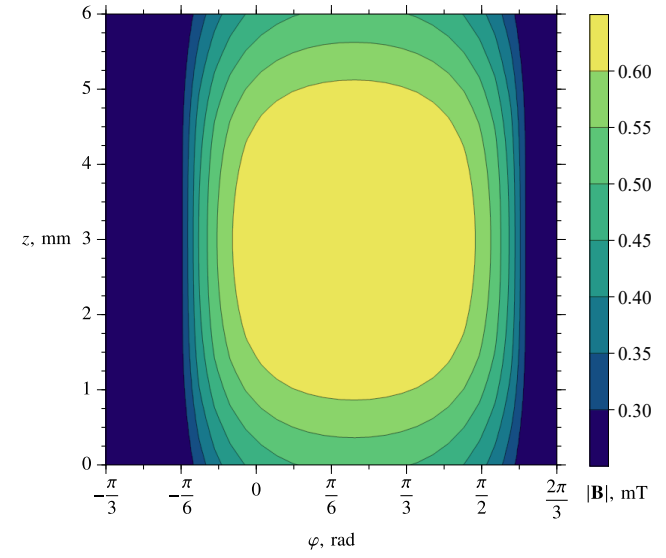
(b) Inner disc at  $z = 3$  mm



(c) Inner shell at  $\rho = 5.5$  mm



(d) Outer disc at  $z = 0$  mm



(e) Outer shell at  $\rho = 9$  mm

Figure 10: Magnitude of the magnetic field  $|\mathbf{B}|$  of a coil with an azimuthal current density  $J_\varphi = 1 \text{ MA/m}^2$  (20 A), and asymmetric geometry  $\rho' \in [3, 8] \text{ mm}$ ,  $\varphi' \in [-\frac{\pi}{6}, \frac{3\pi}{5}] \text{ rad}$ ,  $z' \in [1, 5] \text{ mm}$ .  $|\mathbf{B}|$  is shown on four rectangular cylindrical surfaces (b-e), inside and outside the volume of current, shown in white on (a). A tolerance of  $1 \times 10^{-7}$  was set for the series in  $B_\rho$  and  $B_z$ .

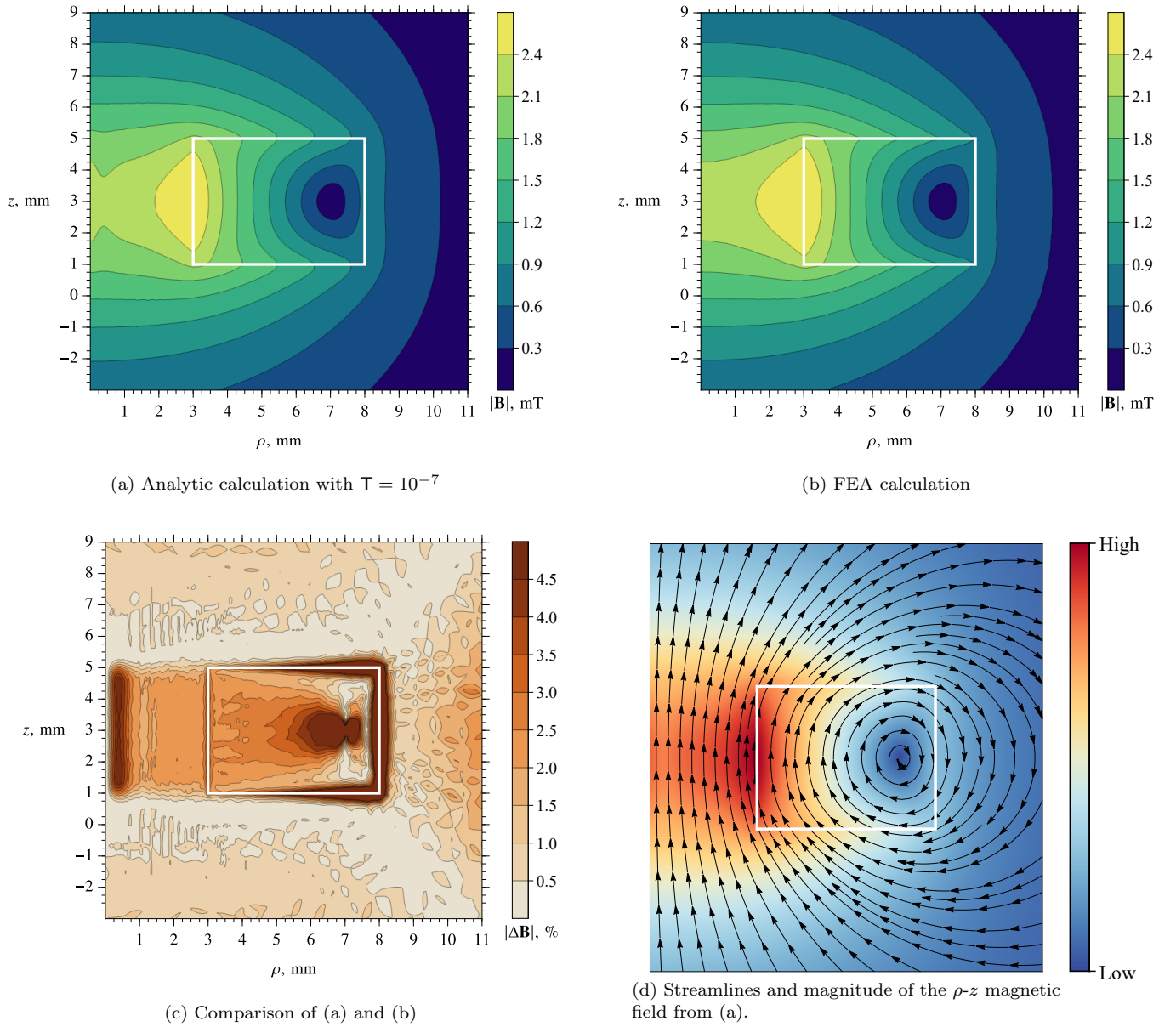


Figure 11: A section of the axisymmetric field from a coil equivalent to Figure 10 with  $\varphi' \rightarrow \varphi' \in [0, 2\pi]$  rad. Shown in (a,b,d) is the magnitude of the magnetic field  $|\mathbf{B}|$ ; (c) the absolute relative difference of analytic and FEA models of the magnetic field  $|\Delta\mathbf{B}|$ . A summary of the FEA simulation results are given in Table 5.

Table 4: Analytic results for a coil with an azimuthal current density  $J_\varphi = 1 \text{ MA/m}^2$  (20 A). The field points encapsulate all equations in Section 4.4.  $T = 10^{-9}$  was set for the series in  $B_\rho$  and  $B_z$ .

Field Point			Source Limits						Magnetic Flux Density			
$\rho$	$\varphi$	$z$	$\rho'_1$	$\rho'_2$	$\varphi'_1$	$\varphi'_2$	$z'_1$	$z'_2$	Test	$B_\rho$	$B_\varphi$	$B_z$
2	$\frac{5\pi}{24}$	$\frac{31}{10}$	3	8	$-\frac{\pi}{6}$	$\frac{3\pi}{5}$	1	5	Standard	0.00002947	0.00000035	0.00152624
2		$\frac{31}{10}$	3	8	0	$2\pi$	1	5	Case b.	0.00002464	0	0.00244883
$x$	$y$	$z$								$B_x$	$B_y$	$B_z$
0	0	5	3	8	$-\frac{\pi}{6}$	$\frac{3\pi}{5}$	1	5	Case a.	0.00015319	0.00012405	0.00072303
0	0	5	3	8	0	$2\pi$	1	5	Cases a,b	0	0	0.00188618

Table 5: Summary of quarter FEA model parameters and results with a comparison to the analytic results in Figure 11.

Tetrahedra in matter	19,452
Tetrahedra in vacuum	119,645
Total energy error, %	0.000844
Total energy, mJ	0.000404
Delta energy, %	0.000267
Mean $ \Delta\mathbf{B} $ , %	1.29
Max $ \Delta\mathbf{B} $ , %	152.19

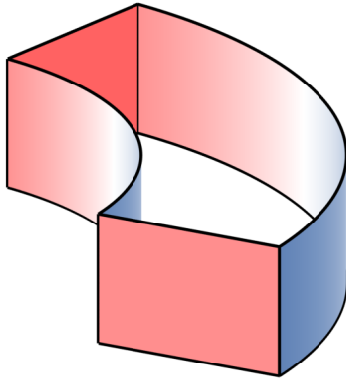
Figure 12:  $\varrho$  from  $\mathbf{M}_\perp \cdot \mathbf{n}$ .

Figure 12, a solution is found of form

$$\begin{aligned} \mathbf{B}(\rho > 0) = & \frac{M_\perp \mu_0}{4\pi} \sum_{m,n,q=1}^2 (-1)^{m+n+q} \left[ (\check{B}_\rho^{(1)} + \check{B}_\rho^{(2)}) \mathbf{e}_\rho \right. \\ & \left. + (\check{B}_\varphi^{(1)} + \check{B}_\varphi^{(2)}) \mathbf{e}_\varphi + (\check{B}_z^{(1)} + \check{B}_z^{(2)}) \mathbf{e}_z \right], \end{aligned} \quad (251)$$

where  $\check{B}_b^{(a)}$  denotes the summand from the definite integral of  $B_b^{(a)}$ .

### 5.1.1 Radial component – diametric magnetisation

Applying the  $\phi$  and  $t$  substitutions (21) to the shell surfaces (245) gives

$$\begin{aligned} B_\rho^{(1)} = & -2 \sum_{m,q=1}^2 (-1)^{m+q} \rho'_m \int_1^{\cos(\frac{1}{2}\Phi_q)} [\rho + \rho'_m(1-2t^2)] \\ & \times \left( \operatorname{sgn}(\Phi_q) \cos(\varphi^* - \varphi) \frac{1-2t^2}{\sqrt{1-t^2}} + 2 \sin(\varphi^* - \varphi) t \right) \\ & \times \int_{z'_1}^{z'_2} \frac{dz' dt}{[\rho^2 + 2\rho\rho'_m(1-2t^2) + \rho'^2_m + (z-z')^2]^{3/2}}, \end{aligned} \quad (252)$$

where care is taken to realise the elliptic (cosine term) and non-elliptic (sine term) parts of the integral. The  $z'$ -integral is solved using (F16)

$$\begin{aligned} B_\rho^{(1)} = & \frac{1}{\rho} \sum_{m,n,q=1}^2 (-1)^{m+n+q} \frac{\rho'_m Z_n}{R_{m,n}} \\ & \int_1^{\cos(\frac{1}{2}\Phi_q)} \left( 1 + \frac{\rho - \rho'_m}{(\rho + \rho'_m)(1 - \kappa_m^2 t^2)} \right) \\ & \times \left( \operatorname{sgn}(\Phi_q) \frac{\cos(\varphi^* - \varphi)}{R_{m,n}} \frac{1-2t^2}{w_{m,n}(t)} + \frac{2 \sin(\varphi^* - \varphi) t}{\sqrt{1 - k_{m,n}^2 t^2}} \right) dt, \end{aligned} \quad (253)$$

$$B_\rho^{(1)}(\mathbf{r}) = \sum_{m=1}^2 (-1)^m \rho'_m \int_{z'_1}^{z'_2} \int_{\varphi'_1}^{\varphi'_2} \cos(\varphi^* - \varphi') [\rho - \rho'_m \cos(\varphi - \varphi')] \hat{G}_m^3 d\varphi' dz', \quad (245)$$

$$B_\rho^{(2)}(\mathbf{r}) = \sum_{q=1}^2 (-1)^q \sin(\varphi^* - \varphi'_q) \int_{z'_1}^{z'_2} \int_{\rho'_1}^{\rho'_2} [\rho - \rho' \cos(\varphi - \varphi'_q)] \hat{G}_q^3 d\rho' dz', \quad (246)$$

$$B_\varphi^{(1)}(\mathbf{r}) = \sum_{m=1}^2 (-1)^m \rho'^2_m \int_{z'_1}^{z'_2} \int_{\varphi'_1}^{\varphi'_2} \cos(\varphi^* - \varphi') \sin(\varphi - \varphi') \hat{G}_m^3 d\varphi' dz', \quad (247)$$

$$B_\varphi^{(2)}(\mathbf{r}) = \sum_{q=1}^2 (-1)^q \sin(\varphi^* - \varphi'_q) \sin(\varphi - \varphi'_q) \int_{z'_1}^{z'_2} \int_{\rho'_1}^{\rho'_2} \rho' \hat{G}_q^3 d\rho' dz', \quad (248)$$

$$B_z^{(1)}(\mathbf{r}) = \sum_{m=1}^2 (-1)^m \rho'_m \int_{z'_1}^{z'_2} \int_{\varphi'_1}^{\varphi'_2} \cos(\varphi^* - \varphi') (z - z') \hat{G}_m^3 d\varphi' dz', \quad (249)$$

$$B_z^{(2)}(\mathbf{r}) = \sum_{q=1}^2 (-1)^q \sin(\varphi^* - \varphi'_q) \int_{z'_1}^{z'_2} \int_{\rho'_1}^{\rho'_2} (z - z') \hat{G}_q^3 d\rho' dz'. \quad (250)$$

where we used the partial fraction expansion

$$\frac{\rho + \rho'_m(1-2t^2)}{(\rho + \rho'_m)^2 - 4\rho\rho'_m t^2} = \frac{1}{2\rho} \left( 1 + \frac{\rho - \rho'_m}{(\rho + \rho'_m)(1 - \kappa_m^2 t^2)} \right). \quad (254)$$

With the further expansion

$$\frac{(\rho - \rho'_m)(1-2t)}{(\rho + \rho'_m)(1 - \kappa_m^2 t^2)} = \frac{2(\rho - \rho'_m)}{\kappa_m^2(\rho + \rho'_m)} \left( 1 + \frac{\kappa_m^2 - 2}{2(1 - \kappa_m^2 t^2)} \right), \quad (255)$$

the elliptic integrals of (253) can be solved by inspection. The elementary integral contains a hyperbolic function, where we can choose the upper integral bound to be 0, and solve each component using (F17) or (F20) (with an additional change of form (F21)). This gives the result

$$\begin{aligned} \check{B}_\rho^{(1)} = & \cos(\varphi^* - \varphi) \frac{\rho'_m Z_n}{\rho R_{m,n}} \left[ - \left( 1 + \frac{2\bar{\varrho}_m}{\varrho_m \kappa_m^2} \right) \mathsf{F}(\phi_q; k_{n,m}^2) \right. \\ & \left. + 2\mathsf{D}(\phi_q; k_{n,m}^2) - \frac{\bar{\varrho}_m(\kappa_m^2 - 2)}{\varrho_m \kappa_m^2} \mathsf{P}(\phi_q; \kappa_m^2, k_{n,m}^2) \right] \\ & + \frac{\sin(\varphi^* - \varphi)}{2\rho^2} \left[ \varrho_m \bar{\varrho}_m \tanh^{-1} \left( \frac{\hat{G}_{m,n,q}^{-1}}{Z_n} \right) - Z_n \hat{G}_{m,n,q}^{-1} \right]. \end{aligned} \quad (256)$$

The  $z'$ -integral of the section surfaces (246) are given by (F16)

$$\begin{aligned} B_\rho^{(2)} = & \sum_{n,q=1}^2 (-1)^{n+q} Z_n \sin(\varphi^* - \varphi'_q) \int_{\rho'_1}^{\rho'_2} \\ & \times \frac{[\rho' \cos \Phi_q - \rho] d\rho'}{(\rho^2 - 2\rho \cos(\Phi_q)\rho' + \rho'^2) \sqrt{L_n^2 - 2\rho \cos(\Phi_q)\rho' + \rho'^2}}, \end{aligned} \quad (257)$$

and the  $\rho'$ -integral is given by (F20)

$$\begin{aligned} \check{B}_\rho^{(2)} = & \sin(\varphi^* - \varphi'_q) \left[ \sin \Phi_q \tan^{-1} \Upsilon_{m,n,q} \right. \\ & \left. - \cos \Phi_q \tanh^{-1} \left( \frac{\hat{G}_{m,n,q}^{-1}}{Z_n} \right) \right], \end{aligned} \quad (258)$$

## 5.1 Diametric magnetisation

where

$$\Upsilon = \frac{Z(\rho' - \rho \cos \Phi)}{\rho \sin \Phi G^{-1}}. \quad (259)$$

Combining (256) and (258) gives the complete solution to the radial component (242).

### 5.1.2 Azimuthal component – diametric magnetisation

Applying the  $\phi$  and  $t$  substitutions (21) to the shell surfaces (247) gives

$$\begin{aligned} B_\varphi^{(1)} = & -4 \sum_{m,q=1}^2 (-1)^{m+q} \rho_m'^2 \int_1^{\cos(\frac{1}{2}\Phi_q)} \left( \cos(\varphi^* - \varphi) \right. \\ & \times t(1-2t^2) + 2 \sin(\varphi^* - \varphi) \operatorname{sgn}(\Phi_q) t^2 \sqrt{1-t^2} \Big) \quad (260) \\ & \times \int_{z'_1}^{z'_2} \frac{dz' dt}{[\rho^2 + 2\rho\rho'_m(1-2t^2) + \rho'^2_m + (z-z')^2]^{3/2}}, \end{aligned}$$

that is similar to (252). The  $z'$ -integral is solved using (F16)

$$\begin{aligned} B_\varphi^{(1)} = & -\frac{2}{\rho} \sum_{m,n,q=1}^2 (-1)^{m+n+q} \rho'_m Z_n \int_1^{\cos(\frac{1}{2}\Phi_q)} \\ & \times \left\{ \left( 1 - \frac{\rho^2 + \rho'^2}{\rho_m^2 - 4\rho\rho'_m t^2} \right) \frac{\cos(\varphi^* - \varphi)t}{\sqrt{R_{m,n} - 4\rho\rho'_m t^2}} + \operatorname{sgn}(\Phi_q) \right. \\ & \times \left. \frac{\sin(\varphi^* - \varphi)}{R_{m,n}} \left[ t^2 + \frac{\bar{\rho}_m^2}{4\rho\rho'_m} \left( 1 - \frac{1}{1-\kappa_m^2 t^2} \right) \right] \frac{1}{w_{m,n}(t)} \right\} dt, \quad (261) \end{aligned}$$

where we have a similar partial fraction expansion to (256) for the elementary integral (that can be solved with (F17) and (F20)) and

$$\frac{t^2(1-t^2)}{(\rho+\rho')^2 - 4\rho\rho't^2} = \frac{1}{4\rho\rho'} \left[ t^2 + \frac{(\rho-\rho')^2}{4\rho\rho'} \left( 1 - \frac{1}{1-\kappa^2 t^2} \right) \right] \quad (262)$$

for the elliptic integral. By inspection, this gives

$$\begin{aligned} \check{B}_\varphi^{(1)} = & \sin(\varphi^* - \varphi) \frac{2\bar{\rho}_m Z_n}{\rho R_{m,n}} \left( \frac{\bar{\rho}_m^2}{4\rho\rho'_m} [\Pi(\phi_q; \kappa_m^2, k_{n,m}^2) \right. \\ & \left. - F(\phi_q; k_{n,m}^2)] - D(\phi_q; k_{n,m}^2) \right) - \frac{\cos(\varphi^* - \varphi)}{2\rho^2} \\ & \times \left[ Z_n \hat{G}_{m,n,q}^{-1} + (\rho^2 + \rho'^2_m) \tanh^{-1} \left( \frac{\hat{G}_{m,n,q}^{-1}}{Z_n} \right) \right]. \quad (263) \end{aligned}$$

The  $z'$ -integral of the section surfaces (248) is given by (F16)

$$\begin{aligned} B_\varphi^{(2)} = & \sum_{n,q=1}^2 (-1)^{n+q} Z_n \sin(\varphi'_q - \varphi^*) \int_{\rho'_1}^{\rho'_2} \\ & \times \frac{\rho' d\rho'}{(\rho^2 - 2\rho \cos(\Phi_q)\rho' + \rho'^2) \sqrt{L_n^2 - 2\rho \cos(\Phi_q)\rho' + \rho'^2}}, \quad (264) \end{aligned}$$

and the  $\rho'$ -integral is given by (F20)

$$\begin{aligned} \check{B}_\varphi^{(2)} = & \sin(\varphi^* - \varphi'_q) \left[ \cos \Phi_q \tan^{-1} \Upsilon_{m,n,q} \right. \\ & \left. + \sin \Phi_q \tanh^{-1} \left( \frac{\hat{G}_{m,n,q}^{-1}}{Z_n} \right) \right]. \quad (265) \end{aligned}$$

Combining (263) and (265) gives the complete solution to the azimuthal component (243).

### 5.1.3 Axial component – diametric magnetisation

Applying the  $\phi$  and  $t$  substitutions (21) to the shell surfaces (249) gives

$$\begin{aligned} B_z^{(1)} = & -2 \sum_{m,q=1}^2 (-1)^{m+q} \rho'_m \int_1^{\cos(\frac{1}{2}\Phi_q)} \\ & \times \left( 2 \sin(\varphi^* - \varphi) t + \cos(\varphi^* - \varphi) \operatorname{sgn}(\Phi_q) (1-2t^2) \right) \quad (266) \\ & \times \int_{z'_1}^{z'_2} \frac{(z-z') dz' dt}{[\rho^2 + 2\rho\rho'_m(1-2t^2) + \rho'^2_m + (z-z')^2]^{3/2}}. \end{aligned}$$

The  $z'$ -integral is solved using (F16)

$$\begin{aligned} B_z^{(1)} = & -2 \sum_{m,n,q=1}^2 (-1)^{m+n+q} \rho'_m \int_1^{\cos(\frac{1}{2}\Phi_q)} \\ & \times \left( \frac{2 \sin(\varphi^* - \varphi) t}{\sqrt{R_{m,n} - 4\rho\rho'_m t^2}} + \frac{\operatorname{sgn}(\Phi_q) \cos(\varphi^* - \varphi)}{R_{m,n}} \frac{1-2t^2}{w_{m,n}(t)} \right) dt, \quad (267) \end{aligned}$$

where the elementary part of the  $\rho'$ -integral is given by (F17) and the elliptic part by inspection, giving

$$\begin{aligned} \check{B}_z^{(1)} = & \frac{\sin(\varphi^* - \varphi)}{\rho} \hat{G}_{m,n,q}^{-1} + \frac{2\rho'_m \cos(\varphi^* - \varphi)}{R_{m,n}} \\ & \times [F(\phi_q; k_{n,m}^2) - D(\phi_q; k_{n,m}^2)]. \quad (268) \end{aligned}$$

The  $z'$ -integral of the section surfaces (250) is given by (F16)

$$\begin{aligned} B_z^{(2)} = & \sum_{n,q=1}^2 (-1)^{n+q} \sin(\varphi^* - \varphi'_q) \\ & \times \int_{\rho'_1}^{\rho'_2} \frac{1}{\sqrt{L_n^2 - 2\rho \cos(\Phi_q)\rho' + \rho'^2}} d\rho', \quad (269) \end{aligned}$$

then using (F15) with (F18) and (F19) gives

$$\check{B}_z^{(2)} = \sin(\varphi^* - \varphi'_q) \ln \left( \rho'_m - \rho \cos \Phi_q + \hat{G}_{n,m,q}^{-1} \right). \quad (270)$$

Combining (268) and (270) gives the complete solution to the axial component (244).

### 5.1.4 Singularities – diametric magnetisation

The summands of (251) can be evaluated at all field points given the conditional substitutions given in this section.

## 5.1 Diametric magnetisation

**(a) On the shell plane** When  $\kappa^2 = 1$ , our transformed Legendre form  $\Pi(\phi; 1, k^2)$  will lead to  $\Pi(1; k^2)$ , an unbounded result. To resolve this, we need to employ the special case

$$\begin{aligned} \Pi(\phi; 1, k^2) &\rightarrow F(\phi; k^2) - \frac{1}{1-k^2} \\ &\times \left( E(\phi; k^2) - \sqrt{1-k^2 \sin^2 \phi} \tan \phi \right) \end{aligned} \quad (271)$$

for  $\rho = \rho'_m$  in  $\check{B}_\rho^{(1)}$  and  $\check{B}_\varphi^{(1)}$ . Practically, all terms with the coefficient  $\bar{\varrho}_m$  in (256) and (261) go to zero.

**(b) On the section plane** Equations (258) and (265) are simplified to avoid the singularities

$$\begin{aligned} \check{B}_\rho^{(2)} &\rightarrow -\sin(\varphi^* - \varphi'_q) \tanh^{-1} \frac{\bar{R}_{m,n}}{Z_n}, \\ \check{B}_\varphi^{(2)} &\rightarrow 0, \end{aligned} \quad (272)$$

for  $\varphi = \varphi'_q$ . The second case to consider is the conjugate point

$$\begin{aligned} \check{B}_\rho^{(2)} &\rightarrow \sin(\varphi^* - \varphi'_q) \tanh^{-1} \frac{R_{m,n}}{Z_n}, \\ \check{B}_\varphi^{(2)} &\rightarrow 0, \end{aligned} \quad (273)$$

for  $\varphi \pm \pi = \varphi'_q$ .

**(c) On the disc plane** The radial and azimuthal components vanish, giving

$$\begin{aligned} \check{B}_\rho^{(1)} + \check{B}_\rho^{(2)} &\rightarrow 0, \\ \check{B}_\varphi^{(1)} + \check{B}_\varphi^{(2)} &\rightarrow 0, \end{aligned} \quad (274)$$

for  $z = z'_n$ .

**(d) On the axial line** For  $\rho = \rho'$  in (272), a number of problematic terms cancel by inspection of the partial fraction expansions within (253) and (261). In addition, we need to avoid elementary terms such as  $\tanh^{-1}[\operatorname{sgn}(z-z')]$  or  $\ln[\operatorname{sgn}(z-z')]$ , that may appear, but we can rephrase as with (F22). From this in addition to (272), we have

$$\begin{aligned} \check{B}_\rho^{(1)} &\rightarrow \cos(\varphi^* - \varphi) \frac{Z_n}{R_{m,n}} [K(k_{m,n}^2) - 2D(k_{m,n}^2)] \\ &- \sin(\varphi^* - \varphi) \frac{\operatorname{sgn}(Z_n) Z_n^2}{2\rho'^2} \\ \check{B}_\rho^{(2)} &\rightarrow -\sin(\varphi^* - \varphi'_q) \operatorname{sgn}(Z_n) \ln |Z_n|, \\ \check{B}_\varphi^{(1)} &\rightarrow \sin(\varphi^* - \varphi) \frac{2Z_n}{R_{m,n}} D(k_{m,n}^2) \\ &- \cos(\varphi^* - \varphi) \operatorname{sgn}(Z_n) \left( \frac{Z_n^2}{2\rho'^2} + \ln |Z_n| \right), \end{aligned} \quad (275)$$

for  $(\rho = \rho'_m) \wedge (\varphi = \varphi'_q)$ .

**(e) On the azimuthal line** In addition to (274), from (267)

$$\begin{aligned} \check{B}_z^{(1)} &\rightarrow \cos(\varphi^* - \varphi) \operatorname{sgn} \Phi_q [\tanh^{-1}(\sin \phi_q) - 2 \sin \phi_q] \\ &- \sin(\varphi^* - \varphi) (2 - \sqrt{2} \sqrt{1 - \cos \Phi_q}). \end{aligned} \quad (276)$$

for  $(\rho = \rho'_m) \wedge (z = z'_n)$ .

**(f) On the radial line** In addition to (274), from (270) (noting using (F22))

$$\check{B}_z^{(2)} \rightarrow -\sin(\varphi^* - \varphi'_q) \operatorname{sgn}(\bar{\varrho}_m) \ln |\bar{\varrho}_m|, \quad (277)$$

for  $(\varphi = \varphi'_q) \wedge (z = z'_n)$ .

## 5.1.5 Special cases – diametric magnetisation

For a general solution, this section has conditional substitutions for (251), at specific field points or when considering simplified geometry.

**(a) Inside the volume** As this problem was formulated using the charge model,  $\hat{\mathbf{B}} = \hat{\mathbf{H}}$  outside the region of source charges; however, when the field point and source point are within the same region, the source directionality must be included.

$$\mathbf{B}(\mathbf{r}) \rightarrow \mathbf{B}(\mathbf{r}) + \mu_0 \mathbf{M}_\perp(\mathbf{r}) \quad (278)$$

for  $(\rho'_1 < \rho < \rho'_2) \wedge (\varphi'_1 < \varphi < \varphi'_2) \wedge (z'_1 < z < z'_2)$ , where  $\mathbf{M}_\perp(\mathbf{r}) = M_\perp [\cos(\varphi^* - \varphi) \mathbf{e}_\rho + \sin(\varphi^* - \varphi) \mathbf{e}_\varphi]$ .

**(b) Along the axis** Where the cylindrical basis is not defined, we convert (241) to a Cartesian basis and integrate with  $\rho = 0$  to give

$$\mathbf{B}(\mathbf{r}) \rightarrow \frac{M_\perp \mu_0}{4\pi} \sum_{m,n,q=1}^2 (-1)^{m+n+q} (\check{B}_x \mathbf{e}_x + \check{B}_y \mathbf{e}_y + \check{B}_z \mathbf{e}_z), \quad (279)$$

for  $\rho = 0$ , where

$$\begin{aligned} \check{B}_x &= \frac{Z_n [2\varphi'_q \cos \varphi^* - \sin(\varphi^* - 2\varphi'_q)]}{4\sqrt{\rho'^2_m + Z_n^2}} \\ &- \sin(\varphi^* - \varphi'_q) \cos \varphi'_q \tanh^{-1} \frac{\sqrt{\rho'^2_m + Z_n^2}}{Z_n}, \\ \check{B}_y &= \frac{Z_n [2\varphi'_q \sin \varphi^* - \cos(\varphi^* - 2\varphi'_q)]}{4\sqrt{\rho'^2_m + Z_n^2}} \\ &- \sin(\varphi^* - \varphi'_q) \sin \varphi'_q \tanh^{-1} \frac{\sqrt{\rho'^2_m + Z_n^2}}{Z_n}, \\ \check{B}_z &= \sin(\varphi^* - \varphi'_q) \left( \tanh^{-1} \frac{\rho'_m}{\sqrt{\rho'^2_m + Z_n^2}} - \frac{\rho'_m}{\sqrt{\rho'^2_m + Z_n^2}} \right), \end{aligned} \quad (280)$$

for  $z \neq z'_n$ . For this singularity in (280), the Cartesian integral is repeated with the additional constraint  $z = z'$  to give the axial field

$$\begin{aligned} \check{B}_x &\rightarrow 0, \\ \check{B}_y &\rightarrow 0, \\ \check{B}_z &\rightarrow \sin(\varphi^* - \varphi'_q) (\ln \rho'_m - 1), \end{aligned} \quad (281)$$

for  $z = z'_n$ .

**(c) Axisymmetric** For the rectangular cylinder we have  $\varphi'_q = \{0, 2\pi\}$ . Due to this, the closed surface of (241) changes, removing the section surfaces of charge. By inspection of (256), (263), and (268), the elliptic integrals reduce with (149) and the auxiliary terms go to zero, giving

$$\mathbf{B}(\mathbf{r}) \rightarrow \frac{M_{\perp}\mu_0}{4\pi} \sum_{m,n=1}^2 (-1)^{m+n} (\mathring{B}_{\rho}\mathbf{e}_{\rho} + \mathring{B}_{\varphi}\mathbf{e}_{\varphi} + \mathring{B}_z\mathbf{e}_z), \quad (282)$$

for  $(\varphi'_1 = 0) \wedge (\varphi'_2 = 2\pi) \wedge (\rho > 0)$ , where

$$\begin{aligned} \mathring{B}_{\rho} &= 2 \cos(\varphi^* - \varphi) \frac{\rho'_m Z_n}{\rho R_{m,n}} \left[ \left( 1 + \frac{2\bar{\varrho}_m}{\varrho_m \kappa_m^2} \right) K(k_{n,m}^2) \right. \\ &\quad \left. - 2D(k_{n,m}^2) + \frac{\bar{\varrho}_m(\kappa_m^2 - 2)}{\kappa_m^2 \varrho_m} \Pi(\kappa_m^2; k_{n,m}^2) \right], \\ \mathring{B}_{\varphi} &= 4 \sin(\varphi^* - \varphi) \frac{\rho'_m Z_n}{\rho R_{m,n}} \left[ D(k_{n,m}^2) \right. \\ &\quad \left. + \frac{\bar{\varrho}_m^2}{4\rho \rho'_m} \left( K(k_{n,m}^2) - \Pi(\kappa_m^2; k_{n,m}^2) \right) \right], \\ \mathring{B}_z &= 4 \cos(\varphi^* - \varphi) \frac{\rho'_m}{R_{m,n}} \left[ 2D(k_{n,m}^2) - K(k_{n,m}^2) \right]. \end{aligned} \quad (283)$$

In (283) the unbound result  $\Pi(1; k_{n,m}^2)$  (when  $\kappa_m^2 = 1$ ) occurs when  $\rho = \rho'_m$ , that from (271), gives

$$\begin{aligned} \mathring{B}_{\rho} &\rightarrow 2 \cos(\varphi^* - \varphi) \frac{Z_n}{\sqrt{4\rho'^2_m + Z_n^2}} \left( K(k_{n,m}^2) - 2D(k_{n,m}^2) \right), \\ \mathring{B}_{\varphi} &\rightarrow 4 \sin(\varphi^* - \varphi) \frac{Z_n}{\sqrt{4\rho'^2_m + Z_n^2}} D(k_{n,m}^2). \end{aligned} \quad (284)$$

From (280) and (282),

$$\begin{aligned} \mathbf{B}(\mathbf{r}) &\rightarrow \frac{M_{\perp}\mu_0}{4\pi} \sum_{m,n=1}^2 (-1)^{m+n} \\ &\quad \times \left( \frac{\pi \cos \varphi^* Z_n}{\sqrt{\rho'^2_m + Z_n^2}} \mathbf{e}_x + \frac{\pi \sin \varphi^* Z_n}{\sqrt{\rho'^2_m + Z_n^2}} \mathbf{e}_y \right), \end{aligned} \quad (285)$$

for  $(\varphi'_1 = 0) \wedge (\varphi'_2 = 2\pi) \wedge (\rho = 0)$ .

**(d) Solid** When the rectangular cylinder is not hollow, the closed surface does not have an inner shell, removing the  $m$ -summation

$$\begin{aligned} \mathbf{B}(\mathbf{r}) &\rightarrow \frac{M_{\perp}\mu_0}{4\pi} \sum_{n,q=1}^2 (-1)^{n+q} \left[ \check{B}_{\rho}^{(1)}\mathbf{e}_{\rho} + \check{B}_{\varphi}^{(1)}\mathbf{e}_{\varphi} + \check{B}_z^{(1)}\mathbf{e}_z \right. \\ &\quad \left. + \sum_{m=1}^2 (-1)^m \left( \check{B}_{\rho}^{(2)}\mathbf{e}_{\rho} + \check{B}_{\varphi}^{(2)}\mathbf{e}_{\varphi} + \check{B}_z^{(2)}\mathbf{e}_z \right) \right], \end{aligned} \quad (286)$$

for  $\rho' = \rho_2$ .

**(e) Axisymmetric & Solid** The trivial solution for the diametric magnetisation is when the geometry is both solid

and axisymmetric. Removing the  $m$ -summation from (282) gives a single shell surface to describe the field,

$$\mathbf{B}(\mathbf{r}) \rightarrow \frac{M_{\perp}\mu_0}{4\pi} \sum_{n=1}^2 (-1)^n (\mathring{B}_{\rho}\mathbf{e}_{\rho} + \mathring{B}_{\varphi}\mathbf{e}_{\varphi} + \mathring{B}_z\mathbf{e}_z), \quad (287)$$

with  $(\varphi'_1 = 0) \wedge (\varphi'_2 = 2\pi) \wedge \rho' = \rho_2$ .

## 5.2 Radial magnetisation

Radial magnetisation is defined  $\mathbf{M}_{\rho}(\mathbf{r}, \mathbf{r}') = M_{\rho}[\cos(\varphi - \varphi')\mathbf{e}_{\rho} - \sin(\varphi - \varphi')\mathbf{e}_{\varphi}]$  ( $M_{\varphi}, M_z = 0$ ). Using the current model formulation, the vector potential is

$$\mathbf{A}(\mathbf{r}) = \frac{\mu_0}{4\pi} \oint_S \frac{\mathbf{M}_{\rho}(\mathbf{r}, \mathbf{r}') \times \mathbf{n}(\mathbf{r}, \mathbf{r}')}{|\mathbf{r} - \mathbf{r}'|} d\mathbf{a}', \quad (288)$$

with magnetic field

$$\mathbf{B}(\mathbf{r}) = \frac{\mu_0}{4\pi} \oint_S [\mathbf{M}_{\rho}(\mathbf{r}, \mathbf{r}') \times \mathbf{n}(\mathbf{r}, \mathbf{r}')] \times \frac{\mathbf{r} - \mathbf{r}'}{|\mathbf{r} - \mathbf{r}'|^3} d\mathbf{a}'. \quad (289)$$

After expanding, the three components of the magnetic field are due to disc<sup>(1)</sup> and section<sup>(2)</sup> surfaces of current:

$$B_{\rho}(\mathbf{r}) = \frac{M_{\rho}\mu_0}{4\pi} [B_{\rho}^{(1)}(\mathbf{r}) + B_{\rho}^{(2)}(\mathbf{r})], \quad (290)$$

$$B_{\varphi}(\mathbf{r}) = \frac{M_{\rho}\mu_0}{4\pi} [B_{\varphi}^{(1)}(\mathbf{r}) + \underbrace{B_{\varphi}^{(2)}(\mathbf{r})}_{\text{section}}], \quad (291)$$

$$B_z(\mathbf{r}) = \frac{M_{\rho}\mu_0}{4\pi} \underbrace{B_z^{(1)}(\mathbf{r})}_{\text{disc}}, \quad (292)$$

as illustrated in Figure 13. From (293)-(297), shown next to Figure 13, a solution is found of form

$$\begin{aligned} \mathbf{B}(\rho > 0) &= \frac{M_{\rho}\mu_0}{4\pi} \sum_{m,n,q=1}^2 (-1)^{m+n+q} \left[ (\check{B}_{\rho}^{(1)} + \check{B}_{\rho}^{(2)})\mathbf{e}_{\rho} \right. \\ &\quad \left. + (\check{B}_{\varphi}^{(1)} + \check{B}_{\varphi}^{(2)})\mathbf{e}_{\varphi} + \check{B}_z^{(1)}\mathbf{e}_z \right], \end{aligned} \quad (298)$$

with an equivalent notation to (251), and use as in Section 5.1.

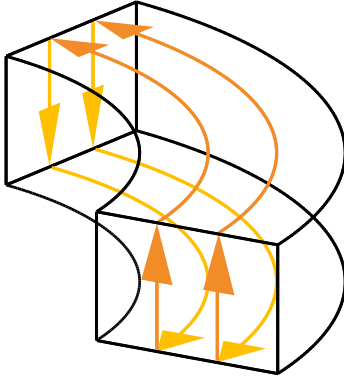
The integrals for the disc surfaces  $(B_{\rho}^{(1)}, B_{\varphi}^{(1)}, B_z^{(1)})$  vary only by a constant to the azimuthal current density (Section 4.2), thus are mathematically equivalent. These disc surfaces combine with the section surfaces to complete a fictitious circuit of current, illustrated in Figure 13.

The integrals for the section surfaces  $(B_{\rho}^{(2)}, B_{\varphi}^{(2)})$  vary only by a constant to those in Section 5.1, albeit rotated  $-\pi/2$  about  $z$  ( $B_{\rho}^{(2)} \rightarrow -B_{\varphi}^{(2)}$ ,  $B_{\varphi}^{(2)} \rightarrow B_{\rho}^{(2)}$ ). This highlights a rotational transform linking the magnetic field from a surface of uniform charge to a surface of uniform current.

### 5.2.1 Radial component – radial magnetisation

From (165) we have the solution to (293),

$$\begin{aligned} \check{B}_{\rho}^{(1)} &= -\frac{2}{\rho} \frac{\rho'_m Z_n}{R_{m,n}} \left[ F(\phi_q; k_{m,n}^2) - \frac{\rho L_n}{Z_n^2 \rho'_m} \right. \\ &\quad \left. \times \left( \frac{\bar{S}_{m,n}^2}{\bar{a}_n^2} \Pi(\phi_q; a_n^2, k_{m,n}^2) + \frac{S_{m,n}^2}{a^2} \Pi(\phi_q; \bar{a}_n^2, k_{m,n}^2) \right) \right], \end{aligned} \quad (299)$$

Figure 13:  $\mathbf{K}$  from  $\mathbf{M}_\rho \times \mathbf{n}$ .

and from (265) we have the solution to (294),

$$\begin{aligned} \check{B}_\rho^{(2)} &= -\sin \Phi_q \tanh^{-1} \left( \frac{\hat{G}_{m,n,q}^{-1}}{Z_n} \right) \\ &\quad - \cos \Phi_q \tan^{-1} \Upsilon_{m,n,q}. \end{aligned} \quad (300)$$

Combining (299) and (300) gives the complete solution to the radial component (290).

### 5.2.2 Azimuthal component – radial magnetisation

From (169) we have the solution to (295),

$$\check{B}_\varphi^{(1)} = \frac{Z}{\rho} \ln \left( \rho_m' - \rho \cos(\Phi_q) + \hat{G}_{m,n,q}^{-1} \right). \quad (301)$$

and from (258) we have the solution to (296)

$$\begin{aligned} \check{B}_\varphi^{(2)} &= \sin \Phi_q \tan^{-1} \Upsilon_{m,n,q} \\ &\quad - \cos \Phi_q \tanh^{-1} \left( \frac{\hat{G}_{m,n,q}^{-1}}{Z_n} \right). \end{aligned} \quad (302)$$

Combining (301) and (302) gives the complete solution to the radial component (291).

### 5.2.3 Axial component – radial magnetisation

From (172) we have the solution to (297)

$$\check{B}_z^{(1)} = -\frac{2\rho_m'}{R_{m,n}} F(\phi_q; k_{m,n}^2) - \varphi'_q \alpha_{m,n}^{(1)} - \varphi'_q \beta_{m,n}^{(1)} + \delta_{m,n,q}^{(1)}, \quad (303)$$

that solves (292).

### 5.2.4 Singularities – radial magnetisation

The summands of (298) can be evaluated at all field points given the conditional substitutions given in this section.

(a) **On the shell plane** Given by (271).

$$B_\rho^{(1)}(\mathbf{r}) = \sum_{n=1}^2 (-1)^n (z'_n - z) \int_{\varphi'_1}^{\varphi'_2} \int_{\rho'_1}^{\rho'_2} \rho' \cos(\varphi - \varphi') \hat{G}_n^3 d\rho' d\varphi', \quad (293)$$

$$B_\rho^{(2)}(\mathbf{r}) = \sum_{q=1}^2 (-1)^q \sin(\varphi'_q - \varphi) \int_{z'_1}^{z'_2} \int_{\rho'_1}^{\rho'_2} \rho' \hat{G}_q^3 d\rho' dz', \quad (294)$$

$$B_\varphi^{(1)}(\mathbf{r}) = \sum_{n=1}^2 (-1)^n (z - z'_n) \int_{\varphi'_1}^{\varphi'_2} \int_{\rho'_1}^{\rho'_2} \rho' \sin(\varphi - \varphi') \hat{G}_n^3 d\rho' d\varphi', \quad (295)$$

$$B_\varphi^{(2)}(\mathbf{r}) = \sum_{q=1}^2 (-1)^q \int_{z'_1}^{z'_2} \int_{\rho'_1}^{\rho'_2} [\rho - \rho' \cos(\varphi - \varphi')] \hat{G}_q^3 d\rho' dz', \quad (296)$$

$$B_z^{(1)}(\mathbf{r}) = \sum_{n=1}^2 (-1)^n \int_{\varphi'_1}^{\varphi'_2} \int_{\rho'_1}^{\rho'_2} [\rho \rho' \cos(\varphi - \varphi') - \rho'^2] \hat{G}_n^3 d\rho' d\varphi'. \quad (297)$$

(b) **On the section plane** Equations (300) and (302) are simplified to avoid the singularities

$$\begin{aligned} \check{B}_\rho^{(2)} &\rightarrow 0, \\ \check{B}_\varphi^{(2)} &\rightarrow -\tanh^{-1} \frac{\bar{R}_{m,n}}{Z_n}, \end{aligned} \quad (304)$$

for  $\varphi = \varphi'_q$ . The second case to consider is the conjugate point

$$\begin{aligned} \check{B}_\rho^{(2)} &\rightarrow 0, \\ \check{B}_\varphi^{(2)} &\rightarrow \tanh^{-1} \frac{R_{m,n}}{Z_n}, \end{aligned} \quad (305)$$

for  $\varphi \pm \pi = \varphi'_q$ .

(c) **On the disc plane** The radial and azimuthal components vanish, giving

$$\begin{aligned} \check{B}_\rho^{(1)} + \check{B}_\rho^{(2)} &\rightarrow 0, \\ \check{B}_\varphi^{(1)} + \check{B}_\varphi^{(2)} &\rightarrow 0, \end{aligned} \quad (306)$$

for  $z = z'_n$ .

(d) **On the axial line** Similar to (275),

$$\begin{aligned} \check{B}_\rho^{(2)} &\rightarrow 0, \\ \check{B}_\varphi^{(2)} &\rightarrow -\operatorname{sgn}(Z_n) \ln |Z_n|, \end{aligned} \quad (307)$$

for  $(\rho = \rho'_m) \wedge (\varphi = \varphi'_q)$ .

(e) **On the azimuthal line** Covered by (174) and (306) for  $(\rho = \rho'_m) \wedge (z = z'_n)$ .

(f) **On the radial line** Covered by (306) for  $(\varphi = \varphi'_q) \wedge (z = z'_n)$ .

### 5.2.5 Special cases – radial magnetisation

For a general solution, this section has conditional substitutions for (298), at specific field points or when considering simplified geometry.

## 5.3 Azimuthal magnetisation

**(a) Inside the volume** As this problem was formulated using the current model, there is no differentiation to  $\mathbf{B}$  being within the source region or not.

**(b) Along the axis** As with (279), (289) gives

$$\mathbf{B}(\mathbf{r}) \rightarrow \frac{M_\rho \mu_0}{4\pi} \sum_{m,n,q=1}^2 (-1)^{m+n+q} (\check{B}_x \mathbf{e}_x + \check{B}_y \mathbf{e}_y + \check{B}_z \mathbf{e}_z), \quad (308)$$

for  $\rho = 0$ , where

$$\begin{aligned} \check{B}_x &= \sin \varphi'_q \left( \tanh^{-1} \frac{\sqrt{\rho'_m^2 + Z_n^2}}{Z_n} + \frac{Z_n}{\sqrt{\rho'_m^2 + Z_n^2}} \right), \\ \check{B}_y &= -\cos \varphi'_q \left( \tanh^{-1} \frac{\sqrt{\rho'_m^2 + Z_n^2}}{Z_n} + \frac{Z_n}{\sqrt{\rho'_m^2 + Z_n^2}} \right), \quad (309) \\ \check{B}_z &= \varphi'_q \left( \frac{\rho'_m}{\sqrt{\rho'_m^2 + Z_n^2}} - \tanh^{-1} \frac{\rho'_m}{\sqrt{\rho'_m^2 + Z_n^2}} \right), \end{aligned}$$

for  $z \neq z'_n$ . For the singularity in (309),

$$\begin{aligned} \check{B}_x &\rightarrow 0, \\ \check{B}_y &\rightarrow 0, \\ \check{B}_z &\rightarrow -\varphi'_q \ln \rho'_m, \end{aligned} \quad (310)$$

for  $z = z'_n$ .

**(c) Axisymmetric** For the rectangular cylinder we have  $\varphi'_q = \{0, 2\pi\}$  which transforms the elliptic integrals and removes the section surfaces of current, as discussed with (282). As there are just two source discs of azimuthal current remaining,  $B_\varphi$  must vanish from orthogonality. By inspection of (178) and (179),

$$\mathbf{B}(\mathbf{r}) \rightarrow \frac{M_\rho \mu_0}{4\pi} \sum_{m,n=1}^2 (-1)^{m+n} (\check{B}_\rho \mathbf{e}_\rho + \check{B}_z \mathbf{e}_z), \quad (311)$$

for  $(\varphi'_1 = 0) \wedge (\varphi'_2 = 2\pi) \wedge (\rho > 0)$ , where

$$\begin{aligned} \check{B}_\rho &= \frac{4\rho'_m Z_n}{\rho R_{m,n}} \left[ K(k_{m,n}^2) - \frac{\rho L_n}{Z_n^2 \rho'_m} \right. \\ &\quad \times \left. \left( \frac{\bar{S}_{m,n}^2}{\bar{a}_n^2} \Pi(a_n^2; k_{m,n}^2) + \frac{S_{m,n}^2}{a^2} \Pi(\bar{a}_n^2; k_{m,n}^2) \right) \right], \quad (312) \end{aligned}$$

$$\check{B}_z = \frac{4\rho'_m}{R_{m,n}} K(k_{m,n}^2) - 2\pi [\alpha_m^{(1)} + \beta_m^{(1)}].$$

In (311) the unbound result  $\Pi(1; k_{m,n}^2)$  (when  $a_n^2 = 1$  or  $\bar{a}_n^2 = 1$ ) occurs when  $z = z'_n$ , that from (306), gives

$$\check{B}_\rho \rightarrow 0. \quad (313)$$

From (309) and (311) with  $\varphi'_q \rightarrow 2\pi$ ,

$$\mathbf{B}(\mathbf{r}) \rightarrow \frac{M_\rho \mu_0}{4\pi} \sum_{m,n=1}^2 (-1)^{m+n} \check{B}_z \mathbf{e}_z \quad (314)$$

for  $(\varphi'_1 = 0) \wedge (\varphi'_2 = 2\pi) \wedge (\rho = 0)$ , requiring  $\check{B}_z \rightarrow -2\pi \ln \rho'_m$  when  $z = z'_n$ .

**(d) Solid** There is no reduction of the summation; however, similar to the disc, a singularity is found in (299) that requires the conditional substitutions

$$\check{B}_\rho^{(1)} \rightarrow -\frac{L_n}{\rho} \tanh^{-1} \frac{\rho \sin \Phi_q}{Z_n}, \quad (315)$$

for  $\rho'_1 = 0$ , and

$$\check{B}_\rho^{(1)} \rightarrow 0, \quad (316)$$

for  $\rho'_1 = 0 \wedge z = z'_n$ .

**(e) Axisymmetric & Solid** The solution is given by (311) except from (315) we have

$$\check{B}_\rho \rightarrow 0, \quad (317)$$

for  $\rho'_1 = 0$ .

### 5.3 Azimuthal magnetisation

Azimuthal magnetisation is defined  $\mathbf{M}_\varphi(\mathbf{r}, \mathbf{r}') = M_\varphi [\sin(\varphi - \varphi') \mathbf{e}_\rho + \cos(\varphi - \varphi') \mathbf{e}_\varphi]$  ( $M_\rho, M_z = 0$ ). Using the charge model formulation, the vector potential is

$$\phi(\mathbf{r}) = \frac{1}{4\pi} \oint_S \frac{\mathbf{M}_\varphi(\mathbf{r}, \mathbf{r}') \cdot \mathbf{n}(\mathbf{r}, \mathbf{r}')}{|\mathbf{r} - \mathbf{r}'|} d\mathbf{a}', \quad (318)$$

with magnetic field

$$\mathbf{B}(\mathbf{r}) = \frac{\mu_0}{4\pi} \oint_S \frac{(\mathbf{r} - \mathbf{r}') [\mathbf{M}_\varphi(\mathbf{r}, \mathbf{r}') \cdot \mathbf{n}(\mathbf{r}, \mathbf{r}')] }{|\mathbf{r} - \mathbf{r}'|^3} d\mathbf{a}'. \quad (319)$$

After expanding, the three components of the magnetic field are due to only section surfaces of charge:

$$\mathbf{B}(\mathbf{r}) = \frac{M_\varphi \mu_0}{4\pi} [B_\rho(\mathbf{r}) \mathbf{e}_\rho + B_\varphi(\mathbf{r}) \mathbf{e}_\varphi + B_z(\mathbf{r}) \mathbf{e}_z] \quad (320)$$

as illustrated in Figure 14. From (321)-(323), shown next to Figure 14, a solution is found of form

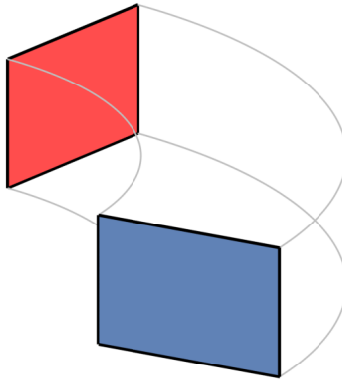
$$\begin{aligned} \mathbf{B}(\rho > 0) &= \frac{M_\varphi \mu_0}{4\pi} \sum_{m,n,q=1}^2 (-1)^{m+n+q} \\ &\quad \times [\check{B}_\rho \mathbf{e}_\rho + \check{B}_\varphi \mathbf{e}_\varphi + \check{B}_z \mathbf{e}_z], \end{aligned} \quad (324)$$

with an equivalent notation to (251), and use as in Section 5.1. These expressions only vary by a constant to (250), (248), and (246), respectively; the section of charge from diametric magnetisation has magnitude dependent upon the azimuth angle, whereas (324) is independent of the azimuth angle.

#### 5.3.1 Radial component – azimuthal magnetisation

From (258) we have the solution to (321)

$$\begin{aligned} \check{B}_\rho &= \sin \Phi_q \tan^{-1} \Upsilon_{m,n,q} \\ &\quad - \cos \Phi_q \tanh^{-1} \left( \frac{\hat{G}_{m,n,q}^{-1}}{Z_n} \right). \end{aligned} \quad (325)$$

Figure 14:  $\varrho$  from  $\mathbf{M}_\varphi \cdot \mathbf{n}$ .

### 5.3.2 Azimuthal component – azimuthal magnetisation

From (265) we have the solution to (322),

$$\begin{aligned} \check{B}_\varphi = & \cos \Phi_q \tan^{-1} \Upsilon_{m,n,q} \\ & + \sin \Phi_q \tanh^{-1} \left( \frac{\hat{G}_{m,n,q}^{-1}}{Z_n} \right). \end{aligned} \quad (326)$$

### 5.3.3 Axial component – azimuthal magnetisation

From (270) we have the solution to (323),

$$\check{B}_z = \ln \left( \rho'_m - \rho \cos \Phi_q + \hat{G}_{n,m,q}^{-1} \right). \quad (327)$$

### 5.3.4 Singularities – azimuthal magnetisation

The summands of (324) can be evaluated at all field points given the conditional substitutions given in this section.

(a) **On the shell plane** Not required for  $\rho = \rho'_m$ .

(b) **On the section plane** From (272)

$$\begin{aligned} \check{B}_\rho & \rightarrow -\tanh^{-1} \frac{\bar{R}_{m,n}}{Z_n}, \\ \check{B}_\varphi & \rightarrow 0, \end{aligned} \quad (328)$$

for  $\varphi = \varphi'_q$ . From (273)

$$\begin{aligned} \check{B}_\rho & \rightarrow \tanh^{-1} \frac{R_{m,n}}{Z_n}, \\ \check{B}_\varphi & \rightarrow 0, \end{aligned} \quad (329)$$

for  $\varphi \pm \pi = \varphi'_q$ .

(c) **On the disc plane** From (274)

$$\begin{aligned} \check{B}_\rho & \rightarrow 0, \\ \check{B}_\varphi & \rightarrow 0, \end{aligned} \quad (330)$$

for  $z = z'_n$ .

$$B_\rho(\mathbf{r}) = \sum_{q=1}^2 (-1)^q \int_{z'_1}^{z'_2} \int_{\rho'_1}^{\rho'_2} [\rho - \rho' \cos(\varphi - \varphi'_q)] \hat{G}_q^3 d\rho' dz', \quad (321)$$

$$B_\varphi(\mathbf{r}) = \sum_{q=1}^2 (-1)^q \sin(\varphi - \varphi'_q) \int_{z'_1}^{z'_2} \int_{\rho'_1}^{\rho'_2} \rho' \hat{G}_q^3 d\rho' dz', \quad (322)$$

$$B_\varphi(\mathbf{r}) = \sum_{q=1}^2 (-1)^q \int_{z'_1}^{z'_2} \int_{\rho'_1}^{\rho'_2} (z - z') \hat{G}_q^3 d\rho' dz', \quad (323)$$

(d) **On the axial line** From (275)

$$\check{B}_\rho \rightarrow -\operatorname{sgn}(Z_n) \ln |Z_n|, \quad (331)$$

for  $(\rho = \rho'_m) \wedge (\varphi = \varphi'_q)$ .

(e) **On the azimuthal line** Covered by (330) for  $(\rho = \rho'_m) \wedge (z = z'_n)$ .

(f) **On the radial line** In addition to (330), from (277)

$$\check{B}_z \rightarrow -\operatorname{sgn}(\bar{\rho}_m) \ln |\bar{\rho}_m|, \quad (332)$$

for  $(\varphi = \varphi'_q) \wedge (z = z'_n)$ .

### 5.3.5 Special cases – azimuthal magnetisation

For a general solution, this section has conditional substitutions for (324), at specific field points or when considering simplified geometry.

(a) **Inside the volume** As this problem was formulated using the charge model,  $\hat{\mathbf{B}} = \hat{\mathbf{H}}$  outside the region of source charges; however, when the field point and source point are within the same region, the source directionality must be included.

$$\mathbf{B}(\mathbf{r}) \rightarrow \mathbf{B}(\mathbf{r}) + \mu_0 \mathbf{M}(\mathbf{r}) \quad (333)$$

for  $(\rho'_1 < \rho < \rho'_2) \wedge (\varphi'_1 < \varphi < \varphi'_2) \wedge (z'_1 < z < z'_2)$ , where  $\mathbf{M}(\mathbf{r}) = M_\varphi \mathbf{e}_\varphi$ .

(b) **Along the axis** As with (279), (319) gives

$$\mathbf{B}(\mathbf{r}) \rightarrow \frac{M_\varphi \mu_0}{4\pi} \sum_{m,n,q=1}^2 (-1)^{m+n+q} (\check{B}_x \mathbf{e}_x + \check{B}_y \mathbf{e}_y + \check{B}_z \mathbf{e}_z), \quad (334)$$

for  $\rho = 0$ , where

$$\begin{aligned} \check{B}_x & = -\cos \varphi'_q \tanh^{-1} \frac{\sqrt{\rho'^2_m + Z_n^2}}{Z_n}, \\ \check{B}_y & = -\sin \varphi'_q \tanh^{-1} \frac{\sqrt{\rho'^2_m + Z_n^2}}{Z_n}, \end{aligned} \quad (335)$$

$$\check{B}_z = \tanh^{-1} \frac{\rho'_m}{\sqrt{\rho'^2_m + Z_n^2}},$$

for  $z \neq z'_n$ . For the singularity in (335),

$$\begin{aligned}\check{B}_x &\rightarrow 0, \\ \check{B}_y &\rightarrow 0, \\ \check{B}_z &\rightarrow \ln \rho'_m,\end{aligned}\quad (336)$$

for  $z = z'_n$ .

**(c) Axisymmetric** With  $\varphi'_q = \{0, 2\pi\}$  and from (282), the volume becomes a perfect insulator

$$\mathbf{B}(\mathbf{r}) \rightarrow 0, \quad (337)$$

for  $(\varphi'_1 = 0) \wedge (\varphi'_2 = 2\pi)$ . The external magnetic is zero; however, there is still an internal magnetic field due to the magnetisation.

**(d) Solid** Not required for  $\rho'_1 = 0$ .

**(e) Axisymmetric & Solid** Covered by (337) for  $(\varphi'_1 = 0) \wedge (\varphi'_2 = 2\pi) \wedge \rho'_1 = 0$ .

## 5.4 Axial magnetisation

Axial magnetisation is defined  $\mathbf{M}_z(\mathbf{r}, \mathbf{r}') = M_z \mathbf{e}_z$  ( $M_\rho, M_\varphi = 0$ ). Using the current model formulation, the vector potential is

$$\mathbf{A}(\mathbf{r}) = \frac{\mu_0}{4\pi} \oint_S \frac{\mathbf{M}_z(\mathbf{r}, \mathbf{r}') \times \mathbf{n}(\mathbf{r}, \mathbf{r}')}{|\mathbf{r} - \mathbf{r}'|} d\mathbf{a}', \quad (338)$$

and magnetic field

$$\mathbf{B}(\mathbf{r}) = \frac{\mu_0}{4\pi} \oint_S [\mathbf{M}_z(\mathbf{r}, \mathbf{r}') \times \mathbf{n}(\mathbf{r}, \mathbf{r}')] \times \frac{\mathbf{r} - \mathbf{r}'}{|\mathbf{r} - \mathbf{r}'|^3} d\mathbf{a}'. \quad (339)$$

After expanding, the three components of the magnetic field are due to shell and section surfaces of current:

$$B_\rho(\mathbf{r}) = \frac{M_z \mu_0}{4\pi} [B_\rho^{(1)}(\mathbf{r}) + B_\rho^{(2)}(\mathbf{r})], \quad (340)$$

$$B_\varphi(\mathbf{r}) = \frac{M_z \mu_0}{4\pi} [B_\varphi^{(1)}(\mathbf{r}) + B_\varphi^{(2)}(\mathbf{r})], \quad (341)$$

$$B_z(\mathbf{r}) = \frac{M_z \mu_0}{4\pi} [\underbrace{B_z^{(1)}(\mathbf{r})}_{\text{shell}} + \underbrace{B_z^{(2)}(\mathbf{r})}_{\text{section}}], \quad (342)$$

as illustrated in Figure 15. From (343)-(348), shown next to Figure 15, a solution is found of form

$$\begin{aligned}\mathbf{B}(\rho > 0) &= \frac{M_z \mu_0}{4\pi} \sum_{m,n,q=1}^2 (-1)^{m+n+q} \left[ (\check{B}_\rho^{(1)} + \check{B}_\rho^{(2)}) \mathbf{e}_\rho \right. \\ &\quad \left. + (\check{B}_\varphi^{(1)} + \check{B}_\varphi^{(2)}) \mathbf{e}_\varphi + (\check{B}_z^{(1)} + \check{B}_z^{(2)}) \mathbf{e}_z \right],\end{aligned}\quad (349)$$

with an equivalent notation to (251), and use as in Section 5.1.

The integrals for the shell surfaces ( $B_\rho^{(1)}, B_\varphi^{(1)}, B_z^{(1)}$ ) vary only by a constant to the azimuthal current density (Section 4.3), thus are mathematically equivalent. The shell surfaces combine with the section surfaces to complete a fictitious circuit of current.

The integrals for the section surfaces (250), (344), and (346), all vary only by a constant:  $M_\perp \sin(\varphi^* - \varphi'_q)$ ,  $M_z \sin(\varphi - \varphi'_q)$ , and  $M_z \cos(\varphi - \varphi'_q)$ . Similar to discussion on radial magnetisation, this highlights a transform between application of the charge and current models and field description – radial  $B_\rho^{(2)}$ , azimuthal  $B_\varphi^{(2)}$ , and axial  $B_z^{(2)}$  components of the field are described by an identical surface integrand.

### 5.4.1 Radial component – axial magnetisation

From (193) we have the solution to (343),

$$\check{B}_\rho^{(1)} = 2 \frac{\rho'_m}{R_{m,n}} [\mathcal{F}(\phi_q; k_{m,n}^2) - 2\mathcal{D}(\phi_q; k_{m,n}^2)], \quad (350)$$

and from (270) we have the solution to (344),

$$\check{B}_\rho^{(2)} = \sin \Phi_q \ln \left( \rho'_m - \rho \cos \Phi_q + \hat{G}_{n,m,q}^{-1} \right). \quad (351)$$

Combining (350) and (351) gives the complete solution to the radial component (340).

### 5.4.2 Azimuthal component – axial magnetisation

From (195) we have the solution to (345),

$$\check{B}_\varphi^{(1)} = \frac{1}{\rho} \hat{G}_{m,n,q}^{-1}. \quad (352)$$

and (346) is identical to (351), thus

$$\check{B}_\varphi^{(2)} = \cos \Phi_q \ln \left( \rho'_m - \rho \cos \Phi_q + \hat{G}_{n,m,q}^{-1} \right). \quad (353)$$

Combining (352) and (353) gives the complete solution to the azimuthal component (341).

### 5.4.3 Axial component – axial magnetisation

From (198) we have the solution to (347),

$$\check{B}_z^{(1)} = \frac{Z_n}{R_{m,n}} \left( \mathcal{F}(\phi_q; k_{m,n}^2) + \frac{\rho'^2_m - \rho^2}{\varrho_m^2} \Pi(\phi_q; \kappa_m^2, k_{m,n}^2) \right). \quad (354)$$

The  $z'$ -integral of the section surfaces (348) is given by (F16)

$$\begin{aligned}B_z^{(2)}(\mathbf{r}) &= -\rho \sum_{n,q=1}^2 (-1)^{n+q} Z_n \sin(\varphi - \varphi'_q) \\ &\quad \times \int_{\rho'_1}^{\rho'_2} \frac{d\rho'}{(\rho^2 - 2\rho \cos(\Phi_q)\rho' + \rho'^2) \sqrt{L_n^2 - 2\rho \cos(\Phi_q)\rho' + \rho'^2}}\end{aligned}\quad (355)$$

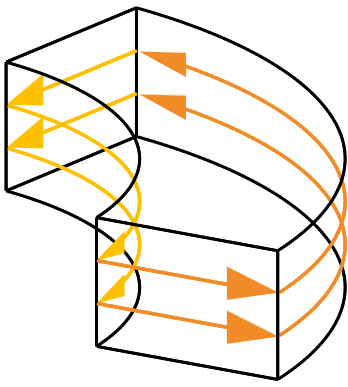
and the  $\rho'$ -integral is given by (F20)

$$\check{B}_z^{(2)}(\mathbf{r}) = -\tan^{-1} \Upsilon_{m,n,q}. \quad (356)$$

Combining (354) and (356) gives the complete solution to the radial component (342).

### 5.4.4 Singularities – axial magnetisation

The summands of (349) can be evaluated at all field points given the conditional substitutions given in this section.

Figure 15:  $\mathbf{K}$  from  $\mathbf{M}_z \times \mathbf{n}$ .

$$B_{\rho}^{(1)}(\mathbf{r}) = \sum_{m=1}^2 (-1)^m \rho'_m \int_{z'_1}^{z'_2} \int_{\varphi'_1}^{\varphi'_2} (z - z') \cos(\varphi - \varphi') \hat{G}_m^3 d\varphi' dz', \quad (343)$$

$$B_{\rho}^{(2)}(\mathbf{r}) = \sum_{q=1}^2 (-1)^q \sin(\varphi - \varphi'_q) \int_{z'_1}^{z'_2} \int_{\rho'_1}^{\rho'_2} (z - z') \hat{G}_q^3 d\rho' dz', \quad (344)$$

$$B_{\varphi}^{(1)}(\mathbf{r}) = \sum_{m=1}^2 (-1)^m \rho'_m \int_{z'_1}^{z'_2} \int_{\varphi'_1}^{\varphi'_2} (z' - z) \sin(\varphi - \varphi') \hat{G}_m^3 d\varphi' dz' \quad (345)$$

$$B_{\varphi}^{(2)}(\mathbf{r}) = \sum_{q=1}^2 (-1)^q \cos(\varphi - \varphi'_q) \int_{z'_1}^{z'_2} \int_{\rho'_1}^{\rho'_2} (z - z') \hat{G}_q^3 d\rho' dz', \quad (346)$$

$$B_z^{(1)}(\mathbf{r}) = \sum_{m=1}^2 (-1)^m \rho'_m \int_{z'_1}^{z'_2} \int_{\rho'_1}^{\rho'_2} [\rho'_m - \rho \cos(\varphi - \varphi')] \hat{G}_m^3 d\varphi' dz' \quad (347)$$

$$B_z^{(2)}(\mathbf{r}) = \rho \sum_{q=1}^2 (-1)^q \sin(\varphi'_q - \varphi) \int_{z'_1}^{z'_2} \int_{\rho'_1}^{\rho'_2} \hat{G}_q^3 d\rho' dz'. \quad (348)$$

(a) **On the shell plane** From (200),

$$\check{B}_z^{(1)} \rightarrow \frac{Z_n}{\sqrt{Z_n + 4\rho'^2_m}} F\left(\phi_q; \frac{4\rho'^2_m}{Z_n + 4\rho'^2_m}\right) \quad (357)$$

for  $\rho = \rho'_m$ . This removes  $\Pi(\phi_q; \kappa_m^2, k_{m,n}^2)$  from (354).

(b) **On the section plane** Equation (356) is simplified to avoid the singularity

$$\check{B}_z^{(2)} \rightarrow 0, \quad (358)$$

for  $\varphi = \varphi'_q$  and  $\varphi \pm \pi = \varphi'_q$ .

(c) **On the disc plane** Not required for  $z = z'_n$ .

(d) **On the axial line** Covered by (358) for  $(\rho = \rho'_m) \wedge (\varphi = \varphi'_q)$ .

(e) **On the azimuthal line** Covered by (174) and (357) for  $(\rho = \rho'_m) \wedge (z = z'_n)$ .

(f) **On the radial line** To avoid  $\ln(0)$  in (353) and (351), from (273) we have

$$\begin{aligned} \check{B}_{\rho}^{(2)} &\rightarrow 0, \\ \check{B}_{\varphi}^{(2)} &\rightarrow -\text{sgn}(\bar{\varrho}_m) \ln |\bar{\varrho}_m|, \end{aligned} \quad (359)$$

for  $(\varphi = \varphi'_q) \wedge (z = z'_n)$ .

#### 5.4.5 Special cases – axial magnetisation

For a general solution, this section has conditional substitutions for (349), at specific field points or when considering simplified geometry.

(a) **Inside the volume** As this problem was formulated using the current model, there is no differentiation to  $\mathbf{B}$  being within the source region or not.

(b) **Along the axis** As with (279), (339) gives

$$\mathbf{B}(\mathbf{r}) \rightarrow \frac{M_z \mu_0}{4\pi} \sum_{m,n,q=1}^2 (-1)^{m+n+q} (\check{B}_x \mathbf{e}_x + \check{B}_y \mathbf{e}_y + \check{B}_z \mathbf{e}_z), \quad (360)$$

for  $\rho = 0$ , where

$$\begin{aligned} \check{B}_x &= \sin \varphi'_q \left( \frac{\rho'_m}{\sqrt{\rho'^2_m + Z_n^2}} - \tanh^{-1} \frac{\rho'_m}{\sqrt{\rho'^2_m + Z_n^2}} \right), \\ \check{B}_y &= \cos \varphi'_q \left( \tanh^{-1} \frac{\rho'_m}{\sqrt{\rho'^2_m + Z_n^2}} - \frac{\rho'_m}{\sqrt{\rho'^2_m + Z_n^2}} \right), \\ \check{B}_z &= -\frac{\varphi'_q Z'_n}{\sqrt{\rho'^2_m + Z_n^2}}, \end{aligned} \quad (361)$$

for  $z \neq z'_n$ . For the singularity in (361),

$$\begin{aligned} \check{B}_x &\rightarrow \sin \varphi'_q (1 - \ln \rho'_m), \\ \check{B}_y &\rightarrow \cos \varphi'_q (\ln \rho'_m - 1), \\ \check{B}_z &\rightarrow 0, \end{aligned} \quad (362)$$

for  $z = z'_n$ .

(c) **Axisymmetric** For the rectangular cylinder we have  $\varphi'_q = \{0, 2\pi\}$ , that transforms the elliptic integrals and removes the section surfaces of current, as discussed with (282). As there are just two source shells of azimuthal current remaining,  $B_{\varphi}$  must vanish from orthogonality, similar to that of the radial magnetisation. By inspection of (204) and (205)

$$\mathbf{B}(\mathbf{r}) \rightarrow \frac{M_z \mu_0}{4\pi} \sum_{m,n=1}^2 (-1)^{m+n} (\check{B}_{\rho} \mathbf{e}_{\rho} + \check{B}_z \mathbf{e}_z), \quad (363)$$

for  $(\varphi'_1 = 0) \wedge (\varphi'_2 = 2\pi) \wedge (\rho > 0)$ , where

$$\begin{aligned} \check{B}_{\rho} &= \frac{4\rho'_m}{R_{m,n}} [2D(k_{m,n}^2) - K(k_{m,n}^2)], \\ \check{B}_z &= -\frac{2Z_n}{R_{m,n}} \left( K(k_{m,n}^2) + \frac{\rho'^2_m - \rho^2}{\rho'^2_m} \Pi(\kappa_m^2; k_{m,n}^2) \right). \end{aligned} \quad (364)$$

## 5.5 Verification & Summary

In (364) the unbound result  $\Pi(1; k_{m,n}^2)$  (when  $\kappa_m^2 = 1$ ) occurs when  $\rho = \rho'_m$ , that from (206) or (357), gives

$$\ddot{B}_z \rightarrow -2 \frac{Z_n}{\sqrt{Z_n^2 + 4\rho'_m}^2} K\left(\frac{4\rho'_m}{Z_n^2 + 4\rho'_m}\right). \quad (365)$$

From (361) and (363),

$$\mathbf{B}(\mathbf{r}) \rightarrow -\frac{M_z \mu_0}{2} \sum_{m,n=1}^2 (-1)^{m+n} \frac{Z_n}{\sqrt{\rho'_m}^2 + Z_n^2} \mathbf{e}_z \quad (366)$$

for  $(\varphi'_1 = 0) \wedge (\varphi'_2 = 2\pi) \wedge (\rho = 0)$ .

**(d) Solid** When the rectangular cylinder is not hollow, the closed surface does not have an inner shell, removing the  $m$ -summation

$$\begin{aligned} \mathbf{B}(\mathbf{r}) \rightarrow & \frac{M_z \mu_0}{4\pi} \sum_{n,q=1}^2 (-1)^{n+q} \left[ \check{B}_\rho^{(1)} \mathbf{e}_\rho + \check{B}_\varphi^{(1)} \mathbf{e}_\varphi + \check{B}_z^{(1)} \mathbf{e}_z \right. \\ & \left. + \sum_{m=1}^2 (-1)^m \left( \check{B}_\rho^{(2)} \mathbf{e}_\rho + \check{B}_\varphi^{(2)} \mathbf{e}_\varphi + \check{B}_z^{(2)} \mathbf{e}_z \right) \right], \end{aligned} \quad (367)$$

for  $\rho' = \rho_2$ .

**(e) Axisymmetric & Solid** The trivial solution for axial magnetisation is when the geometry is both solid and axisymmetric, identical to diametric magnetisation. Removing the  $m$ -summation from (363) gives a single shell surface to describe the field,

$$\mathbf{B}(\mathbf{r}) \rightarrow \frac{M_z \mu_0}{4\pi} \sum_{n=1}^2 (-1)^n (\check{B}_\rho \mathbf{e}_\rho + \check{B}_\varphi \mathbf{e}_\varphi + \check{B}_z \mathbf{e}_z), \quad (368)$$

with  $(\varphi'_1 = 0) \wedge (\varphi'_2 = 2\pi) \wedge \rho' = \rho_2$ .

## 5.5 Verification & Summary

The magnetic field on four surfaces, inside and outside of the volume, are shown in Figure 16 for the radially magnetised magnet. These surfaces are compared with an FEA model, with the absolute relative difference shown in Figure 17. A summary of the FEA simulation results and a quantification of the difference with the analytic result is shown in Table 6. Analytic and FEA results are provided in Table 7 from testing all equations in this section at 9 specific points, chosen to be inclusive of special geometrical cases and removable singularities. A qualitative view of the direction and magnitude of the magnetic field is shown in Figure 19. An equivalent set of figures and tables are given for the remaining magnets (diametric, azimuthal, axial) in Appendix K. The supplementary material of Appendix I contains a numeric evaluation (details in Section 3.6.2) of all analytic integrals of this section compared with all analytic solutions.

Excellent agreement with FEA is seen on all four surfaces presented for each magnet. Regions with a larger difference correlate with a low magnitude of the magnetic field, that is seen most clearly in Figure K.5c and Figure K.5d with reference to Figure K.4d and Figure K.4e. This difference is equivalent to numeric noise in the FEA solution, whereas the analytic results can correctly represent zero, or very small numbers. Elsewhere, there are some artefacts from the mesh discretisation and/or interpolation, as well as randomised and minor numerical differences, indicating that there are no spatial trends or significant differences between results from the analytical solutions and the FEA model.

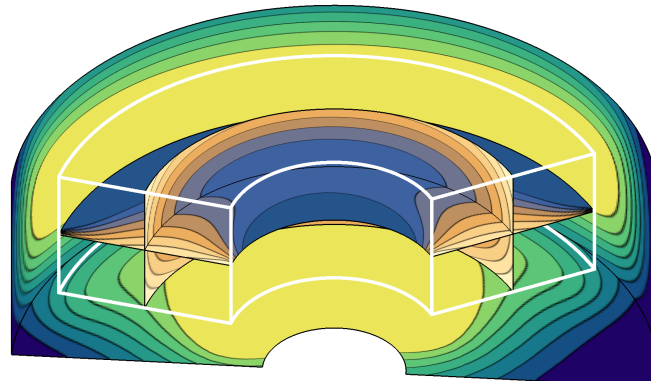
The permanent magnet with radial magnetisation is the only permanent magnet of the set not to be well-described by only elementary and elliptic functions. A part of the solution to the axial component,  $B_z$  is described by a series of regularised beta functions  $\Xi(\nu, p)$  with an axisymmetric component  $\beta^{(1)}$  and an azimuthal component  $\delta^{(1)}$ . The limit of  $\delta^{(1)}$  was shown to be independent of angle, thus in computation there is an axisymmetric spatial convergence of the series. An example is shown in Figure 18, that could be intuited from the nondimensional Figure 5a. The region with  $P \leq 5$  in this context could be considered the far-field. This region may not otherwise be clear to the user of these equations, to know how many terms are required in the analytic solution to achieve a desired precision in a region of interest.

As discussed in Section 3.6, there is complexity here as the magnetic flux density does vary with angle and the absolute remainder of the series is not strictly representative of the absolute accuracy of the solution with a partial sum. That is due to the eight sums for a volume element (for indices  $m, q, n$  over  $\rho', \varphi', z'$ ) for a single field point. The series are computed in isolation for the eight sums, that practically each quantify the field decay. The total of the eight sums may converge sooner, so the incorporation of additional convergence criteria using the change in magnitude of the field at a point may be of interest. Such an optimisation is out the scope of this article. The computation required with the current approach is improved over numeric methods with a discretised solution space, and is comparable to solutions employing Legendre elliptic integrals. A comparison of computational performance and accuracy for the various approaches is presented in Section 6.1.

## 6 Applications and computational efficiency

The magnetic field equations presented in this work are useful not just for calculating field components for design and optimisation purposes, but also in the calculation of magnetic forces and torques for permanent magnet motors, bearings, and couplings. Although the scope of this paper is limited to presenting magnetic field solutions, this section presents examples of using these solutions in the efficient calculations of forces.

Analytic solutions for the force and torque between various arc magnets and coils are complicated to solve. More general magnetic force and torque solutions can be calculated using the analytic magnetic field equations presented in this



(a) Visualisation of the cylindrical surfaces in Cartesian coordinates for radial magnetisation. Magnitudes are normalised for continuous contours.

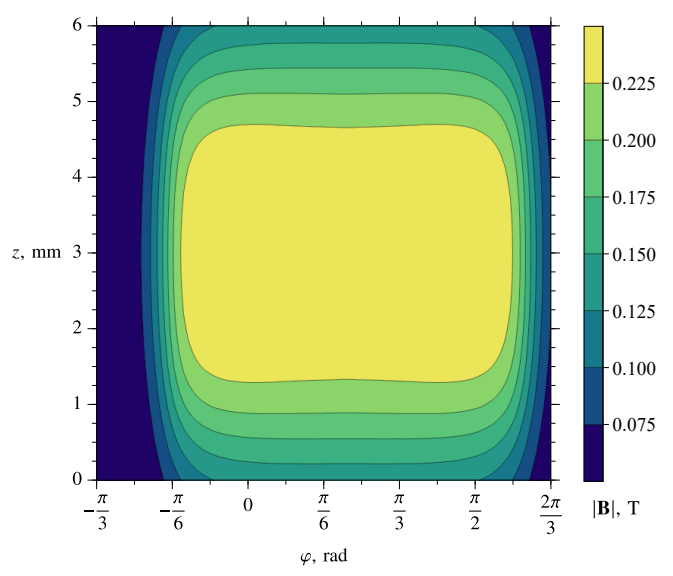
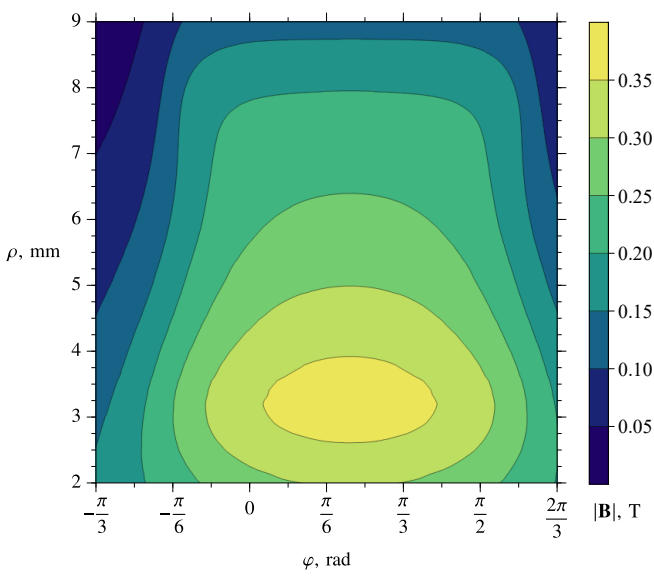
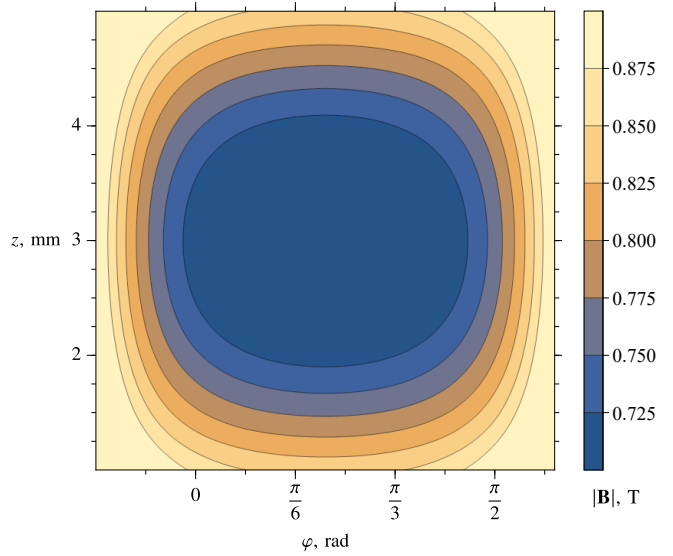
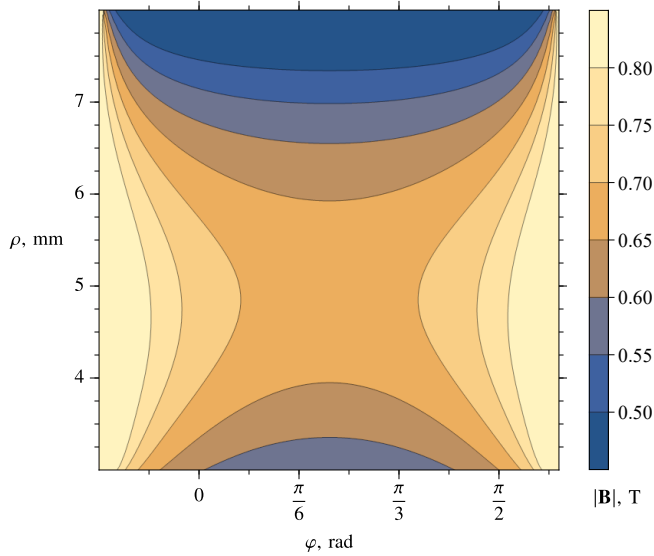


Figure 16: Magnitude of the magnetic field  $|\mathbf{B}|$  of a permanent magnet with radial magnetisation  $M_\rho = 955 \text{ kA/m}$ , and asymmetric geometry  $\rho' \in [3, 8] \text{ mm}$ ,  $\varphi' \in [-\frac{\pi}{6}, \frac{3\pi}{5}] \text{ rad}$ ,  $z' \in [1, 5] \text{ mm}$ .  $|\mathbf{B}|$  is shown on four rectangular cylindrical surfaces (b-e), inside and outside the volume of magnetisation, shown in white on (a).  $R = 10^{-2}$  was set for the series in  $B_z$ .

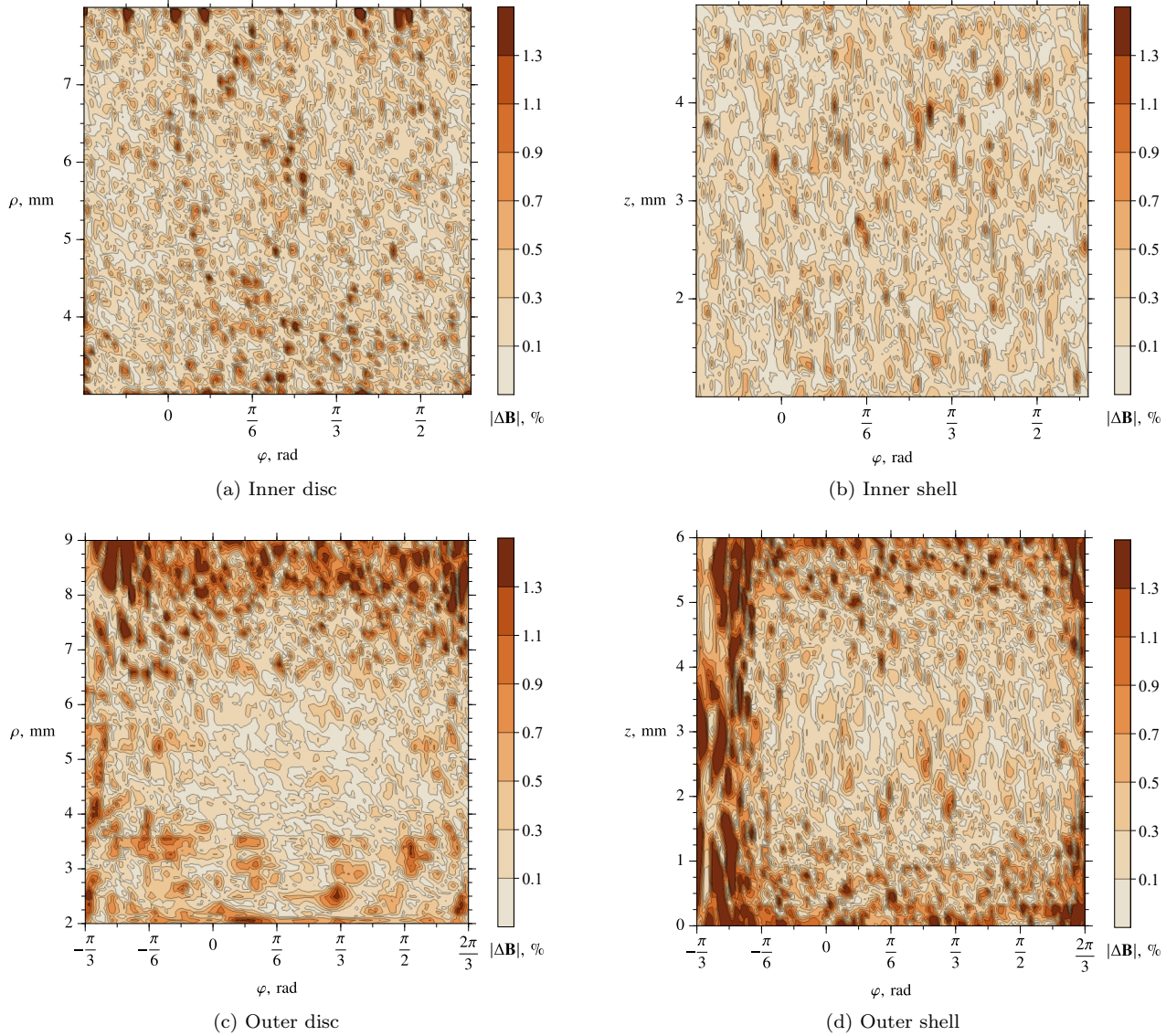


Figure 17: The absolute relative difference of the magnetic field  $|\Delta\mathbf{B}|$  at the fields points shown in Figure 16 with those in an FEA model. A summary of the FEA simulation results are given in Table 6.

Table 6: Summary of FEA model and analytic results comparison for the radial magnetisation shown in Figure 16.

(a) FEA simulation parameters and results

Tetrahedra in matter	192,253
Tetrahedra in vacuum	295,856
Total energy error, %	0.036134
Total energy, J	0.064494
Delta energy, %	0.018559

(b) FEA-Analytic comparison

Figure 17

$ \Delta\mathbf{B} $ , %	(a)	(b)	(c)	(d)
Mean	0.29	0.22	0.41	0.49
Max	44.01	1.61	2.86	3.30

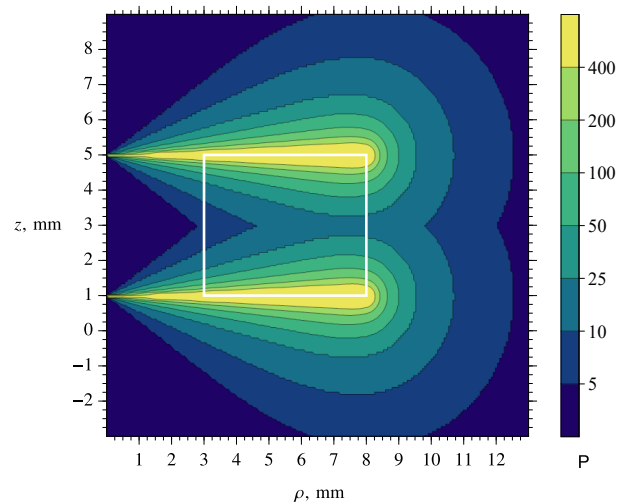


Figure 18: The maximum number of terms  $P$  required from any of the  $\beta^{(1)}$ ,  $\zeta^{(1)}$ ,  $\eta^{(1)}$ , and  $\iota^{(1)}$  series in order to compute the field on an axisymmetric surface with  $R = 10^{-2}$  and dimensions from Figure 16.

Table 7: Comparison of the analytic result with an FEA model for a permanent magnet with radial magnetisation  $M_\rho = 955 \text{ kA/m}$ . The field points encapsulate all equations in Section 5.2, inclusive of removable singularities, field regions, and geometries.  $R = 10^{-8}$  was set for the series in  $B_z$ .

Field Point			Source Limits						Magnetic Flux Density						
$\rho$	$\varphi$	$z$	$\rho'_1$	$\rho'_2$	$\varphi'_1$	$\varphi'_2$	$z'_1$	$z'_2$	Test	Comparison	$B_\rho$	$B_\varphi$	$B_z$		
9	$\frac{5\pi}{24}$	$\frac{31}{10}$	3	8	$-\frac{\pi}{6}$	$\frac{3\pi}{5}$	1	5	Standard	Analytic Result	0.24488567	-0.00030603	0.00965560		
										FEA Difference	0.00069263	0.00000260	0.00008203		
7	$\frac{5\pi}{24}$	$\frac{31}{10}$	3	8	$-\frac{\pi}{6}$	$\frac{3\pi}{5}$	1	5	Special Case a.	Analytic Result	0.54891546	-0.00006130	0.00513018		
										FEA Difference	0.00239386	0.00098335	-0.00007241		
9		$\frac{31}{10}$	3	8	0	$2\pi$	1	5	Special Case c.	Analytic Result	0.21122808	0	0.00930958		
										FEA Difference	0.00034490	-0.00000655	0.00000266		
9	$\frac{5\pi}{24}$	$\frac{31}{10}$	0	8	$-\frac{\pi}{6}$	$\frac{3\pi}{5}$	1	5	Special Case d.	Analytic Result	0.25728534	-0.00044889	0.00990813		
										FEA Difference	0.00077664	0.00002667	-0.00006837		
9		$\frac{31}{10}$	0	8	0	$2\pi$	1	5	Special Case e.	Analytic Result	0.21611166	0	0.00946992		
										FEA Difference	0.00035003	0.00000984	0.00005791		
9	$-\frac{\pi}{6}$	5	3	8	$-\frac{\pi}{6}$	$\frac{3\pi}{5}$	1	5	Singularities b,c,f	Analytic Result	0.04575439	-0.10541986	0.08474435		
										FEA Difference	0.00077113	0.00038666	0.00027561		
8	$-\frac{5\pi}{24}$	5	3	8	$-\frac{\pi}{6}$	$\frac{3\pi}{5}$	1	5	Singularities a,c,e	Analytic Result	-0.06364162	-0.09932524	0.03837016		
										FEA Difference	0.00015694	0.00034618	0.00004605		
8	$-\frac{\pi}{6}$	6	3	8	$-\frac{\pi}{6}$	$\frac{3\pi}{5}$	1	5	Singularities a,b,d	Analytic Result	-0.06633792	-0.07011472	0.07855350		
										FEA Difference	0.00010350	0.00051141	0.00022471		
$x$	$y$	$z$										$B_x$	$B_y$	$B_z$	
0	0	5	3	8	$-\frac{\pi}{6}$	$\frac{3\pi}{5}$	1	5	Special Case b.			Analytic Result	0.13444452	0.10887102	-0.12070557
												FEA Difference	0.00044748	0.00041154	-0.00006066

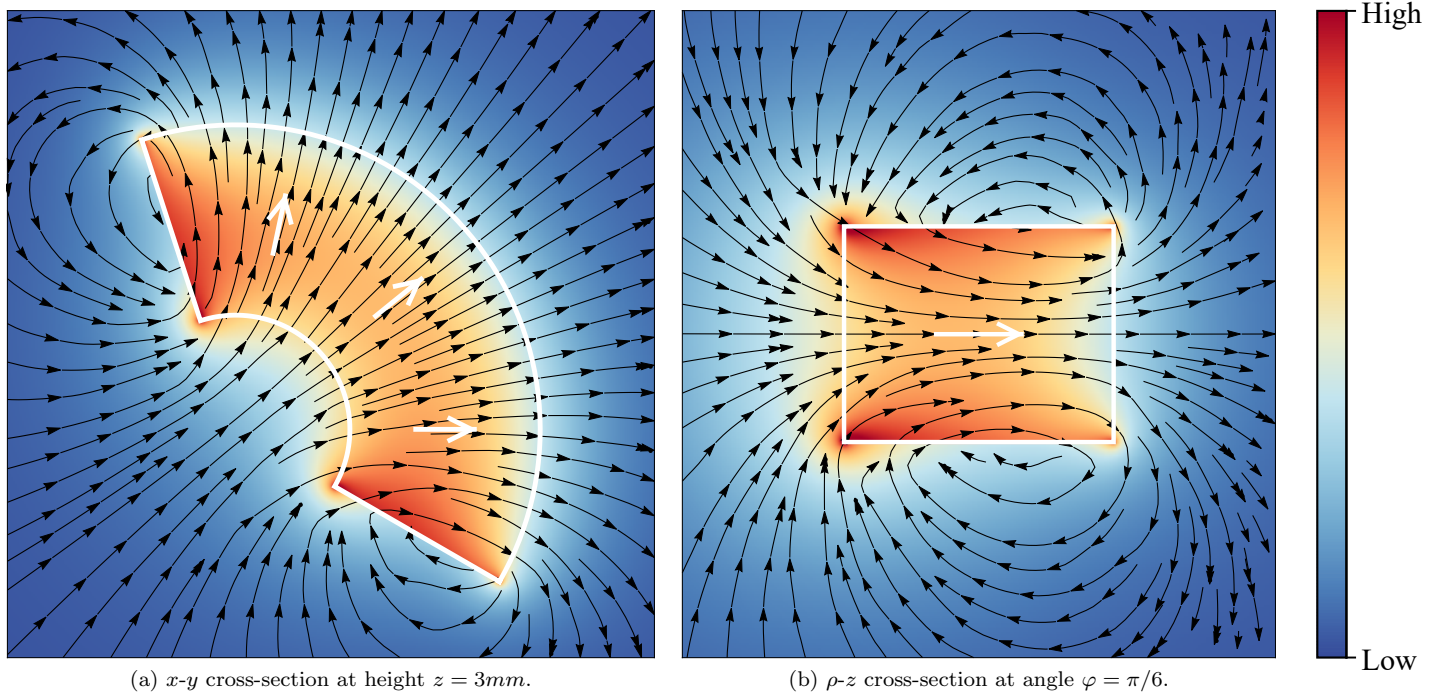


Figure 19: Qualitative view of the magnetic field magnitude (low-high) with overlaid streamlines in black. The outlined geometry and magnetisation direction arrows are identical to Figure 16 and shown in white.

work, via one of several computationally inexpensive methods. Permanent magnet equations are the focus of this section, where the range of field equations presented in this article are benchmarked: the primary field equations and nested cases for singularities and/or limiting geometries. Two case studies are presented: an axisymmetric case of a magnetically levitated ring with a simple analytic force expression; a non-axisymmetric case of (in-part) an axial force coupler with a complex analytic force expression.

A review of the force models is given in Appendix A.5. All computations were completed on a standard desktop PC (3.5 GHz processor E3-1240v5 and 16 GB RAM DDR4) using software outlined in Section 3.6.

## 6.1 Magnetic field at a point

To evaluate the efficiency of typical magnetic field solutions presented in this paper, the computational times of the reference data in Table 7 were recorded for both analytic and numeric procedures. These magnetic field solutions include a number of additional equations that handle special cases and singularities, such as artefacts from the Green's free space function (Section 3.6.1). It is shown in Figure 20 with the red dots, that including these equations will always improve computation time at the field point (excluding  $\mathbf{M}_\rho$  with  $R = 10^{-8}$ ), to around an order of magnitude. Evaluation of expressions containing the transformed Legendre elliptic integrals (in  $\mathbf{M}_\perp$  and  $\mathbf{M}_z$ ) are approximately equivalent to those containing only elementary expressions ( $\mathbf{M}_\phi$ ). Computationally, it can be said these are equivalently closed-form or elementary. The series solutions do not evaluate as fast since they have additional nested elementary/Beta functions, around an order of magnitude slower for  $\mathbf{M}_\rho$  with  $R = 10^{-2}$ . The maximum partial sum remainder  $R$  is determined by the next term in the series and the series limit (91), with a smaller value implying more terms in the series are computed for increased decimal place accuracy.

The analytic solutions evaluate around 2 orders of magnitude faster than an equivalent solution (to 8 decimal places) using numeric methods (Section 3.6.2) — with the caveat of evaluating the partial sum contained in  $B_z$  for radial magnetisation  $\mathbf{M}_\rho$ . The field points in Figure 20 are chosen close to the surface of the magnet, with up to 650 terms required in each evaluation of  $\beta^{(1)}$ ,  $\zeta^{(1)}$ ,  $\eta^{(1)}$ , and  $\iota^{(1)}$  to reach 8 decimal places. Evaluating this many terms in the series can be as computationally expensive as numerically solving the integral; however practically, this level of accuracy is not required for a parametric study using these field equations.

Evaluation of the series with a relatively high remainder is enough to reach the precision of FEA in the near field. This is shown with  $|\mathbf{B}|$  in Figure J.1 and  $|\Delta\mathbf{B}|$  in Figure J.2. Each FEA model of a single magnet in this article (Section 3.6.4) with  $\approx 500k$  tetrahedrons took  $\approx 15$  minutes to compute and achieve a  $|\Delta\mathbf{B}| < 1\%$  for most field points, compared to the analytic solution (excluding those with  $\mathbf{B}$  magnitudes close to zero, where FEA has aforementioned numerical noise). Evaluation times at 35,000 points are shown in Figure 21: with a minimum time of 6.6 ms, maximum time of 602 ms, and mean time of 28.8 ms. This highlights the computational benefit

of finding the series convergence and spatial remainder (Section 3.5) to efficiently sum the series to a required precision, without which, the partial sum of an exact analytic series solution may not be an improved method over direct numeric integration in the near field of a magnet or coil.

## 6.2 Magnetic field gradient

The magnetic field from any charge or current distribution can be modelled as a magnetic dipole when the field points of interest are sufficiently far (or the distributions are localised). Inversely, when a magnetic particle is relatively small, the external magnetic field  $\mathbf{B}_E$  across the localised distribution can be assumed uniform. The force on a magnetic particle is proportional to its magnetic dipole moment  $\mathbf{m}$ , given in either the charge or current  $\mathbf{m}_\rho, \mathbf{m}_J$  models. A complete description of the particle requires the field gradient  $\nabla\mathbf{B}$ , where for example, the force is found via  $[\nabla\mathbf{B}_E] \cdot \mathbf{m}_\rho$  or  $\mathbf{m}_J \cdot [\nabla\mathbf{B}_E]$  (A50), with a drift velocity proportional to  $\mathbf{B} \times \nabla_\perp \mathbf{B}$  [74, pg.416].

Analytic solutions for the field gradient from cylindrical coils and magnets can be readily found using the analytic field solutions in this article. Thus, under the assumption a magnetic particle is small, the analytic force can be found directly. The derivatives to all magnetic field equations in this article are omitted due to the total number of magnetic field equations, each having nine terms in the gradient; however, all derivatives can be immediately found through standard methods or with symbolic mathematical software. A number of key examples are below for the partial derivatives of the special functions used in this article.

The Leibniz integral rule is required to differentiate the elliptic integrals and regularised beta functions. All elliptic and beta moduli are only dependent on  $\rho$  and  $z$  and are common across all field equations. From Table B.1:  $k^2 = 4\rho\rho'/R^2$ ,  $z^2 = \rho'^2/T^2$ , and  $y^2 = Z^2/T^2$ . The methodology is shown for the elliptic integral of the first kind, whereby the chain rule is used on the radicand and the elliptic form returned

$$\begin{aligned} \frac{\partial}{\partial\rho}F(\phi; k^2) &= \int_{t=0}^{\sin\phi} \frac{\partial}{\partial\rho} \frac{1}{\sqrt{(1-t^2)[1-k(\rho)^2t^2]}} dt, \\ &= \frac{2\rho'(\rho'^2 - \rho^2 + Z^2)}{R^4} \int_{t=0}^{\sin\phi} \frac{t^2}{(1-k^2t^2)w(t)} dt, \quad -\frac{\pi}{2} \leq \phi < \frac{3\pi}{2}, \\ \left. \frac{\partial}{\partial\rho}F(\phi; k^2) \right|_{\varphi'_1}^{\varphi'_2} &= \frac{Z^2 - \rho^2 + \rho'^2}{2\rho R^2} [\Pi(\phi; k^2, k^2) - F(\phi; k^2)] \Big|_{\varphi'_1}^{\varphi'_2}, \quad \forall\phi, \end{aligned} \quad (369)$$

where  $\Pi(\phi; k^2, k^2)$  is the brief form of (E29). Evaluation limits are included for the transformed elliptic integral, otherwise integration constants would need to be included. For an azimuthal derivative, the elliptic integral will always vanish, leaving an elementary function:

$$\begin{aligned} \frac{\partial}{\partial\varphi}F(\phi; k^2) &= -\frac{-\text{sgn } \Phi}{\sqrt{(1-\sin^2\phi)(1-k^2\sin^2\phi)}} \frac{\partial}{\partial\varphi} \cos[\frac{1}{2}(\varphi - \varphi')] \\ &= \frac{1}{2\sqrt{1-k^2\sin^2\phi}}. \end{aligned} \quad (370)$$

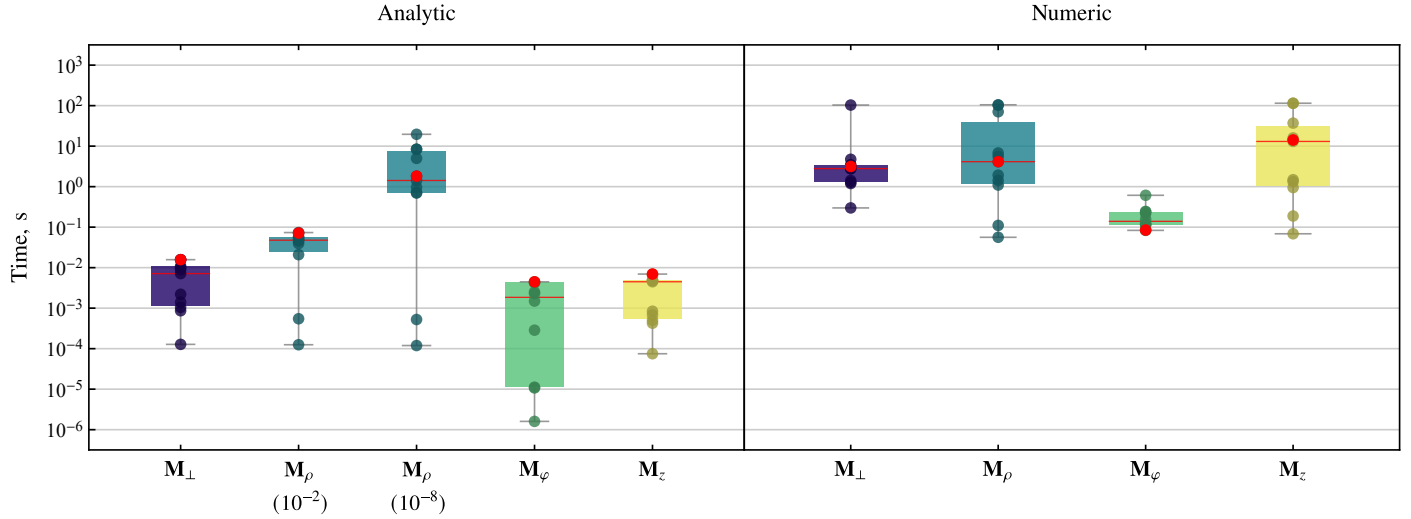


Figure 20: Analytic and numeric magnetic field  $\mathbf{B}$  computation times at the field points in Table 7 with identical geometries for each principal magnetisation direction. Two additional points are included (given in Appendix I) for singular axisymmetric cases. The analytic radial magnetisation is computed for both  $R = 10^{-2}$  and  $R = 10^{-8}$ . The median time is shown with a horizontal red line. The standard field point, with no nested special cases or singularities, is shown with a red dot. Results were obtained using the inbuilt `RepeatedTiming` function in Mathematica (Section 3.6.4) with the analytic solution and numeric integral functions contained in the supplementary material Appendix I.

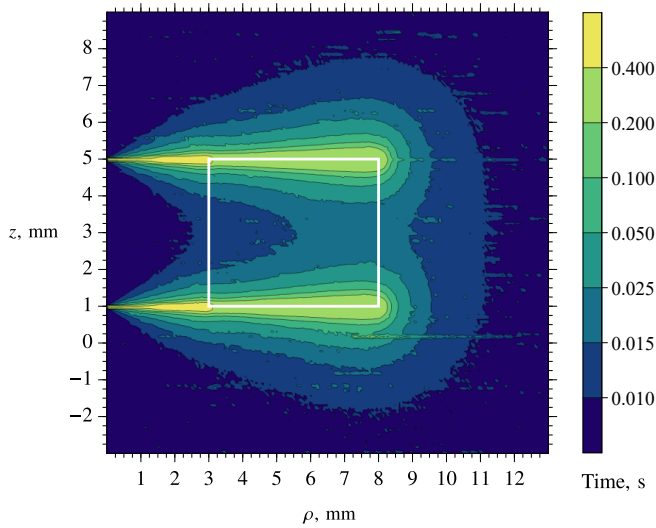


Figure 21: The field point evaluation times from a radially magnetised permanent magnet on a surface at  $\varphi = \frac{\pi}{6}$  with  $R = 10^{-2}$ , dimensions from Figure 16, and maximum terms from Figure 18.

The axial derivative will always follow the same process as the radial derivative:

$$\frac{\partial}{\partial z} F(\phi; k^2) \Big|_{\varphi'_1}^{\varphi'_2} = \frac{Z}{R^2} [F(\phi; k^2) - \Pi(\phi; k^2, k^2)] \Big|_{\varphi'_1}^{\varphi'_2}. \quad (371)$$

Similarly, the elliptic integrals of the second kind follow (369):

$$\begin{aligned} \frac{\partial}{\partial \rho} E(\phi; k^2) &= \int_{t=0}^{\sin \phi} \frac{\partial}{\partial \rho} \frac{\sqrt{1-k(\rho)^2 t^2}}{\sqrt{1-t^2}} dt, \\ \frac{\partial}{\partial \rho} E(\phi; k^2) \Big|_{\varphi'_1}^{\varphi'_2} &= \frac{2\rho'(\rho^2 - \rho'^2 - Z^2)}{R^4} D(\phi; k^2) \Big|_{\varphi'_1}^{\varphi'_2}. \end{aligned} \quad (372)$$

The elliptic integrals of the third kind have three different elliptic characteristics:  $a^2 = 2\rho/(\rho + L)$ ,  $\bar{a}^2 = 2\rho/(\rho - L)$ , and  $\kappa^2 = 4\rho\rho'/\rho^2$ . The product and chain rules are used on the radicand, then a complicated partial fraction expansion is required to return to the Legendre forms, similar to (253)-(256), separating the non-elliptic terms:

$$\begin{aligned} \frac{\partial}{\partial \rho} \Pi(\kappa^2; \phi, k^2) &= \int_{t=0}^{\sin \phi} \frac{\partial}{\partial \rho} \frac{[1-\kappa(\rho)^2 t^2]^{-1}}{\sqrt{(1-t^2)[1-k(\rho)^2 t^2]}} dt, \\ &= \frac{1}{\rho} \int_{t=0}^{\sin \phi} \left( \frac{(Z^2 - \rho^2 + \rho'^2)k^2}{2R^2(1-k^2 t^2)} - \frac{\bar{\rho}\kappa^2}{\rho(1-\kappa^2 t^2)} \right) \\ &\quad \times \frac{t^2}{(1-\kappa^2 t^2)w(t)} dt, \quad -\frac{\pi}{2} \leq \phi < \frac{3\pi}{2}, \end{aligned}$$

$$\begin{aligned} \frac{\partial}{\partial \rho} \Pi(\kappa^2; \phi, k^2) \Big|_{\varphi'_1}^{\varphi'_2} &= \left[ \left( \frac{1}{2\rho} - \frac{1}{\bar{\rho}} - \frac{\rho}{R^2} \right) \Pi(\phi; \kappa^2, k^2) \right. \\ &\quad + \left( \frac{1}{\rho} - \frac{1}{\bar{\rho}} + \frac{\rho}{R^2} \right) \Pi(\phi; \kappa^2, k^2) + \frac{\rho}{2\rho\bar{\rho}} F(\phi; k^2) \\ &\quad \left. - \frac{\rho'\rho R \hat{G} \sin \Phi}{\bar{\rho}(\rho^2 + \rho'^2 - 2\rho\rho' \cos \Phi)} \right] \Big|_{\varphi'_1}^{\varphi'_2}, \quad \forall \phi. \end{aligned} \quad (373)$$

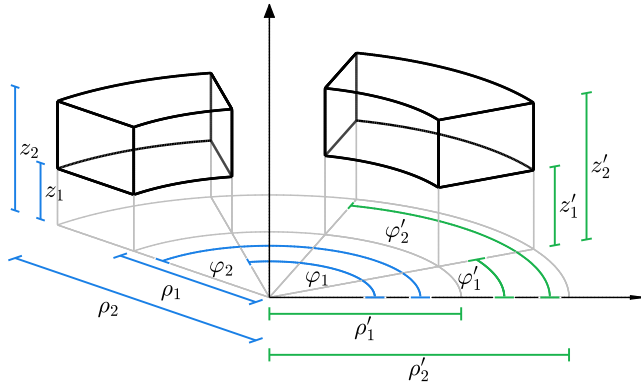


Figure 22: Parameterisation of geometry for two coaxial rectangular cylindrical sectors. Primed and unprimed cylindrical parameters define the integration regions of two magnetic sources, with a force acting on the unprimed.

The regularised beta functions are similar to (370), from (E15):

$$\begin{aligned} \frac{\partial}{\partial \rho} I(z^2; a, b) &= B(a, b)^{-1} z^{2(a-1)} (1-z^2)^{b-1} \frac{\partial}{\partial \rho} z(\rho)^2 \\ &= -\frac{2\rho}{T^2 B(a, b)} z^{2a} (1-z^2)^{b-1}. \end{aligned} \quad (374)$$

### 6.3 An axisymmetric force

Magnetisation is the magnetic dipole moment density, and analytic force solutions on these distributions require integration of the external magnetic field instead of differentiation. The integral assumes the magnetisation is uniform across the region, but the region need not be within a uniform external field. If the magnetisation is not uniform, it can be split into uniform principal components  $\{\mathbf{M}_\perp, \mathbf{M}_\rho, \mathbf{M}_\varphi, \mathbf{M}_z\}$  and solutions superimposed.

For a magnetic levitation case study, consider the force between two coaxial permanent magnets with axial magnetisations:

$$\begin{aligned} \text{Magnet 1, } \mathbf{M}'_z(\mathbf{r}, \mathbf{r}') &= M'_z \mathbf{e}_z, \\ \text{Magnet 2, } \mathbf{M}_z(\mathbf{r}, \mathbf{r}') &= M_z \mathbf{e}_z. \end{aligned} \quad (375)$$

Using the current model formulation (A26) and Figure 22, the force on magnet 2 due to magnet 1 is

$$\begin{aligned} \mathbf{F} &= M_z \sum_{m=1}^2 (-1)^m \rho_m \int_{z_1}^{z_2} \int_{\varphi_1}^{\varphi_2} (B_{E\rho} \mathbf{e}_\rho - B_{E\rho} \mathbf{e}_z) d\varphi dz \\ &\quad + M_z \sum_{q=1}^2 (-1)^q \int_{z_1}^{z_2} \int_{\rho_1}^{\rho_2} (B_{E\varphi} \mathbf{e}_\varphi - B_{E\varphi} \mathbf{e}_z) d\rho dz, \end{aligned} \quad (376)$$

where  $\mathbf{B}_E = B_{E\rho} \mathbf{e}_\rho + B_{E\varphi} \mathbf{e}_\varphi + B_{Ez} \mathbf{e}_z$  is given by (339). The inverse force is found by reciprocity of  $\mathbf{r}$  and  $\mathbf{r}'$ , that is just a change of sign due to the Green's function. If both magnets are axisymmetric, the section surfaces cancel ( $q$ -summation) and  $B_{Ez} \mathbf{e}_\rho$  integrates to zero over  $2\pi$ . The force between the magnets only has an axial component  $F_z$ , dependent on the radial field of magnet 1:

$$F_z = -M_z \sum_{m=1}^2 (-1)^m \rho_m \int_{z_1}^{z_2} B_{E\rho} dz \int_0^{2\pi} d\varphi. \quad (377)$$

In fact, any magnet here is interchangeable with a shell of azimuthal current (thin solenoid). The analytic solution is known for  $B_{E\rho}$  (364); however, integration of this function requires integrals of elliptic integrals that are only known in limiting cases. It is useful to alter the order of integration, starting with substituting in (339):

$$\begin{aligned} F_z &= \frac{M_z M'_z \mu_0}{2} \sum_{m, \dot{m}=1}^2 (-1)^{m+\dot{m}} \rho_m \rho'_{\dot{m}} \\ &\quad \times \int_{z_1}^{z_2} \int_{z'_1}^{z'_2} \int_{\varphi'_1=0}^{\varphi'_2=2\pi} \frac{(z' - z) \cos \varphi'}{\hat{G}_{m, \dot{m}}^{-3}} d\varphi' dz' dz. \end{aligned} \quad (378)$$

The  $z'$  integral and  $t$ -substitution are known from (192)

$$\begin{aligned} F_z &= 2M_z M'_z \mu_0 \sum_{m, m, \dot{n}=1}^2 (-1)^{m+\dot{m}+\dot{n}} \rho_m \rho'_{\dot{m}} \int_{t=0}^1 \frac{1-2t^2}{\sqrt{1-t^2}} \\ &\quad \times \int_{z_1}^{z_2} \frac{z - z'_n}{[\rho_m^2 + 2(1-2t^2)\rho_m \rho'_{\dot{m}} + \rho'_{\dot{m}}^2 + (z - z'_n)^2]^{1/2}} dz dt \end{aligned} \quad (379)$$

and the  $z'$  integral found using (F15) and (F19)

$$\begin{aligned} F_z &= 2M_z M'_z \mu_0 \sum_{m, n, \dot{m}, \dot{n}=1}^2 (-1)^{m+n+\dot{m}+\dot{n}} \rho_m \rho'_{\dot{m}} \\ &\quad \times \int_{t=0}^1 \frac{1-2t^2}{\sqrt{1-t^2}} \ln \left( Z_{n, \dot{n}} + \sqrt{R_{m, \cdot, \dot{n}}^2 - 4\rho_m \rho'_{\dot{m}} t^2} \right) dt. \end{aligned} \quad (380)$$

It is necessary to simplify (380) by applying the (Leibniz) product rule. This avoids direct integration of the logarithm and removes integration constants that cancel over the summations. This gives the integral

$$\begin{aligned} F_z &= 8M_z M'_z \mu_0 \sum_{m, n, \dot{m}, \dot{n}=1}^2 (-1)^{m+n+\dot{m}+\dot{n}} \frac{\rho_m^2 \rho'_{\dot{m}}^2 Z_{n, \dot{n}}}{R_{m, \cdot, \dot{n}}} \\ &\quad \times \int_{t=0}^1 \frac{t^2(t^2-1)}{(\rho_m^2 - 4\rho_m^2 \rho'_{\dot{m}}^2 t^2) w_{m, \cdot, \dot{n}}(t)} dt. \end{aligned} \quad (381)$$

that has an identical partial fraction expansion (262) and integral (261) as seen before, giving

$$F_z = 2M_z M'_z \mu_0 \sum_{m, n, \dot{m}, \dot{n}=1}^2 (-1)^{m+n+\dot{m}+\dot{n}} \check{F}_z, \quad (382)$$

with summand

$$\begin{aligned} \check{F}_z &= \frac{Z_{n, \dot{n}}}{R_{m, \cdot, \dot{n}}} \left( \frac{\bar{\rho}_{m, \dot{m}}^2}{4} [\Pi(k_{m, \dot{m}}^2; k_{m, \cdot, \dot{n}}^2) \right. \\ &\quad \left. - K(k_{m, \cdot, \dot{n}}^2)] - \rho_m \rho'_{\dot{m}} D(k_{m, \cdot, \dot{n}}^2) \right). \end{aligned} \quad (383)$$

For the summand singularity when the radii are equal,

$$\check{F}_z(\rho_m = \rho'_{\dot{m}}) = -\frac{\rho'^2_{\dot{m}} Z_{n, \dot{n}}}{\sqrt{Z_{n, \dot{n}} + 4\rho'^2_{\dot{m}}}} D(k_{n, \dot{n}}^2). \quad (384)$$

For the special case when a magnet is solid, the  $m$  and/or  $\dot{m}$  summation indexes can be removed as the respective shell

of current vanishes. The result of (382) has been previously attained using an alternate method [110]; however, the derivation simplicity here highlights the benefit to using the transformed Legendre forms.

Remarkably, the force expression of (383) is as efficient as calculating a single standard field point for  $\mathbf{M}_\perp$  or  $\mathbf{M}_z$ . This result can be used to both check and benchmark various semi-analytic methods. We define a semi-analytic method as calculating a mesh of analytic field points to estimate the force. The advantage of semi-analytic methods is not requiring explicit force equations between each permutation of permanent magnet magnetisation and/or geometry — here we have only shown one such permutation, and it is likely that for more complex geometries, such as 3D rotations, the integrals required would no longer be tractable. The semi-analytic methods of interest here use the Maxwell Stress Tensor (MST) (A43)

$$\mathbf{F} = \sum_i a^{(i)} [\mathbf{B}^{(i)} \otimes \mathbf{B}^{(i)} - \frac{1}{2}(\mathbf{B}^{(i)} \cdot \mathbf{B}^{(i)})\mathcal{I}] \cdot \mathbf{n}^{(i)}, \quad (385)$$

the charge model (A42)

$$\mathbf{F} = \sum_i a^{(i)} (\mathbf{M}^{(i)} \cdot \mathbf{n}^{(i)}) \mathbf{B}_E^{(i)}, \quad (386)$$

and the current model (A42)

$$\mathbf{F} = \sum_i a^{(i)} (\mathbf{M}^{(i)} \times \mathbf{n}^{(i)}) \times \mathbf{B}_E^{(i)}, \quad (387)$$

where the bounding surfaces are discretised into  $i$  surface elements. Each surface element has an area  $a$  with a normal  $n$  and field  $\mathbf{B}$  calculated at the area centroid. For an expression to approximate (383), we use  $\mathbf{M}$  from (339) and  $\mathbf{B}$  from (349). Convergence results over time are shown in Figure 23. A basic discretisation procedure was followed for surface mesh elements: splitting each surface into evenly spaced segments and linearly increasing the number of elements in each refinement. This is illustrated for each method in Figure 24, where a closed surface is required for the MST, two open disc surfaces for the charges, and two open shell surfaces for the currents.

The semi-analytic methods converge very quickly. The analytic solution took 2.2 ms and the charge model was within 1% after 2.3 ms and 0.1% after 6 ms. In this case, the MST and current models do not converge as quickly, due to the increased surface area and variant magnetic field through the local regions. The MST surface can be an arbitrary shape within the air-gap, and efficiency will change dependent on choice. For such a simple problem, FEA is comparatively inefficient.

## 6.4 A non-axisymmetric force

As an alternative to (376), using the charge model formulation, the force on magnet 2 due to magnet 1 is

$$\mathbf{F} = M_z \sum_{n=1}^2 (-1)^n \int_{\varphi_1}^{\varphi_2} \int_{\rho_1}^{\rho_2} \rho \mathbf{B}_E \, d\rho \, d\varphi. \quad (388)$$

Using both the charge and current models interchangeably for the sources (magnet 1) and field points (magnet 2) gives four

combinations of solutions for each force basis vector. This provides a set of 64 quadruple integrals to choose from to describe the problem. In addition, we can use a number of integral transforms such as (238) and (239). The goal is to show that using the compendium of magnetic field solutions, we can readily find analytic solutions for the force between differently magnetised arc magnets or coils; however, solutions for the field are more general, and semi-analytic solutions for the force and torque are sufficient due to the increased complexity and evaluation time.

Substituting into (388):  $\mathbf{B}_{E\rho}$  from (J7), and  $\mathbf{B}_{E\varphi}$  from (J8), gives

$$F_x = \frac{M_z M'_z \mu_0}{4\pi} \sum_{n,\dot{n}=1}^2 (-1)^{n+\dot{n}} \int_{\varphi_1}^{\varphi_2} \int_{\rho_1}^{\rho_2} \int_{\varphi'_1}^{\varphi'_2} \int_{\rho'_1}^{\rho'_2} \times \frac{\rho \rho' [\rho' \cos \varphi' - \rho \cos \varphi]}{\hat{G}_{n,\dot{n}}^{-3}} \, d\rho' \, d\varphi' \, d\rho \, d\varphi, \quad (389)$$

and

$$F_y = \frac{M_z M'_z \mu_0}{4\pi} \sum_{n,\dot{n}=1}^2 (-1)^{n+\dot{n}} \int_{\varphi_1}^{\varphi_2} \int_{\rho_1}^{\rho_2} \int_{\varphi'_1}^{\varphi'_2} \int_{\rho'_1}^{\rho'_2} \times \frac{\rho \rho' [\rho' \sin \varphi' - \rho \sin \varphi]}{\hat{G}_{n,\dot{n}}^{-3}} \, d\rho' \, d\varphi' \, d\rho \, d\varphi, \quad (390)$$

with a projection to the Cartesian basis ( $\mathbf{F} = F_x \mathbf{e}_x + F_y \mathbf{e}_y + F_z \mathbf{e}_z$ ). Substituting into (376):  $\mathbf{B}_{E\rho}$  from (343) and (344), then  $\mathbf{B}_{E\varphi}$  from (345) and (346) gives

$$F_z = \frac{M_z M'_z \mu_0}{4\pi} \left( \sum_{m,\dot{m}=1}^2 (-1)^{m+\dot{m}} \rho_m \rho'_m \int_{z_1}^{z_2} \int_{\varphi_1}^{\varphi_2} \int_{z'_1}^{z'_2} \int_{\varphi'_1}^{\varphi'_2} \right. \\ \times \frac{\cos(\varphi - \varphi')(z' - z)}{\hat{G}_{m,\dot{m}}^{-3}} \, d\varphi' \, dz' \, d\varphi \, dz + \sum_{m,\dot{q}=1}^2 (-1)^{m+\dot{q}} \rho_m \\ \times \int_{z_1}^{z_2} \int_{\varphi_1}^{\varphi_2} \int_{z'_1}^{z'_2} \int_{\rho'_1}^{\rho'_2} \frac{\sin(\varphi - \varphi'_q)(z' - z)}{\hat{G}_{m,\dot{q}}^{-3}} \, d\rho' \, dz' \, d\varphi \, dz \\ + \sum_{q,\dot{m}=1}^2 (-1)^{q+\dot{m}} \int_{z_1}^{z_2} \int_{\rho_1}^{\rho_2} \int_{z'_1}^{z'_2} \int_{\varphi'_1}^{\varphi'_2} \frac{\rho'_m(z - z') \sin(\varphi_q - \varphi')}{\hat{G}_{q,\dot{m}}^{-3}} \\ \times d\varphi' \, dz' \, d\rho \, dz + \sum_{q,\dot{q}=1}^2 (-1)^{q+\dot{q}} \cos(\varphi_q - \varphi'_q) \\ \left. \times \int_{z_1}^{z_2} \int_{\rho_1}^{\rho_2} \int_{z'_1}^{z'_2} \int_{\rho'_1}^{\rho'_2} (z' - z) \hat{G}_{q,\dot{q}}^3 \, d\rho' \, dz' \, d\rho \, dz \right). \quad (391)$$

The diametric components  $F_x$  and  $F_y$  can be solved using a similar process. Ideally, we want to solve all integrals of  $\mathbf{F}$  using the same method and fundamental transforms. This can be done using the aforementioned integral transforms (238)

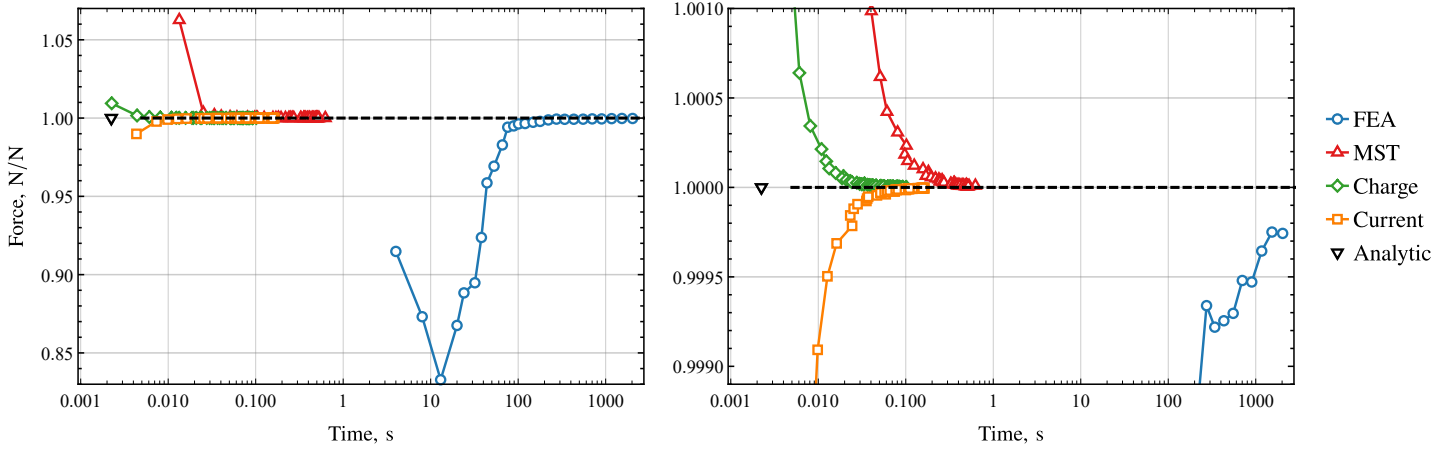


Figure 23: Analytic, semi-analytic, and numeric computation times for the force between two coaxial permanent magnet rings. The force is normalised to the analytic result of 17.4301 N. The magnetisations are  $M_z = 800 \text{ kA/m}$  and  $M'_z = -955 \text{ kA/m}$ , with axisymmetric geometries  $\rho \in [5, 8] \text{ mm}$ ,  $\varphi \in [0, 2\pi] \text{ rad}$ ,  $z \in [5, 10] \text{ mm}$  and  $\rho' \in [5, 10] \text{ mm}$ ,  $\varphi' \in [0, 2\pi] \text{ rad}$ ,  $z' \in [0, 4] \text{ mm}$ . The semi-analytic surface meshes are shown in Figure 24.

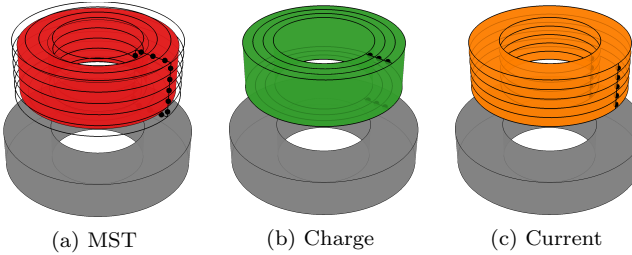


Figure 24: Alternative surface meshes of semi-analytic methods for calculating the force on the upper  $M_z$  magnet in an axisymmetric system. The magnetic field on each surface element is calculated at the black dots.

and (239) on both (389) and (390). We will only show

$$\begin{aligned} F_x &= \frac{M_z M'_z \mu_0}{4\pi} \left( \sum_{n=1}^2 (-1)^n \int_{z_1}^{z_2} \int_{\varphi_1}^{\varphi_2} \int_{\rho_1}^{\rho_2} \int_{\varphi'_1}^{\varphi'_2} \int_{\rho'_1}^{\rho'_2} \frac{\rho'(z' - z)}{\hat{G}_{n,n}^{-3}(\cos \varphi)^{-1}} d\rho' d\varphi' d\rho d\varphi dz \right. \\ &+ \sum_{m,n=1}^2 (-1)^{m+n} \int_{z_1}^{z_2} \int_{\varphi_1}^{\varphi_2} \int_{\varphi'_1}^{\varphi'_2} \int_{\rho'_1}^{\rho'_2} \frac{\rho\rho'(z - z')}{\hat{G}_{n,n}^{-3}(\cos \varphi)^{-1}} d\rho' d\varphi' d\varphi dz \\ &\left. + \sum_{n,q=1}^2 (-1)^{n+q} \int_{\varphi_1}^{\varphi_2} \int_{\rho_1}^{\rho_2} \int_{z'_1}^{z'_2} \int_{\rho'_1}^{\rho'_2} \frac{\rho'(z' - z) \sin \varphi}{\hat{G}_{n,n}^{-3}} d\rho' dz' d\rho d\varphi \right), \end{aligned} \quad (392)$$

with  $F_y$  found by inspection. This gives 8 quadruple integrals and 2 quintuple integrals to solve in order to find an analytic solution for the force. We summarise the steps:

1. Integrate all with respect to  $z$  or  $z'$  (once) using (F16), then all integrands will be of form  $f(\rho, \rho', \varphi)\hat{G}$ ;
2. Change the form of  $\hat{G}$  to an integral-series with (43) and (E10);
3. Complete all elementary integrals with respect to  $\varphi$  and/or  $\varphi'$ . This requires separating out the  $\nu = 0$  terms

prior for the single integrals, and the  $\nu = 0$  and  $\nu = 1$  terms for the double integrals to avoid singularities, e.g. (51);

4. Complete any remaining integrals that are with respect to  $\rho$ ,  $\rho'$ ,  $z$ , and/or  $z'$ , using Section 3.3.1 for radial integrals and Section 3.3.2 for axial integrals.

The final analytic result is of the form

$$\begin{aligned} \mathbf{F} &= M_z M'_z \frac{\mu_0}{4\pi} \sum_{m,n,q,\dot{m},\dot{n},\dot{q}=1}^2 (-1)^{m+n+q+\dot{m}+\dot{n}+\dot{q}} \\ &\times (\check{F}_x \mathbf{e}_x + \check{F}_y \mathbf{e}_y + \check{F}_z \mathbf{e}_z), \end{aligned} \quad (393)$$

with the summands and ancillary functions contained in Appendix H (H1, H2) due to their length. The force is complicated to compute as there are a number of nested summations. The partial sum was computed by expanding all summands in the expression, then summing each until a particular tolerance was met. As the entire expression is part of a series, the computational efficiency of the force components are very sensitive to the relative positions between magnets.

This is highlighted in Figure 25, with the evaluation time of the force components for two magnet positions shown with a vertical offset – one ‘close’ and one ‘far’. When the magnets are close, it is highlighted that this analytic solution has no practical use for both a fast and accurate computation of the force. The series would require significant treatment (as demonstrated in Section 3) to remove any closed-form terms and find an improved summation order.

Instead of deriving such complex and inefficient analytic force equations, the field solutions can provide a fast and accurate computation of the force. In addition, field-based methods are not being significantly effected by scaling the problem with additional magnets and removing axial symmetry. An example is shown in Figure 26, that models part of an axial force coupler, where the lower magnets have alternating poles. A basic discretisation procedure was used for the semi-analytical methods, as outlined in Section 6.3 and illustrated

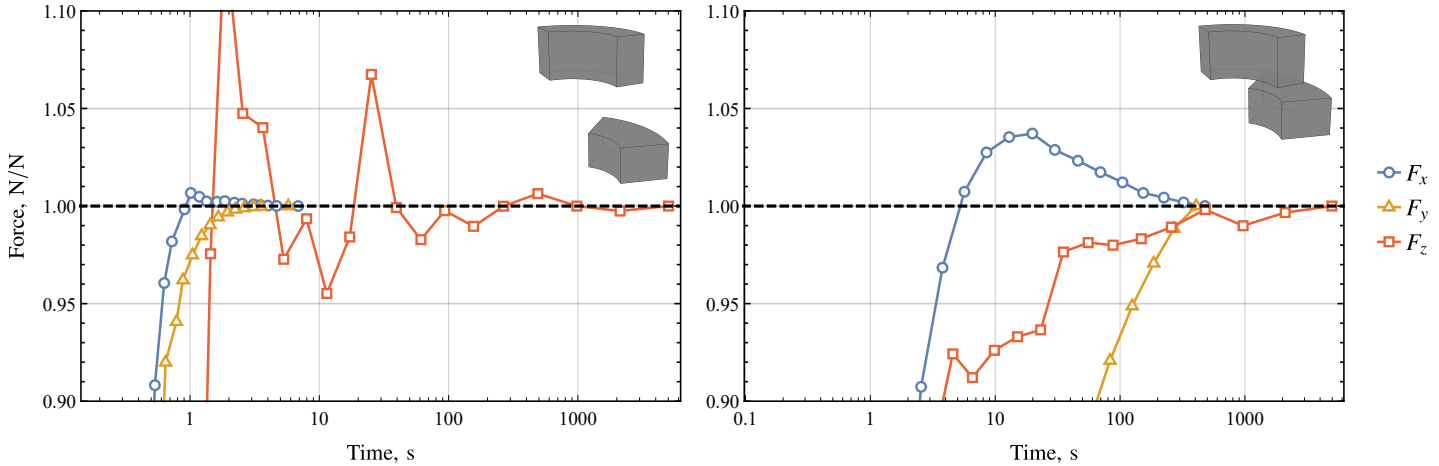


Figure 25: Partial sum convergence times of an exact analytic series for the force between axially magnetised arcs. For the figure on the left, the magnetisations are  $M_z = 800 \text{ kA/m}$  and  $M'_z = -955 \text{ kA/m}$ , with arc geometries of  $\rho \in [5, 8] \text{ mm}$ ,  $\varphi \in [-\frac{\pi}{12}, \frac{5\pi}{12}] \text{ rad}$ ,  $z \in [10, 15] \text{ mm}$  and  $\rho' \in [5, 10] \text{ mm}$ ,  $\varphi' \in [-\frac{\pi}{6}, \frac{\pi}{6}] \text{ rad}$ ,  $z' \in [0, 4] \text{ mm}$ . For the figure on the right, a single change of  $z$  to  $z \in [5, 10] \text{ mm}$  is made. Each component of  $\mathbf{F}$  was summed to an equal tolerance.

in Figure 27. The charge model was within 1% of the converged value after 1.1 s and 0.1% after 8 s, whereas FEA was within 1% after 100 s and 0.1% after 192 s. Depending on the accuracy required, the semi-analytic methods can be several orders of magnitude faster than an FEA model and simple to implement. The computational efficiency of the semi-analytic methods shown here can be significantly improved with an adaptive meshing algorithm and vectorisation of the field (and force) calculations.

## 7 Conclusion

Previous literature predominantly found (or pursued) analytic solutions in terms of Legendre (or related Heuman, Jacobi, Carlson) elliptic integrals as these special functions well-describe the field from a cylindrical geometry, are well understood in the literature, and have computational efficiency analogous to a closed-form expression. However in cases where the solution is not an elliptic integral, a solution can ‘always’ be found using a series expansion. Ideally, such a series can converge on an exact solution with a finite number of terms. These series are expanded about the singularity in the Green’s function and will have numerical issues close to this; however, this is also true for standard integration methods requiring a higher level of discretisation in such regions, or FEA with a higher mesh density required on the surface and immediate surrounding region.

In this article we provide new series solution forms dependent on geometry:  $\Xi(\nu, p)$  (disc),  $\xi(\nu, p)$  (shell),  $\tau(\nu, p)$  (volume). These summands arise from a standard  $1/r$  cylindrical harmonic expansion (toroidal, Fourier-Bessel), with terms containing the regularised beta function. The non-dimensional spatial convergence of these series is shown and implementation algorithms are provided for calculating a partial sum to a particular absolute remainder or tolerance. There exists optimisation for this calculation either through including additional convergence parameters or approximating the finite series [111]. We have ensured that where a series solution

is required, the series only forms a part of the solution: the closed-form functions and/or Legendre elliptic integrals, together with a few terms of the series provide an accurate ‘far-field’ result. More terms are required in the ‘near-field’, with such spatial definitions provided by this article. A few terms may only be required for a parametric study [112], with a low tolerance or remainder for assessing a large region, before narrowing down.

To the authors knowledge, we show the first analytic solutions to a cylindrical arc permanent magnet with uniform radial magnetisation, a disc with a uniform azimuthal current density, and a cylindrical arc with a uniform azimuthal current. A significantly simplified analytic solution is given for a cylindrical arc permanent magnet with uniform diametric magnetisation. For all magnetisations or azimuthal current densities in this compendium we ensure no removable singularities and provide reduced formulae for special cases: inside the volume, along the axis, axisymmetric and/or solid. A detailed methodology is provided for further simplification and/or investigation of some existing analytic solutions. In addition, this article provides a derivation for all cases, including a comparison with FEA (when appropriate). All analytic solutions found agreement to the original analytic integral, calculated via a numeric integration outlined in Section 3.6 and shown in the supplementary material.

The methodology herein can be extended for solving the magnetic field from more complex geometries in cylindrical or spherical coordinates, such as: azimuthal current density in a helix and toroid; diametric magnetisation of a sphere and elliptic cylinder. The series in this article can also be extended for consideration in related solutions with a conical-shape permanent magnet [113] or coil [114].

The parametrised cylindrical arc geometry seen throughout the results of Sections 4 and 5, along with surface plots, was chosen carefully to not ‘hide’ any deficiencies in the results. The solutions presented in this article are generalised and not limited to use in a local coordinate system. The magnetic field from the superposition of multiple magnets and coils can be readily modelled in axisymmetric or non-

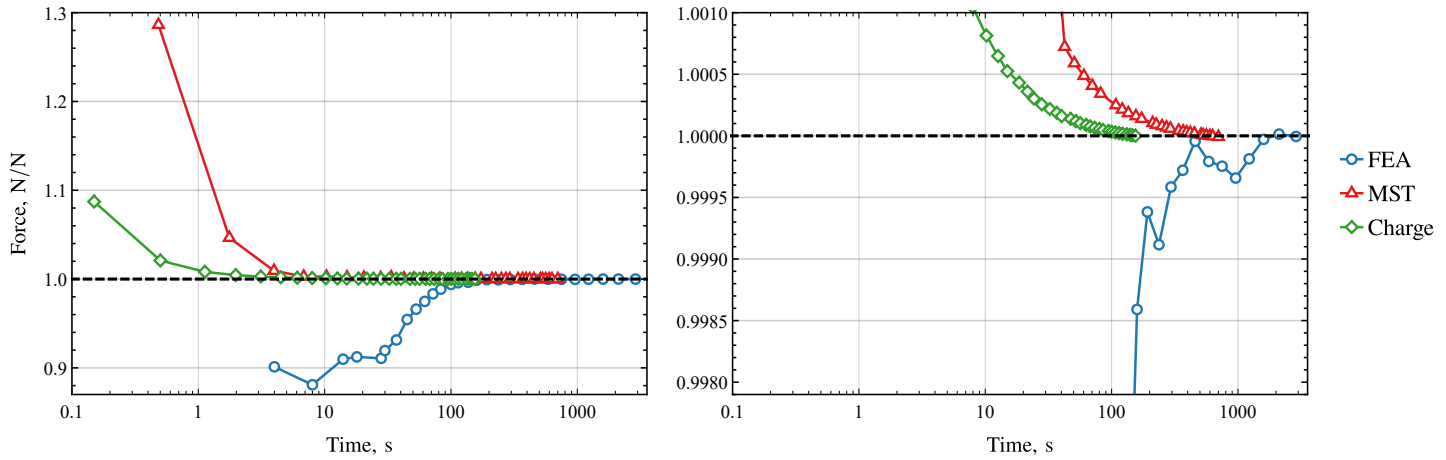


Figure 26: Semi-analytic and numeric computation times for the force  $|\mathbf{F}|$  on coaxial permanent magnet arcs. The force is normalised to the converged charge model result of  $|\mathbf{F}|=9.0011\text{ N}$  ( $F_x = -0.785\text{ N}$ ,  $F_y = 4.972\text{ N}$ ,  $F_z = -7.462\text{ N}$ ). The magnetisations are  $M_z = -955\text{ kA/m}$  and  $M_z^{(i)} = (-1)^i 955\text{ kA/m}$  for  $i = 1 \rightarrow 4$ , with asymmetric geometries  $\rho \in [5, 10]\text{ mm}$ ,  $\varphi \in [-\frac{3\pi}{32}, \frac{11\pi}{32}]\text{ rad}$ ,  $z \in [6, 11]\text{ mm}$  and  $\rho' \in [5, 10]\text{ mm}$ ,  $\varphi'^{(i)} \in [\frac{\pi}{32}, \frac{15\pi}{32}] + (i-1)\frac{\pi}{2}\text{ rad}$  for  $i = 1 \rightarrow 4$ ,  $z' \in [0, 5]\text{ mm}$ . The semi-analytic surface meshes are shown in Figure 27. The current model is not shown for clarity as the convergence is poor for this particular geometry and is alternating about 1: the normalised force remains within  $1 \pm 0.01$  after 340s.

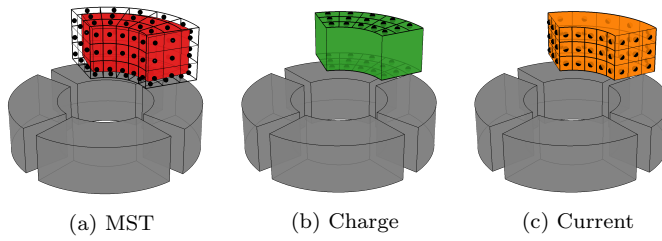


Figure 27: Alternative surface meshes of semi-analytic methods for calculating the force on the upper  $M_z$  magnet in a non-axisymmetric system. The magnetic field on each surface element is calculated at the black dots.

axisymmetric systems, such as linear or rotary permanent magnet machines with a multipole array.

The work in this article is reproducible with an example using each equation provided in both the supplemental material and an online repository [115] (Appendix I).

## Support

This work was supported in part by the Advanced Electromagnetics Group; in part by the Australian Government Research Training Program Scholarship; and in part by the Faculty of SET, University of Adelaide.

## Acknowledgements

The authors thank James Vidler for indulging numerous lengthy discussions on special functions — amongst the other mathematical topics covered in this article. The authors appreciate the articulate and detailed comments provided by the reviewers that improved the manuscript quality.

## References

- [1] N. Ha-Van, C. Simovski, F. Cuesta, P. Jayathurathnage, S. Tretyakov, *Physical Review Applied* **2023**, *20*, 1 014044.
- [2] M. Boyvat, M. Sitti, *Advanced Science* **2021**, *8*, 17 2101198.
- [3] S. Brooks, G. Mahler, J. Cintorino, J. Tuozzolo, R. Michnoff, *Physical Review Accelerators and Beams* **2020**, *23*, 11 112401.
- [4] M. Packer, P. Hobson, N. Holmes, J. Leggett, P. Glover, M. Brookes, R. Bowtell, T. Fromhold, *Physical Review Applied* **2021**, *15*, 6 064006.
- [5] A. Ramos-Sebastian, S. Hwang, S. H. Kim, *Advanced Science* **2022**, *9*, 23 2201968.
- [6] Y. Wu, S. Yakov, A. Fu, G. Yossifon, *Advanced Science* **2023**, *10*, 8 2204931.
- [7] R. Engel-Herbert, T. Hesjedal, *Journal of Applied Physics* **2005**, *97*, 7.
- [8] R. Ravaud, G. Lemarquand, *Progress in Electromagnetics Research* **2009**, *98* 207.
- [9] G. Akoun, J.-P. Yonnet, *IEEE Transactions on Magnetics* **1984**, *20*, 5 1962.
- [10] J. Janssen, J. Paulides, E. Lomonova, *COMPEL - The international journal for computation and mathematics in electrical and electronic engineering* **2010**, *29*, 4 984.
- [11] C. Rubeck, J.-P. Yonnet, H. Allag, B. Delinchant, O. Chadebec, *IEEE Transactions on Magnetics* **2013**, *49*, 1 144.

- [12] J. L. O'Connell, W. S. Robertson, B. S. Cazzolato, *Journal of Magnetism and Magnetic Materials* **2020**, *510* 166894.
- [13] F. Olver, D. Lozier, R. Boisvert, C. Clark, *The NIST Handbook of Mathematical Functions*, Cambridge University Press, New York, NY, **2010**.
- [14] H. Bateman, A. Erdélyi, *Higher transcendental functions*, volume 1, McGraw-Hill Book Company, **1953**.
- [15] I. S. Gradshteyn, I. M. Rhyzhik, *Table of integrals, series, and products*, Elsevier, **2014**.
- [16] J. L. Synge, *Classical Dynamics*, Springer Berlin Heidelberg, Berlin, Heidelberg, **1960**.
- [17] E. P. Furlani, *Permanent Magnet and Electromechanical Devices: Materials, Analysis, and Applications*, Electromagnetism. Elsevier Science, **2001**.
- [18] P. M. Morse, H. Feshbach, *Methods of theoretical physics*, volume 1 & 2 of *International series in pure and applied physics*, McGraw-Hill, New York, **1953**.
- [19] J. Pearson, S. Olver, M. Porter, *Numerical Algorithms* **2017**, *74*, 3 821.
- [20] M. Forbes, W. S. P. Robertson, A. C. Zander, J. J. H. Paulides, *IEEE Transactions on Magnetics* **2021**, *57*, 2 1.
- [21] J. M. D. Coey, *IEEE Transactions on Magnetics* **2011**, *47*, 12 4671.
- [22] A. R. Insinga, R. Bjørk, A. Smith, C. R. H. Bahl, *Phys. Rev. Appl.* **2016**, *5* 064014.
- [23] A. Insinga, A. Smith, C. Bahl, K. Nielsen, R. Bjørk, *Phys. Rev. Appl.* **2019**, *12* 064034.
- [24] P. F. Byrd, *Handbook of elliptic integrals for engineers and scientists*, Springer-Verlag, Berlin, New York, 2d ed. edition, **1971**.
- [25] M. Sagawa, S. Fujimura, N. Togawa, H. Yamamoto, Y. Matsuura, *Journal of Applied Physics* **1984**, *55*, 6 2083.
- [26] J. J. Croat, J. F. Herbst, R. W. Lee, F. E. Pinkerton, *Journal of Applied Physics* **1984**, *55*, 6 2078.
- [27] K. Halbach, *Nuclear Instruments and Methods In Physics Research* **1981**, *187*, 1 109.
- [28] K. Halbach, *Nuclear Instruments and Methods* **1980**, *169*, 1 1 .
- [29] J. P. Blewett, *Journal of Applied Physics* **1947**, *18*, 11 968.
- [30] C. L. Bartberger, *Journal of Applied Physics* **1950**, *21*, 11 1108.
- [31] W. A. Perkins, J. C. Brown, *Journal of Applied Physics* **1964**, *35*, 11 3337.
- [32] M. W. Garrett, *Journal of Applied Physics* **1963**, *34*, 9 2567.
- [33] S. Babic, *Physics* **2021**, *3*, 4 1054.
- [34] R. Bulirsch, *Numerische Mathematik* **1965**, *7*, 1 78.
- [35] R. Bulirsch, *Numerische Mathematik* **1969**, *13*, 4 305.
- [36] B. Carlson, *Journal of Research of the National Institute of Standards and Technology* **2002**, *107*, 5 413.
- [37] T. Fukushima, *Journal of Computational and Applied Mathematics* **2012**, *236*, 7 1961.
- [38] N. Derby, S. Olbert, *American Journal of Physics* **2010**, *78*, 3 229.
- [39] J. P. Boyd, *Applied Mathematics and Computation* **2012**, *218*, 13 7005.
- [40] E. Furlani, *Journal of Magnetism and Magnetic Materials* **1994**, *135*, 2 205.
- [41] E. Furlani, S. Reznik, A. Kroll, *IEEE Transactions on Magnetics* **1995**, *31*, 1 844.
- [42] E. Furlani, S. Reznik, W. Janson, *IEEE Transactions on Magnetics* **1994**, *30*, 5 2916.
- [43] F. Masiero, E. Sinibaldi, *Advanced Science* **2023**, *10*, 2301033.
- [44] J. P. Selvaggi, S. Salon, O.-M. Kwon, M. V. K. Chari, *IEEE Transactions on Magnetics* **2007**, *43*, 10 3833.
- [45] A. Caciagli, R. J. Baars, A. P. Philipse, B. W. Kuipers, *Journal of Magnetism and Magnetic Materials* **2018**, *456* 423.
- [46] V. T. Nguyen, T.-F. Lu, *Progress In Electromagnetics Research C* **2018**, *87* 163.
- [47] F. Slanovc, M. Ortner, M. Moridi, C. Abert, D. Suess, *Journal of Magnetism and Magnetic Materials* **2022**, *559* 169482.
- [48] R. Ravaud, G. Lemarquand, V. Lemarquand, C. Depollier, *Progress In Electromagnetics Research B* **2009**, *13* 1.
- [49] R. Ravaud, G. Lemarquand, V. Lemarquand, *Progress In Electromagnetics Research B* **2010**, *24* 17.
- [50] M. Fontana, F. Salsedo, M. Bergamasco, *Sensors (Basel, Switzerland)* **2013**, *13* 7618.
- [51] K. Nielsen, R. Bjørk, *Journal of Magnetism and Magnetic Materials* **2020**, *507* 166799.
- [52] R. Ravaud, G. Lemarquand, V. Lemarquand, C. Depollier, *IEEE Transactions on Magnetics* **2008**, *44*, 8 1982.
- [53] S. Babic, C. Akyel, *Progress In Electromagnetics Research C* **2008**, *5* 71.

- [54] H. Rakotoarison, J.-P. Yonnet, B. Delinchant, *IEEE Transactions on Magnetics* **2007**, *43*, 4 1261.
- [55] C. Heuman, *Journal of Mathematics and Physics* **1941**, *20*, 1-4 127.
- [56] J. Selvaggi, S. Salon, M. Chari, *PIERS Proceedings* **2010**, *244*.
- [57] R. Ravaud, G. Lemarquand, V. Lemarquand, *IEEE Transactions on Magnetics* **2009**, *45*, 7 2920.
- [58] R. Ravaud, G. Lemarquand, V. Lemarquand, C. Depollier, *Progress in Electromagnetics Research* **2008**, *88* 307.
- [59] R. Ravaud, G. Lemarquand, *Progress in Electromagnetics Research* **2009**, *95* 309.
- [60] R. Ravaud, G. Lemarquand, *Progress In Electromagnetics Research B* **2009**, *13* 309.
- [61] B. Azzerboni, G. Saraceno, E. Cardelli, *IEEE Transactions on Magnetics* **1998**, *34*, 5 2601.
- [62] E. Durand, *Electrostatique*, volume 1, Masson, Paris, France, **1964**.
- [63] F. Reich, O. Stahn, W. Muller, *Continuum Mechanics and Thermodynamics* **2016**, *28*, 5 1435.
- [64] E. A. Ponce, S. B. Leeb, *IEEE Transactions on Magnetics* **2020**, *56*, 3 1.
- [65] U. Ausserlechner, *Progress In Electromagnetics Research B* **2012**, *38* 71.
- [66] R. Ravaud, G. Lemarquand, S. Babic, V. Lemarquand, C. Akyel, *IEEE Transactions on Magnetics* **2010**, *46*, 9 3585.
- [67] F. Maurer, B. Kawkabani, J. Kristiansen Nøland, *IEEE Transactions on Magnetics* **2020**, *56*, 7 1.
- [68] J. P. Selvaggi, S. J. Salon, M. V. K. Chari, *IEEE Transactions on Magnetics* **2010**, *46*, 10 3715.
- [69] T. Fukushima, *Celestial Mechanics and Dynamical Astronomy* **2009**, *105*, 4 305.
- [70] T. Fukushima, *Numerische Mathematik* **2010**, *116*, 4 687.
- [71] C. Snow, *Magnetic fields of cylindrical coils and annular coils.*, Number ii, 29 p. in National Bureau of Standards applied mathematics series ;38. U.S. Govt. Print. Off., Washington, **1953**.
- [72] J. Conway, *IEEE Transactions on Magnetics* **2001**, *37*, 4 2977.
- [73] L. Urankar, *IEEE Transactions on Magnetics* **1980**, *16*, 5 1283.
- [74] J. D. Jackson, *Classical electrodynamics*, Wiley, New York, **1962**.
- [75] W. R. Smythe, *Static and dynamic electricity*, International series in pure and applied physics. McGraw-Hill, New York, 3 edition, **1967**.
- [76] L. Urankar, *IEEE Transactions on Magnetics* **1990**, *26*, 3 1171.
- [77] Y. Chu, *IEEE Transactions on Magnetics* **1998**, *34*, 2 502.
- [78] M. Alberto González, D. Elám Cárdenas, *IEEE Access* **2021**, *9* 7483.
- [79] M. Prantner, N. Parspour, *Journal of Magnetism and Magnetic Materials* **2021**, *517* 167365.
- [80] P. Granum, M. L. Madsen, J. T. K. McKenna, D. L. Hodgkinson, J. Fajans, *Nuclear Instruments and Methods in Physics Research Section A: Accelerators, Spectrometers, Detectors and Associated Equipment* **2022**, *1034* 166706.
- [81] R. Jackson, *IEEE Transactions on Electron Devices* **1999**, *46*, 5 1050.
- [82] S. Babic, C. Akyel, In *Proceedings of 1997 Asia-Pacific Microwave Conference*, volume 1. **1997** 201–204.
- [83] J. Conway, *Monthly Notices Of The Royal Astronomical Society* **2000**, *316*, 3 540.
- [84] S. H. Callaghan, Edmund E.; Maslen, The magnetic field of a finite solenoid, Technical report, NASA, **1960**, URL <https://ntrs.nasa.gov/citations/19980227402>.
- [85] P. Martín-Luna, B. Gimeno, D. González-Iglesias, D. Esperante, C. Blanch, N. Fuster-Martínez, P. Martínez-Reviriego, J. Fuster, *IEEE Transactions on Magnetics* **2023**, *59*, 4 1.
- [86] L. Urankar, *IEEE Transactions on Magnetics* **1982**, *18*, 3 911.
- [87] J. Conway, *IEEE Transactions on Magnetics* **2006**, *42*, 5 1538.
- [88] L. Forbes, S. Crozier, D. Doddrell, *IEEE Transactions on Magnetics* **1997**, *33*, 5 4405.
- [89] D. Zhang, C. S. Koh, *IEEE Transactions on Magnetics* **2012**, *48*, 1 62.
- [90] V. Danilov, M. Ianovici, *Nuclear Instruments and Methods* **1971**, *94*, 3 541.
- [91] S. Babic, Z. Andjelic, B. Krstajic, S. Salon, *IEEE Transactions on Magnetics* **1988**, *24*, 6 3162.
- [92] R. Ravaud, G. Lemarquand, V. Lemarquand, S. Babic, C. Akyel, *Journal of Electromagnetic Waves and Applications* **2010**, *24*, 10 1405.
- [93] L. Urankar, *IEEE Transactions on Magnetics* **1982**, *18*, 6 1860.

- [94] B. Azzerboni, E. Cardelli, M. Raugi, A. Tellini, G. Tina, *IEEE Transactions on Magnetics* **1993**, *29*, 3 2090.
- [95] F. Maurer, B. Kawkabani, J. K. Nøland, *IEEE Transactions on Magnetics* **2020**, *56*, 2 1.
- [96] Q.-G. Lin, *European Journal of Physics* **2021**, *42*, 3 035206.
- [97] V. Labinac, N. Erceg, D. Kotnik-Karuza, *American Journal of Physics* **2006**, *74*, 7 621.
- [98] A. P. Telegin, N. I. Klevets, *Journal of Magnetism and Magnetic Materials* **2004**, *277*, 3 257.
- [99] D. T. E. H. van Casteren, J. J. H. Paulides, E. A. Lomonova, *IEEE Transactions on Magnetics* **2017**, *53*, 11 1.
- [100] M. Abramowitz, I. Stegun, *Handbook of mathematical functions with formulas, graphs, and mathematical tables*, U S Department of Commerce, Washington, D.C., **1972**.
- [101] B. Carlson, *Journal of symbolic computation* **1999**, *28*, 6 739.
- [102] E. Jahnke, *Tables of higher functions*, McGraw-Hill, New York, 6th ed. rev / by friedrich losch edition, **1960**.
- [103] T. Fukushima, *Journal of Computational and Applied Mathematics* **2011**, *235*, 14 4140.
- [104] H. S. Cohl, A. R. P. Rau, J. E. Tohline, D. A. Browne, J. E. Cazes, E. I. Barnes, *Phys. Rev. A* **2001**, *64* 052509.
- [105] H. Exton, *Multiple hypergeometric functions and applications*, E. Horwood, Chichester, Eng, **1976**.
- [106] E. R. Hansen, *A table of series and products*, Prentice-Hall, **1975**.
- [107] D. J. Jeffrey, A. D. Rich, *ACM Trans. Math. Softw.* **1994**, *20*, 1 124–135.
- [108] J. Stewart, *Calculus*, Cengage Learning, Australia, eighth edition, metric version. edition, **2016**.
- [109] J. A. Stratton, *Electromagnetic theory*, International series in physics. McGraw-Hill, New York, 1st ed. edition, **1941**.
- [110] W. Robertson, B. Cazzolato, A. Zander, *IEEE Transactions on Magnetics* **2011**, *47*, 8 2045.
- [111] S. Lubkin, *Journal of Research of the National Bureau of Standards* **1952**, *48*, 3 228.
- [112] J. S. Agashe, D. P. Arnold, *Journal of Physics D: Applied Physics* **2008**, *41*, 10 105001.
- [113] S. Hart, K. Hart, J. P. Selvaggi, *IEEE Transactions on Magnetics* **2020**, *56*, 7 1.
- [114] M. Smith, N. Fokas, K. Hart, S. I. Babic, J. P. Selvaggi, *Progress In Electromagnetics Research B* **2021**, *90* 1.
- [115] <https://github.com/AUMAG/mag-cyl-field>, **2024**.
- [116] C. Truesdell, R. Toupin, *The Classical Field Theories*, volume III/1, Springer Berlin Heidelberg, **1960**.
- [117] A. Kovetz, *The principles of electromagnetic theory / Attay Kovetz.*, Cambridge University Press, Cambridge [England] ; New York, **1990**.
- [118] C.-t. Tai, *Dyadic Green's functions in electromagnetic theory*, The Intext monograph series in electrical engineering. IEEE Press, Scranton, 2 edition, **1993**.
- [119] G. L. Lamb, *Introductory applications of partial differential equations with emphasis on wave propagation and diffusion* G.L. Lamb, Jr., Wiley, New York, **1995**.
- [120] M. Liu, K. Stierstadt, *Thermodynamics, Electrodynamics, and Ferrofluid Dynamics*, Springer Berlin Heidelberg, Berlin, Heidelberg, **2009**.
- [121] G. N. Watson, *A treatise on the theory of Bessel functions*. 2nd ed, Cambridge University Press, **1966**.
- [122] G. Eason, B. Noble, I. N. Sneddon, *Philosophical transactions of the Royal Society of London. Series A: Mathematical and physical sciences* **1955**, *247*, 935 529.
- [123] N. M. Temme, *Special functions an introduction to the classical functions of mathematical physics*, Wiley, New York, **1996**.
- [124] R. B. Paris, *Journal of Classical Analysis* **2013**, *2*, 2 183.
- [125] N. M. Temme, *Journal of Computational and Applied Mathematics* **2003**, *153*, 1-2 441.
- [126] M. Cvitkovic, A.-S. Smith, J. Pande, *Journal of Physics A: Mathematical and Theoretical* **2017**, *50*, 26 24.
- [127] H. Bateman, A. Erdélyi, *Higher transcendental functions*, volume 2, McGraw-Hill Book Company, **1953**.
- [128] G. Labahn, M. Mutrie, Reduction of elliptic integrals to legendre normalform, Technical Report 97-21, Waterloo, Ontario, **1997**.

## A A Review of background theory

Electromagnetic theory presented in this article is reproduced from the classic texts [116, 109, 18, 74]. A modern summary of the theory is given by [17, §3][117, §3-4]. The formulation of solutions to partial differential equations is well-covered in [118, 119]. This section covers the relevant theory to be applied in analytic formulations to modern problems in engineering and computational physics. All models are included in this section as they are all used within this article toward analytic solutions, dependent on geometry.

If there is bound current density  $\mathbf{J}$  within a volume, the induced magnetisation  $\mathbf{M}_J$  can be represented entirely by a vector potential  $\mathbf{A}$ . Conversely, if there is a bound ‘magnetic’ charge density  $\varrho$  within the volume, the induced magnetisation  $\mathbf{M}_\varrho$  can be represented entirely by a scalar potential

## A.1 Equivalent current distribution (current model)

$\phi$ . The bound densities  $\{\mathbf{J}, \varrho\}$  are not fundamental entities, and are often referred to as equivalent (fictitious) current and charge, in the (Amperian) current and (Coulombian) charge models [17], respectively.

At a macroscopic scale, it can be assumed that at a point in time, the global effect from all sources of magnetic and electric fields have propagated a region. This static assumption removes the time dependence in Maxwell's equations, decoupling the magnetic  $\{\mathbf{B}, \mathbf{H}\}$  and electric field  $\{\mathbf{E}, \mathbf{D}\}$  equations. Maxwell's magnetostatic equations, with no free sources of current or charge are:

$$\nabla \times \mathbf{H} = 0 \quad (\text{A1})$$

$$\nabla \times \mathbf{E} = 0 \quad (\text{A2})$$

$$\nabla \cdot \mathbf{B} = 0 \quad (\text{A3})$$

$$\nabla \cdot \mathbf{D} = 0. \quad (\text{A4})$$

To show equivalence, we adopt the Heaviside-Lorentz system of units [120]; in this approach, the magnetic and electric fields are regularised (Appendix C) to have equivalent base SI units of  $\sqrt{\text{J/m}^3}$ . In free space  $\hat{\mathbf{B}} = \hat{\mathbf{H}}$  and  $\hat{\mathbf{E}} = \hat{\mathbf{D}}$ , where the fields would otherwise be differentiated by the permeability  $\mu_0$  and permittivity  $\epsilon_0$  constants, respectively. To remove the auxiliary fields  $\mathbf{H}$  and  $\mathbf{D}$ , the constitutive field relations in matter

$$\hat{\mathbf{M}}_J = \hat{\mathbf{B}} - \hat{\mathbf{H}} \quad (\text{A5}) \quad \hat{\mathbf{M}}_\varrho \equiv \hat{\mathbf{P}} = \hat{\mathbf{D}} - \hat{\mathbf{E}} \quad (\text{A6})$$

are substituted respectively into (A1) and (A4) to give Maxwell's magnetostatic equations in matter:

$$\nabla \times \hat{\mathbf{B}} = \nabla \times \hat{\mathbf{M}}_J \quad (\text{A7}) \quad \nabla \times \hat{\mathbf{E}} = 0 \quad (\text{A8})$$

$$\nabla \cdot \hat{\mathbf{B}} = 0 \quad (\text{A9}) \quad \nabla \cdot \hat{\mathbf{E}} = -\nabla \cdot \hat{\mathbf{M}}_\varrho. \quad (\text{A10})$$

Further, introduction of the vector  $\mathbf{A}$  and scalar  $\phi$  potentials

$$\hat{\mathbf{B}} = \nabla \times \hat{\mathbf{A}} \quad (\text{A11}) \quad \hat{\mathbf{H}} \equiv \hat{\mathbf{E}} = -\nabla \hat{\phi} \quad (\text{A12})$$

into equations (A7)-(A10) gives the governing equations

$$\nabla \times \nabla \times \hat{\mathbf{A}} = \nabla \times \hat{\mathbf{M}}_J \quad (\text{A13}) \quad \nabla^2 \hat{\phi} = \nabla \cdot \hat{\mathbf{M}}_\varrho, \quad (\text{A14})$$

noting use of the vector Laplacian identity (F1) and Lorenz gauge  $\nabla \cdot \mathbf{A} = 0$  ( $\nabla^2 \hat{\mathbf{A}} = -\nabla \times \hat{\mathbf{M}}_J$ ). A general solution to the vector (A13) and scalar (A14) Poisson equations are found using

$$\nabla \times \nabla \times \mathcal{G}(\mathbf{r}, \mathbf{r}') = -\nabla \times [\mathcal{I} \delta(\mathbf{r} - \mathbf{r}')] \quad (\text{A15})$$

$$\nabla^2 G(\mathbf{r}, \mathbf{r}') = \delta(\mathbf{r} - \mathbf{r}'), \quad (\text{A16})$$

where  $\mathcal{G} = \nabla \times [\mathcal{I} G(\mathbf{r}, \mathbf{r}')$ ] is the dyadic Green's function [18, pg.1788],  $\mathcal{I}$  is the idemfactor,  $G$  is the scalar Green's function with free space solution [119, §4]

$$G(\mathbf{r}, \mathbf{r}') = -\frac{1}{4\pi |\mathbf{r} - \mathbf{r}'|} \quad (\text{A17})$$

if  $\mathbf{r} \neq \mathbf{r}'$ ,  $\mathbf{r}$  is a field point, and  $\mathbf{r}'$  is a source point. Useful eigenvalue expansions to (A17) may also be employed in cylindrical [18, pg.1263] or spherical [18, pg.1274] coordinates.

Considering Maxwell's equations between two regions with varying properties, the normal and tangential components of

the field are [109, pg.37]

$$\mathbf{n} \cdot [\nabla \times \hat{\mathbf{A}}] = 0 \quad (\text{A18}) \quad [\nabla \hat{\phi}] \times \mathbf{n} = 0 \quad (\text{A19})$$

$$\mathbf{n} \times [\nabla \times \hat{\mathbf{A}}] = \hat{\mathbf{M}}_J \times \mathbf{n} \quad (\text{A20}) \quad [\nabla \hat{\phi}] \cdot \mathbf{n} = \hat{\mathbf{M}}_\varrho \cdot \mathbf{n} \quad (\text{A21})$$

where  $[\mathbf{a}]$  is a jump discontinuity across two sides of a surface  $S$  ( $a_+ - a_-$ ), and  $\mathbf{n}$  is the outward facing normal. The vector and scalar potentials must additionally satisfy both the inhomogeneous and homogeneous equations

$$\begin{aligned} \nabla \times \nabla \times \hat{\mathbf{A}} &= \hat{\mathbf{J}}, & \nabla^2 \hat{\phi} &= \hat{\varrho}, & \text{for } \mathbf{r} \text{ inside } S, \\ \nabla \times \nabla \times \hat{\mathbf{A}} &= 0, & \nabla^2 \hat{\phi} &= 0, & \text{for } \mathbf{r} \text{ outside } S. \end{aligned}$$

The resulting integral formulations only have closed-form solutions if the magnetisation and permeability are not a function of  $\mathbf{r}'$ . In cases with a high gradient or a jump discontinuity, the integral can be split at these region boundaries.

### A.1 Equivalent current distribution (current model)

The current model represents a permanent magnet as a distribution of closed current loops, arranged perpendicular to the magnetisation. This bound current must resolve, at least in part, to a surface current distribution over the region boundary. Derivation of the current model from the vector potential proceeds.

To find a form to apply the divergence theorem (F9), (A13) is multiplied by  $\mathcal{G}$ , then subtracted from (A15) multiplied by  $\mathbf{A}$ , and both sides integrated, to give

$$\begin{aligned} &\int_V \mathcal{G}(\mathbf{r}, \mathbf{r}') \cdot [\nabla' \times \hat{\mathbf{M}}_J(\mathbf{r}')] d\mathbf{v}' \\ &+ \int_V \left\{ \hat{\mathbf{A}}(\mathbf{r}') \cdot [\nabla' \times \nabla' \times \mathcal{G}(\mathbf{r}, \mathbf{r}')] \right. \\ &\quad \left. - \mathcal{G}(\mathbf{r}, \mathbf{r}') \cdot [\nabla' \times \nabla' \times \hat{\mathbf{A}}(\mathbf{r}')] \right\} d\mathbf{v}' \\ &= - \int_V \hat{\mathbf{A}}(\mathbf{r}') \cdot \{\nabla' \times [\mathcal{I} \delta(\mathbf{r} - \mathbf{r}')] \} d\mathbf{v}', \end{aligned} \quad (\text{A22})$$

where  $\nabla'$  is operating on the primed, or source coordinates. Applying (F11) to the left-hand side of (A22) and (F14) to the right,

$$\begin{aligned} &\int_V \mathcal{G} \cdot (\nabla' \times \hat{\mathbf{M}}_J) d\mathbf{v}' \\ &+ \oint_S \left\{ \mathcal{G} \cdot [\mathbf{n} \times (\nabla' \times \hat{\mathbf{A}})] + (\nabla' \times \mathcal{G}) \cdot (\mathbf{n} \times \hat{\mathbf{A}}) \right\} d\mathbf{s}' \\ &= - \int_V (\nabla' \times \hat{\mathbf{A}}) \cdot (\mathcal{I} \delta) d\mathbf{v}' - \oint_S (\hat{\mathbf{A}} \times \mathbf{n}) \cdot (\mathcal{I} \delta) d\mathbf{s}' \\ &= - \begin{cases} \nabla \times \hat{\mathbf{A}}(\mathbf{r}), & \text{for } \mathbf{r} \text{ inside } S, \\ \hat{\mathbf{A}}(\mathbf{r}) \times \mathbf{n}, & \text{for } \mathbf{r} \text{ on } S, \\ 0, & \text{for } \mathbf{r} \text{ outside } S. \end{cases} \end{aligned} \quad (\text{A23})$$

Equation (A23) simplifies with both (A20) and the Dirichlet boundary condition  $\mathbf{n} \times [\mathbf{A}] = 0$ , that comes from (A18) and

## A.2 Equivalent charge distribution (charge model)

application of Stokes' theorem (F8), to give

$$-\nabla \times \hat{\mathbf{A}} = \int_V \mathcal{G} \cdot (\nabla' \times \hat{\mathbf{M}}_J) dv' + \oint_S \mathcal{G} \cdot (\hat{\mathbf{M}}_J \times \mathbf{n}) ds'. \quad (\text{A24})$$

The unprimed curls on both sides of (A24) can be taken out of the primed integral, and then removed as if  $\nabla \times \mathbf{A} = \mathcal{G} \cdot \mathbf{b}$  then  $\mathbf{A} = G\mathbf{b} + \nabla a$  for some arbitrary function of position  $a$  and vector  $\mathbf{b}$ , and knowing  $\mathbf{A}$  is uniquely defined by the Lorenz gauge [74, pg.140]. This gives the magnetic vector potential

$$\hat{\mathbf{A}} = - \int_V G(\nabla' \times \hat{\mathbf{M}}_J) dv' - \oint_S G(\hat{\mathbf{M}}_J \times \mathbf{n}) ds', \quad (\text{A25})$$

that is an analytic formulation for describing the magnetic field at any field point (where  $\mathbf{r} \neq \mathbf{r}'$ ) due to a magnetisation vector. It follows (A25), from (A11) and using (F4)

$$\hat{\mathbf{B}} = \int_V (\nabla' \times \hat{\mathbf{M}}_J) \times \nabla G dv' + \oint_S (\hat{\mathbf{M}}_J \times \mathbf{n}) \times \nabla G ds', \quad (\text{A26})$$

where

$$\nabla G = \frac{\mathbf{r} - \mathbf{r}'}{4\pi |\mathbf{r} - \mathbf{r}'|^3}. \quad (\text{A27})$$

Equations (A25) and (A26) are given in [109, pg. 242] and [17, pg.128].

## A.2 Equivalent charge distribution (charge model)

The charge model represents a permanent magnet as a distribution of 'magnetic' charges, arranged parallel to the magnetisation. The bound charge must resolve, at least in-part, to a surface charge distribution over the region boundary. Derivation of the charge model from the scalar potential proceeds.

With an equivalent first step as Section A.1, (A14) is multiplied by  $G$ , then subtracted from (A16) multiplied by  $\phi$ , and both sides integrated, to give

$$\begin{aligned} & \int_V \left\{ \hat{\phi}(\mathbf{r}') [\nabla'^2 G(\mathbf{r}, \mathbf{r}')] - G(\mathbf{r}, \mathbf{r}') [\nabla'^2 \hat{\phi}(\mathbf{r}')] \right\} dv' \\ & + \int_V G(\mathbf{r}, \mathbf{r}') [\nabla' \cdot \hat{\mathbf{M}}_\varrho(\mathbf{r}')] dv' = \int_V \hat{\phi}(\mathbf{r}') \delta(\mathbf{r} - \mathbf{r}') dv'. \end{aligned} \quad (\text{A28})$$

Equation (A28) simplifies using (F13)

$$\begin{aligned} & \int_V G(\nabla' \cdot \hat{\mathbf{M}}_\varrho) dv' + \oint_S \{ [\hat{\phi}(\nabla' G) - G(\nabla' \hat{\phi})] \cdot \mathbf{n} \} ds' \\ & = \begin{cases} \hat{\phi}(\mathbf{r}), & \text{for } \mathbf{r} \text{ inside } S, \\ 0, & \text{for } \mathbf{r} \text{ outside } S. \end{cases} \end{aligned} \quad (\text{A29})$$

A Neumann boundary condition  $[\nabla G] \cdot \mathbf{n} = 0$  arises from the choice of  $G$ , shown from the application of the divergence theorem, as the Green's function is a solution to Laplace's equation inside  $S$ , and the outward flux over  $S$  is a constant.

In combination with (A21), this gives the magnetic scalar potential

$$\hat{\phi}(\mathbf{r}) = \int_V G(\nabla' \cdot \hat{\mathbf{M}}_\varrho) dv' - \oint_S G(\hat{\mathbf{M}}_\varrho \cdot \mathbf{n}) ds' \quad (\text{A30})$$

that is (as with (A25)) an analytic formulation for describing the magnetic field at any field point (where  $\mathbf{r} \neq \mathbf{r}'$ ) due to a magnetisation vector. It follows (A30), from (A12), that

$$\hat{\mathbf{H}} = \oint_S (\nabla G) (\hat{\mathbf{M}}_\varrho \cdot \mathbf{n}) ds' - \int_V (\nabla G) (\nabla' \cdot \hat{\mathbf{M}}_\varrho) dv', \quad (\text{A31})$$

where the unprimed operator has been brought into the integral. Equations (A30) and (A31) are given in [109, pg. 184] and [17, pg.132].

## A.3 Mixed boundary conditions (combined model)

The scalar potential formulation of the electrostatic and magnetostatic problems are mathematically equivalent for bound matter with no free charge or current density. It follows the Helmholtz theorem for magnetostatics in free space is

$$\hat{\mathbf{B}}(\mathbf{r}) = \hat{\mathbf{H}}(\mathbf{r}) = \nabla \times \hat{\mathbf{A}}(\mathbf{r}) - \nabla \hat{\phi}(\mathbf{r}). \quad (\text{A32})$$

It is typical that  $\mathbf{M}_J$  and  $\mathbf{M}_\varrho$  are only considered in isolation, where either  $\mathbf{A}$  or  $\phi$  is set equal to zero, this using either the charge or current models in a problem formulation. It is postulated that if  $\mathbf{M}_J \equiv \mathbf{M}_\varrho$  then  $\nabla \times \mathbf{A} \equiv -\nabla \phi$ . With linear matter, the magnetic field basis for each orthogonal component of the magnetisation can be solved independently using superposition; the field of a permanent magnet can be modelled as having both magnetic charge and current without loss of generality. Further, for a particular basis, basis vectors of the magnetic field can be formulated as being due to a source current or charge: the distinction is arbitrary due to the mathematical equivalence [109, pg. 228].

## A.4 Current distribution (filament model)

The filament model represents a coil as a distribution of closed current loops, analogous to the current model; however, the current is considered free as opposed to bound. This assumes the current path is always parallel to a region boundary, with no stipulation for when it is perpendicular. This allows the modelling of a complete current path as segments, that in isolation do not obey continuity.

A particular solution of (A13) from (A25) is

$$\hat{\mathbf{A}}(\mathbf{r}) = - \int_V G(\mathbf{r}, \mathbf{r}') \hat{\mathbf{J}}(\mathbf{r}') dv' \quad (\text{A33})$$

with (A26)

$$\hat{\mathbf{B}}(\mathbf{r}) = \int_V \hat{\mathbf{J}}(\mathbf{r}') \times \nabla G(\mathbf{r}, \mathbf{r}') dv', \quad (\text{A34})$$

both describing the magnetic field due to a volumetric current density  $\mathbf{J}$  with a homogeneous boundary condition  $[\hat{\mathbf{M}}_J] \times \mathbf{n} = 0$ , where  $\mathbf{J} \equiv \nabla \times \hat{\mathbf{M}}_J$ . Thus, equation (A33) is the general solution in the absence of surface current density. If

## A.5 Force models

the equivalent magnetisation  $\hat{\mathbf{M}}_J$  is uniform throughout  $V$ , then  $\mathbf{J}$  must be zero. There must also be no net flux of current emanating from the enclosed volume. This is shown by taking the divergence of (A33) and applying the divergence theorem (F9);

$$\nabla \cdot \mathbf{A} = \int_V \nabla' \cdot (G \mathbf{J}) dv' = \oint_S G \mathbf{J} \cdot \mathbf{n} da' = 0, \quad (\text{A35})$$

noting use of identity (F3) with  $\nabla \cdot \mathbf{J} = 0$  and  $\nabla G = -\nabla' G$ . Looking at the flux through a cross-section of (A33) (that is continuous), then Stoke's theorem (F8) can be applied successively as with Ampère's law, to give the current  $I$  in a filament that is in the plane orthogonal to  $\mathbf{n}$ :

$$\int_S \mathbf{J} \cdot \mathbf{n} da' = \int_S \mathbf{A} \cdot \mathbf{n} da = \oint_C \mathbf{B} \cdot d\mathbf{l} = I. \quad (\text{A36})$$

If  $\mathbf{J}$  is uniform throughout  $V$ , then any cross-section through  $V$  will have a constant current. Further, taking the limit as the cross-section reduces to a point, it becomes a filament of  $I$  along the path  $d\mathbf{l}$  of  $\mathbf{J}$ :

$$\int_V \mathbf{J} dv \rightarrow (\mathbf{J} \cdot \mathbf{n}) \int_V da d\mathbf{l} \rightarrow I \int_C d\mathbf{l}. \quad (\text{A37})$$

Therefore, a volumetric current distribution can be resolved into filaments, through a cross-section, that all close upon themselves in the volume, each with a vector potential

$$\hat{\mathbf{A}}(\mathbf{r}) = -\hat{I} \oint_C G(\mathbf{r}, \mathbf{r}') d\mathbf{l}', \quad (\text{A38})$$

and magnetic flux density, following (A26), of

$$\hat{\mathbf{B}}(\mathbf{r}) = \hat{I} \oint_C d\mathbf{l}' \times \nabla G(\mathbf{r}, \mathbf{r}'). \quad (\text{A39})$$

Equations (A38) and (A39) is often referred to as the Biot-Savart law, given in [109, pg. 231] and [17, pg.103].

## A.5 Force models

From the Lorentz force equation and using the charge and current models, the force densities over bound charge and current are:

$$\mathbf{f}_v = \hat{\varrho} \hat{\mathbf{B}}_E + (\hat{\mathbf{J}} \times \hat{\mathbf{B}}_E) \quad (\text{A40})$$

with units N/m<sup>3</sup> and substitution  $\hat{\mathbf{B}} = \hat{\mathbf{H}} \equiv \hat{\mathbf{E}}$  (A12,A32);

$$\mathbf{f}_s = \hat{\sigma} \hat{\mathbf{B}}_E + (\hat{\mathbf{K}} \times \hat{\mathbf{B}}_E) \quad (\text{A41})$$

with units N/m<sup>2</sup>. The external field  $\hat{\mathbf{B}}_E(\mathbf{r})$  in (A40) and (A41) is the superposition of all magnetic fields from all sources, excluding those from  $\{\varrho, \mathbf{J}, \sigma, \mathbf{K}\}$ . Those distributions are linked to magnetisations in the charge and current models (Sections A.1 and A.2), giving

$$\begin{aligned} \mathbf{F} &= \int_V [\hat{\varrho} \hat{\mathbf{B}}_E + (\hat{\mathbf{J}} \times \hat{\mathbf{B}}_E)] dv + \oint_S [\hat{\sigma} \hat{\mathbf{B}}_E + (\hat{\mathbf{K}} \times \hat{\mathbf{B}}_E)] da \\ &= \int_V \{[(\nabla \times \hat{\mathbf{M}}_J) \times \hat{\mathbf{B}}_E] - [(\nabla \cdot \hat{\mathbf{M}}_\varrho) \hat{\mathbf{B}}_E]\} dv \\ &\quad + \oint_S \{[(\hat{\mathbf{M}}_J \times \mathbf{n}) \times \hat{\mathbf{B}}_E] + [(\hat{\mathbf{M}}_\varrho \cdot \mathbf{n}) \hat{\mathbf{B}}_E]\} da. \end{aligned} \quad (\text{A42})$$

Equation (A42) is integrated over the field points, or unprimed coordinates. Information on the source points, in primed coordinates, is contained in  $\mathbf{B}_E$ . Alternatively, using the total field  $\mathbf{B}$  from all sources, the force can be found using the Maxwell stress tensor [74, pg.193]

$$\mathbf{F} = \oint_S [\hat{\mathbf{B}} \otimes \hat{\mathbf{B}} - \frac{1}{2}(\hat{\mathbf{B}} \cdot \hat{\mathbf{B}})\mathcal{I}] \cdot \mathbf{n} da, \quad (\text{A43})$$

with idemfactor  $\mathcal{I}$ . In (A43),  $\mathbf{B}$  cannot overlap any source of  $\{\varrho, \mathbf{J}, \sigma, \mathbf{K}\}$  as the field will be in-part undefined. To avoid any undefined cases, (A42) and (A43) can be combined, ensuring no double contributions to the force.

For a complete description of the field, it will be shown how the magnetic dipoles  $\mathbf{m}_\varrho$  and  $\mathbf{m}_J$ , respectively for the charge and current models, relate to the magnetisations  $\{\hat{\mathbf{M}}_\varrho, \hat{\mathbf{M}}_J\}$ . First, taking  $\mathbf{M}_\varrho = 0$  in (A42): using the vector triple product (F6) then permuting the terms gives a form to apply the divergence theorem (F9)

$$\begin{aligned} \mathbf{F} &= \int_V [(\nabla \times \hat{\mathbf{M}}_J) \times \hat{\mathbf{B}}_E] dv \\ &\quad + \oint_S [(\hat{\mathbf{M}}_J \cdot \hat{\mathbf{B}}_E)\mathcal{I} - \hat{\mathbf{M}}_J \otimes \hat{\mathbf{B}}_E] \cdot \mathbf{n} da. \end{aligned} \quad (\text{A44})$$

Expansion of the new volume integrand with application of (F7) gives a form that in-part will cancel the original volume integrand

$$\begin{aligned} \nabla \cdot [(\hat{\mathbf{M}}_J \cdot \hat{\mathbf{B}}_E)\mathcal{I} - \hat{\mathbf{M}}_J \otimes \hat{\mathbf{B}}_E] \\ = \hat{\mathbf{M}}_J \cdot (\nabla \hat{\mathbf{B}}_E) - \hat{\mathbf{M}}_J (\nabla \cdot \hat{\mathbf{B}}_E) - (\nabla \times \hat{\mathbf{M}}_J) \times \hat{\mathbf{B}}_E, \end{aligned} \quad (\text{A45})$$

thus with  $\nabla \cdot \mathbf{B} = 0$ ,

$$\mathbf{F} = \int_V \hat{\mathbf{M}}_J \cdot (\nabla \hat{\mathbf{B}}_E) dv. \quad (\text{A46})$$

Taking  $\mathbf{M}_J = 0$  in (A42) and permuting terms as with (A44) gives the familiar forms:

$$\mathbf{F} = \oint_S (\hat{\mathbf{B}}_E \otimes \hat{\mathbf{M}}_\varrho) \cdot \mathbf{n} da - \int_V [(\nabla \cdot \hat{\mathbf{M}}_\varrho) \hat{\mathbf{B}}_E] dv \quad (\text{A47})$$

that with expansion

$$\nabla \cdot (\hat{\mathbf{B}}_E \otimes \hat{\mathbf{M}}_\varrho) = (\nabla \hat{\mathbf{B}}_E) \cdot \hat{\mathbf{M}}_\varrho + (\nabla \cdot \hat{\mathbf{M}}_\varrho) \hat{\mathbf{B}}_E, \quad (\text{A48})$$

cancels the original volume integrand

$$\mathbf{F} = \int_V (\nabla \hat{\mathbf{B}}_E) \cdot \hat{\mathbf{M}}_\varrho dv. \quad (\text{A49})$$

From (A46) and (A49), the sum of the force on both dipoles, assuming a uniform gradient field through  $V$  is

$$\mathbf{F} = (\nabla \mathbf{B}_E) \cdot \mathbf{m}_\varrho + \mathbf{m}_J \cdot (\nabla \mathbf{B}_E), \quad (\text{A50})$$

where  $\mathbf{m}$  has units A·m<sup>2</sup> and  $\nabla \mathbf{B}_E$  in N·A<sup>-1</sup>m<sup>-2</sup>. The dipole forces are equivalent ( $\mathbf{m}_\varrho \equiv \mathbf{m}_J$ ) in cases when  $\nabla \times \mathbf{B}_E = 0$  due to the identity

$$(\nabla \mathbf{B}) \cdot \mathbf{m} = \mathbf{m} \cdot (\nabla \mathbf{B}) - \mathbf{m} \times (\nabla \times \mathbf{B}), \quad (\text{A51})$$

and this assumption also gives an equivalent alternate form

$$\mathbf{m} \cdot (\nabla \mathbf{B}) = (\mathbf{m} \cdot \nabla) \mathbf{B} + \mathbf{m} \times (\nabla \times \mathbf{B}). \quad (\text{A52})$$

## B Nomenclature

In this article summation notation is used to simplify definite integrals:

$$\int_{f_1}^{f_2} df = f \Big|_{f_1}^{f_2} = \sum_{p=1}^2 (-1)^p f_p.$$

The integrals are with respect to the cylindrical parameters  $\rho'$ ,  $\varphi'$ , and  $z'$  that have the respective index and limits:

Parameter	Index	Limit
$\rho'$	$m$	$\{\rho'_1, \rho'_2\}$
$\varphi'$	$q$	$\{\varphi'_1, \varphi'_2\}$
$z'$	$n$	$\{z'_1, z'_2\}$ .

A subscript of the index on the parameter is used to identify the respective limit substitution. For example,

$$\begin{aligned} g &= \rho' + \varphi' + z', \\ g_m &= \rho'_m + \varphi'_m + z'_m, \\ g_{n,q} &= \rho'_n + \varphi'_q + z'_n. \end{aligned}$$

For brevity, commonly occurring expressions that are replaced with variables or functions are listed in Table B.1. A summary of function forms and definitions is given in Table B.2. An electronic version of both tables can be found in the supplementary material (Appendix I).

## C Units

The fields in Heaviside-Lorentz units relate to the standard MKS units by the transformations

$$\hat{\mathbf{H}} = \mathbf{H}\sqrt{\mu_0} \quad \hat{\mathbf{E}} = \mathbf{E}\sqrt{\epsilon_0} \quad \hat{\mathbf{B}} = \mathbf{B}/\sqrt{\mu_0}$$

$$\hat{\mathbf{D}} = \mathbf{D}/\sqrt{\epsilon_0} \quad \hat{\mathbf{M}} = \mathbf{M}\sqrt{\mu_0} \quad \hat{\mathbf{P}} = \mathbf{P}/\sqrt{\epsilon_0}$$

$$\hat{\mathbf{A}} = \mathbf{A}/\sqrt{\mu_0} \quad \hat{\phi} = \phi\sqrt{\mu_0}$$

with units of  $\sqrt{\text{J/m}^3}$ . Similarly, the sources have the transforms

$$\hat{\mathbf{J}} = \mathbf{J}\sqrt{\mu_0} \quad \hat{\varrho} = \varrho/\sqrt{\epsilon_0}$$

with units of  $\sqrt{\text{J/m}^5}$ ,

$$\hat{\mathbf{K}} = \mathbf{K}\sqrt{\mu_0} \quad \hat{\sigma} = \sigma/\sqrt{\epsilon_0}$$

with units of  $\sqrt{\text{J/m}^3}$ , and

$$\hat{I} = I\sqrt{\mu_0}$$

with units of  $\sqrt{\text{J/m}}$ .

## D Algorithms

Pseudocode is provided for four algorithms used to calculate finite summations to the series solutions presented in this article (Table 3). The algorithms are informed by the limit of the

Table B.1: Defined variables and functions

Equation	Description
$\varrho = \rho + \rho'$	
$\bar{\varrho} = \rho - \rho'$	Radial difference
$\Phi = \varphi - \varphi' \equiv 2\phi - \pi$	Azimuthal difference
$Z = z - z'$	Axial difference
$\phi = \frac{1}{2}(\Phi + \pi)$	Elliptic amplitude
$\Psi =  \Phi  - \pi$	Transformed elliptic amplitude
$w^2(t) = (1 - t^2)(1 - k^2t^2)$	Elliptic radicand
$k = \sqrt{4\rho\rho'/R^2}$	Elliptic parameter
$k^2 = 4\rho\rho'/R^2$	
$\bar{k}^2 = 4\rho\rho'/\bar{R}^2$	Elliptic modulus
$a^2 = 2\rho/(\rho + L)$	
$\bar{a}^2 = 2\rho/(\rho - L)$	Elliptic characteristic
$\kappa^2 = 4\rho\rho'/\varrho^2$	
$L^2 = \rho^2 + Z^2$	
$R^2 = \varrho^2 + Z^2$	
$\bar{R}^2 = \bar{\varrho}^2 + Z^2$	
$S^2 = L + \rho'$	
$\bar{S}^2 = L - \rho'$	Radii
$T^2 = L^2 + \rho'^2$	
$\bar{T}^2 = L^2 - \rho'^2$	
$\hat{G} = 1/\sqrt{T^2 - 2\rho\rho' \cos \Phi}$	Green's function
$\mathbf{n} = [\tilde{\Phi}]$	Elliptic function staircase
$\mathbf{q} = (-1)^{\lfloor 2\tilde{\Phi} + 1 \rfloor}$	Elliptic function square wave
$\mathbf{t} = 1 - 2[\tilde{\Phi}] - \tilde{\Phi}$	Elliptic function triangle wave
$\tilde{\rho} = \rho/\rho'$	
$\tilde{Z} = Z/\rho'$	
$\tilde{\Phi} = \Phi/(2\pi)$	
$\Upsilon = \frac{Z(\rho' - \rho \cos \Phi)}{\rho \sin \Phi \hat{G}^{-1}}$	Hypergeometric/Beta moduli
$\omega = 1 + [\Phi/\pi - 1]$	Beta function staircase
$v(\nu) = \nu - 2[\nu/2]$	Even/odd conditional
$\tilde{\rho} = \rho/\rho'$	Normalised radial distance
$\tilde{Z} = Z/\rho'$	Normalised axial distance
$\tilde{\Phi} = \Phi/(2\pi)$	Normalised azimuthal angle
$\Upsilon = \frac{Z(\rho' - \rho \cos \Phi)}{\rho \sin \Phi \hat{G}^{-1}}$	Arctan argument

series and terminate after a maximum guaranteed remainder  $R$  is met (Algorithm 1,2), or a maximum tolerance  $T$  is met (Algorithm 3,4).

**Algorithm 1** Using (93) to compute a partial sum of  $\beta^{(1)}$  or  $\delta^{(1)}$  with a specified maximum remainder.

```

1: if  $\beta^{(1)}$  then                                ▷ choose series
2:   summand( $p$ ) =  $\Xi(-1, p + 1)$ 
3: else if  $\zeta^{(1)}$  then
4:   summand( $p$ ) =  $\Xi(2p, 0) \chi^{(\zeta)}(2p)$ 
5: else if  $\eta^{(1)}$  then
6:   summand( $p$ ) =  $\Xi(2p + 1, 0) \chi^{(\eta)}(2p + 1)$ 
7: else if  $\iota^{(1)}$  then
8:   summand( $p$ ) =  $\Xi(2p + 1, 0) \chi^{(\iota)}(2p + 1)$ 
9: end if                                            ▷ calculate  $\forall r$ 
10:

```

Table B.2: Function source and description

Function	Description
$F(\theta; k)$	(E19) Incomplete elliptic integral: first kind
$F(\theta; k)$	(38) Transformed elliptic integral: first kind
$K(k)$	(E23) Complete elliptic integral: first kind
$E(\theta; k)$	(E20) Incomplete elliptic integral: second kind
$E(\theta; k)$	(40) Transformed elliptic integral: second kind
$E(k)$	(E24) Complete elliptic integral: second kind
$\Pi(\theta; a, k)$	(E21) Incomplete elliptic integral: third kind
$\Pi(\theta; a, k)$	(41) Transformed elliptic integral: third kind
$\Pi(a; k)$	(E25) Complete elliptic integral: third kind
$D(\theta; k)$	(E22) Incomplete elliptic integral: Legendre type
$D(\theta; k)$	(42) Transformed elliptic integral: Legendre type
$D(k)$	(E26) Complete elliptic integral: Legendre type
$R_C(x, y)$	(174) Carlson elliptic integral: $R_F(x, y, y)$
$gd^{-1}(a)$	(174) inverse Gudermannian function
$I(\mu, \eta, \lambda)$	(E1) The Lipschitz-Hankel integral
$F(a, b; c; \lambda)$	(E6,E7) Gauss' hypergeometric function/series
$F\left(\begin{matrix} a, b \\ c \end{matrix}; \lambda\right)$	
${}_pF_q$	Generalised hypergeometric function
$\Gamma(\mu)$	(E9,E32) Gamma function
$B(\lambda; a, b)$	(E15) Incomplete beta function
$B(a, b)$	(E17) Complete beta function
$I(\lambda; a, b)$	(E16) Regularised beta function
$\binom{n}{k}$	(E30) Binomial coefficient
$(n)_k$	(E31) Pochhammer symbol
$n!$	(E34) Factorial
$\lfloor n \rfloor$	(E36) Floor function
$\lceil n \rceil$	Nearest integer function ( $\frac{1}{2} \rightarrow$ nearest even)
$\Xi(\nu, p)$	(55) Radial regularised beta summand
$\xi(\nu, p)$	(61) Axial regularised beta summand
$\tau(\nu, p)$	(89) Radial-Axial regularised beta summand
$\alpha^{(n)}$	(52,58,86) Elementary functions
$\beta^{(n)}$	(53,59,87) Single series of $\Xi(\nu, p)$ , $\xi(\nu, p)$ , $\tau(\nu, p)$
$\gamma^{(n)}$	(54,60,88) Double series of $\Xi(\nu, p)$ , $\xi(\nu, p)$ , $\tau(\nu, p)$
$\delta^{(n)}$	(119) Computational form of $\gamma^{(3)}$
$\delta^{(n)}$	(75,83,222) Reduced form of $\gamma^{(n)}$
$\chi(\nu)$	(103,110) Computational forms of $\delta^{(1)}$ , $\delta^{(2)}$
$\zeta^{(n)}(\nu)$	(76) Even/odd conditional for $\delta^{(1)}$ , $\delta^{(2)}$ , $\gamma^{(3)}$
$\eta^{(n)}(\nu)$	(104,111,120) Limit & computation term of $\chi(\nu)$
$\iota^{(n)}(\nu)$	(105,112,121) Limit & computation term of $\chi(\nu)$
$s(x)$	(106,113,122) Limit & computation term of $\chi(\nu)$
$\lambda(\nu)$	(73) Beta function square wave
$\vartheta$	(220) Fourier series summand
$\epsilon_\nu$	(235) Reduced form of $\delta^{(3)}$
$\varsigma(n, ., l)$	(43) Neumann factor
	(H2) Ancillary functions for axial arc forces

```

11: function SERIES1( $\rho'$ ,  $\rho$ ,  $\varphi'$ ,  $\varphi$ ,  $z'$ ,  $z$ ,  $R$ , summand)
12:    $p = 0$ 
13:   partial_sum = summand( $p$ )
14:    $p = p + 1$ 

```

```

15:   next_term = summand( $p$ )
16:   if  $z^2 < \frac{1}{2}$  then
17:      $L = \frac{4\rho^2\rho'^2}{T^2}$ 
18:   else
19:      $L = \frac{\rho^2}{L^2}$ 
20:   end if
21:   while  $(R \leq \frac{\text{next\_term}}{1 - L})$  and ( $p \leq \max$ ) do
22:      $p = p + 1$ 
23:     partial_sum = partial_sum + next_term
24:     next_term = summand( $p$ )
25:   end while
26:   return partial_sum                                 $\triangleright p - 1$  terms
27: end function

```

**Algorithm 2** Using (100) to compute a partial sum of  $\beta^{(2)}$  or  $\delta^{(2)}$  with a specified maximum remainder.

```

1: if  $\beta^{(2)}$  then                                          $\triangleright$  choose series
2:   summand( $p$ ) =  $\xi(-1, p + 1)$ 
3: else if  $\zeta^{(2)}$  then
4:   summand( $p$ ) =  $\xi(2p, 0) \chi^{(\zeta)}(2p)$ 
5: else if  $\eta^{(2)}$  then
6:   summand( $p$ ) =  $\xi(2p + 1, 0) \chi^{(\eta)}(2p + 1)$ 
7: else if  $\iota^{(2)}$  then
8:   summand( $p$ ) =  $\xi(2p + 1, 0) \chi^{(\iota)}(2p + 1)$ 
9: end if
10: function SERIES2( $\rho'$ ,  $\rho$ ,  $\varphi'$ ,  $\varphi$ ,  $z'$ ,  $z$ ,  $R$ , summand)           $\triangleright$  calculate  $\forall r$ 
11:    $p = 0$ 
12:   partial_sum = summand( $p$ )
13:    $p = p + 1$ 
14:   next_term = summand( $p$ )
15:    $L = \left( \frac{2\rho\rho'}{\rho^2 + \rho'^2} \right)^2$ 
16:   while  $(R \leq \frac{\text{next\_term}}{1 - L})$  and ( $p \leq \max$ ) do
17:      $p = p + 1$ 
18:     partial_sum = partial_sum + next_term
19:     next_term = summand( $p$ )
20:   end while
21:   return partial_sum                                 $\triangleright p - 1$  terms
22: end function

```

**Algorithm 3** Using (116) and (115) to compute a partial sum of  $\beta^{(3)}$  or  $\gamma^{(3)}$  with a specified tolerance.

```

1: if  $\beta^{(3)}$  then                                          $\triangleright$  choose series
2:   summand( $\nu, p$ ) =  $\binom{2+2p}{1+p} * \frac{(2+n+\frac{p}{2})_{1/2+p}}{4^p(1+p)!} \tau_{m,n}(\nu, p)$ 
3: else if  $\zeta^{(3)}$  then
4:   summand( $\nu, p$ ) =  $\frac{\chi^{(\zeta)}(2p)}{(2+p)_{1+p}} \tau(\nu, p - \frac{1}{2})$ 
5: else if  $\eta^{(3)}$  then
6:   summand( $\nu, p$ ) =  $\frac{\chi^{(\eta)}(2p+1)}{(\frac{5}{2}+p)_{3/2+p}} \tau(\nu, p)$ 
7: else if  $\iota^{(3)}$  then

```

---

```

8:   summand( $\nu, p$ ) =  $\frac{\chi^{(\nu)}(2p+1)}{(\frac{5}{2}+p)_{3/2+p}} \tau(\nu, p)$ 
9: end if
10:   $\triangleright$  calculate  $\forall r$ 
11: function SERIES3AXIAL( $\rho', \rho, \varphi', \varphi, z', z, T, \text{summand}$ )
12:    $p = 1$ 
13:    $\nu = 1$ 
14:    $L_p = \left( \frac{2\rho\rho'}{\rho^2 + \rho'^2} \right)^2$ 
15:    $L_\nu = \frac{\rho'^2}{\rho^2 + \rho'^2}$ 
16:   next_term_p = summand(0, p)
17:   next_term_nu = summand( $\nu, 0$ )
18:   while  $\left( \frac{T}{10} \leq \frac{\text{next\_term\_p}}{1 - L_p} \right)$  and ( $p \leq \max$ ) do
19:      $p = p + 1$ 
20:     next_term_p = summand(0, p)
21:   end while
22:   while  $\left( \frac{T}{10} \leq \frac{\text{next\_term\_nu}}{1 - L_\nu} \right)$  and ( $\nu \leq \max$ ) do
23:      $\nu = \nu + 1$ 
24:     next_term_nu = summand( $\nu, 0$ )
25:   end while
26:   partial_sum =  $\sum_{pp=0}^{p-1} \sum_{\nu\nu=0}^{\nu-1} \text{summand}(\nu\nu, pp)$ 
27:   return partial_sum  $\triangleright (p-1) * (\nu-1)$  terms
28: end function

```

---

**Algorithm 4** Using (93) to compute a partial sum of  $a\beta^{(1)} + b\delta^{(3)}$  in (221) or (233) with a specified tolerance.

```

1:    $\triangleright$  calculate  $\forall r$ 
2: function SERIES3RADIAL( $\rho', \rho, \varphi', \varphi, z', z, T, \text{summand}$ )
3:    $p = 0$ 
4:   initial_sum =  $\Xi(-1, p+1)$ 
5:    $p = p + 1$ 
6:   next_term =  $\Xi(-1, p+1)$ 
7:   if  $z^2 < \frac{1}{2}$  then
8:      $L = \frac{4\rho^2\rho'^2}{T^2}$ 
9:   else
10:     $L = \frac{\rho^2}{L^2}$ 
11:   end if
12:   while  $\left( T \leq \frac{\text{next\_term}}{1 - L} \right)$  and ( $p \leq \max$ ) do
13:      $p = p + 1$ 
14:     initial_sum = initial_sum + next_term
15:     next_term =  $\Xi(-1, p+1)$ 
16:   end while
17:   if  $\varphi' \in [0, 2\pi]$  then  $\triangleright$  axisymmetric
18:     partial_sum = initial_sum
19:     +  $\sum_{pp=0}^{\lfloor p/2-1 \rfloor} \binom{2+2pp}{pp} \Xi(1+2pp, 0)$ 
20:   else
21:     partial_sum =  $[\Phi + \frac{1}{2}\sin(2\Phi)] * \text{initial\_sum}$ 
22:     +  $\sum_{\nu=0}^{p-1} \Xi(\nu, 0) \sum_{pp=0}^{\lfloor \nu/2 \rfloor} \binom{1+\nu}{pp} \lambda(\nu - 2pp)$ 
23:   end if
24:   return partial_sum  $\triangleright p-1$  terms

```

---

23: **end function**

---

## E Definitions

### E.1 Beta function relationships

From the Lipschitz-Hankel integral

$$I(\mu, \eta, \lambda) = \int_0^\infty e^{-as} J_\mu(bx) J_\eta(cx) s^\lambda ds, \quad (E1)$$

a solution to Poisson's equation in 3-D cylindrical coordinates is given by (43) [18, pg.1263]. Equivalent forms to (44), that are commonly seen are [74, pg.86]:

$$I(\nu, \nu, 0) = \frac{2}{\pi} \int_0^\infty K_\nu(\rho s) I_\nu(\rho' s) \cos[(z - z')s] ds \quad (E2)$$

and [121, pg.389]

$$I(\nu, \nu, 0) = \operatorname{Re} \left[ \frac{1}{\pi \sqrt{\beta \gamma}} Q_{\nu - \frac{1}{2}}(\zeta) \right] \quad (E3)$$

and [122]

$$I(\nu, \nu, 0) = \frac{(-1)^\nu k}{\pi \sqrt{\rho \rho'}} \int_0^{\pi/2} \frac{\cos(2\nu\psi)}{\sqrt{1 - k^2 \sin^2(\psi)}} d\psi \quad (E4)$$

and [14, pg.122]

$$I(\nu, \nu, 0) = (2\pi\rho\rho'\zeta)^{-\frac{1}{2}} (2\zeta)^{-\nu} \frac{\Gamma(\nu + \frac{1}{2})}{\Gamma(\nu + 1)} \times F\left[\frac{1}{4}(2\nu + 3), \frac{1}{4}(2\nu + 1); \nu + 1; \zeta^{-2}\right], \quad (E5)$$

where  $k^2 = (4\rho\rho')/[(\rho + \rho')^2 + (z - z')^2]$  and  $\zeta = [\rho^2 + \rho'^2 + (z - z')^2]/(2\rho\rho')$ . The shorthand  $F(a, b; c; \lambda)$  implies Gauss' hypergeometric series  ${}_2F_1(a, b; c; \lambda)$ , that is

$$\begin{aligned} F(a, b; c; \lambda) &= \sum_{p=0}^{\infty} \frac{(a)_p (b)_p}{(c)_p p!} \lambda^p \\ &= \frac{\Gamma(c)}{\Gamma(a)\Gamma(b)} \sum_{p=0}^{\infty} \frac{\Gamma(a+p)\Gamma(b+p)}{\Gamma(c+p)p!} \lambda^p. \end{aligned} \quad (E6)$$

Hypergeometric functions are a general form for many functions, and often reduce with special cases to: elementary functions, a range of orthogonal polynomials, elliptic functions, incomplete beta/gamma functions, associated Legendre functions, etc. Mathematical software may determine if a given hypergeometric function reduces to a special case in order to apply an optimal computation algorithm, but this may not be possible in most cases when rational numbers are not used.

If  $\operatorname{Re}(c) > \operatorname{Re}(a) > 0$  in (E6), Euler's integral form is defined

$$F(a, b; c; \lambda) = \frac{\Gamma(c)}{\Gamma(b)\Gamma(c-b)} \int_0^1 \frac{t^{b-1} (1-t)^{c-b-1}}{(1-t\lambda)^a} dt. \quad (E7)$$

A useful integrable form follows from (E5) and (E6)

$$\begin{aligned} I(\nu, \nu, 0) &= (2\pi\rho\rho'\zeta)^{-\frac{1}{2}} (2\zeta)^{-\nu} \frac{\Gamma(\nu + \frac{1}{2})}{\Gamma[\frac{1}{4}(2\nu + 3)]\Gamma[\frac{1}{4}(2\nu + 1)]} \\ &\times \sum_{p=0}^{\infty} \frac{\Gamma[\frac{1}{4}(2\nu + 3) + p]\Gamma[\frac{1}{4}(2\nu + 1) + p]}{\Gamma(\nu + p + 1)p!} \zeta^{-2p}. \end{aligned} \quad (E8)$$

## E.2 Elliptic integrals

To remove non-integer inputs to the Gamma function  $\Gamma$  (allowing transformation to factorial form) and to significantly simplify the expression of (E8), Legendre's duplication formula [14, pg.5]

$$\Gamma(2\mu) = 2^{2\mu-1} \sqrt{\pi} \Gamma(\mu) \Gamma(\mu + \tfrac{1}{2}) \quad (\text{E9})$$

is used to give

$$I(\nu, \nu, 0) = (2\pi\rho\rho'\zeta)^{-\frac{1}{2}} (2\zeta)^{-\nu} \sum_{p=0}^{\infty} \frac{\Gamma[\nu + 2p + \frac{1}{2}]}{4^p \Gamma(\nu + p + 1) p!} \zeta^{-2p} \quad (\text{E10})$$

or

$$I(\nu, \nu, 0) = 2\sqrt{\frac{2}{\pi\rho\rho'\zeta}} \frac{1}{2^{3\nu}\zeta^\nu} \times \sum_{p=0}^{\infty} \frac{\Gamma[2(\nu + 2p)]}{2^{6p} \Gamma(\nu + p + 1)\Gamma(\nu + 2p) p!} \zeta^{-2p}; \quad (\text{E11})$$

however, (E11) introduces a singularity at  $\nu = p = 0$  – resolved by summing the series from  $\nu = 1$  and finding  $\nu = 0$  terms from (E10). Given the series

$$\sum_p A_p F(p\alpha + \mu, p\beta + \eta; p\gamma + \epsilon; \lambda), \quad (\text{E12})$$

if  $\beta = \gamma \neq 0$  then the Pfaff transform

$$F(a, b; c; \lambda) = (1 - \lambda)^{-a} F\left(a, c - b; c; \frac{\lambda}{\lambda - 1}\right) \quad (\text{E13})$$

eliminates  $p$  from the second argument [106, pg.425]. When  $c - a = 1$  in  $F(a, b; c; \lambda)$  [14, pg.89], it has the special case

$$B(\lambda; a, b) = a^{-1} \lambda^a (1 - \lambda)^b F(a + b, 1; a + 1; \lambda), \quad (\text{E14})$$

where  $B(\lambda; a, b)$  is the incomplete beta function

$$B(\lambda; a, b) = \int_0^\lambda t^{a-1} (1-t)^{b-1} dt. \quad (\text{E15})$$

The regularised beta function

$$I(\lambda; a, b) = \frac{B(\lambda; a, b)}{B(a, b)} \quad (\text{E16})$$

and beta function

$$B(1; a, b) = B(a, b) = \frac{\Gamma(a)\Gamma(b)}{\Gamma(a+b)}. \quad (\text{E17})$$

are used for recurrence relations (Appendix G). To avoid a common singularity

$$B(\tfrac{1}{2}, 0, \lambda) = \int_0^\lambda \left( \frac{1}{\sqrt{t}} + \frac{\sqrt{t}}{1-t} \right) dt = 2 \tanh^{-1} \sqrt{\lambda}. \quad (\text{E18})$$

## E.2 Elliptic integrals

The canonical incomplete Legendre elliptic integral definitions are

$$F(\theta; k^2) = \int_{t=0}^{\sin \theta} \frac{1}{\sqrt{(1-t^2)(1-k^2t^2)}} dt, \quad (\text{E19})$$

$$E(\theta; k^2) = \int_{t=0}^{\sin \theta} \frac{\sqrt{1-k^2t^2}}{\sqrt{1-t^2}} dt, \quad (\text{E20})$$

$$\Pi(\theta; a^2, k^2) = \int_{t=0}^{\sin \theta} \frac{1}{(1-a^2t^2)\sqrt{(1-t^2)(1-k^2t^2)}} dt, \quad (\text{E21})$$

$$\begin{aligned} D(\theta; k^2) &= \int_{t=0}^{\sin \theta} \frac{t^2}{\sqrt{(1-t^2)(1-k^2t^2)}} dt \\ &= \int_{t=0}^{\sin \theta} \frac{1-(1-k^2t^2)}{k^2\sqrt{(1-t^2)(1-k^2t^2)}} dt \\ &= \frac{F(\theta, k) - E(\theta, k)}{k^2}, \end{aligned} \quad (\text{E22})$$

with complete forms

$$F\left(\frac{\pi}{2}; k^2\right) = K(k^2), \quad (\text{E23})$$

$$E\left(\frac{\pi}{2}; k^2\right) = E(k^2), \quad (\text{E24})$$

$$\Pi\left(\frac{\pi}{2}; a^2, k^2\right) = \Pi(a^2; k^2), \quad (\text{E25})$$

$$D\left(\frac{\pi}{2}; k^2\right) = D(k^2), \quad (\text{E26})$$

and properties

$$F(-\theta, k) = -F(\theta, k), \quad (\text{E27})$$

$$F(\pi \pm \theta, k) = 2K(k) \pm F(\theta, k). \quad (\text{E28})$$

A common special case for the elliptic integral of the third kind is

$$\Pi(\theta; k^2, k^2) = \frac{1}{1-k^2} \left( E(\theta, k^2) - \frac{k^2 \sin(2\theta)}{2\sqrt{(1-k^2 \sin^2 \theta)}} \right). \quad (\text{E29})$$

## E.3 Series terms

Common terms found in the hypergeometric series expansions (E6) are

$$\binom{n}{k} = \frac{n!}{k!(n-k)!} = \prod_{i=1}^k \frac{n+1-i}{i}, \quad (\text{E30})$$

$$(n)_k = \frac{\Gamma(n+k)}{\Gamma(n)}, \quad (\text{E31})$$

$$\Gamma(1+\lambda) = \lambda \Gamma(\lambda), \quad (\text{E32})$$

$$\Gamma(\lambda) = (\lambda - 1)!, \quad (\text{E33})$$

$$n! = n \cdot (n-1)!. \quad (\text{E34})$$

Towards closed-form series solutions or a summand simplification, [106, pg.14] gives the identity

$$\sum_{n=0}^{\infty} \sum_{k=0}^{\infty} f(k, n) = \sum_{n=0}^{\infty} \sum_{k=0}^{\lfloor n/2 \rfloor} f(k, n-2k) \quad (\text{E35})$$

where the floor function

$$\lfloor n/2 \rfloor = \begin{cases} \frac{1}{2}n, & \text{for even } n \\ \frac{1}{2}(n-1), & \text{for odd } n. \end{cases} \quad (\text{E36})$$

## F Integral transforms & identities

General transforms and identities used within this article are summarised below.

$$\nabla^2 \mathbf{A} = \nabla(\nabla \cdot \mathbf{A}) - \nabla \times (\nabla \times \mathbf{A}) \quad (\text{F1})$$

$$\nabla \cdot (\mathbf{A} \times \mathbf{B}) = (\nabla \times \mathbf{A}) \cdot \mathbf{B} - (\nabla \times \mathbf{B}) \cdot \mathbf{A} \quad (\text{F2})$$

$$\nabla \cdot (\psi \mathbf{A}) = \psi(\nabla \cdot \mathbf{A}) + \mathbf{A} \cdot (\nabla \psi) \quad (\text{F3})$$

$$\nabla \times (\psi \mathbf{A}) = \psi(\nabla \times \mathbf{A}) + (\nabla \psi) \times \mathbf{A} \quad (\text{F4})$$

$$\mathbf{A} \cdot (\mathbf{B} \times \mathbf{C}) = \mathbf{B} \cdot (\mathbf{C} \times \mathbf{A}) = \mathbf{C} \cdot (\mathbf{A} \times \mathbf{B}) \quad (\text{F5})$$

$$\mathbf{A} \times (\mathbf{B} \times \mathbf{C}) = (\mathbf{A} \cdot \mathbf{C})\mathbf{B} - (\mathbf{A} \cdot \mathbf{B})\mathbf{C} \quad (\text{F6})$$

$$\mathbf{A} \times (\nabla \times \mathbf{B}) = (\nabla \mathbf{B}) \cdot \mathbf{A} - \mathbf{A} \cdot (\nabla \mathbf{B}) \quad (\text{F7})$$

$$\int_S (\nabla \times \mathbf{A}) \cdot d\mathbf{S} = \oint_C \mathbf{A} \cdot dl \quad (\text{F8})$$

$$\int_V \nabla \cdot \mathbf{A} dv = \oint_S \mathbf{A} \cdot \mathbf{n} da \quad (\text{F9})$$

A corollary to (F9) is Green's first identity, for  $\mathbf{A} \rightarrow \mathbf{B} \times \nabla \times \mathbf{A}$  and using (F2)

$$\begin{aligned} & \int_V [(\nabla \times \mathbf{A}) \cdot (\nabla \times \mathbf{B}) - \mathbf{B} \cdot (\nabla \times \nabla \times \mathbf{A})] dv \\ &= \oint_S [\mathbf{B} \times (\nabla \times \mathbf{A})] \cdot \mathbf{n} da. \end{aligned} \quad (\text{F10})$$

Green's second identity is obtained by swapping  $\mathbf{A}$  and  $\mathbf{B}$  in (F10) then subtracting from (F10)

$$\begin{aligned} & \int_V [\mathbf{A} \cdot (\nabla \times \nabla \times \mathbf{B}) - \mathbf{B} \cdot (\nabla \times \nabla \times \mathbf{A})] dv \\ &= \oint_S \{[\mathbf{B} \cdot [\mathbf{n} \times (\nabla \times \mathbf{A})] + (\nabla \times \mathbf{B}) \cdot (\mathbf{A} \times \mathbf{n})\} da, \end{aligned} \quad (\text{F11})$$

where  $\mathbf{n}$  has been brought inside the brackets using (F5).

The scalar analogue to (F10) for  $\mathbf{A} \rightarrow \psi \nabla \phi$  in (F9), and using (F2)

$$\int_V (\nabla \phi \cdot \nabla \psi + \phi \nabla^2 \psi) dv = \oint_S \phi \nabla \psi \cdot \mathbf{n} da. \quad (\text{F12})$$

Similarly, the scalar analogue to (F11)

$$\int_V (\phi \nabla^2 \psi - \psi \nabla^2 \phi) dv = \oint_S (\phi \nabla \psi - \psi \nabla \phi) \cdot \mathbf{n} da. \quad (\text{F13})$$

Another corollary to (F9), with  $\mathbf{A} \rightarrow \mathbf{A} \times \mathbf{B}$  and using (F2) on the left-hand side and (F5) on the right, gives

$$\int_V \mathbf{A} \cdot (\nabla \times \mathbf{B}) dv = \int_V \mathbf{B} \cdot (\nabla \times \mathbf{A}) dv + \oint_S \mathbf{B} \cdot (\mathbf{A} \times \mathbf{n}) da. \quad (\text{F14})$$

### F.1 Elementary integrals

The integral reduction from [15, pg.67]

$$\begin{aligned} & \int \frac{mx + n}{(a + 2bx + cx^2)^p} dx = \\ & \frac{bn - am + (cn - bm)x}{2(p-1)(ac - b^2)(a + 2bx + cx^2)^{p-1}} \\ &+ \frac{(2p-3)(cn - bm)}{2(p-1)(ac - b^2)} \int \frac{1}{(a + 2bx + cx^2)^{p-1}} dx, \end{aligned} \quad (\text{F15})$$

is useful for three special cases seen in this work; when  $p = 3/2$

$$\int \frac{mx + n}{(a + 2bx + cx^2)^{3/2}} dx = \frac{bn - am + (cn - bm)x}{(ac - b^2)\sqrt{a + 2bx + cx^2}}; \quad (\text{F16})$$

when  $p = 1/2$  and  $cn = bm$

$$\int \frac{mx + n}{(a + 2bx + cx^2)^{1/2}} dx = \frac{(am - bn)\sqrt{a + 2bx + cx^2}}{ac - b^2}; \quad (\text{F17})$$

and when  $p = 1/2$  and  $cn \neq bm$  it will lead into a second reduction, adapted from [15, pg.94]

$$\begin{aligned} \int \sqrt{(a + 2bx + cx^2)} dx &= \frac{cx + b}{2c} \sqrt{a + 2bx + cx^2} \\ &+ \frac{ac - b^2}{2c} \int \frac{1}{\sqrt{a + 2bx + cx^2}} dx, \end{aligned} \quad (\text{F18})$$

which contains the integral (with  $n = -1$  [15, pg.94])

$$\begin{aligned} & \int \frac{1}{\sqrt{a + 2bx + cx^2}} dx = \\ & \frac{1}{\sqrt{c}} \log(b + cx + \sqrt{c}\sqrt{a + 2bx + cx^2}). \end{aligned} \quad (\text{F19})$$

The integral from [15, pg.93]

$$\begin{aligned} & \int \frac{mx + n}{(d + a + bx + cx^2)\sqrt{a + bx + cx^2}} dx \\ &= \frac{m}{c\sqrt{d}} \tan^{-1} \sqrt{\frac{a + bx + cx^2}{d}} - \frac{2cn - bm}{c\sqrt{d[b^2 - 4c(a + d)]}} \\ & \times \tan^{-1} \left( \frac{d}{\sqrt{d[b^2 - 4c(a + d)]}} \frac{b + 2cx}{\sqrt{a + bx + cx^2}} \right), \quad d > 0, \\ &= \frac{m}{2c\sqrt{-d}} \ln \left( \frac{\sqrt{-d} - \sqrt{a + bx + cx^2}}{\sqrt{-d} + \sqrt{a + bx + cx^2}} \right) \\ &+ \frac{2cn - bm}{c\sqrt{d[b^2 - 4c(a + d)]}} \\ & \times \tan^{-1} \left( \sqrt{\frac{d}{b^2 - 4c(a + d)}} \frac{b + 2cx}{\sqrt{a + bx + cx^2}} \right), \quad d < 0, \end{aligned} \quad (\text{F20})$$

is commonly seen in this article for non-elliptic integrals. The form of (F20) typically comes from a second integral of (F16). For brevity, a useful simplification of the logarithm is

$$\int \frac{1}{1 - x^2} dx = \frac{1}{2} \ln \left( \frac{1+x}{1-x} \right) = \tanh^{-1} x, \quad (\text{F21})$$

for  $x < 1$ , and we note the basic property for odd functions

$$\operatorname{sgn}(x) \tan^{-1} |x| = \tan^{-1} x. \quad (\text{F22})$$

Similarly,

$$\int \frac{1}{\sqrt{a-x^2}} dx = \operatorname{sgn}(a-x) \ln(a-x). \quad (\text{F23})$$

## G Recurrence relations

### G.1 Beta and hypergeometric functions

Standard recurrence relations for the regularised beta function are [123, pg. 289]

$$I(\lambda; a, b) = \lambda I(\lambda; a-1, b) + (1-\lambda) I(\lambda; a, b-1), \quad (\text{G1})$$

$$I(\lambda; a, b) = I(\lambda; a+1, b) + \frac{\lambda^a (1-\lambda)^b}{a B(a, b)}, \quad (\text{G2})$$

$$I(\lambda; a, b) = I(\lambda; a, b+1) - \frac{\lambda^a (1-\lambda)^b}{b B(a, b)}. \quad (\text{G3})$$

Decrementing both  $a$  and  $b$  in (G2) and (G3), then respectively substituting  $I(\lambda; a, b-1)$  and  $I(\lambda; a-1, b)$  into (G1) gives

$$I(\lambda; a+1, b+1) = I(\lambda; a, b) + \frac{\lambda^a (1-\lambda)^b [a\lambda + b(\lambda-1)]}{ab B(a, b)}, \quad (\text{G4})$$

where  $a$  and  $b$  have been incremented. A useful transform then follows for the ratio

$$\frac{I(\lambda; a+1, b+1)}{I(\lambda; a, b)} = 1 + \frac{a\lambda + b(\lambda-1)}{b} F\left(\begin{matrix} a+b, 1 \\ 1+a \end{matrix}; \lambda\right)^{-1}, \quad (\text{G5})$$

where a number of terms cancel with the transform (E14). Following the process of (G5), with two successive iterations of (G3), another useful transform is

$$\frac{I(\lambda; a, b+2)}{I(\lambda; a, b)} = 1 + \frac{a}{b} \left( 1 + \frac{(a+b)(1-\lambda)}{1+b} \right) F\left(\begin{matrix} a+b, 1 \\ 1+a \end{matrix}; \lambda\right)^{-1}. \quad (\text{G6})$$

A final transform from (G3) and (G4) is

$$\begin{aligned} & I(\lambda; a+1, b+1) I(\zeta; c, d+1) \\ &= \left( I(\lambda; a, b) + \frac{\lambda^a (1-\lambda)^b [a\lambda + b(\lambda-1)]}{ab B(a, b)} \right) \\ & \times \left( I(\zeta; c, d) + \frac{\zeta^c (1-\zeta)^d}{d B(c, d)} \right), \end{aligned} \quad (\text{G7})$$

where in a similar process to (G5), gives

$$\begin{aligned} & \frac{I(\lambda; a+1, b+1) I(\zeta; c, d+1)}{I(\lambda; a, b) I(\zeta; c, d)} \\ &= 1 + \frac{c}{d F(c+d, 1; c+1; \zeta)} + \frac{a\lambda + b(\lambda-1)}{b F(a+b, 1; a+1; \lambda)} \\ & + \frac{c[a\lambda + b(\lambda-1)]}{bd F(a+b, 1; a+1; \lambda) F(c+d, 1; c+1; \zeta)}. \end{aligned} \quad (\text{G8})$$

Asymptotic expansions of the set of hypergeometric functions,  $F(\alpha + \epsilon_1 p, \beta + \epsilon_2 p; \gamma + \epsilon_3 p; \lambda)$  as  $p \rightarrow \infty$ , can be reduced to canonical forms by transformation formulae [124, 125]. The two of interest for this work are

$$\begin{aligned} F(a, b; c; \lambda) &= -\frac{\Gamma(c-1)\Gamma(a-c+1)\Gamma(b-c+1)}{\Gamma(a)\Gamma(b)\Gamma(1-c)} \\ & \times \lambda^{1-c} (1-\lambda)^{c-a-b} F\left(\begin{matrix} 1-a, 1-b \\ 2-c \end{matrix}; \lambda\right) \\ & + \frac{\Gamma(a-c+1)\Gamma(b-c+1)}{\Gamma(1-c)\Gamma(a+b-c+1)} F\left(\begin{matrix} a, b \\ a+b-c+1 \end{matrix}; 1-\lambda\right) \end{aligned} \quad (\text{G9})$$

and

$$\begin{aligned} F(a, b; c; \lambda) &= \\ & \frac{e^{\pi ai}}{\lambda^a} \frac{\Gamma(c)\Gamma(b-c+1)}{\Gamma(c-a)\Gamma(a+b-c+1)} F\left(\begin{matrix} a, a-c+1 \\ a+b-c+1 \end{matrix}; 1-\lambda^{-1}\right) \\ & + \frac{\Gamma(c)\Gamma(b-c+1)}{\Gamma(a)\Gamma(b-a+1)} \frac{\lambda^{a-c}}{(1-\lambda)^{a+b-c}} F\left(\begin{matrix} 1-a, c-a \\ b-a+1 \end{matrix}; \lambda^{-1}\right). \end{aligned} \quad (\text{G10})$$

The asymptotic expansion of the hypergeometric function as  $|p| \rightarrow \infty$  with  $\epsilon_2 = 0, \epsilon_3 = 1$  [126]:

$$F(\alpha + \epsilon p, \beta; \gamma + p; \lambda) \sim \begin{cases} \frac{1}{(1-\epsilon\lambda)^\beta}, & \text{if } |\lambda| < 1/\epsilon, \\ \frac{1}{(1-\epsilon\lambda)^\beta} + \delta(p), & \text{if } |\lambda| > 1/\epsilon, \end{cases} \quad (\text{G11})$$

is valid for  $b \notin \mathbb{Z} \setminus \mathbb{N}$  and  $\lambda < 1$ , where

$$\begin{aligned} \delta(p) &= \frac{\sqrt{2\pi}}{\Gamma(\beta)} \frac{(\epsilon-1)^{\alpha-\gamma+\frac{1}{2}}}{\epsilon^{\alpha-\frac{1}{2}}} \frac{\lambda^{1-\gamma} (\epsilon\lambda-1)^{\beta-1}}{(1-\lambda)^{\alpha+\beta-\gamma}} p^{\beta-\frac{1}{2}} \\ & \times \left[ \frac{1}{\epsilon^\epsilon \lambda} \left( \frac{\epsilon-1}{1-\lambda} \right)^{\epsilon-1} \right]^p. \end{aligned} \quad (\text{G12})$$

The asymptotic expansion of the hypergeometric function as  $|\gamma + \epsilon_3 p| \rightarrow \infty$  with  $\epsilon_1 = 0, \epsilon_2 = 0$  [126]:

$$F(\alpha, \beta; \gamma + \epsilon p; \lambda) \sim 1 + \frac{\alpha\beta}{\gamma + \epsilon p} \lambda. \quad (\text{G13})$$

### G.2 Elliptic integrals

The classical method for reducing elliptic integrals to Legendre normal form (E19, E20, E21) is given by [127, pg.296], with a useful summary and modern approach given by [128]. The elliptic integral

$$\int R[t, w(t)] dt, \quad w^2 = a_0 t^4 + 4a_1 t^3 + 6a_2 t^2 + 4a_3 t + a_4 \quad (\text{G14})$$

is a rational function that can be expressed as the sum of three integrals, an elementary function and two linear combinations with constant coefficients. A partial fraction decomposition gives

$$\begin{aligned} \int R[t, w(t)] dt &= \int R_0(t) dt + \sum_{n=0}^N a_n \int \frac{t^n}{w(t)} dt \\ & + \sum_{m=1}^M \sum_{p=1}^m b_{m,p} \int \frac{1}{(t-c_m)^p w(t)} dt, \end{aligned} \quad (\text{G15})$$

that have the recurrence relations

$$\begin{aligned} t^n w(t) &= (n+2)a_0 I_{n+3} + 2(2n+3)a_1 I_{n+2} \\ &\quad + 6(n+1)a_2 I_{n+1} + 2(2n+1)a_3 I_n + na_4 I_{n-1}, \end{aligned} \quad (\text{G16})$$

$$\begin{aligned} \frac{w(t)}{(t-c)^p} &= (2-p)b_0 H_{p-3} + 2(3-2p)b_1 H_{p-2} \\ &\quad + 6(1-p)b_2 H_{p-1} + 2(1-2p)b_3 H_p - pb_4 H_{p+1}, \end{aligned} \quad (\text{G17})$$

where

$$I_n = \int \frac{t^n}{w(t)} dt, \quad H_p = \int \frac{1}{(t-c)^p w(t)} dt,$$

and noting use of the identity

$$w^2(t) = b_0(t-c)^4 + 4b_1(t-c)^3 + 6b_2(t-c)^2 + 4b_3(t-c) + b_4.$$

## H Analytic force functions

From (393), the components of the force are

$$\begin{aligned} \check{F}_x &= \sin \varphi \sum_{p=0}^{\infty} \left[ -\varphi' \varsigma(0, p) - \frac{\cos(2\varphi - \varphi') + 2\varphi \sin \varphi'}{4 \sin \varphi} \varsigma(1, p) \right. \\ &\quad \left. - \sum_{\nu=2}^{\infty} \frac{\nu \cot(\varphi) \cos(\nu \Phi) + \sin(\nu \Phi)}{\nu^3 - \nu} \varsigma(\nu, p) + \sum_{u=0}^{\infty} \left( (\varphi' + \cot \varphi) \right. \right. \\ &\quad \times \varsigma(0, p, u) + \frac{\cos(2\varphi - \varphi')}{2 \sin \varphi} \varsigma(1, p, u) - \sum_{\nu=2}^{\infty} \frac{\sin(\nu \Phi)}{\nu} \varsigma(\nu, p, u) \left. \right) \end{aligned}$$

$$\begin{aligned} \check{F}_y &= \cos \varphi \sum_{p=0}^{\infty} \left[ \varphi' \varsigma(0, p) - \frac{\sin(2\varphi - \varphi') - 2\varphi \cos \varphi'}{4 \cos \varphi} \varsigma(1, p) \right. \\ &\quad \left. - \sum_{\nu=2}^{\infty} \frac{\nu \tan(\varphi) \cos(\nu \Phi) - \sin(\nu \Phi)}{\nu^3 - \nu} \varsigma(\nu, p) + \sum_{u=0}^{\infty} \left( (\tan \varphi - \varphi') \right. \right. \\ &\quad \times \varsigma(0, p, u) + \frac{\sin(2\varphi - \varphi')}{2 \cos \varphi} \varsigma(1, p, u) + \sum_{\nu=2}^{\infty} \frac{\sin(\nu \Phi)}{\nu} \varsigma(\nu, p, u) \left. \right) \end{aligned}$$

$$\begin{aligned} \check{F}_z &= \sum_{p=0}^{\infty} \left\{ -\cos(\Phi)(1+2p)\varsigma(0, p, 0, 0, 0) - \frac{1}{8}[4\varphi\varphi' - 2\varphi'^2 \right. \\ &\quad \left. + \cos(2\Phi)](2+2p)\varsigma(1, p, 0, 0, 0) - \sum_{\nu=2}^{\infty} \frac{1}{2} \left( \frac{\cos[(\nu-1)\Phi]}{(\nu-1)^2} \right. \right. \\ &\quad \left. + \frac{\cos[(\nu+1)\Phi]}{(\nu+1)^2} \right) (1+2p+\nu)\varsigma(\nu, p, 0, 0, 0) \\ &\quad + \sum_{u=0}^{\infty} \left[ \cos(\Phi)\varsigma(0, p, u, 0, 1) + \frac{\cos(2\Phi)}{4} \varsigma(1, p, u, 0, 1) \right. \\ &\quad \left. - \sum_{\nu=2}^{\infty} \left( \frac{\cos[(\nu-1)\Phi]}{\nu-1} - \frac{\cos[(\nu+1)\Phi]}{\nu+1} \right) \varsigma(\nu, p, u, 0, 1) \right. \\ &\quad \left. - \sum_{\nu,o=0}^{\infty} \frac{\cos(\Phi) \cos(\nu \Phi)}{1+2p+\nu} \varsigma(\nu, p, u, o, 0) \right] \right\} \end{aligned} \quad (\text{H1})$$

with the ancillary functions

$$\begin{aligned} \varsigma(\nu, p) &= \epsilon_{\nu} \frac{\rho^2}{2\sqrt{\pi}} \frac{\Gamma(\frac{1}{2} + \nu + 2p)}{p! (\nu + p)!} \left( \frac{L^2}{\rho^2} \right)^{\frac{1}{2} - \frac{\nu}{2} - p} \\ &\quad \times B(z^2; \frac{1}{2}(2 + \nu + 2p), \frac{1}{2}(-1 + \nu + 2p)), \end{aligned} \quad (\text{H2})$$

$$\begin{aligned} \varsigma(\nu, p, u) &= \epsilon_{\nu} \frac{\rho'^2}{4\sqrt{\pi}} \frac{\Gamma(1 + \frac{\nu}{2} + p) \Gamma(\frac{1}{2} + \nu + 2p + u)}{p! (\nu + p)! \Gamma(2 + \frac{\nu}{2} + p + u)} \\ &\quad \times \left( 1 + \frac{Z^2}{\rho'^2} \right)^{-\frac{\nu}{2} - p - u} B(x^2; \frac{1}{2}(1 + \nu + 2p), \frac{1}{2}(\nu + 2p + 2u)), \end{aligned}$$

$$\begin{aligned} \varsigma(\nu, p, u, o, l) &= \epsilon_{\nu} \frac{\rho \rho' \operatorname{sgn} Z}{8\sqrt{\pi}} \left( \frac{\rho \rho'}{\rho^2 + \rho'^2} \right)^{\nu+2p} \left( \frac{\rho^2}{\rho^2 + \rho'^2} \right)^o \\ &\quad \times \frac{(1 + \nu + 2p) \Gamma(\frac{1}{2} + \frac{\nu}{2} + p) \Gamma(\frac{1}{2} + \nu + 2p + u + o)}{p! (\nu + p)! \Gamma(\frac{3}{2} + \frac{\nu}{2} + p + o) \Gamma(\frac{3}{2} + \frac{\nu}{2} + p + u)} \\ &\quad \times \left[ \left( \frac{\rho'^2}{\rho^2 + \rho'^2} \right)^u + l \left( \frac{\rho^2}{\rho^2 + \rho'^2} \right)^u \right] B(y^2; \frac{1}{2}, \nu + 2p + u + o). \end{aligned}$$

## I Supplementary material

The supplementary material contains a Mathematica notebook file and package that implements the analytic solutions given in this article: evaluating the 3-D magnetic field at all points except for inherent singularities on the bounding surface, that are dependent on choice of Green's function. A comparison to the original numeric integral is given to 8 decimal places for all equations. In addition, the analytic force solutions are provided. A copy of this material can also be found online [115] that may be for the benefit of future updates or translating to other languages/software.

## J Principal magnetisation integral table and illustrations

This appendix contains Table J.1 and Table J.2: a set of integrals that are directly or indirectly solved in this article with a physical interpretation of charge and current distributions on a surface or within a volume.

## K Coil and magnet figures & tables

This appendix contains figures (Figure K.1 to Figure K.9) and tables (Table K.1 to Table K.6) generated from the analytic solutions in Sections 4 and 5. Results are compared with FEA and tabulated for assisting the reader with reproducibility.

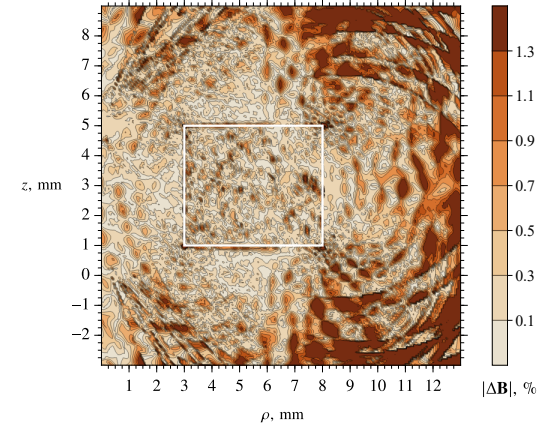
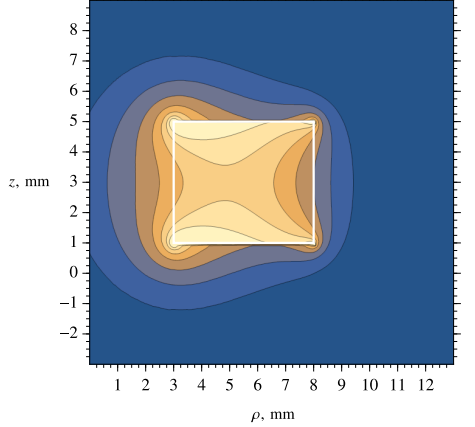
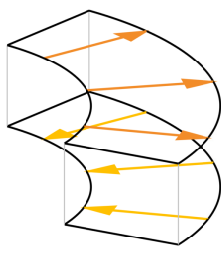
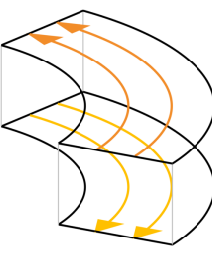
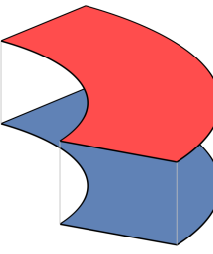
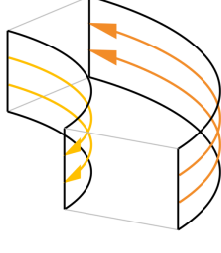
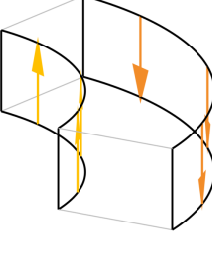
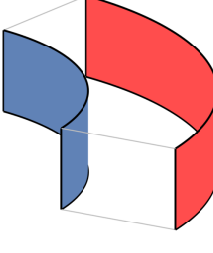
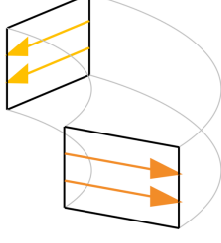
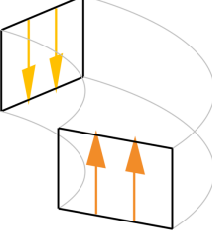
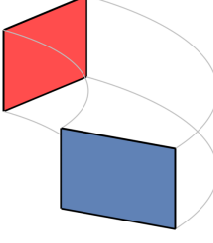
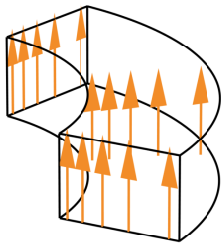
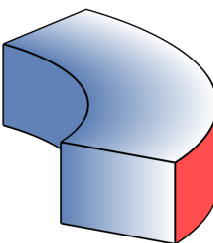


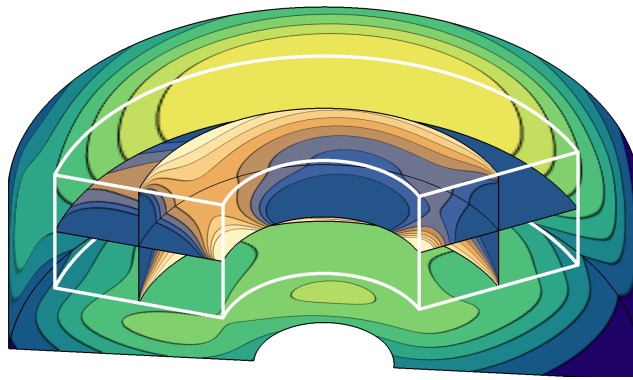
Figure J.1: Magnitude of the magnetic field  $|\mathbf{B}|$  of a permanent magnet with radial magnetisation  $M_\rho = 955 \text{ kA/m}$ , and asymmetric geometry  $\rho' \in [3, 8] \text{ mm}$ ,  $\varphi' \in [-\frac{\pi}{6}, \frac{3\pi}{5}] \text{ rad}$ ,  $z' \in [1, 5] \text{ mm}$ : an additional contour in Figure 16a. The magnet cross-section is shown in white.  $R = 10^{-2}$  was set for the series in  $B_z$ .

Table J.1: Integral formulations from cylindrical surfaces with a magnetic charge  $\sigma$  or current density  $\mathbf{K}$  due to a uniform magnetisation. In addition, shown is the volumetric charge  $\varrho$  and current density  $\mathbf{J}$  when the divergence or curl of the magnetisation is non-zero, respectively. Direction (Dir.) stipulates for each model, the direction of current flow or the direction connecting positive and negative magnetic charges – visualised with the figures in Table J.2. Shorthand  $G$  is shown for the Green's function  $G(\rho', \varphi', z')$ . The sign of each component is based upon a positive outward normal.

Geom.	Source	Dir.	$B_\rho$	$B_\varphi$	$B_z$
Disc	$\mathbf{K}$	$\rho$	$(z' - z) \iint_{\rho' \varphi'} \hat{G}^3 \rho' \sin(\varphi - \varphi') \quad (\text{J1})$	$(z' - z) \iint_{\rho' \varphi'} \hat{G}^3 \rho' \cos(\varphi - \varphi') \quad (\text{J2})$	$\rho \iint_{\rho' \varphi'} \hat{G}^3 \rho' \sin(\varphi - \varphi') \quad (\text{J3})$
	$\mathbf{K}$	$\varphi$	$(z - z') \iint_{\rho' \varphi'} \hat{G}^3 \rho' \cos(\varphi - \varphi') \quad (\text{J4})$	$(z' - z) \iint_{\rho' \varphi'} \hat{G}^3 \rho' \sin(\varphi - \varphi') \quad (\text{J5})$	$\iint_{\rho' \varphi'} \hat{G}^3 [\rho'^2 - \rho \rho' \cos(\varphi - \varphi')] \quad (\text{J6})$
	$\sigma$	$z$	$\iint_{\rho' \varphi'} \hat{G}^3 [\rho'^2 \cos(\varphi - \varphi') - \rho \rho'] \quad (\text{J7})$	$-\iint_{\rho' \varphi'} \hat{G}^3 \rho'^2 \sin(\varphi - \varphi') \quad (\text{J8})$	$(z' - z) \iint_{\rho' \varphi'} \hat{G}^3 \rho' \quad (\text{J9})$
Shell	$\mathbf{K}$	$\varphi$	$\rho' \iint_{\varphi' z'} \hat{G}^3 \cos(\varphi - \varphi')(z - z') \quad (\text{J10})$	$-\rho' \iint_{\varphi' z'} \hat{G}^3 \sin(\varphi - \varphi')(z - z') \quad (\text{J11})$	$\rho' \iint_{\varphi' z'} \hat{G}^3 [\rho' - \rho \cos(\varphi - \varphi')] \quad (\text{J12})$
	$\mathbf{K}$	$z$	$-\rho'^2 \iint_{\varphi' z'} \hat{G}^3 \sin(\varphi - \varphi') \quad (\text{J13})$	$\rho' \iint_{\varphi' z'} \hat{G}^3 [\rho - \rho' \cos(\varphi - \varphi')] \quad (\text{J14})$	$0 \quad (\text{J15})$
	$\sigma$	$\rho$	$\rho' \iint_{\varphi' z'} \hat{G}^3 [\rho' \cos(\varphi - \varphi') - \rho] \quad (\text{J16})$	$-\rho'^2 \iint_{\varphi' z'} \hat{G}^3 \sin(\varphi - \varphi') \quad (\text{J17})$	$-\rho' \iint_{\varphi' z'} \hat{G}^3 (z - z') \quad (\text{J18})$
Section	$\mathbf{K}$	$\rho$	$\sin(\varphi' - \varphi) \iint_{\rho' z'} \hat{G}^3 (z - z') \quad (\text{J19})$	$-\cos(\varphi - \varphi') \iint_{\rho' z'} \hat{G}^3 (z - z') \quad (\text{J20})$	$\rho \sin(\varphi - \varphi') \iint_{\rho' z'} \hat{G}^3 \quad (\text{J21})$
	$\mathbf{K}$	$z$	$\sin(\varphi' - \varphi) \iint_{\rho' z'} \hat{G}^3 \rho' \quad (\text{J22})$	$\iint_{\rho' z'} \hat{G}^3 [\rho - \rho' \cos(\varphi - \varphi')] \quad (\text{J23})$	$0 \quad (\text{J24})$
	$\sigma$	$\varphi$	$\iint_{\rho' z'} \hat{G}^3 [\rho' \cos(\varphi - \varphi') - \rho] \quad (\text{J25})$	$\sin(\varphi - \varphi') \iint_{\rho' z'} \hat{G}^3 \rho' \quad (\text{J26})$	$-\iint_{\rho' z'} \hat{G}^3 (z - z') \quad (\text{J27})$
Volume	$\mathbf{J}$	$\varphi$	$-\iiint_{\rho' \varphi' z'} \hat{G}^3 \rho' \sin(\varphi - \varphi') \quad (\text{J28})$	$\iiint_{\rho' \varphi' z'} \hat{G}^3 [\rho - \rho' \cos(\varphi - \varphi')] \quad (\text{J29})$	$0 \quad (\text{J30})$
	$\varrho$	$\rho$	$\iiint_{\rho' \varphi' z'} \hat{G}^3 [\rho' \cos(\varphi - \varphi') - \rho] \quad (\text{J31})$	$-\iiint_{\rho' \varphi' z'} \hat{G}^3 \rho' \sin(\varphi - \varphi') \quad (\text{J32})$	$-\iiint_{\rho' \varphi' z'} \hat{G}^3 (z - z') \quad (\text{J33})$

Table J.2: Illustrations of surface and volumetric charge or current densities from Table J.1. Each surface density is shown on two faces, with an opposing current direction or charge.

Geometry	Figure and equation reference		
Disc	(J1-3)	(J4-6)	(J7-9)
			
	Figure J.3	Figure J.4	Figure J.5
Shell	(J10-12)	(J13-15)	(J16-18)
			
	Figure J.6	Figure J.7	Figure J.8
Section	(J19-21)	(J22-24)	(J25-27)
			
	Figure J.9	Figure J.10	Figure J.11
Volume	(J28-30)	(J31-33)	
			
	Figure J.12	Figure J.13	



(a) Visualisation of the cylindrical surfaces in Cartesian coordinates for diametric magnetisation. Magnitudes are normalised for continuous contours.

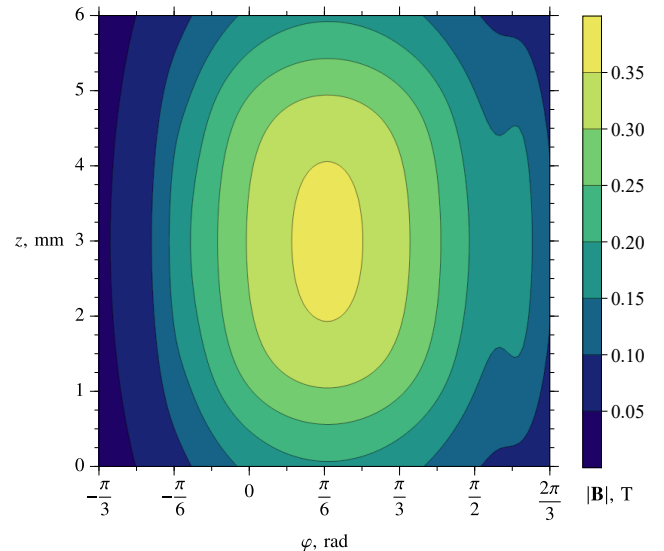
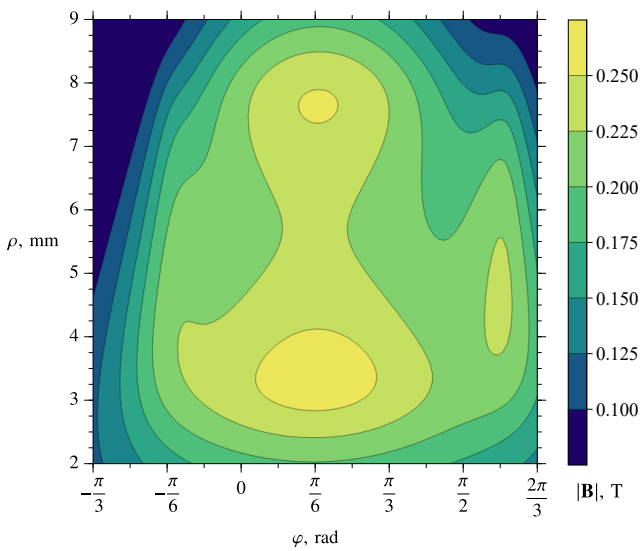
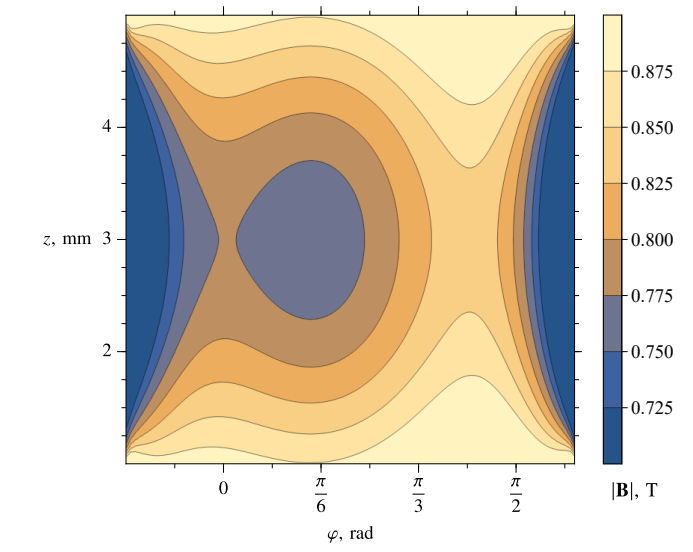
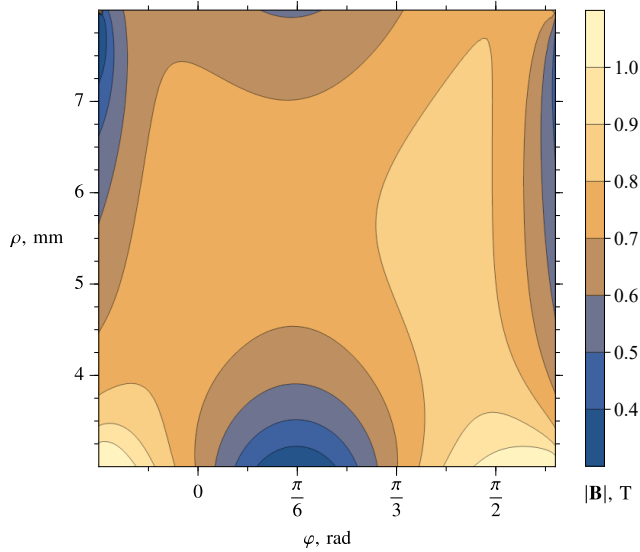


Figure K.1: Magnitude of the magnetic field  $|\mathbf{B}|$  of a permanent magnet with diametric magnetisation  $M_{\perp} = 955$  kA/m,  $\varphi^* = \pi/6$ , and asymmetric geometry  $\rho' \in [3, 8]$  mm,  $\varphi' \in [-\frac{\pi}{6}, \frac{3\pi}{5}]$  rad,  $z' \in [1, 5]$  mm.  $|\mathbf{B}|$  is shown on four rectangular cylindrical surfaces (b-e), inside and outside the volume of magnetisation, shown in white on (a).

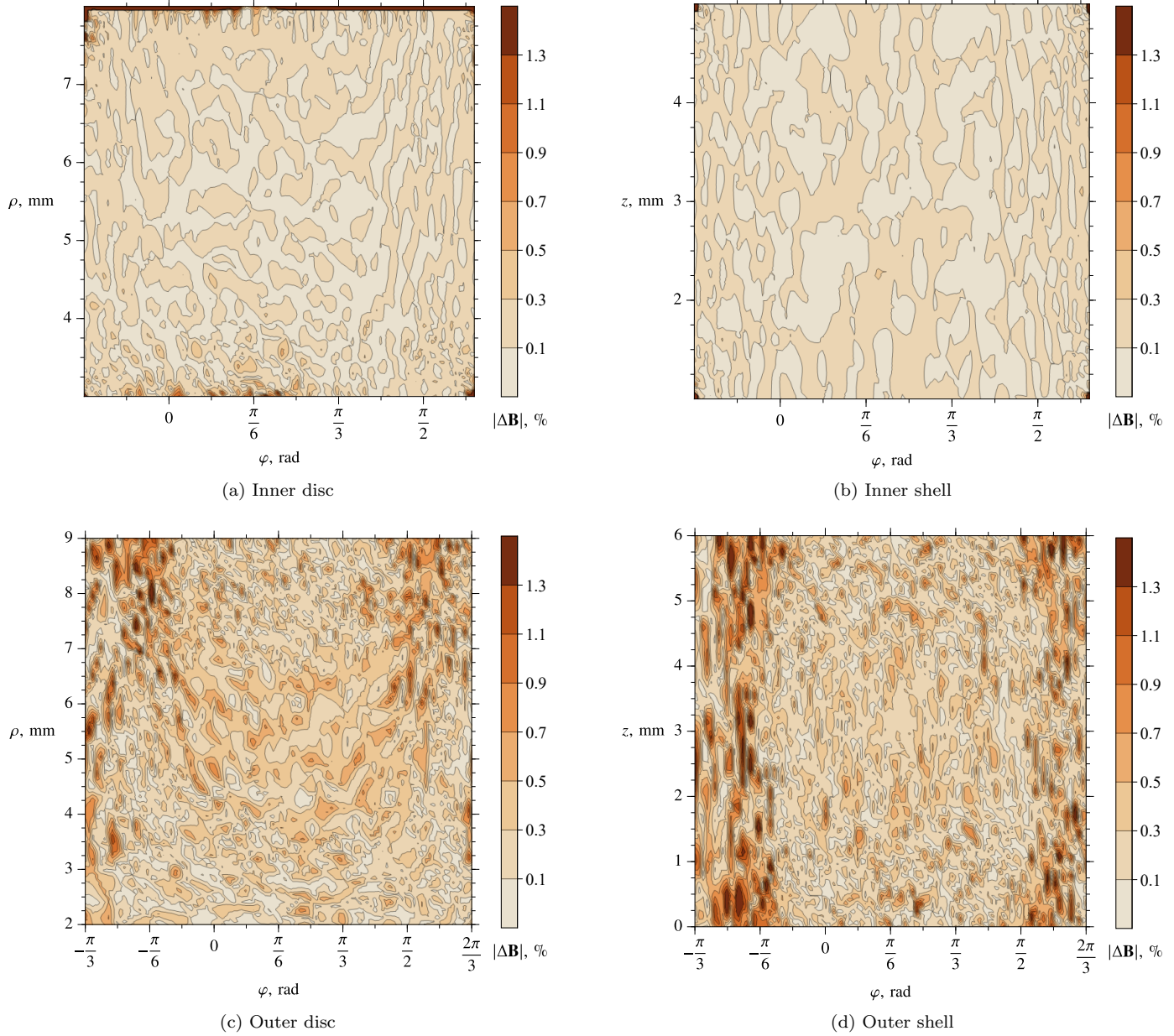


Figure K.2: The absolute relative difference of the magnetic field  $|\Delta\mathbf{B}|$  at the fields points shown in Figure K.1 with those in an FEA model. A summary of the FEA simulation results are given in Table K.1.

Table K.1: Summary of FEA model and analytic results comparison for the diametric magnetisation shown in Figure K.1.

(a) FEA simulation parameters and results		(b) FEA-Analytic comparison				
		Figure K.2				
		$ \Delta\mathbf{B} $ , %	(a)	(b)	(c)	(d)
Tetrahedra in matter	91,017					
Tetrahedra in vacuum	397,172					
Total energy error, %	0.008357					
Total energy, J	0.061971					
Delta energy, %	0.000342					

Table K.2: Comparison of the analytic result with an FEA model for a permanent magnet with diametric magnetisation  $M_\perp = 955 \text{ kA/m}$ ,  $\varphi^* = \pi/6$ . The field points encapsulate all equations in Section 5.1, inclusive of removable singularities, field regions, and geometries.

Field Point			Source Limits						Magnetic Flux Density					
$\rho$	$\varphi$	$z$	$\rho'_1$	$\rho'_2$	$\varphi'_1$	$\varphi'_2$	$z'_1$	$z'_2$	Test		Comparison	$B_\rho$	$B_\varphi$	$B_z$
9	$\frac{5\pi}{24}$	$\frac{31}{10}$	3	8	$-\frac{\pi}{6}$	$\frac{3\pi}{5}$	1	5	Standard	Analytic Result	0.35886722	0.01541823	0.0123206	
										FEA Difference	0.00093640	-0.00015097	0.0001756	
7	$\frac{5\pi}{24}$	$\frac{31}{10}$	3	8	$-\frac{\pi}{6}$	$\frac{3\pi}{5}$	1	5	Special Case a.	Analytic Result	0.69666433	-0.13682707	0.01255680	
										FEA Difference	0.00126020	0.00008486	0.00042681	
9	$\frac{5\pi}{24}$	$\frac{31}{10}$	3	8	0	$2\pi$	1	5	Special Case c.	Analytic Result	0.38988989	0.01766719	0.01281247	
										FEA Difference	0.00346473	-0.00046817	0.00009424	
9	$\frac{5\pi}{24}$	$\frac{31}{10}$	0	8	$-\frac{\pi}{6}$	$\frac{3\pi}{5}$	1	5	Special Case d.	Analytic Result	0.37680422	0.01650502	0.01265951	
										FEA Difference	0.00217526	-0.00006866	-0.00008838	
9	$\frac{5\pi}{24}$	$\frac{31}{10}$	0	8	0	$2\pi$	1	5	Special Case e.	Analytic Result	0.42011345	0.01963054	0.01333390	
										FEA Difference	0.00383436	-0.00055734	-0.00005755	
9	$-\frac{\pi}{6}$	5	3	8	$-\frac{\pi}{6}$	$\frac{3\pi}{5}$	1	5	Singularities b,c,f	Analytic Result	-0.05283942	-0.10630808	0.00501431	
										FEA Difference	0.00050087	0.00044318	0.00006397	
8	$-\frac{5\pi}{24}$	5	3	8	$-\frac{\pi}{6}$	$\frac{3\pi}{5}$	1	5	Singularities a,c,e	Analytic Result	-0.12706206	-0.01442552	-0.06078350	
										FEA Difference	0.00014631	0.00055291	-0.00002550	
8	$-\frac{\pi}{6}$	6	3	8	$-\frac{\pi}{6}$	$\frac{3\pi}{5}$	1	5	Singularities a,b,d	Analytic Result	-0.08575036	-0.08687165	-0.03159199	
										FEA Difference	0.00027164	0.00059761	-0.00001232	
$x$	$y$	$z$									$B_x$	$B_y$	$B_z$	
0	0	5	3	8	$-\frac{\pi}{6}$	$\frac{3\pi}{5}$	1	5	Special Case b.	Analytic Result	0.06907925	0.05798272	-0.09242139	
										FEA Difference	0.00064440	0.00038714	0.00000102	

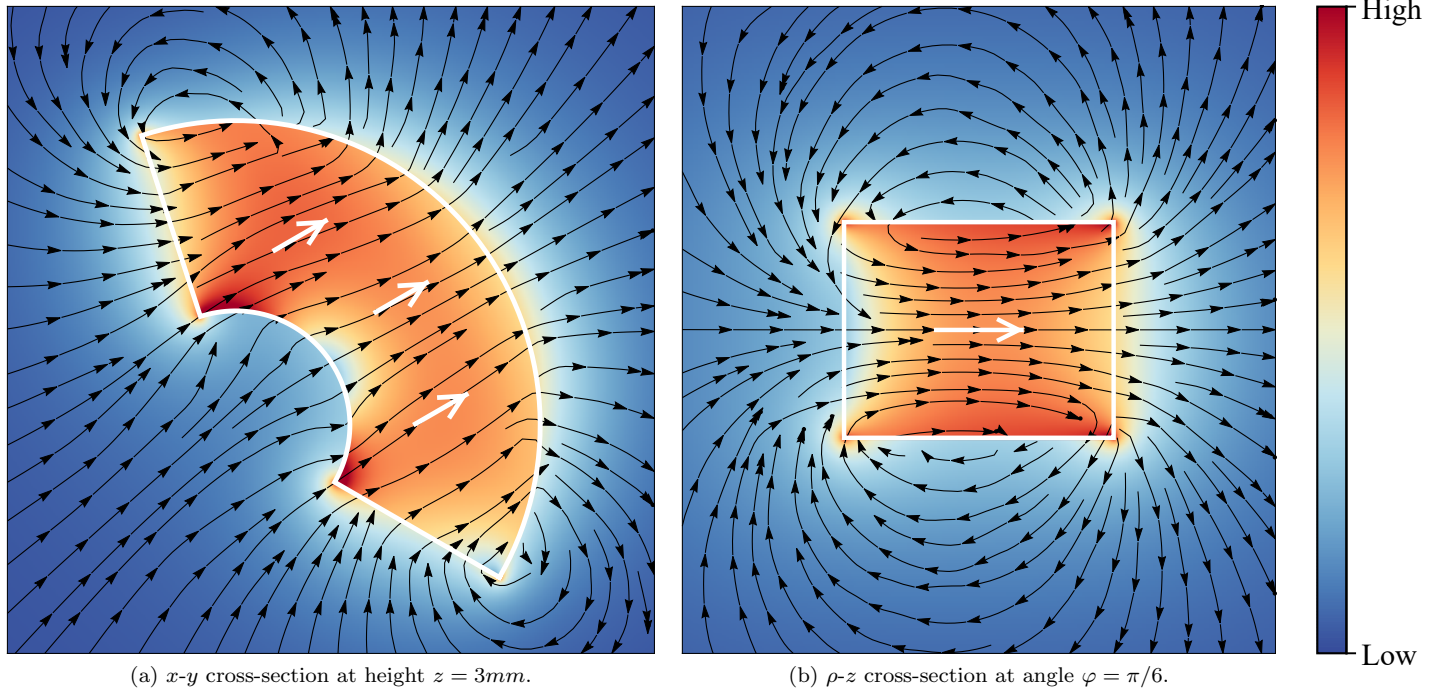
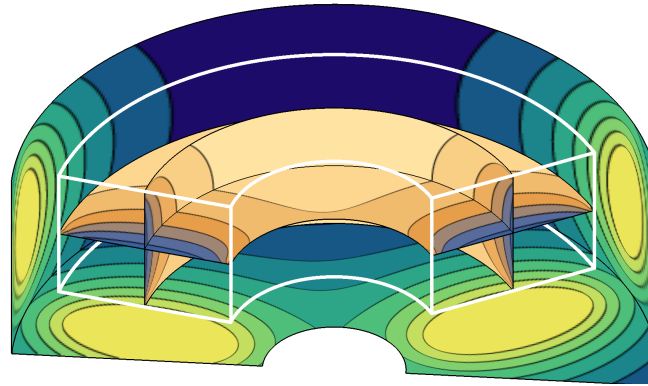
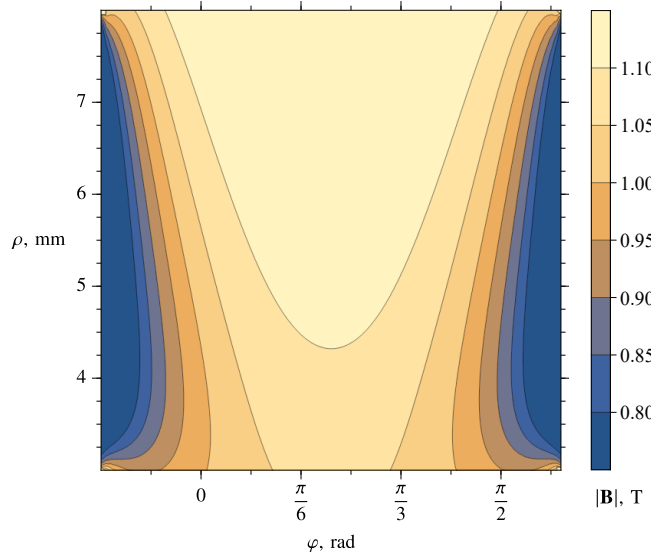


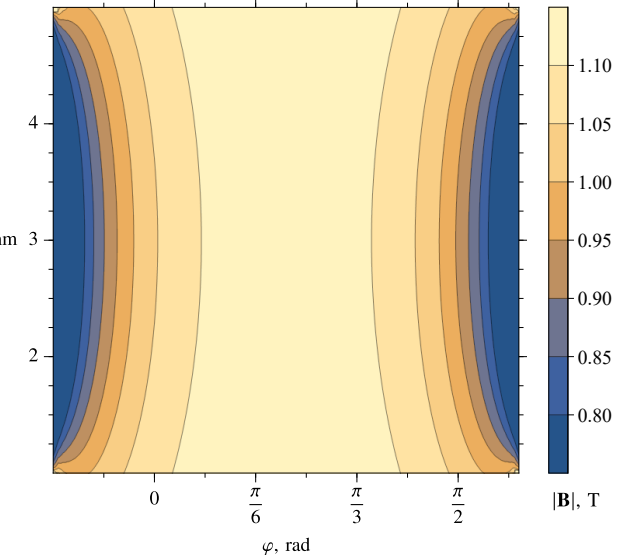
Figure K.3: Qualitative view of the magnetic field magnitude (low-high) with overlaid streamlines in black. The outlined geometry and magnetisation direction arrows are identical to Figure K.1 and shown in white.



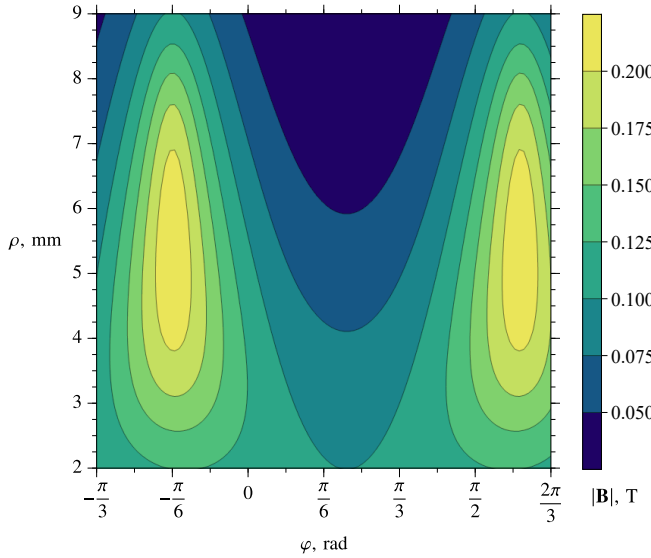
(a) Visualisation of the cylindrical surfaces in Cartesian coordinates for azimuthal magnetisation. Magnitudes are normalised for continuous contours.



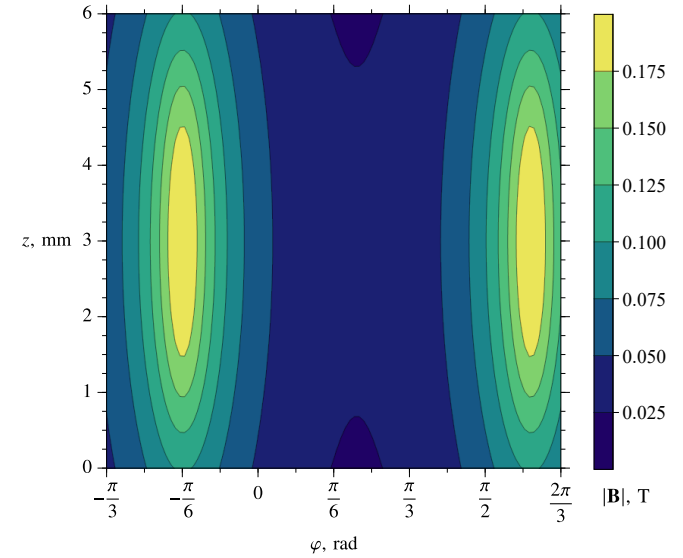
(b) Inner disc at  $z = 3$  mm



(c) Inner shell at  $\rho = 5.5$  mm



(d) Outer disc at  $z = 0$  mm



(e) Outer shell at  $\rho = 9$  mm

Figure K.4: Magnitude of the magnetic field  $|\mathbf{B}|$  of a permanent magnet with azimuthal magnetisation  $M_\varphi = 955 \text{ kA/m}$ , and asymmetric geometry  $\rho' \in [3, 8] \text{ mm}$ ,  $\varphi' \in [-\frac{\pi}{6}, \frac{3\pi}{5}] \text{ rad}$ ,  $z' \in [1, 5] \text{ mm}$ .  $|\mathbf{B}|$  is shown on four rectangular cylindrical surfaces (b-e), inside and outside the volume of magnetisation, shown in white on (a).

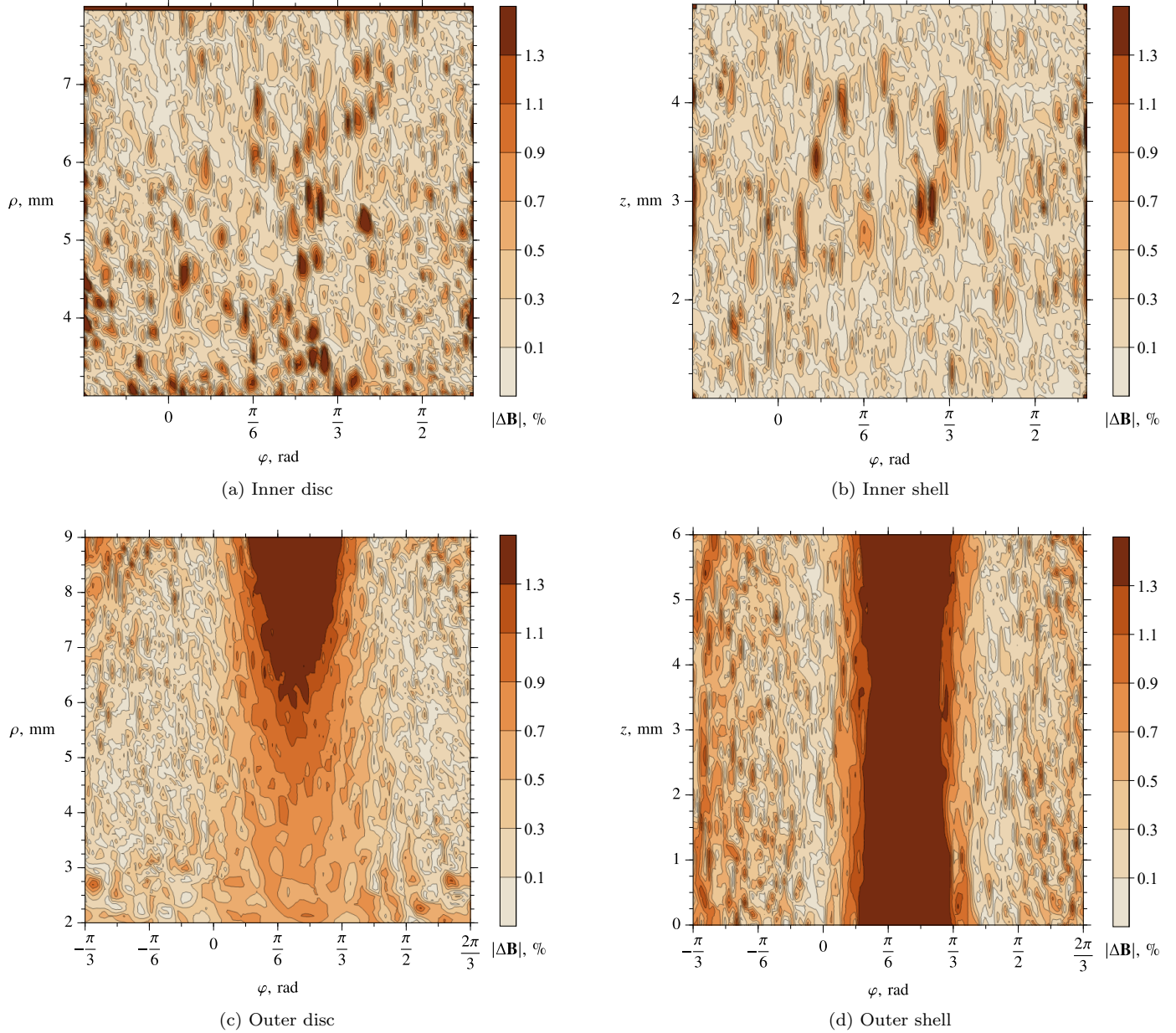


Figure K.5: The absolute relative difference of the magnetic field  $|\Delta\mathbf{B}|$  at the fields points shown in Figure K.4 with those in an FEA model. A summary of the FEA simulation results are given in Table K.3.

Table K.3: Summary of FEA model and analytic results comparison for the azimuthal magnetisation shown in Figure K.4.

(a) FEA simulation parameters and results		(b) FEA-Analytic comparison			
		Figure K.5			
		(a)	(b)	(c)	(d)
Tetrahedra in matter	91,409				
Tetrahedra in vacuum	396,923				
Total energy error, %	0.004856				
Total energy, J	0.029524				
Delta energy, %	0.027436				

Table K.4: Comparison of the analytic result with an FEA model for a permanent magnet with azimuthal magnetisation  $M_\varphi = 955 \text{ kA/m}$ . The field points encapsulate all equations in Section 5.3, inclusive of removable singularities, field regions, and geometries.

Field Point			Source Limits						Magnetic Flux Density					
$\rho$	$\varphi$	$z$	$\rho'_1$	$\rho'_2$	$\varphi'_1$	$\varphi'_2$	$z'_1$	$z'_2$	Test		Comparison	$B_\rho$	$B_\varphi$	$B_z$
9	$\frac{5\pi}{24}$	$\frac{31}{10}$	3	8	$-\frac{\pi}{6}$	$\frac{3\pi}{5}$	1	5	Standard	Analytic Result	-0.00098665	-0.02735309	-0.00002238	
FEA Difference										FEA Difference	-0.00003637	0.00061000	-0.00002043	
7	$\frac{5\pi}{24}$	$\frac{31}{10}$	3	8	$-\frac{\pi}{6}$	$\frac{3\pi}{5}$	1	5	Special Case a.	Analytic Result	-0.00121245	1.15272490	-0.00004258	
FEA Difference										FEA Difference	0.00037186	0.00348886	0.00050653	
9		$\frac{31}{10}$	3	8	0	$2\pi$	1	5	Special Case c.	Analytic Result	0	0	0	
FEA Difference										FEA Difference	-0.00000282	-0.00000027	-0.00000503	
9	$\frac{5\pi}{24}$	$\frac{31}{10}$	0	8	$-\frac{\pi}{6}$	$\frac{3\pi}{5}$	1	5	Special Case d.	Analytic Result	-0.00125494	-0.03240929	-0.00002681	
FEA Difference										FEA Difference	-0.00003403	0.00063505	-0.00000772	
9		$\frac{31}{10}$	0	8	0	$2\pi$	1	5	Special Case e.	Analytic Result	0	0	0	
FEA Difference										FEA Difference	-0.00001637	-0.00000090	-0.00001159	
9	$-\frac{\pi}{6}$	5	3	8	$-\frac{\pi}{6}$	$\frac{3\pi}{5}$	1	5	Singularities b,c,f	Analytic Result	-0.13055702	-0.00261183	-0.07915012	
FEA Difference										FEA Difference	-0.00076039	0.00017352	-0.00014746	
8	$-\frac{5\pi}{24}$	5	3	8	$-\frac{\pi}{6}$	$\frac{3\pi}{5}$	1	5	Singularities a,c,e	Analytic Result	-0.13060910	0.10456431	-0.12183068	
FEA Difference										FEA Difference	-0.00074368	0.00009855	-0.00007233	
8	$-\frac{\pi}{6}$	6	3	8	$-\frac{\pi}{6}$	$\frac{3\pi}{5}$	1	5	Singularities a,b,d	Analytic Result	-0.07776879	-0.00309965	-0.13400025	
FEA Difference										FEA Difference	-0.00057768	0.00023500	-0.00018297	
$x$	$y$	$z$									$B_x$	$B_y$	$B_z$	
0	0	5	3	8	$-\frac{\pi}{6}$	$\frac{3\pi}{5}$	1	5	Special Case b.	Analytic Result	0.06928255	-0.08555682	0	
FEA Difference										FEA Difference	-0.00039150	0.00053968	0.00002642	

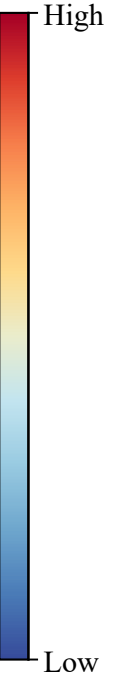
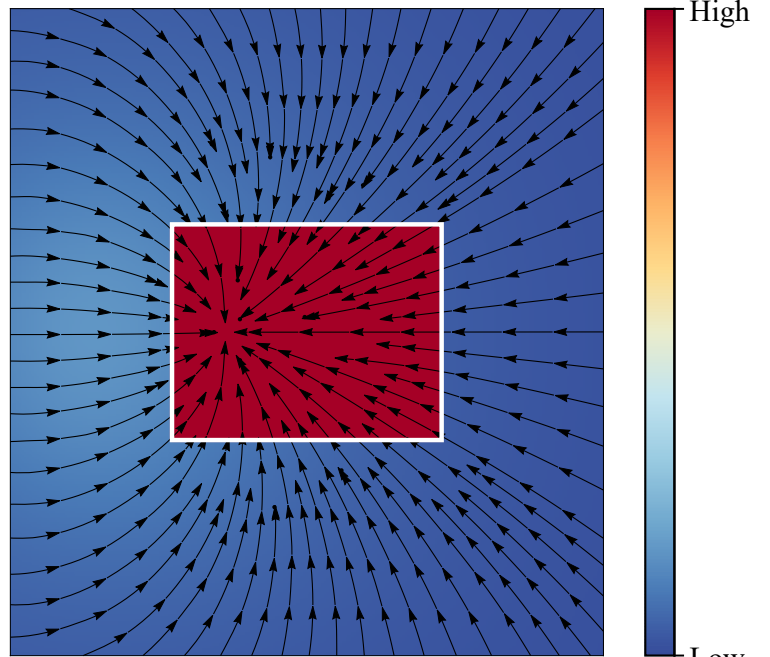
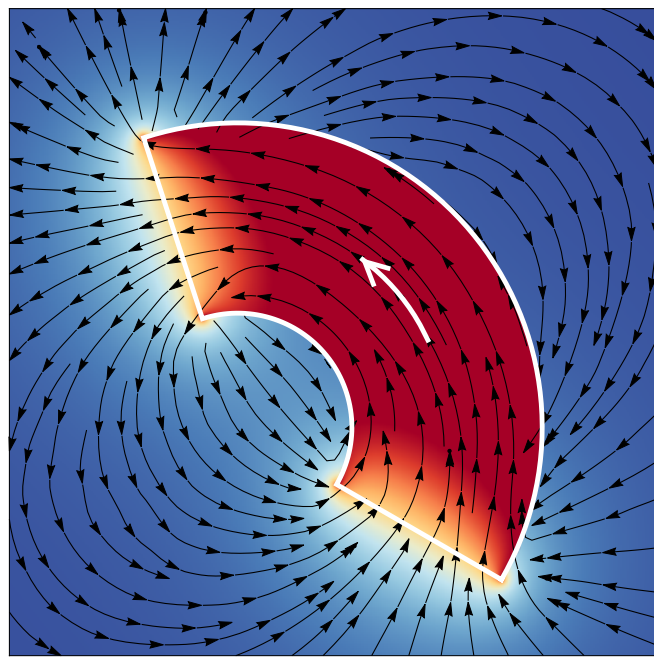
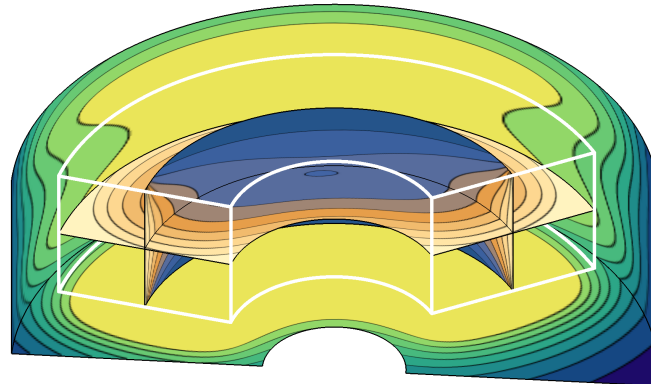
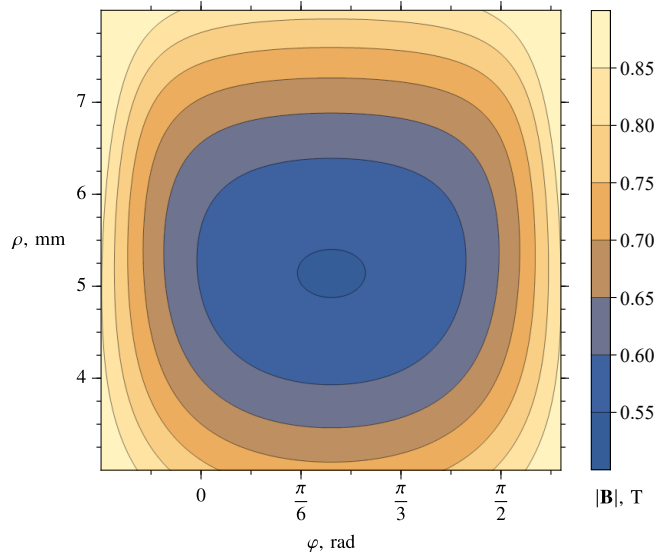


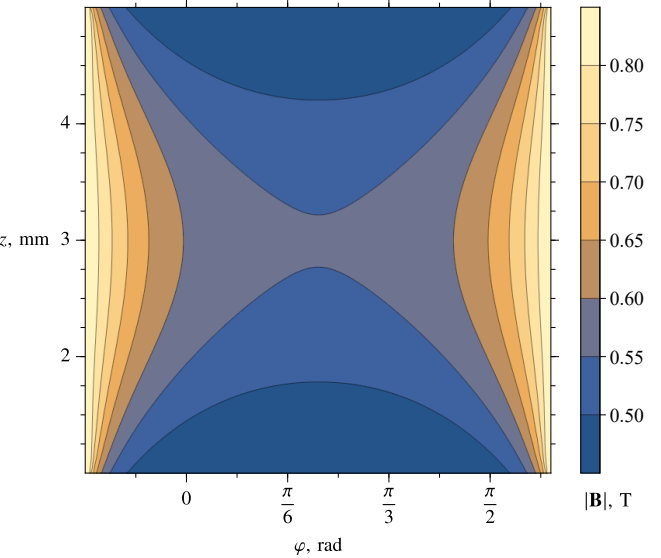
Figure K.6: Qualitative view of the magnetic field magnitude (low-high) with overlaid streamlines in black. The outlined geometry and magnetisation direction arrows are identical to Figure K.4 and shown in white.



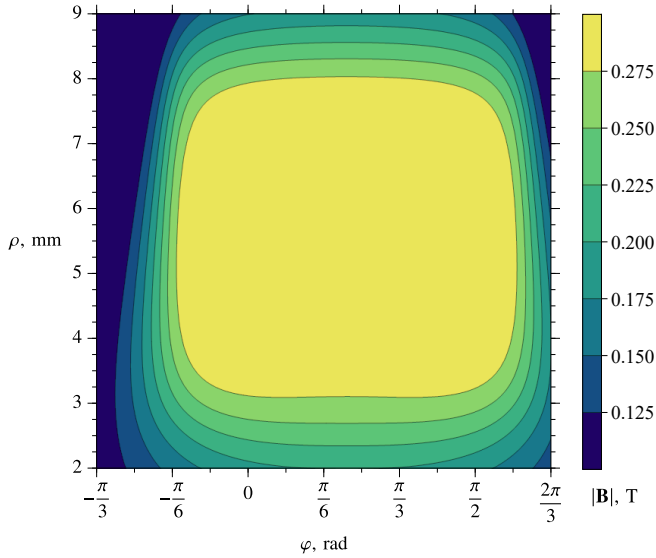
(a) Visualisation of the cylindrical surfaces in Cartesian coordinates for axial magnetisation. Magnitudes are normalised for continuous contours.



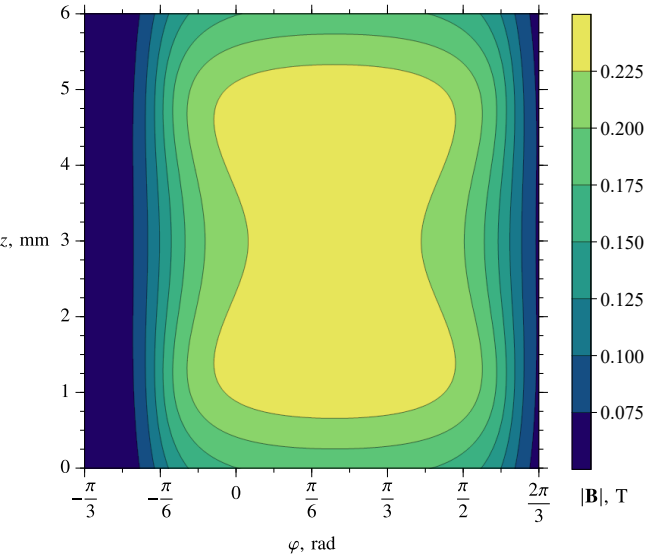
(b) Inner disc at  $z = 3$  mm



(c) Inner shell at  $\rho = 5.5$  mm



(d) Outer disc at  $z = 0$  mm



(e) Outer shell at  $\rho = 9$  mm

Figure K.7: Magnitude of the magnetic field  $|\mathbf{B}|$  of a permanent magnet with axial magnetisation  $M_z = 955 \text{ kA/m}$ , and asymmetric geometry  $\rho' \in [3, 8] \text{ mm}$ ,  $\varphi' \in [-\frac{\pi}{6}, \frac{3\pi}{5}] \text{ rad}$ ,  $z' \in [1, 5] \text{ mm}$ .  $|\mathbf{B}|$  is shown on four rectangular cylindrical surfaces (b-e), inside and outside the volume of magnetisation, shown in white on (a).

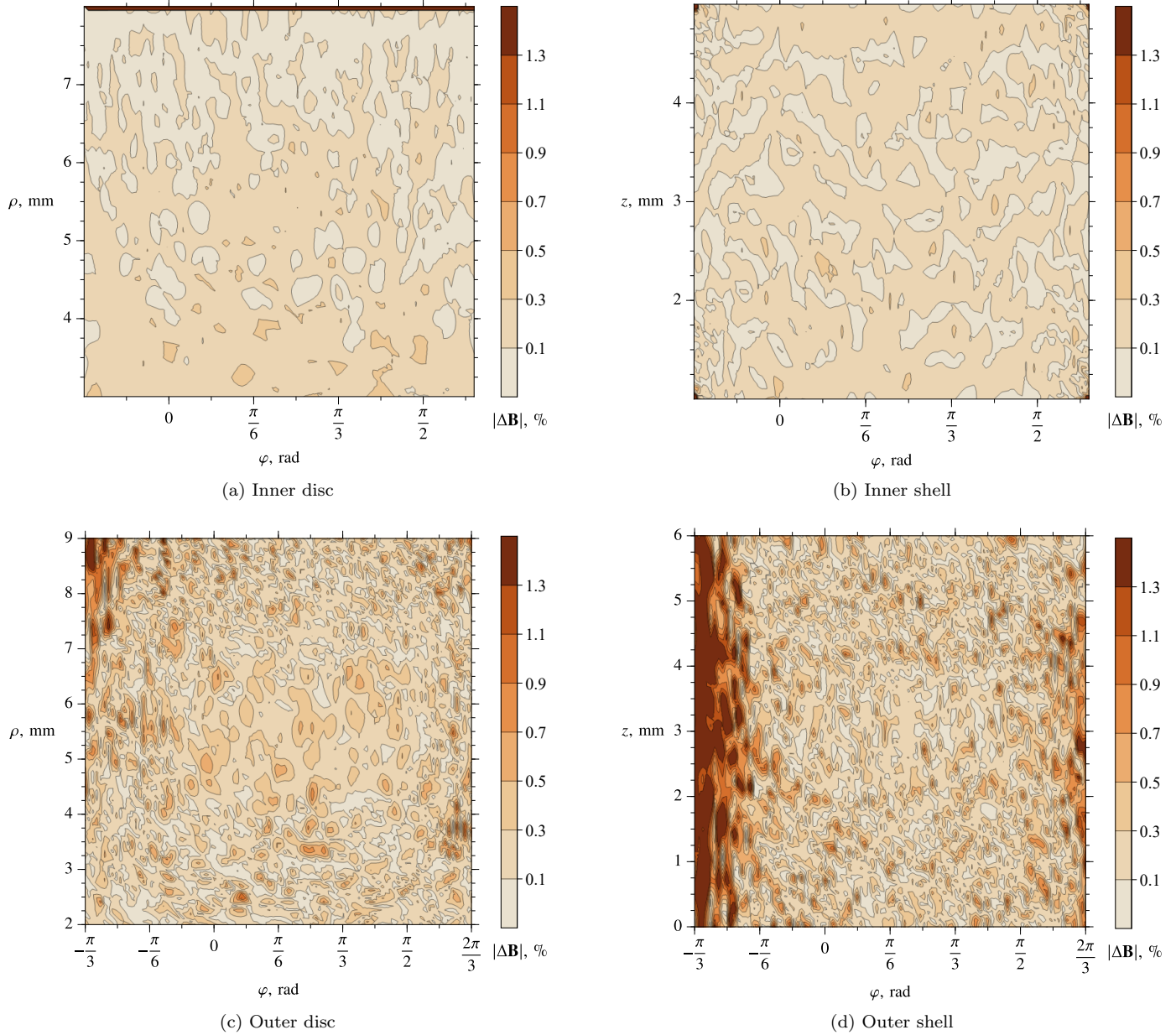


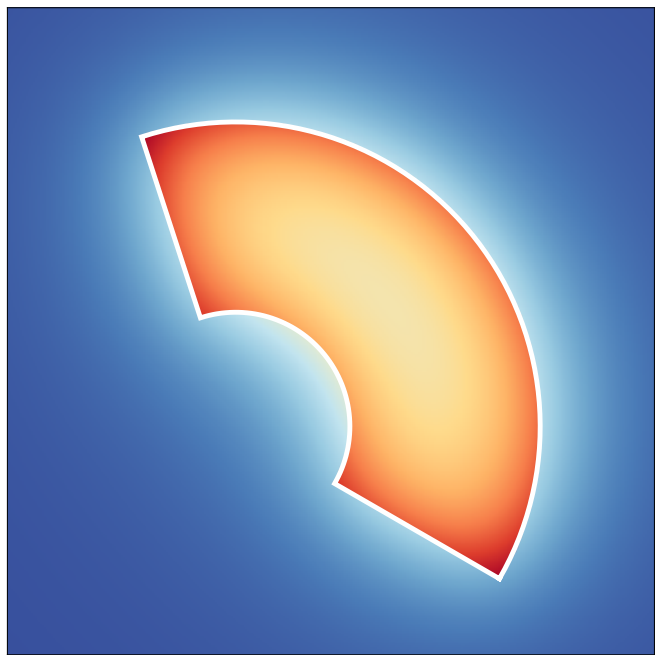
Figure K.8: The absolute relative difference of the magnetic field  $|\Delta\mathbf{B}|$  at the fields points shown in Figure K.7 with those in an FEA model. A summary of the FEA simulation results are given in Table K.5.

Table K.5: Summary of FEA model and analytic results comparison for the axial magnetisation shown in Figure K.7.

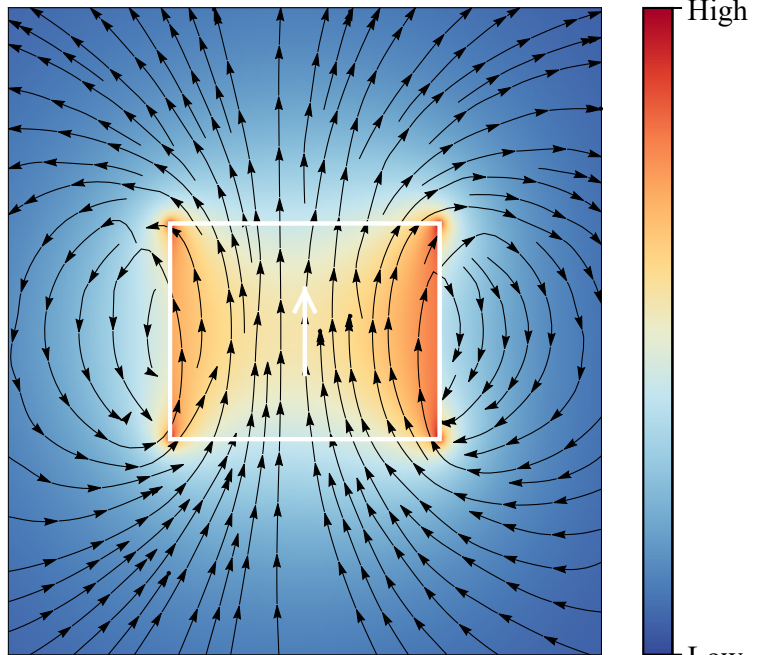
(a) FEA simulation parameters and results		(b) FEA-Analytic comparison				
		Figure K.8				
		$ \Delta\mathbf{B} $ , %	(a)	(b)	(c)	(d)
Tetrahedra in matter	88,075	Mean	0.96	0.16	0.25	0.40
Tetrahedra in vacuum	400,088	Max	128.02	45.72	1.78	3.20
Total energy error, %	0.007089					
Total energy, J	0.067948					
Delta energy, %	0.000342					

Table K.6: Comparison of the analytic result with an FEA model for a permanent magnet with axial magnetisation  $M_z = 955 \text{ kA/m}$ . The field points encapsulate all equations in Section 5.4, inclusive of removable singularities, field regions, and geometries.

Field Point			Source Limits						Test	Comparison	Magnetic Flux Density		
$\rho$	$\varphi$	$z$	$\rho'_1$	$\rho'_2$	$\varphi'_1$	$\varphi'_2$	$z'_1$	$z'_2$			$B_\rho$	$B_\varphi$	$B_z$
9	$\frac{5\pi}{24}$	$\frac{31}{10}$	3	8	$-\frac{\pi}{6}$	$\frac{3\pi}{5}$	1	5	Standard	Analytic Result	0.01242510	-0.00001393	-0.23580908
										FEA Difference	0.00004475	0.00001013	0.00039301
7	$\frac{5\pi}{24}$	$\frac{31}{10}$	3	8	$-\frac{\pi}{6}$	$\frac{3\pi}{5}$	1	5	Special Case <i>a.</i>	Analytic Result	0.01266085	-0.00003269	0.66334318
										FEA Difference	0.00073254	-0.00010102	0.00068139
9		$\frac{31}{10}$	3	8	0	$2\pi$	1	5	Special Case <i>c.</i>	Analytic Result	0.01292303	0	-0.25790066
										FEA Difference	0.00002447	0.00002765	0.00118312
9	$\frac{5\pi}{24}$	$\frac{31}{10}$	0	8	$-\frac{\pi}{6}$	$\frac{3\pi}{5}$	1	5	Special Case <i>d.</i>	Analytic Result	0.01276678	-0.00001494	-0.24487782
										FEA Difference	-0.00006579	-0.00000944	0.00040799
9		$\frac{31}{10}$	0	8	0	$2\pi$	1	5	Special Case <i>e.</i>	Analytic Result	0.01344896	0	-0.27334318
										FEA Difference	0.00004256	-0.00004102	0.00128077
9	$-\frac{\pi}{6}$	5	3	8	$-\frac{\pi}{6}$	$\frac{3\pi}{5}$	1	5	Singularities <i>b,c,f</i>	Analytic Result	0.11310076	-0.05950873	-0.05720141
										FEA Difference	0.00034513	-0.00013975	0.00072464
8	$-\frac{5\pi}{24}$	5	3	8	$-\frac{\pi}{6}$	$\frac{3\pi}{5}$	1	5	Singularities <i>a,c,e</i>	Analytic Result	0.08547084	-0.10119477	-0.05944892
										FEA Difference	0.00001957	-0.00006369	0.00066719
8	$-\frac{\pi}{6}$	6	3	8	$-\frac{\pi}{6}$	$\frac{3\pi}{5}$	1	5	Singularities <i>a,b,d</i>	Analytic Result	0.12866196	-0.11076231	0.05821848
										FEA Difference	0.00005530	-0.00017009	0.00101517
$x$	$y$	$z$								$B_x$	$B_y$	$B_z$	
0	0	5	3	8	$-\frac{\pi}{6}$	$\frac{3\pi}{5}$	1	5	Special Case <i>b.</i>	Analytic Result	-0.07272022	-0.05888767	-0.08114685
										FEA Difference	0.00011472	0.00010381	0.00073041



(a)  $x$ - $y$  cross-section at height  $z = 3\text{mm}$ .



(b)  $\rho$ - $z$  cross-section at angle  $\varphi = \pi/6$ .

Figure K.9: Qualitative view of the magnetic field magnitude (low-high) with overlaid streamlines in black. The outlined geometry and magnetisation direction arrows are identical to Figure K.7 and shown in white. The in-plane  $x$ - $y$  field in (a) is zero.